Defense Threat Reduction Agency
8725 John J. Kingman Road, MS 6201
Fort Belvoir, VA 22060-6201

DTRA-TR-03-47

TECHNICAL REPORT

Characterization of the Infrasound Field in the Central Pacific

Approved for public release; distribution is unlimited.

June 2006

DESTRUCTION NOTICE

FOR CLASSIFIED documents, follow the procedures in DoD 5550.22-M, National Industrial Security Program Operating Manual, Chapter 5, Section 7 (NISPOM) or DoD 5200.1-R, Information Security Program Regulation, Chapter 1X.

FOR UNCLASSIFIED limited documents, destroyed by any method that will prevent disclosure of contents or reconstruction of the document.

Retention of this document by DoD contractors is authorized in accordance with DoD 5220.22M, Industrial Security manual.

PLEASE NOTIFY THE DEFENSE THREAT REDUCTION AGENCY, ATTN: IMMI, 8725 JOHN J. KINGMAN ROAD, MS-6201, FT. BELVOIR, VA 22060-6201. IF YOUR ADDRESS IS INCORRECT, IF YOU WISH IT DELETED FROM THE DISTRIBUTION LIST, OR IF THE ADDRESSEE IS NO LONGER EMPLOYED BY YOUR ORGANIZATION.

DISTRIBUTION LIST UPDATE

This mailer is provided to enable DTRA to maintain current distribution lists for reports. (We would appreciate you providing the requested information.)

❑ Add the individual listed to your distribution list.

❑ Delete the cited organization/individual.

❑ Change of address.

> Note:
> Please return the mailing label from the document so that any additions, changes, corrections or deletions can be made easily. For distribution cancellation or more information call DTRA/BDMI (703) 767-4724.

NAME: _____

ORGANIZATION: _____

OLD ADDRESS	**NEW ADDRESS**
_____	_____
_____	_____
_____	_____

TELEPHONE NUMBER: (   ) _____

DTRA PUBLICATION NUMBER/TITLE	**CHANGES/DELETIONS/ADDITONS, etc.** *(Attach Sheet if more Space is Required)*
_____	_____
_____	_____
_____	_____

DTRA or other GOVERNMENT CONTRACT NUMBER: _____

CERTIFICATION of NEED-TO-KNOW BY GOVERNMENT SPONSOR (if other than DTRA):

SPONSORING ORGANIZATION: _____

CONTRACTING OFFICER or REPRESENTATIVE: _____

SIGNATURE: _____

DEFENSE THREAT REDUCTION AGENCY
ATTN: BDLMI
8725 John J Kingman Road, MS 6201
Fort Belvoir, VA 22060-6201

DEFENSE THREAT REDUCTION AGENCY
ATTN: BDLMI
8725 John J Kingman Road, MS 6201
Fort Belvoir, VA 22060-6201

1. AGENCY USE ONLY (Leave blank)	2. REPORT DATE	3. REPORT TYPE AND DATES COVERED
	June 2006	Technical

4. TITLE AND SUBTITLE	5. FUNDING NUMBERS
Characterization of the Infrasound Field in the Central Pacific	C - DTRA 01-00-C-0106 PE - YYYA PR - OH TA OO WU - DH99810

6. AUTHOR(S)

Claus Hetzer and Milton Garces

7. PERFORMING ORGANIZATION NAME(S) AND ADDRESS(ES)	8. PERFORMING ORGANIZATION REPORT
University of Hawaii Infrasound Laboratory 73-4460 Queen Kaahamanu Highway, # 119 Kailua-Kona, HI 96740-2638	

9. SPONSORING/MONITORING AGENCY NAME(S) AND ADDRESS(ES)	10. SPONSORING/MONITORING AGENCY REPORT NUMBER
Defense Threat Reduction Agency 8725 John J. Kingman Road, MSC 6201 Fort Belvoir, VA 22060-6201 NTD/D. Barber	DTRA-TR-03-47

11. SUPPLEMENTARY NOTES

12a. DISTRIBUTION/AVAILABILITY STATEMENT	12B. DISTRIBUTION CODE
Approved for public release; distribution is unlimited.	

13. ABSTRACT (Maximum 200 words)

This document reviews the results of three years of infrasound recording and analysis at the Infrasound Laboratory (ISLA) of the University of Hawaii. ISLA is responsible for the operation and maintenance of infrasound station I59US, Kona, Hawaii. I59US entered into operations in July 2000 and was certified into the International Monitoring System (IMS) of the Comprehensive Nuclear-Test Ban Treaty (CTBT) in December 2001. The array site is in a tropical rainforest on the slopes of Hualalai Volcano, Hawaii Island, Hawaii. Per IMS specifications at the time of the installation, the array consists of four microphones arranged as a triangle with a 2 km baseline and a central element. This site is well-forested with 20-30 m ohia trees, 2-3 m tree ferns, and ground ferns, which form a multilayered wind barrier.

14. SUBJECT TERMS		15.NUMBER OF PAGES
Earthquakes Microbaroms Algorithms Infrasonic		230
		16. PRICE CODE

17. SECURITY CLASSIFICATION OF THIS PAGE	18. SECURITY CLASSIFICATION OF REPORT	19. SECURITY CLASSIFICATION OF ABSTRACT	20. LIMITATION OF ABSTRACT
UNCLASSIFIED	UNCLASSIFIED	UNCLASSIFIED	SAR

CONVERSION TABLE

Conversion Factors for U.S. Customary to metric (SI) units of measurement.

MULTIPLY ──────────────► BY ──────────────► TO GET

TO GET ◄────────────── BY ◄────────────── DIVIDE

angstrom	1.000 000 x E -10	meters (m)
atmosphere (normal)	1.013 25 x E +2	kilo pascal (kPa)
bar	1.000 000 x E +2	kilo pascal (kPa)
barn	1.000 000 x E -28	meter^2 (m^2)
British thermal unit (thermochemical)	1.054 350 x E +3	joule (J)
calorie (thermochemical)	4.184 000	joule (J)
cal (thermochemical/cm^2)	4.184 000 x E -2	mega joule/m^2 (MJ/m^2)
curie	3.700 000 x E +1	*giga bacquerel (GBq)
degree (angle)	1.745 329 x E -2	radian (rad)
degree Fahrenheit	$t_k = (t°f + 459.67)/1.8$	degree kelvin (K)
electron volt	1.602 19 x E -19	joule (J)
erg	1.000 000 x E -7	joule (J)
erg/second	1.000 000 x E -7	watt (W)
foot	3.048 000 x E -1	meter (m)
foot-pound-force	1.355 818	joule (J)
gallon (U.S. liquid)	3.785 412 x E -3	meter^3 (m^3)
inch	2.540 000 x E -2	meter (m)
jerk	1.000 000 x E +9	joule (J)
joule/kilogram (J/kg) radiation dose absorbed	1.000 000	Gray (Gy)
kilotons	4.183	terajoules
kip (1000 lbf)	4.448 222 x E +3	newton (N)
kip/inch^2 (ksi)	6.894 757 x E +3	kilo pascal (kPa)
ktap	1.000 000 x E +2	newton-second/m^2 (N-s/m^2)
micron	1.000 000 x E -6	meter (m)
mil	2.540 000 x E -5	meter (m)
mile (international)	1.609 344 x E +3	meter (m)
ounce	2.834 952 x E -2	kilogram (kg)
pound-force (lbs avoirdupois)	4.448 222	newton (N)
pound-force inch	1.129 848 x E -1	newton-meter (N-m)
pound-force/inch	1.751 268 x E +2	newton/meter (N/m)
pound-force/foot^2	4.788 026 x E -2	kilo pascal (kPa)
pound-force/inch^2 (psi)	6.894 757	kilo pascal (kPa)
pound-mass (lbm avoirdupois)	4.535 924 x E -1	kilogram (kg)
pound-mass-foot^2 (moment of inertia)	4.214 011 x E -2	kilogram-meter^2 (kg-m^2)
pound-mass/foot^3	1.601 846 x E +1	kilogram-meter^3 (kg/m^3)
rad (radiation dose absorbed)	1.000 000 x E -2	**Gray (Gy)
roentgen	2.579 760 x E -4	coulomb/kilogram (C/kg)
shake	1.000 000 x E -8	second (s)
slug	1.459 390 x E +1	kilogram (kg)
torr (mm Hg, 0° C)	1.333 22 x E -1	kilo pascal (kPa)

*The bacquerel (Bq) is the SI unit of radioactivity; 1 Bq = 1 event/s.
**The Gray (GY) is the SI unit of absorbed radiation.

1. Introduction

The objectives of this project were to characterize the infrasonic background field, improve phase identifications for detected signals, and quantify the temporal variability of infrasonic wave propagation in the Central Pacific. We fulfilled these goals by evaluating and optimizing infrasonic detection algorithms for I59US, performing detection and location analyses for specific events in the Pacific and the America, and interpreting long term seasonal trends in the dominant infrasonic signals routinely observed in Hawaii.

This document reviews the results of three years of infrasound recording and analysis at the Infrasound Laboratory (ISLA) of the University of Hawaii. ISLA is responsible for the operation and maintenance of infrasound station I59US, Kona, Hawaii. I59US entered into operations in July 2000 and was certified into the International Monitoring System (IMS) of the Comprehensive Nuclear-Test-Ban Treaty (CTBT) in December 2001. The array site is in a tropical rainforest on the slopes of Hualalai Volcano, Hawaii Island, Hawaii. Per IMS specifications at the time of installation, the array consists of four microphones arranged as a triangle with a 2 km baseline and a central element (Figure 1; Table 1). The site is well-forested with 20-30 m ohia trees, 2-3 m tree ferns, and ground ferns, which form an effective multi-layered wind barrier. Also, the three large shield volcanoes to the east of the array block the prevalent trade winds. This combination of natural wind shelters makes I59US one of the quietest stations in the IMS.
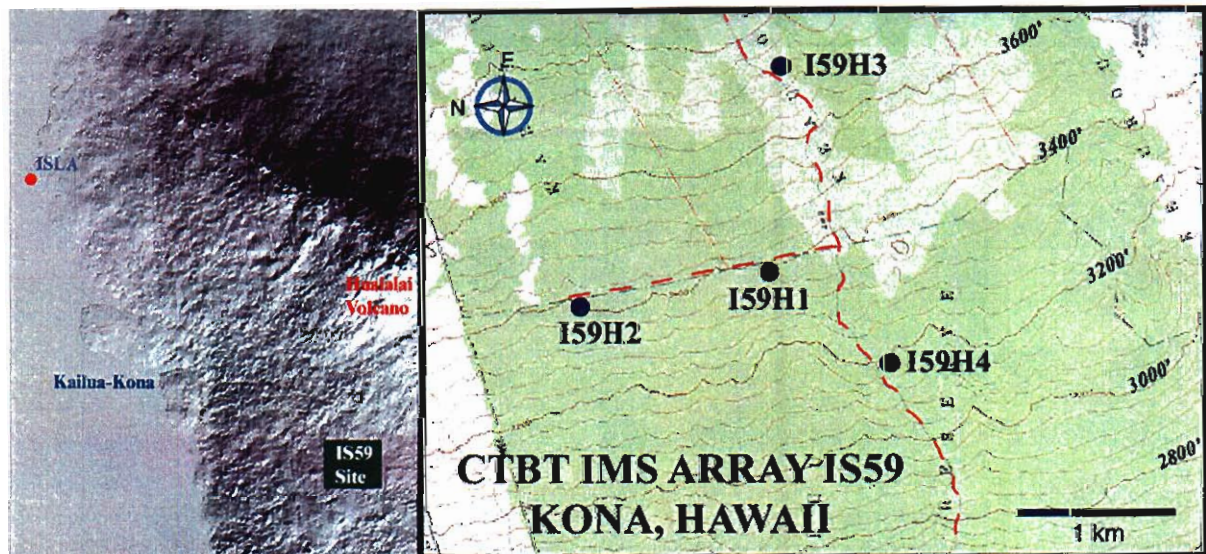

Figure 1. Location and geometry of infrasound station I59US.

Table 1. Location information for elements of I59US.

Site Code	Latitude (WGS90)	Longitude	Elevation (km)
I59H1	19.591462828	-155.893589010	1.0335
I59H2	19.600888742	-155.895253381	1.0409
I59H3	19.590991540	-155.881745617	1.1301
I59H4	19.585484295	-155.898760685	0.9620

Pressure data is collected using four Chaparral-5 microphones sampled at 20 sps by Science Horizons AIM 24-bit digitizers and transmitted via radio telemetry to the ISLA, where it is repackaged into a CD-1 stream which is sent to the IMS International Data Center (IDC) in Vienna. The data are also written locally to a CSS 3.0 flatfile database for data quality control, processing, and archiving. Until December 2003 a second CD-1 datastream was forwarded to the Center for Monitoring Research (CMR).

The major topics covered in this report are:

1. Discussion of the various detection methods for infrasonic arrivals, including manual (visual) detection, STA/LTA ratios, persistence of azimuth and slowness using InfraTool, and the PMCC method of Cansi (1995).
2. Discussion of infrasonic signals from ocean waves recorded at I59US and their characteristics, including seasonal and diurnal patterns and relationships with ocean wave heights.
3. Discussion of microbarom signals recorded at I59US and their characteristics, including seasonal patterns and utility for storm location and monitoring.
4. An overview and discussion of the long-distance detections made by I59US, specifically of bolide signals and rockets.
5. A discussion of some of the regional signals that add to the ambient infrasonic field at I59US, including small explosions, thunder, and aircraft.
6. A summary of studies conducted using a portable infrasonic array, intended to study local infrasonic events at close range.

Some of this work has previously been reported at the annual Seismic Research Review (Garcés and Hetzer, 2001; Garcés and Hetzer, 2002; Garcés and Hetzer, 2003), and in two papers published in Geophysical Research Letters (Garcés et al., 2003a; Garcés et al., in press). In addition, the extensive forensic infrasound studies carried out by ISLA after the space shuttle Columbia disaster, which have been previously integrated into the official infrasound report (Bass, 2003), are attached here as appendices.

2. History and performance of detection algorithms at I59US

Initial signal analysis was performed manually, as the typical signal characteristics and therefore the optimal methods for automatic detection were undetermined. Arrival records date back to June 19, 2000, and manual detection continued until March 2001. During this time period data was loaded and processed using Sandia National Laboratories' MatSeis analysis software, and arrivals were identified, selected and recorded by the analyst. This process was time-consuming, tedious, and error-prone because it imposed no quantifiable standards for what constituted an arrival and what did not, and because it calculated arrival azimuth and slowness for each arrival using FK analysis, which is prone to spatial aliasing errors. Also, because it relied on visual recognition of arrivals, emergent arrivals with low signal-to-noise were more difficult to detect and therefore may have been underrepresented in the arrival records. Similarly, the first arrival of an emergent signal could not be visually extracted from the ambient noise. Finally, since each arrival was recorded at a single point in time with no associated duration, accurate recording of a repetitive series of arrivals from the same source would have required a separate arrival for each pulse or group of pulses, each of which would need to have an associated azimuth and slowness calculation. This was prohibitive in its demands on the analyst and generally resulted in one or two representative arrivals being recorded and the rest ignored.

Nonetheless, since many arrivals greater than 1 Hz had signal-to-noise ratios large enough for visual identification, the process appeared satisfactory for initial identification of the dominant regional sources of infrasonic signals. 665 arrivals were recorded using this method, which was slanted toward high-amplitude, impulsive arrivals (Table 2). 132 arrivals were identified as surf, with two major source areas identified. 97 arrivals were identified as related to man-made explosions, either onshore or offshore. Microbaroms, which are generated by interactions of ocean waves that generate standing waves, were generally detected by selecting a long section of data and performing FK analysis. If individual microbarom bursts could be identified in the waveform, one burst was chosen and the results of the FK analysis were assigned to it. During our initial tests, we associated microbarom signal to specific storms in the Pacific. Signals that arrived from the general direction of Kona-Keahole International Airport were interpreted to be related to aircraft takeoffs and landings, but these signals displayed a wide range of characteristics that were unlikely to all be related to the same source.

Table 2. Infrasonic detections made by the manual method.

Phase	Description	Arrivals
ik,iws,inw	Surf	132
ia	Aircraft	154
im	Microbaroms	215
ip, in	Munitions	97
it,iw,its,iep,is,in	Unknown and Various	73

While lacking in the number and reliability of arrivals generated by subsequent methods, this method was nonetheless very valuable in identifying several major, persistent sound sources when coupled with ground-truth gathering field visits and observations. Persistent sources of sound were detected from azimuths ~235° (Kualanui) and ~320° (Makalawena), which were identified as related to surf (Figure 2), and at ~60°, which was interpreted as being related to exercises at the Pohakuloa Training Area. At this time preliminary

phase names were developed to associate arrivals with their sources; these codes would be subsequently modified and consolidated.

In response to the limits of this method, a semi-automatic detector was developed. This detector was based on the Short-Term Average/Long-Term Average (STA/LTA) method combined with a correlation threshold. The waveforms would be loaded and the STA/LTA ratio would be calculated for each. The detector would then step through the STA/LTA waveforms using a 20-second window with 75% overlap. Any window containing an STA/LTA value greater than a specified threshold on 3 of the 4 channels that also had a mean cross-correlation value (excluding autocorrelation) exceeding a second specified threshold was marked as an arrival. Once the STA/LTA analysis was complete, a preliminary azimuth and slowness were calculated for each arrival using FK analysis, and the results were presented to the analyst for verification.

This method solved some of the problems of the manual detection method. It applied a strict, yet adjustable, quantified standard for what constituted an arrival, and it freed up the

Figure 2. Map of part of the west coast of Hawai'i Island showing the locations of station I59US and the two major sources of surf infrasound.

analyst to perform more detailed event screening while the detector was running. This detector, however, was not without its own limitations. Emergent arrivals tend to have lower STA/LTA ratios than impulsive arrivals. Since the algorithm relied on the STA/LTA as its first detection alarm, it was little better at detecting emergent, low S/N arrivals than the manual detector.

Because of this limitation a modified version of Los Alamos National Laboratory's InfraTool software was put into operation. InfraTool uses a version of the Fast FK method to calculate instantaneous azimuth, slowness and correlation at specified intervals throughout the waveform. An arrival can be indicated by an elevated correlation statistic, azimuth and slowness values that remain constant over a period of time, or both. Data was generally passed through InfraTool once the STA/LTA detection process was complete. InfraTool proved adept at detecting the long-duration, emergent arrivals missed by the STA/LTA detector, but provided no solution for the detection of shorter-duration events; the combination of the two detectors, while somewhat ponderous, was reasonably effective.

The STA/LTA and InfraTool detectors operated for 10 months, from March to December 2001. In that time, 3173 detections were registered in the high-frequency (i.e. above the microbarom peak) band (Table 3), of which 1220 were associated with the two major surf sound locations (Figure 3). It is likely that the true ratio of surf to other events was higher, for surf arrivals can have low signal-to-noise levels when waves are small and thus may not have set off the STA/LTA detector. Because it relied only on amplitude ratios and operated most efficiently on impulsive arrivals, the STA/LTA detector was also very adept at detecting seismic P-wave arrivals; 21 earthquakes were recorded in this time period.

Table 3. Infrasonic detections made by the STA/LTA automatic detector.

Phase	Description	Arrivals
ik, iws	Surf	1220
im	Microbaroms	2875
iep	Earthquakes	21
ia	Aircraft	112
ip	Pohakuloa	194
in	Offshore	398
its,ib	Telesonic	7
iw,iu	Unknown	1221

Because of their continuous nature, microbaroms were not detected by the STA/LTA method; these continued to be identified manually, often by performing FK analysis on the entire 4-hour segment of data at once. 2875 microbarom arrivals are recorded for this time period, corresponding to distinct storm systems. All phase classifications for the STA/LTA detector are listed in Table 3. The main benefit to using this detector was to confirm that infrasonic arrivals could be detected automatically at I59US, and to reinforce the knowledge of the repeating sources first identified using manual detection.
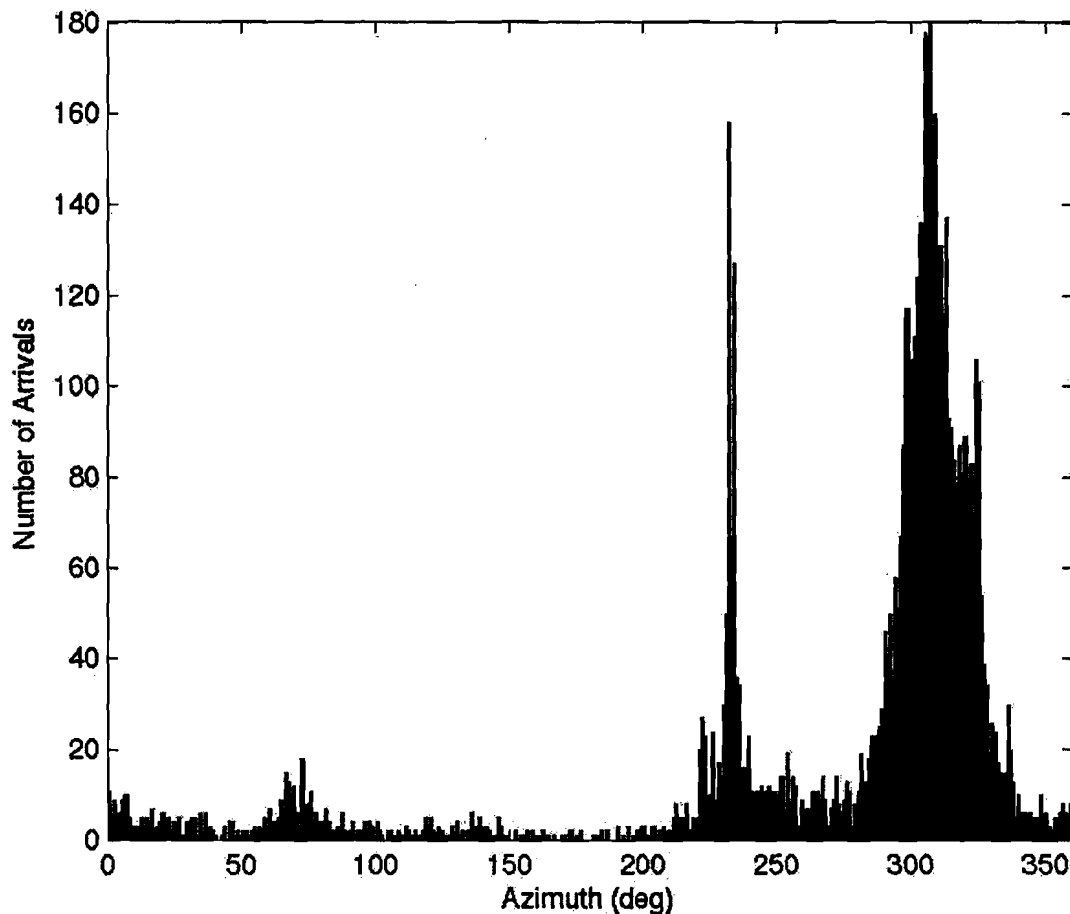
Figure 3. Histogram of arrivals detected via the STA/LTA and InfraTool method from March to December 2001. The dominance of the two major surf locations at 235° and 320° are evident.

One of the main limitation of the aforementioned detectors is that they rely in frequency-wavenumber analysis for an estimate of the arrival azimuth and speed of an infrasonic signal. Due to the relatively large aperture of I59US, low-amplitude signals with frequencies greater than 0.5 Hz are aliased. This leads to errors in the estimate of arrival features for emergent arrivals, which in turn can lead to substantial location errors (Garces et al., 2002, 2003). This realization encouraged a continuing search for a reliable automatic detection process. The possibility of a native executable to perform a function similar to InfraTool was explored, but initial versions of the software were very slow and did not eliminate spatial aliasing, so the project was eventually discarded as redundant. A copy of the Progressive Multi-Channel Correlation (PMCC) software described by Cansi (1995) was obtained, tested, and finally adopted and integrated into operations in December 2001.

PMCC is a time-domain detector that uses the correlation between various groupings of three sensors to obtain an estimate of the consistency of specified closure relations. If the consistency is below a certain threshold, a detection is registered. This detector has performed well for S/N ratios that are close to unity and for all frequencies.

6

The PMCC algorithm is based on analysis of overlapping windows of data. The cross-correlation function of the data from two stations determines a time delay between the two; summation of time delays over an array yields the lag closure of the signal. Time delays from a perfectly-correlated signal should cancel each other out exactly, resulting in a lag closure of zero; high lag-closure values indicate an uncorrelated signal. The consistency (Johnson and Dudgeon, 1993) of the lag closure is used as the primary detection trigger of the PMCC method. A subset of the array is used for an initial time-delay calculation, which yields an initial value of arrival azimuth and slowness. Using these values, the time delay for additional subsets is calculated, and these can then be included in the calculation by examining a much shorter section of the time window for correlated signal; if the point of maximum correlation requires significant variation in azimuth, velocity, or time, the arrival is discarded. This optimizes computation time over a large array, and also allows initial false alarms caused by the presence of correlated noise in the first subset to be eliminated when not present in further subsets.

During the calculation each time window is filtered into a number of frequency segments, which are analyzed individually for similarity of azimuth, slowness, and consistency. Each frequency band within each time window represents a "pixel" of data (Figure 4). Pixels adjacent in time and/or frequency are then compared for similarity of calculated features, and nearest-neighbor groups of pixels with similar features are classified together as "families". Families that meet a specified minimum size criterion are placed in a table of detections.
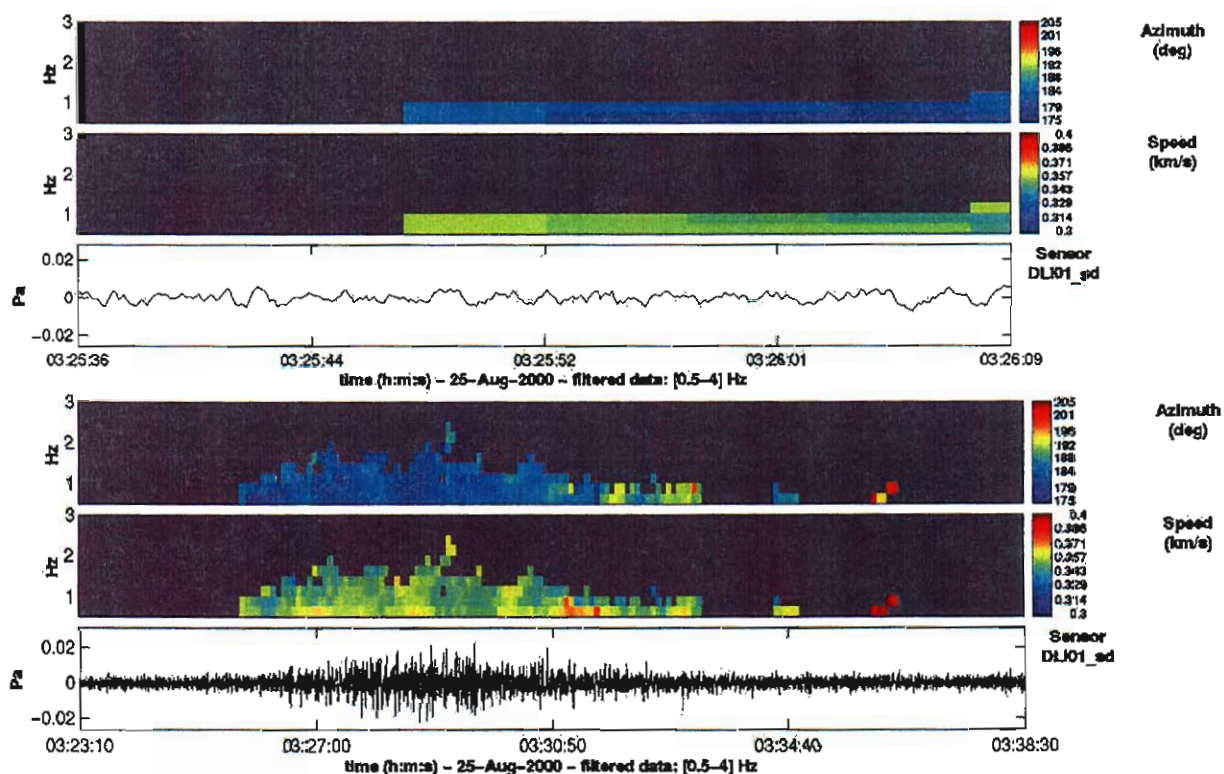
Figure 4. PMCC results showing the pixel-like nature of detections in time-frequency space (top) and the grouping of related detection pixels into families (bottom).

Table 4. PMCC detection parameters for the various sets used by ISLA.

PMCC Parameter	High-Frequency	Microbarom	High-Speed	Very-Low-Frequency
Window Length	30 sec	90 sec	30 sec	300 sec
Window Overlap	5 sec	20 sec	5 sec	50 sec
Max Consistency	0.2 sec	0.5 sec	0.2 sec	5 sec
Passband	0.5-4.0 Hz	0.1-0.5 Hz	0.5-4.0 Hz	0.033-0.1 Hz
Trace Velocity	0.3-0.45 km/s	0.3-0.45 km/s	0.45-0.8 km/s	0.25-0.45 sec
Max Azimuth Variation	10°	10°	10°	10°

ISLA Parameter				
Correlation	0.6	0.7	0.6	0.5
Family Size	14	N/A	N/A	N/A

The automated, near-real-time event-detection procedure is as follows. A script is used to generate an initialization file that contains all of the detection parameters as well as the names of and paths to the data files. This initialization file is then passed to the PMCC executable file, which processes the data and generates a file containing the aforementioned table of families. This table is then analyzed, sorted and filtered using specified parameter thresholds, and a Center for Seismic Studies (CSS) arrival table containing arrival time, azimuth, slowness, amplitude, and arrival id is created using the detections that successfully pass the thresholds. Currently an arrival must have a consistency of 0.6 or be comprised of at least 14 pixels in order to be recorded. The waveform data in the local CSS database is stored in 4-hour segments, and the PMCC detector processes an entire segment at once, two hours after its normal ending time (to ensure maximum data inclusion). Weekly bulletins of detections are produced both before (the "unfiltered" bulletin) and after (the "filtered" bulletin) the second set of thresholds is applied.

The PMCC algorithm uses a number of calculated quantities to determine its detection thresholds. In addition, a detection must satisfy specified trace velocity limits, arrival azimuth variation limits and duration limits, and must appear on a specified minimum number of stations (generally one less than the number of stations in the array), in order to be placed in the detection table. Each variation in detection parameters requires a separate instance of the detector with a unique initialization file.

At present, ISLA personnel use two sets of detection parameters ("high-frequency" and "microbarom" sets) for normal event processing, with two additional sets ("high-speed" and "very-low-frequency") in development. The four iterations through the waveform data currently require a total of about 20-30 minutes of computation time per 4-hour segment on a SunBlade 1000 running Solaris 8. Independent parameters include analysis-window length and overlap, maximum consistency, minimum and maximum frequency and trace velocity, and maximum azimuthal variation permissible for inclusion in a family. Other parameters are dependent on these.

The PMCC method provides a number of advantages over the previous detectors. First, it runs as a command-line executable, reading a specified initialization file for operating parameters and

generating output files in specific formats. This means that it can be set up to run automatically, providing a script is written to generate the appropriate initialization file. It also comes with a GUI front-end which generates the startup files and displays the results from the output files in a user-friendly, readable format, and offers several secondary analysis tools. Its method of splitting up the passband for analysis makes it easier for narrow-band signals to be detected, and improves the detection of low S/N signals by excluding any noise at other frequencies. Its requirement of multiple pixels all with matching features reduces the potential false alarm rate, and as the processing is accomplished by a precompiled binary file it is very fast, generally taking less than 10 minutes for a run through an undecimated 4-hour dataset on a dual-processor Sunblade 1000. Drawbacks to the software include the inability to bridge data gaps (PMCC can currently only deal with contiguous segments of data), somewhat cryptic input and output file formats, and lack of flexibility in the format of the initialization file. PMCC also requires minimum and maximum acceptable trace velocity boundaries; an arrival that falls outside of these boundaries will not be recorded. It should also be noted that PMCC is not used in actual real time at ISLA. We process data in 4-hour segments to reduce CPU usage and allow for any backfilling of missing or late data.

There has been some debate regarding the relative merits of PMCC and InfraTool, and regarding which package should be used for automatic detection. While some of this debate may well be related to the limited availability of PMCC software, there are valid questions about the relative performance of the two packages. Appendix A contains a comparison of the packages under very specific circumstances. While hardly comprehensive, it does summarize the most common categories of infrasonic signals and how the packages differ in the effectiveness of their detections at I59US. The greatest advantage of PMCC seen so far is the ability to detect coherent signals even when S/N appears to be near unity (Figure 5). At present, PMCC is used for all signal detection, automatic or manual. MatSeis is still used for specific processing and display tasks, such as power spectrum and spectrogram generation, array responses, and waveform display.

The PMCC algorithm has performed admirably, generating a large number of diverse detections. Even after imposing a requirement that a detection possess either a minimum correlation of 0.6 or be comprised of at least 14 pixels, over 150,000 arrivals have been detected from January 1, 2002 to December 2, 2003 (Figures 6 & 7). Arrivals generally have sonic trace velocities (Figure 8) and tend toward higher frequencies because of the preponderance of surf arrivals (Figure 9). Arrivals are recorded in bulletin files, which are fixed-column-width text files containing the relevant arrival features as calculated by PMCC. Of particular interest are the maximum, minimum, and mean frequencies, which were not provided by any of the previous detection methods used by ISLA. These data are very useful for estimating source proximity and associating similar arrivals with the same source. A sample bulletin file is shown in Table 5. An overview of some of the typical signals observed in Hawaii follows; the events will be discussed in some more detail in subsequent sections.

Surf Arrivals

Detections from azimuths of 234±10° and 320±10° are classified as surf events, with assigned phase names of "ik" and "iws" respectively. The signals generally occur as sets of impulsive, evenly spaced arrivals with relatively high (> 2 Hz) frequency content. Other azimuths may also
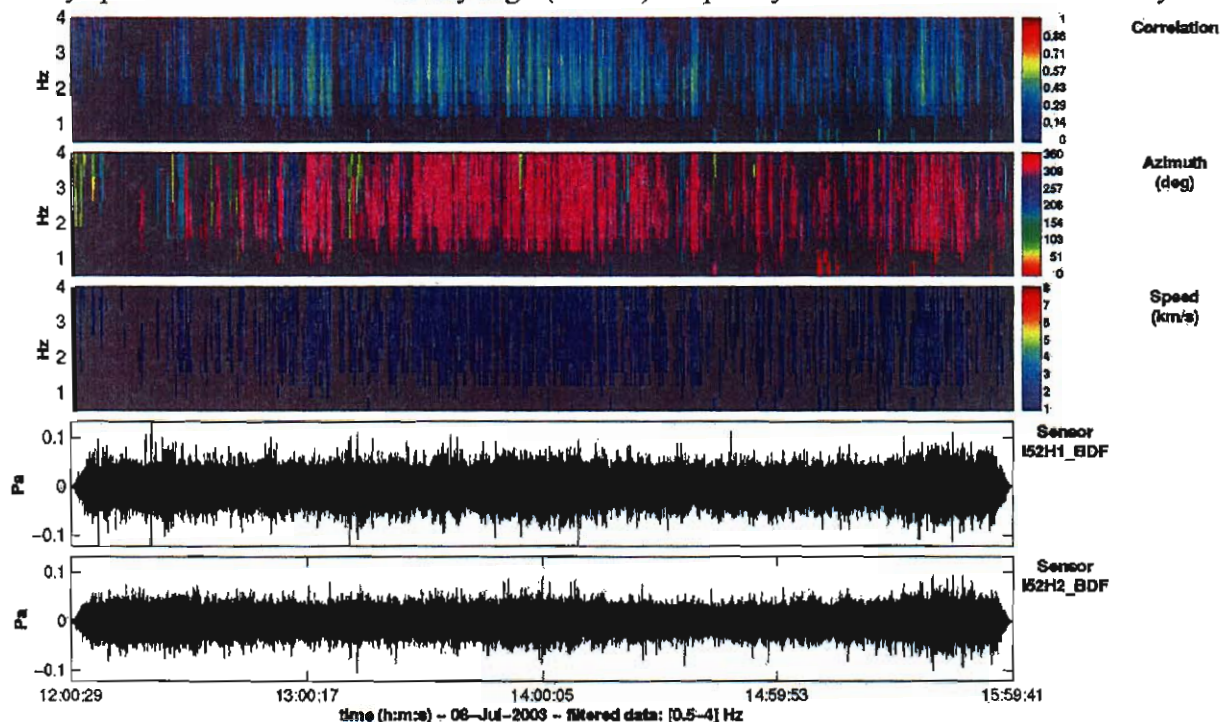

Figure 5. PMCC results showing strong detection when signal-to-noise is close to unity. Image is of an arrival of unknown origin from station I52GB, Diego Garcia.

contribute surf signals, especially during periods of increased wave energy, but not with the consistency of the two areas specified above.

Pohakuloa Training Area Arrivals

Detections from 65±30° are identified as coming from the Pohakuloa Training Area and are assigned to the "ip" phase. Pohakuloa events generally occur as clusters of one or more irregularly spaced impulsive arrivals, and tend to have fairly high frequency content. Other signals from this azimuth may be more emergent with poor signal-to-noise.

Possible Volcanic Arrivals

Detections from 110±10° are identified as coming from the general direction of Kilauea Volcano. These signals are tentatively assigned to the "iv" phase. To date the majority of these events have featured signal-to-noise of approximately unity; the events tend to occur at lower frequencies (~0.9 Hz), where the noise floor is higher. This precludes visual analysis of the arrivals. Also, no definitive correlation has yet been found between the infrasonic events and peaks in thermal activity in Pu'u 'O'o crater. While significant infrasound has been found to be generated by the Kilauea lava tube system (Garces et al., in press), it remains to be demonstrated

whether effusive eruptive activity at Kilauea has sufficient energy to produce infrasound that can be observed at I59US.

Microbarom Arrivals

Detections in the 0.1-0.5 Hz frequency band are assigned the "im" phase ID and are believed to be generated by ocean wave interactions caused by severe weather, often at distances of several thousand kilometers. Correlation has been drawn between the arrival azimuth of microbarom events and areas of high ocean wave height.

Each of these arrival identities will be discussed in the following chapters. Research to improve automatic phase-name assignment based on multiple features is ongoing and is expected to make phase identifications more reliable as well as reducing the number of arrivals labeled as iu or "unknown".
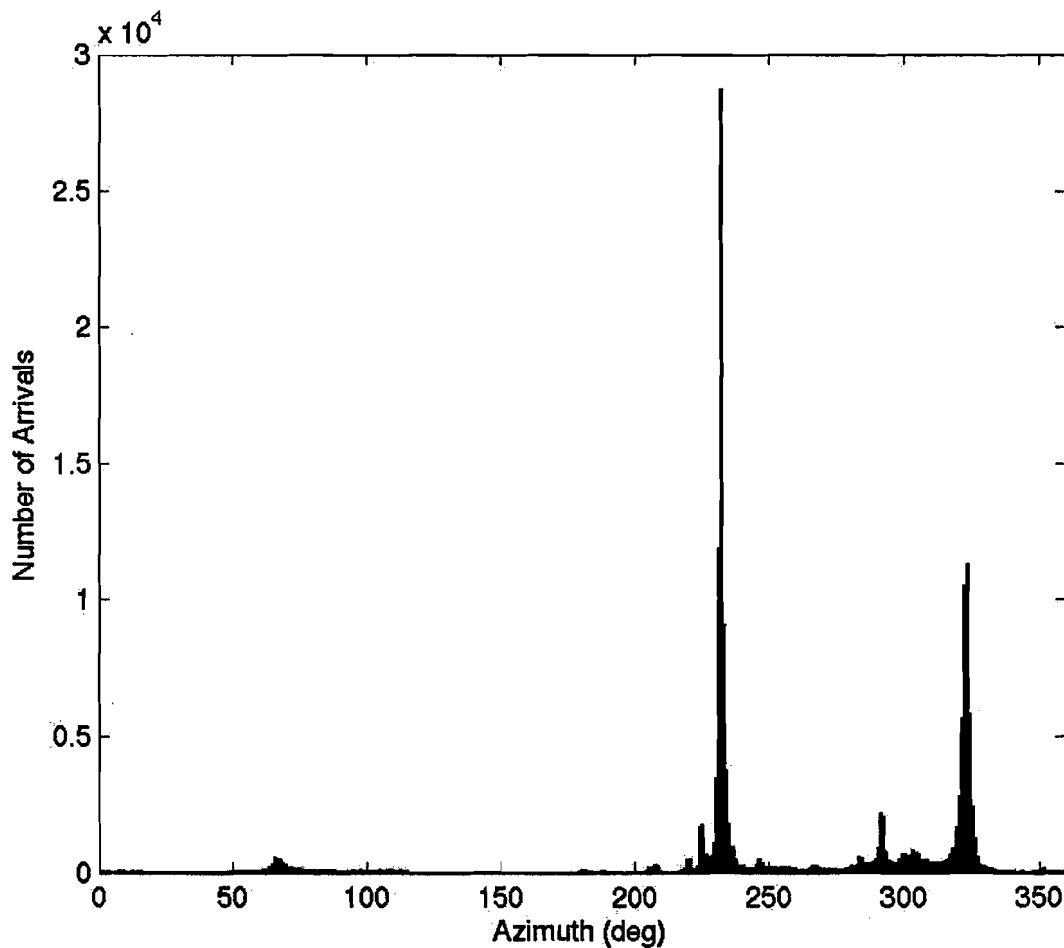
Figure 6. Histogram showing number of arrivals on 2002 and 2003 per 1-degree bin over azimuth. Note the major surf sound sources around 234° and 324°.
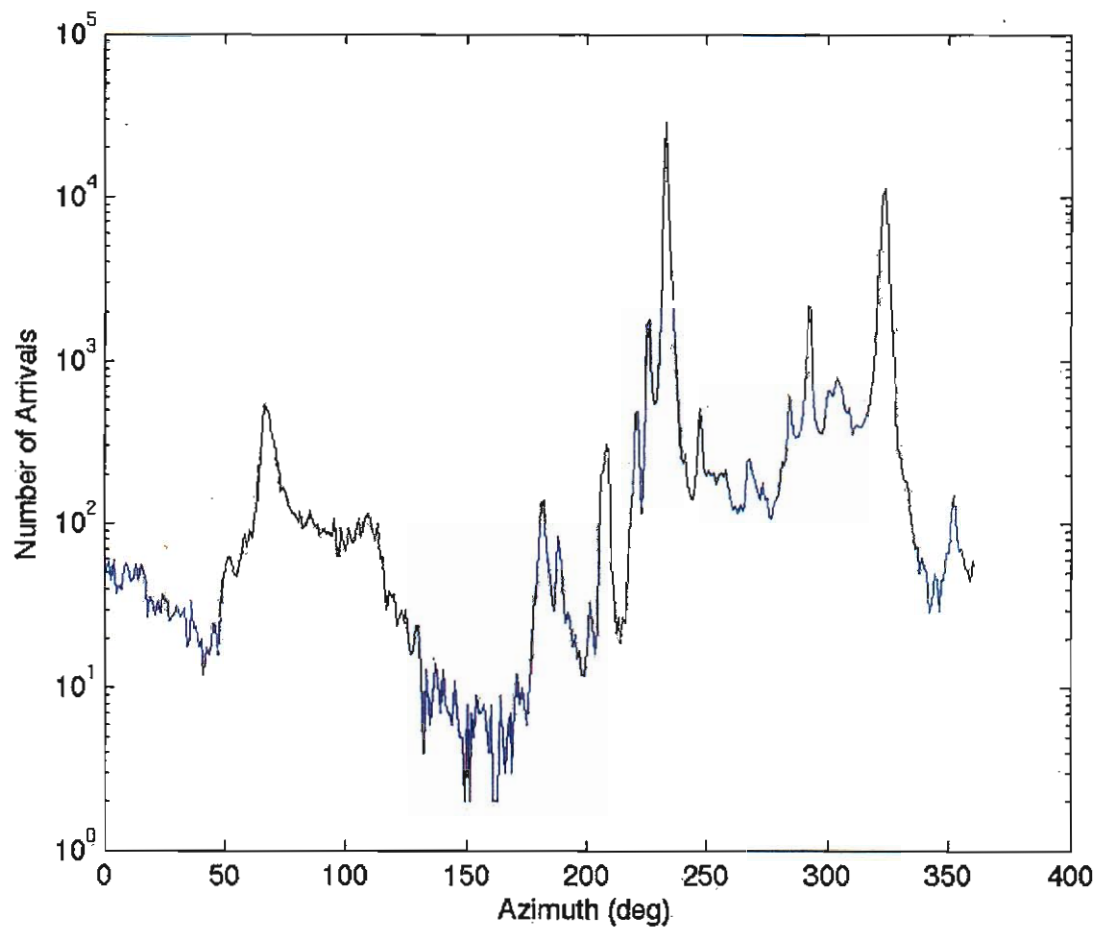
Figure 7. Same information as Figure 6, but with a logarithmic ordinate axis to allow additional persistent sources to be identified.

12
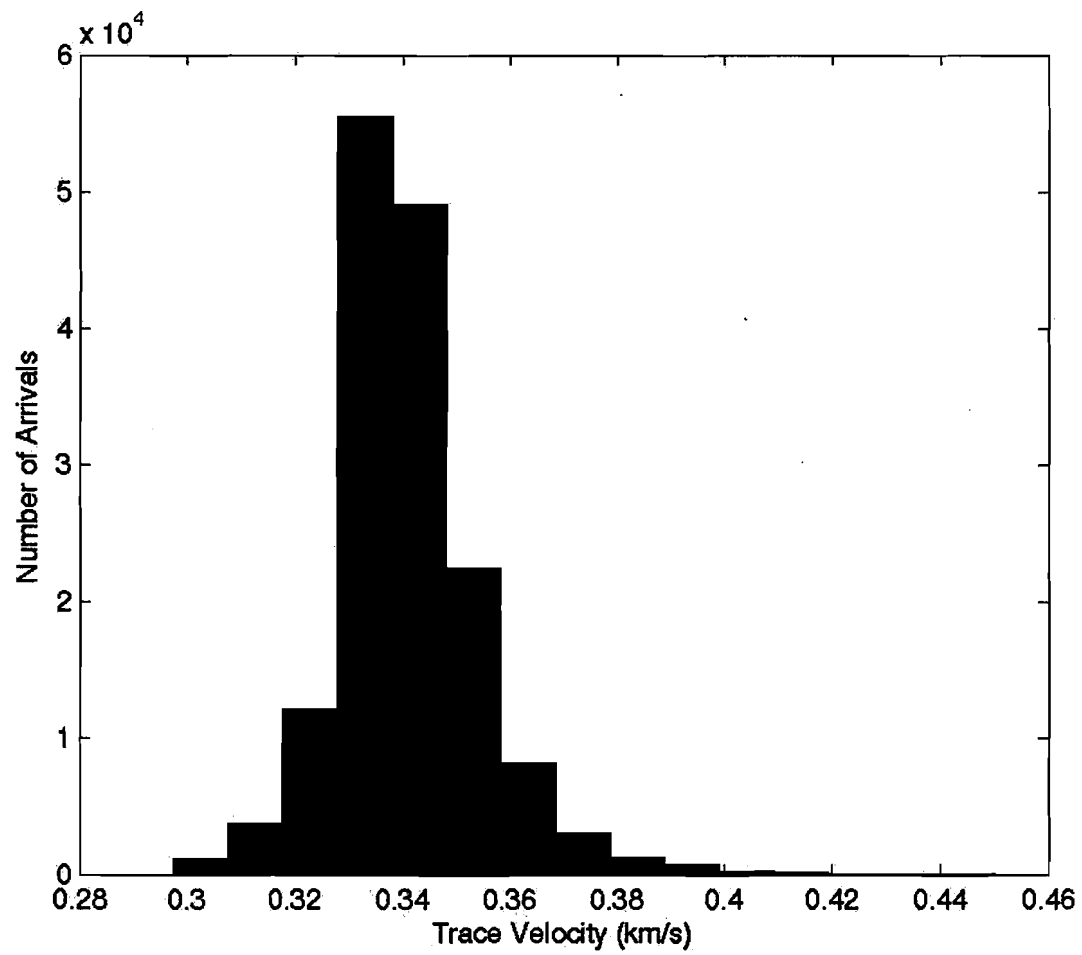
Figure 8. Histogram over trace velocity showing that the majority of events possess sonic trace velocities.
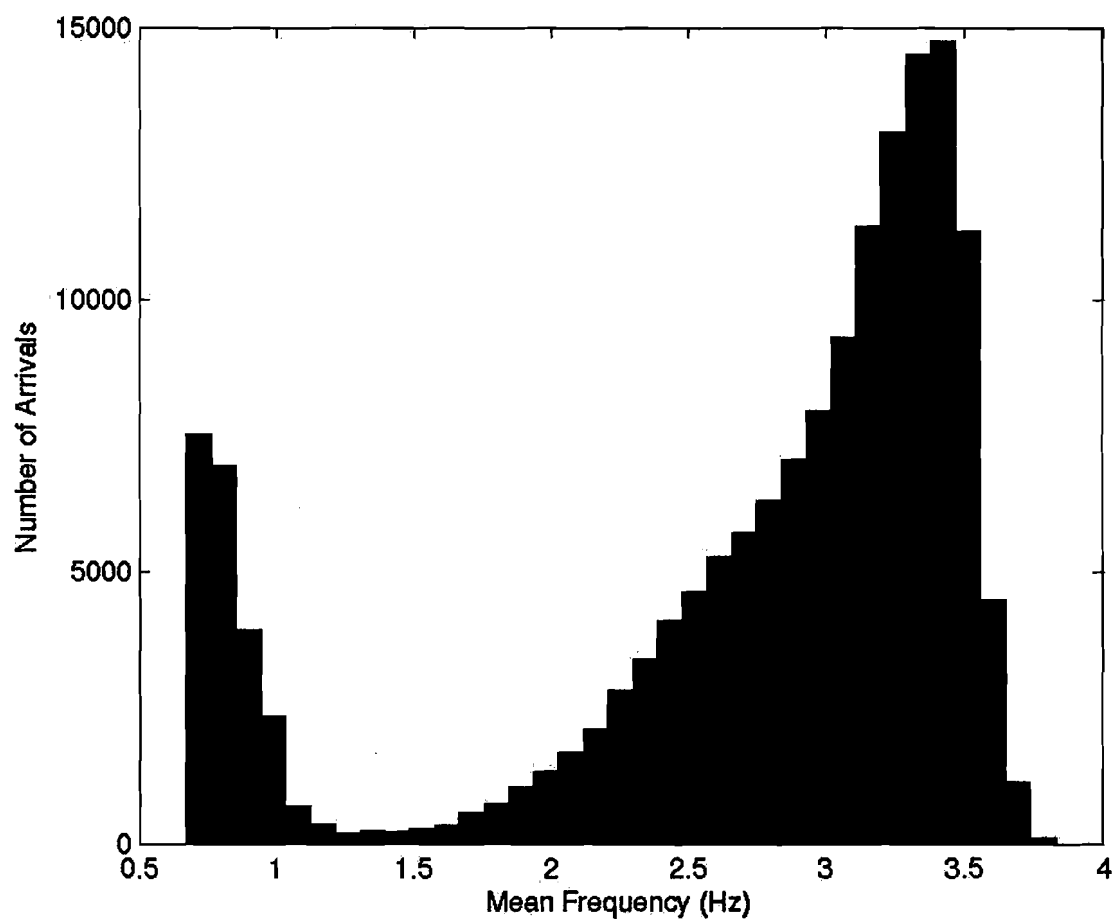
Figure 9. Histogram over frequency showing the general high-frequency character of arrivals at I59US. Most surf signals have mean frequencies higher than 2 Hz. The large number of arrivals at the lower frequencies are interpreted to be microbarom energy leaking into the 0.5-4 Hz passband used for these detections.

Table 5. Sample bulletin file from I59US. Phase refers to a preliminary source identification made on the basis of arrival azimuth. Phases ik and iws are the major southwest and northwest surf sources respectively, ip is the Pohukuloa Training Area, and iu (not shown) is an unknown source.

Date/Time	Azimuth	Slowness	Correlation	MeanFreq	Amp	FamSize	Duration	MinFreq	MaxFreq	Phase
2003-Aug-01 12:05:15	322.5	312.36	0.45	2.85	0.9	59	75	1.73	3.83	iws
2003-Aug-01 12:09:50	322.7	311.46	0.34	2.6	0.8	20	40	2.08	3.48	iws
2003-Aug-01 12:13:25	323.2	314.18	0.34	2.67	0.8	26	35	2.08	3.48	iws
2003-Aug-01 12:16:00	322.5	310.57	0.4	3.26	0.7	18	25	2.42	3.83	iws
2003-Aug-01 12:16:40	323.3	311.46	0.5	2.86	1.2	78	80	1.38	3.83	iws
2003-Aug-01 12:22:15	231.3	325.53	0.43	3.62	0.7	19	70	3.12	3.83	ik
2003-Aug-01 12:24:35	321.5	321.66	0.32	3.45	0.6	14	35	2.77	3.83	iws
2003-Aug-01 12:30:20	40.5	279.27	0.63	2.78	1.2	35	25	1.73	3.83	ip
2003-Aug-01 12:34:35	322.2	310.57	0.35	2.94	0.7	19	30	2.08	3.83	iws
2003-Aug-01 12:39:20	323	309.68	0.41	2.94	0.7	19	35	2.42	3.48	iws
2003-Aug-01 12:40:40	325.5	315.09	0.35	2.93	0.7	16	40	2.42	3.83	iws
2003-Aug-01 12:41:30	322.5	311.46	0.39	3.01	0.8	31	45	2.08	3.83	iws
2003-Aug-01 12:42:30	322.6	310.57	0.3	2.75	0.8	15	35	2.08	3.12	iws
2003-Aug-01 12:43:35	322.2	313.27	0.37	3.11	1	19	40	2.08	3.83	iws
2003-Aug-01 12:45:10	322.5	310.57	0.31	3.03	0.7	22	50	2.42	3.83	iws
2003-Aug-01 12:47:00	322.6	311.46	0.43	3.27	0.8	68	90	2.42	3.83	iws
2003-Aug-01 12:48:35	322.5	311.46	0.35	3.25	0.7	14	30	2.77	3.83	iws
2003-Aug-01 12:49:15	322.6	310.57	0.48	3	1	57	55	1.73	3.83	iws
2003-Aug-01 12:50:30	322.5	310.57	0.36	3.55	0.6	15	40	2.77	3.83	iws
2003-Aug-01 12:51:45	322.3	311.46	0.44	3.15	0.8	71	90	2.08	3.83	iws
2003-Aug-01 12:53:25	37.7	246.19	0.37	2.99	0.8	18	25	2.42	3.83	ip
2003-Aug-01 12:54:05	322.7	312.36	0.52	2.71	1.3	70	55	1.38	3.83	iws
2003-Aug-01 12:55:05	322.1	312.36	0.35	3.2	0.8	25	45	2.42	3.83	iws
2003-Aug-01 12:55:55	232.8	329.5	0.5	3.48	1	15	25	3.12	3.83	ik
2003-Aug-01 12:56:45	322.7	312.36	0.53	2.99	1.1	40	40	2.08	3.83	iws
2003-Aug-01 12:57:35	322.6	311.46	0.48	3	1	148	195	1.73	3.83	iws
2003-Aug-01 13:01:00	322.7	311.46	0.42	3.12	0.9	63	85	1.73	3.83	iws
2003-Aug-01 13:02:35	322.8	310.57	0.37	3.41	0.7	20	45	2.77	3.83	iws
2003-Aug-01 13:03:40	323.9	310.57	0.37	3.09	0.9	57	80	1.73	3.83	iws
2003-Aug-01 13:08:55	322.6	312.36	0.34	2.66	1.1	44	70	1.38	3.83	iws
2003-Aug-01 13:10:25	322.2	312.36	0.31	2.95	0.8	18	20	2.08	3.83	iws
2003-Aug-01 13:11:35	322.7	311.46	0.44	3.03	1.1	124	160	1.38	3.83	iws
2003-Aug-01 13:20:25	322.7	310.57	0.33	2.7	0.8	18	35	2.08	3.12	iws
2003-Aug-01 13:23:00	321.8	322.62	0.41	2.91	1.2	67	85	1.73	3.83	iws
2003-Aug-01 13:24:40	322.8	313.27	0.4	2.95	1.1	41	60	2.08	3.83	iws
2003-Aug-01 13:25:45	322.9	313.27	0.37	2.79	1.1	64	85	2.08	3.83	iws
2003-Aug-01 13:27:15	322.7	316.94	0.34	2.8	0.9	31	45	1.73	3.83	iws
2003-Aug-01 13:31:50	323.8	309.68	0.37	3.08	0.8	21	25	2.42	3.83	iws
2003-Aug-01 13:33:10	321.7	315.09	0.4	3.01	0.9	24	45	2.08	3.83	iws
2003-Aug-01 13:34:20	232.8	328.5	0.42	3.5	0.9	14	25	3.12	3.83	ik
2003-Aug-01 13:35:00	323.3	311.46	0.43	2.8	1.2	34	30	1.73	3.83	iws
2003-Aug-01 13:35:40	323.8	312.36	0.36	3.09	0.8	18	25	2.08	3.83	iws
2003-Aug-01 13:36:55	323.3	310.57	0.3	2.62	0.9	14	30	2.08	3.12	iws
2003-Aug-01 13:38:35	324.1	312.36	0.39	2.85	0.9	36	60	2.08	3.48	iws

3. Surf Arrivals

High-Frequency Arrivals
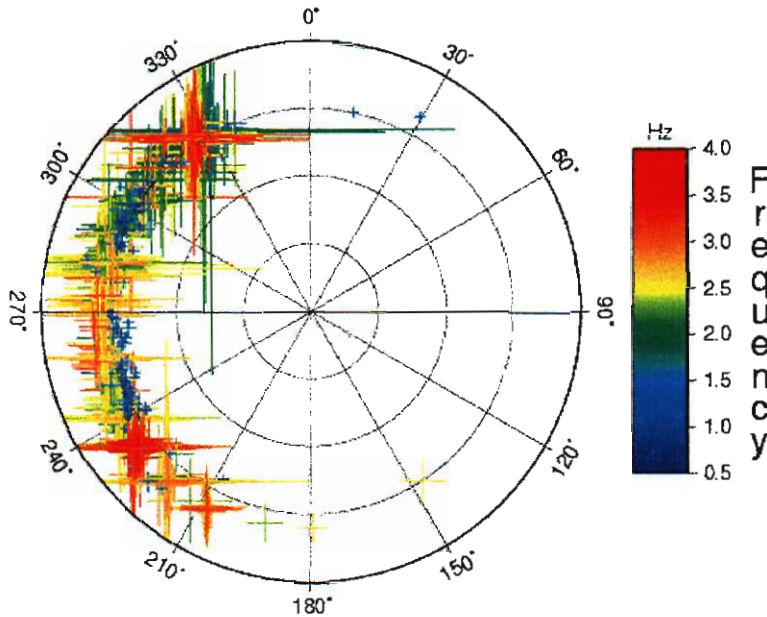
Figure 10. Polar plot showing arrival positions in azimuth and slowness for the high-surf period of January 8-14, 2003. Although distinct areas of high-frequency energy can be identified (red clusters), almost the entire west coast of the island appears to be generating infrasound.

A prominent component of the ambient coherent infrasonic field in island environments is related to breaking ocean waves. A breaking wave may generate infrasound by (1) violently collapsing against itself, as in the production of a tube, (2) slamming against a cliff, and (3) impacting against a shallow reef. During times of low surf, signals may emanate from a handful of bays along the coast of the island; it is theorized that edge waves become trapped in these bays and resonate, generating more sound than they might ordinarily. However, when surf gets high, many more sources along the coast start to emit sound, acoustically illuminating the shoreline (Figure 10). The signals generally occur as sets of impulsive, evenly spaced arrivals with relatively high frequency content (Figure 11); average frequencies tend to be above 2 Hz. During periods of high activity, groups of surf signals will often be sufficiently closely spaced in time such that the PMCC detector will treat them as a single, long-duration event. This is due to the use of overlapping windows: before the windows have moved past one surf signal another one with similar features may enter the window, causing the PMCC algorithm to extend the family. This is a fairly frequent occurrence, as surf signals can persist for hours, but appears to be more prevalent in the surf signals from more distant sources; this may be due to temporal spreading of the original impulse such that the coherent packets of energy become more closely spaced in time than the sources were (Figure 12). Future work would address this problem using shorter-duration windows.

The effect of these persistent high-frequency signals can also be seen in the amplitude spectra from I59US (e.g. Figure 13). The surf signals cause the spectrum, which slopes downward from the microbarom peak as frequency increases, to begin rising at around 2 Hz, peak around 4 Hz, and then decline again until the antialiasing filter kicks in around 8 Hz. This secondary peak can, however, be overwhelmed by noise when local wind speeds are high.
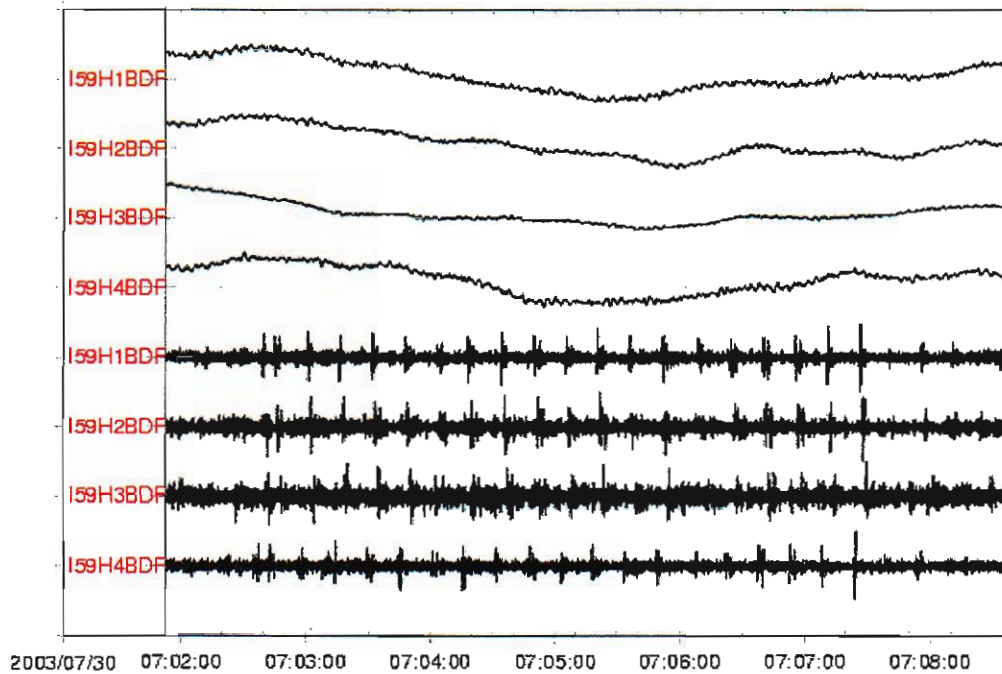
Figure 11. Raw (top) and high-passed filtered (bottom) waveforms showing typical strong surf signals from Kualanui Point, Hawaii Island.
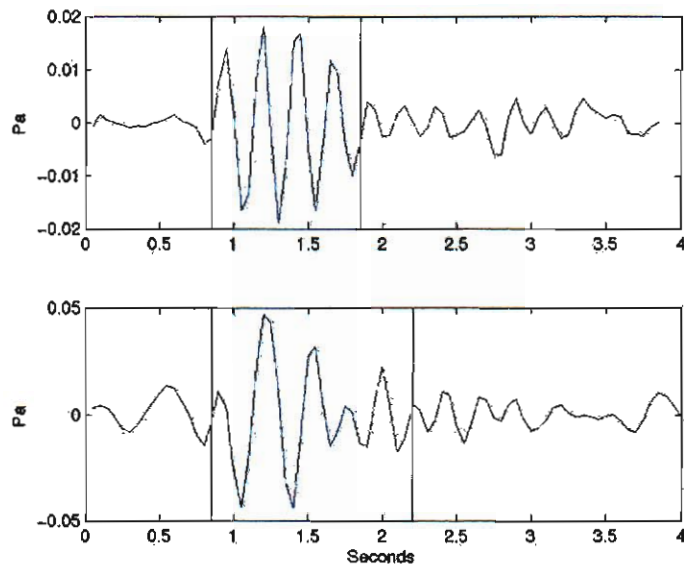
Figure 12. Filtered waveforms showing the difference in duration and period between surf arrivals from a distance of ~9 km (top) and ~26 km (bottom) for different events.
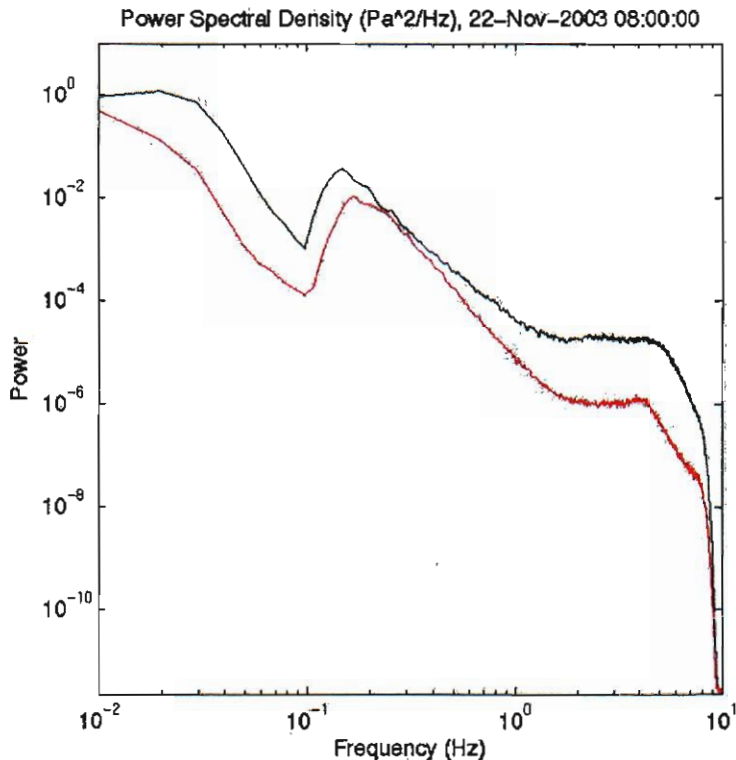
Figure 13. Power spectral density of channel I59H1 on November 22 (black), when the mean sustained wind speed was 1.03 m/s, and December 1 (red), when the mean sustained wind speed was 0.76 m/s. The met station at I59US is somewhat sheltered by trees, so the wind speed aloft may have been larger.

A strong correlation has been observed between significant wave height, as measured by ocean wave buoys, and infrasonic signal levels. During January of 2003 a number of very large ocean swells moved through Hawaiian waters. The wave heights from these swells were measured by a buoy near Waimea Bay, O'ahu. The Waimea buoy is located at 21.6733 N 158.1167 W, at a range of 326 km and a bearing of 315.2 degrees from I59US. Thus, depending on the dominant period (10-18 s), a NW swell would take between 7 to 10 hours to travel from Waimea Bay to Hawai'i Island. When the wave height plot is shifted in order to account for the swell propagation time from O'ahu to Hawai'i Island, a strong correlation can be seen between the strength of the infrasonic spectra and the significant wave height (Figure 14). However, an obvious discrepancy is that the swell of January 5 was not observed in Kona. This discrepancy can be easily explained by the different exposure angle of the Waimea buoy and the high dependence on swell direction of the surf observed on the Western side of the Big Island of Hawaii. A numerical coastal wave model was used to visualize the swell patterns in the lee of the Islands (Figure 15). The model was initialized at the boundaries with the output spectrum from the global Wave Watch III wave model (Tolman et al., 2002) corresponding to January 10, 2003 and using a period of 17 s and a significant wave height of 6 meters arriving from 320°. The Hawaii chain shadows NNW swells from reaching the Kona coast, and this is likely the reason why this swell did not reach the coast and was not observed acoustically.

In addition to the correlation between wave heights and surf signal strength, a strong diurnal pattern to surf event detection is evident. As shown in Figure 16, surf signals are strongest at night, between the hours of 05:00 and 18:00 GMT (19:00 to 08:00 Hawaii time). This may be due to quieter conditions resulting from dying winds, or a diurnal change in boundary layer conditions. A trend is also visible on an annual scale, with increased surf activity in the summer months as compared to the winter (Figure 17). This is surprising, as swell heights are invariably higher in the winter than the summer. This apparent discrepancy may be explainable by

Figure 14. Overlay of ocean wave height from the Waimea buoy (blue) over the spectrogram for one channel of I59US during the month of January 2003. The red tick marks denote GMT time for the acoustic data, the scale for the wave height is on the right hand side, and the vertical axis on the left hand side is infrasonic frequency, in Hertz.

boundary layer condition variations; it is also possible that differences in swell directions may preferentially excite infrasound in areas farther from the array in winter than in summer, but a plot of detection azimuths as a function of time shows no such seasonal trend (Figure 18). It is possible that the increased number of surf sources shown in Figure 17 during winter may degrade the performance of the detector through cross-interference, preventing adjacent data pixels from being grouped together into families.
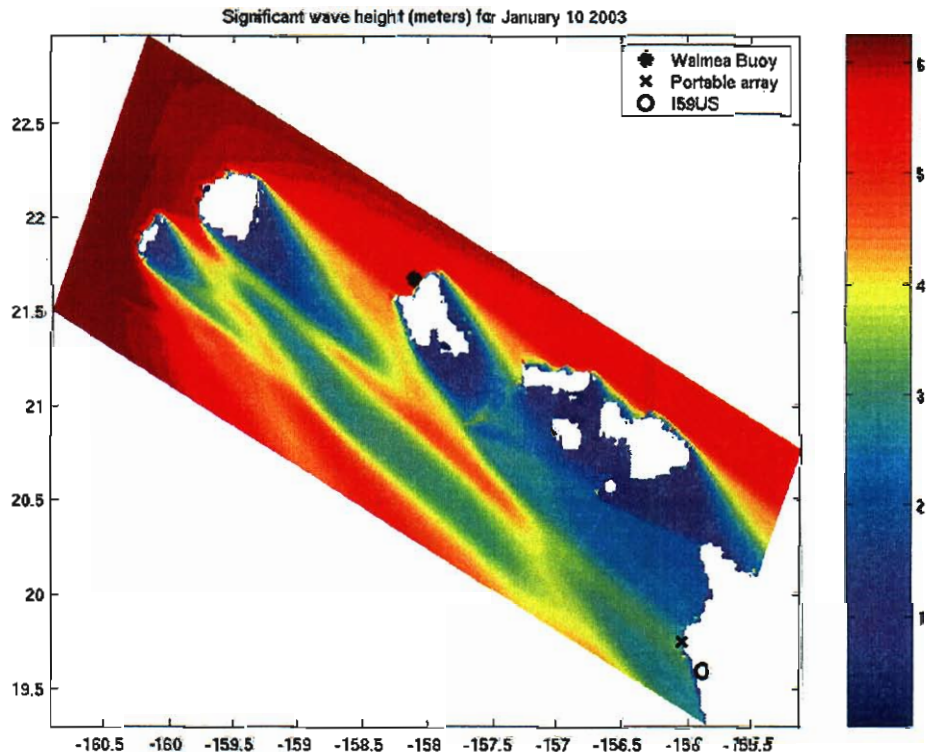
Figure 15. Island shadow map for a typical NW winter swell. The location of the Waimea buoy, I59US, and the portable array are shown in the figure. The color bar shows significant wave height in meters. For this swell direction, the western coast of the island of Hawaii is heavily shadowed by the island chain. Figure from Garcés et al., in press.
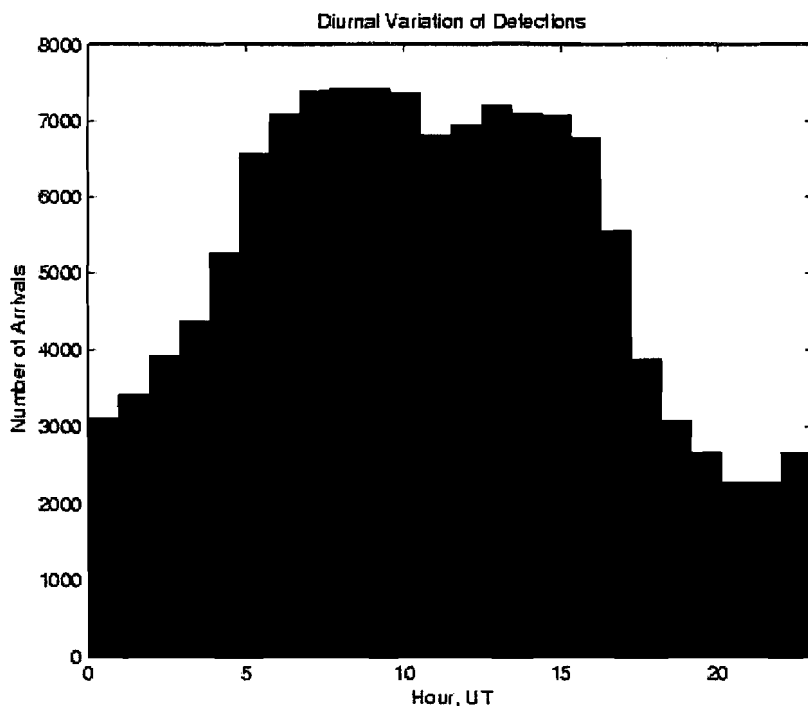
Figure 16. Histogram of arrival time-of-day for surf signals from January 2002 to December 2003. Signals are most prevalent between 05:00 and 18:00 UT, which is 19:00 to 08:00 Hawaii time.

Future research in the area of surf acoustics would focus on associations between surf infrasound signals, boundary layer conditions, and characteristics of the local ocean wave field, including height, period, and direction. Of particular interest are times when the dominant signal source changes from one point on the coast to another tens of kilometers away. These changes are often abrupt, sometimes taking place in less than an hour, and complete, with signal from one source vanishing almost totally and being replaced by signal from the other.
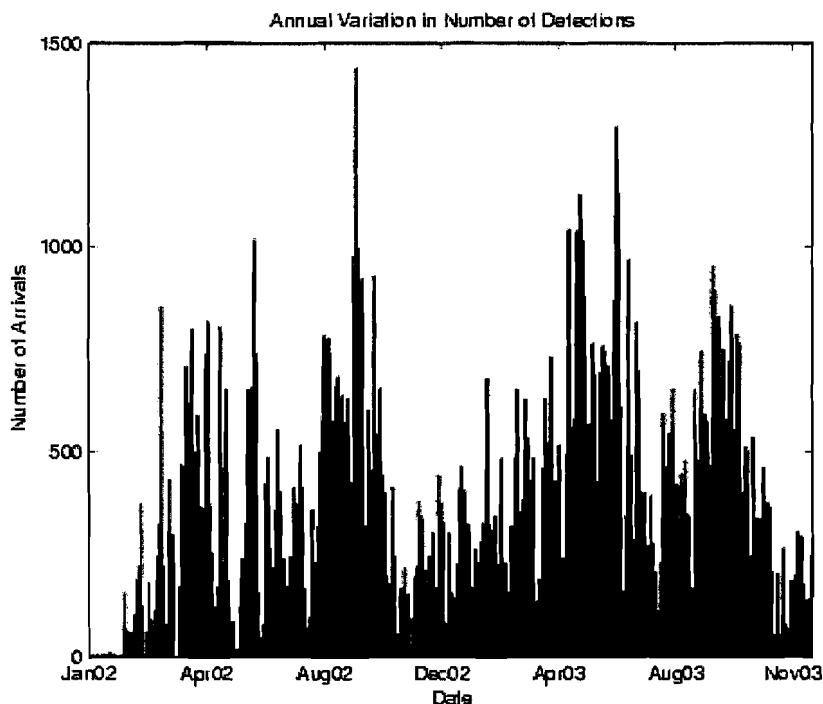
Figure 17. Histogram of arrival date for surf signals from January 2002 to December 2003. Signals appear to be consistently less numerous in winter than in summer.

20
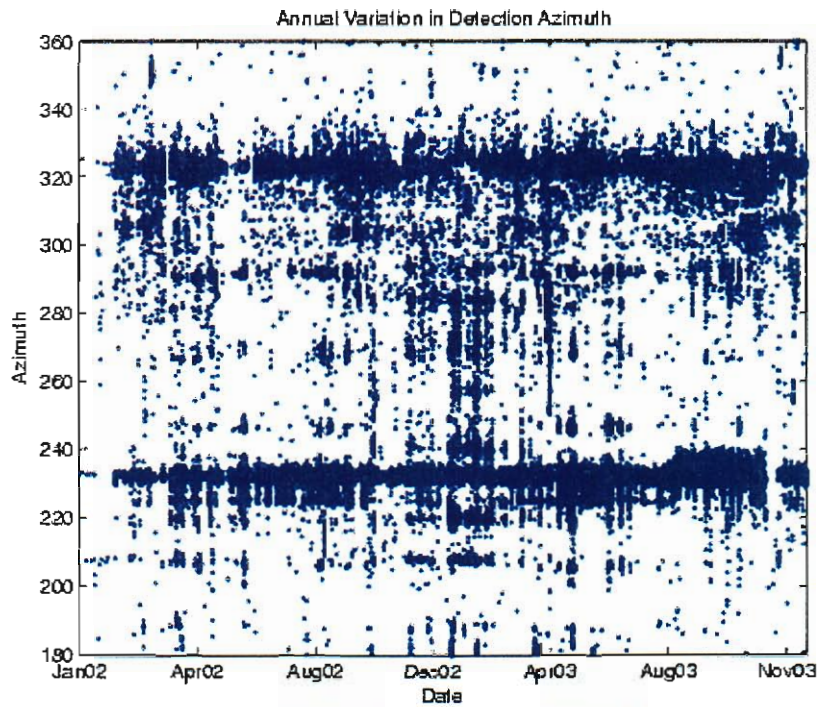
Figure 18. Plot of surf arrival azimuth as a function of time. Major
sources of surf infrasound can be seen as horizontal linear
trends in the data. Although little seasonal variation can be
seen in the signals from the two major surf sources, signals can
be seen to arrive from a greater range of azimuths during
winter months.

4. Microbaroms

Microbaroms are low-frequency infrasonic waves that form the major source of noise in the 0.1-0.7 Hz frequency band. They are believed to originate from the interaction of ocean surface waves of opposite but nearly-equal wavenumbers (Longuet-Higgins, 1950; Hasselmann, 1963; Posmentier, 1967; Arendt and Fritts, 2000), and have been shown to have a common source with microseisms (Donn and Naini, 1973; Ponomaryov et al., 1998). Despite their common source, microseisms and microbaroms will have very different propagation paths. Energy launched near a vertical angle to the ocean surface and towards the ocean floor couples well with the bedrock, and energy launched just below the ocean surface may not reach the ground. In contrast, energy launched near a vertical angle into the atmosphere never returns back to the ground, and most of the infrasonic signals recorded by ground stations correspond to energy launched near the horizontal angle at the source. Numerous researchers have linked microbarom and microseism generation to severe weather such as hurricanes and thunderstorms (e.g. Goerke and Woodward, 1966; Donn and Posmentier, 1967; Ponomaryov et al., 1998, Bhattacharyya et al., 2003). Microbaroms are an omnipresent and persistent source of noise, and a significant impediment to nuclear test monitoring since the expected peak frequency of a 1-kT nuclear explosion falls within the microbarom passband.

For a specified ocean surface wave velocity u_z, the far-field acoustic pressure, p, in a homogeneous atmosphere can be expressed as (Arendt and Fritts, 2000),

$$p\left(x, y, z, t - \frac{R}{c}\right) = -\frac{\rho_0}{8\pi c}\frac{\partial}{\partial t}\int \frac{z}{R^2}u_z^2 dx' dy'$$

$$R^2 = (x - x')^2 + (y - y')^2 + z^2$$

(1)

where x, y, and z are the spatial coordinates in a Cartesian reference frame, x' and y' are the Cartesian coordinates of integration over the ocean surface, ρ_o is the atmospheric density, and c is the atmospheric sound speed. Note that the acoustic pressure is proportional to the integral of the square of the ocean surface velocity. After expressing the ocean surface velocity as sinusoidal terms corresponding to propagating surface wave trains, we find propagating acoustic solutions only exist for surface waves that interact with each other at near the same frequency and nearly antiparallel directions. All other solutions are non-propagating.

The period and amplitude of an ocean wave depend on the wind speed and fetch of a severe weather disturbance. Although high wind speeds are possible in a hurricane, such winds are usually highly localized, have a relatively small fetch, and thus do not efficiently generate large ocean waves. Ocean surface waves that propagate for long ranges usually have periods of 8-12 seconds. Due to the nonlinear interaction introduced by the square of the velocity, the acoustic solution will have approximately twice the ocean wave frequency (frequency doubling). This can be understood as an acoustic coupling, as for sound to be efficiently radiated in the atmosphere it is necessary for the horizontal wavelength of the ocean wave field to match the acoustic wavelength. Due to the slow propagation speed of deep water waves, their wavelength tends to be too small for acoustic coupling unless two surface wavetrains are propagating nearly opposite

to each other, in which case one of the nonlinear terms allows the existence of a large horizontal wavelength (small horizontal wavenumber) that encourages efficient coupling to the atmosphere. This nonlinear term corresponds to an acoustic frequency that is the sum of the frequencies of the interacting surface wave trains, or approximately twice the dominant frequency of the ocean wave.

The wavenumber solution space for the surface wave velocity corresponds to two waves propagating in almost parallel but opposite directions. However, the acoustic solution space is isotropic, which implies that even a very directional surface wave field can generate infrasonic waves along all azimuths. This isotropic acoustic radiation pattern helps explain the pervasiveness of the microbarom signals. When ocean waves propagate exactly against each other at the same frequency, the nonlinear interaction produces a piston-like displacement of the ocean surface, and launches sound straight up to the atmosphere. Maximum acoustic energy is radiated in the vertical direction, and although it may contribute to the atmosphere's heating (Rind, 1977), this energy is lost to space and cannot be recorded by ground-based stations. Infrasound arrays would only record microbarom signals that are launched close to the horizontal, corresponding to ocean waves interacting at slightly dissimilar frequencies and slightly off the antiparallel directions. Thus, only a small fraction of the total acoustic energy launched into the atmosphere by microbarom sources reaches the ground.

Microbaroms are recorded almost continuously at I59US, but are not always correlated across the array. This may be due to the array's large aperture, which was designed to minimize coherent microbarom signals, or to the low number of elements (4). Nevertheless, coherent microbarom burst detections number in the hundreds per day (Figure 19), and can vary significantly in azimuth. Often the azimuth recorded at the array points to an area of significant wave heights corresponding to seasonal storms, but sometimes distant storms are drowned out by local weather conditions. The large mountains adjacent to I59US appear to cause acoustic shadow zones for energy arriving close to the horizontal. Season trends in azimuth match the trends in Pacific storm system location, with N and NW swells dominating in winter and trade (E) and South swells predominant in summer; this trend can be seen on scales of one year (Figure 20) and two (Figure 21). No seasonal trend was visible in the amplitudes of the signals (Figure 21), but a similar trend can be seen in the number of arrivals; microbarom arrivals are most prevalent in winter (North Pacific storms) and early summer (tropical storms), and calmer in spring and early autumn (Figure 22). Microbaroms also show variation on a diurnal scale, although not as strongly as do the surf arrivals (Figure 23). The difference in the time where signals are strongest may be due to differences in the way that various frequencies propagate in the boundary layer. Also, the range of values in the microbarom histogram is less pronounced than in the surf histogram; it is possible that the low-frequency, large-azimuth microbarom signals are less subject to local atmospheric effects than the surf signals.
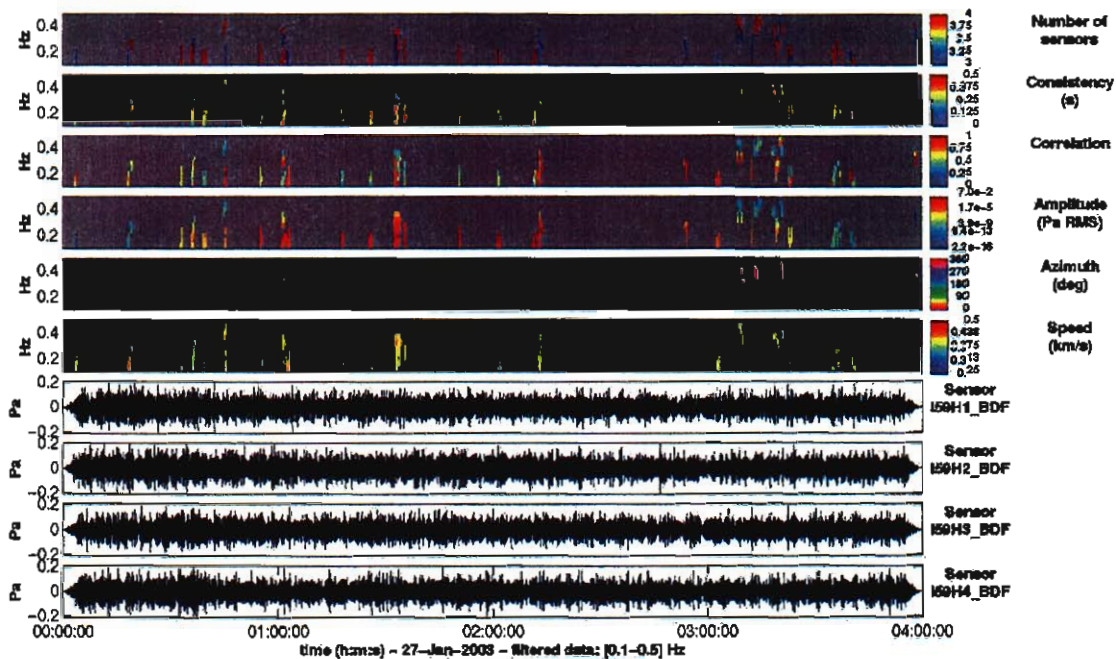
Figure 19: PMCC results showing microbarom bursts typical of station I59US.
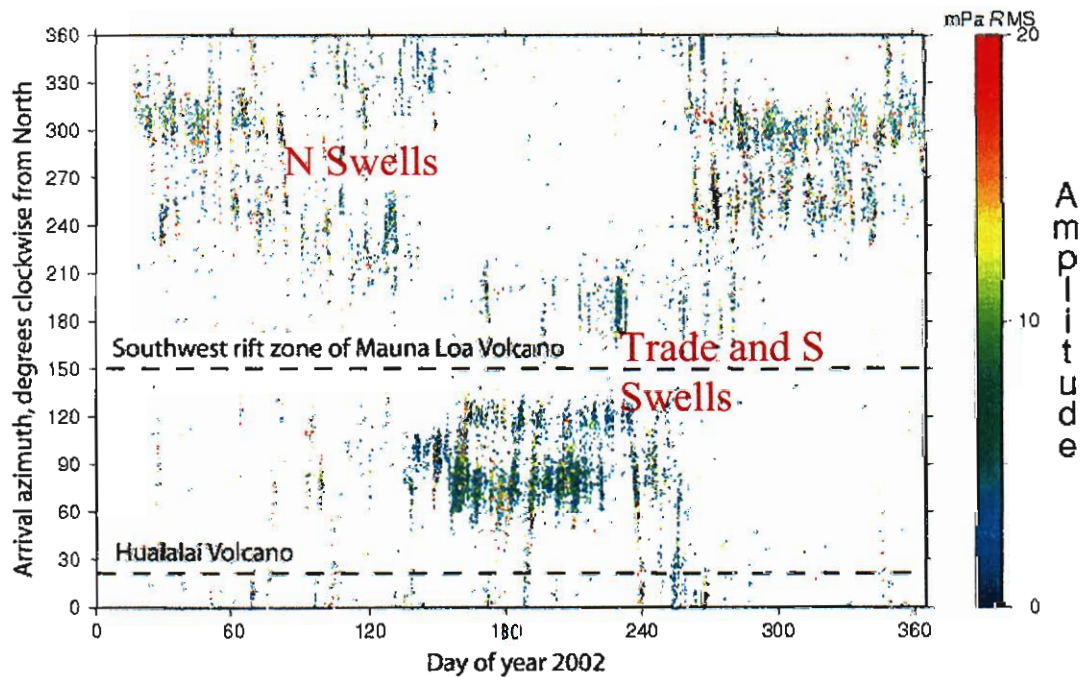
Figure 20. Plot of microbarom arrivals for the year 2002 showing seasonal azimuth trends and the acoustic shadow zones created by the nearby mountains.
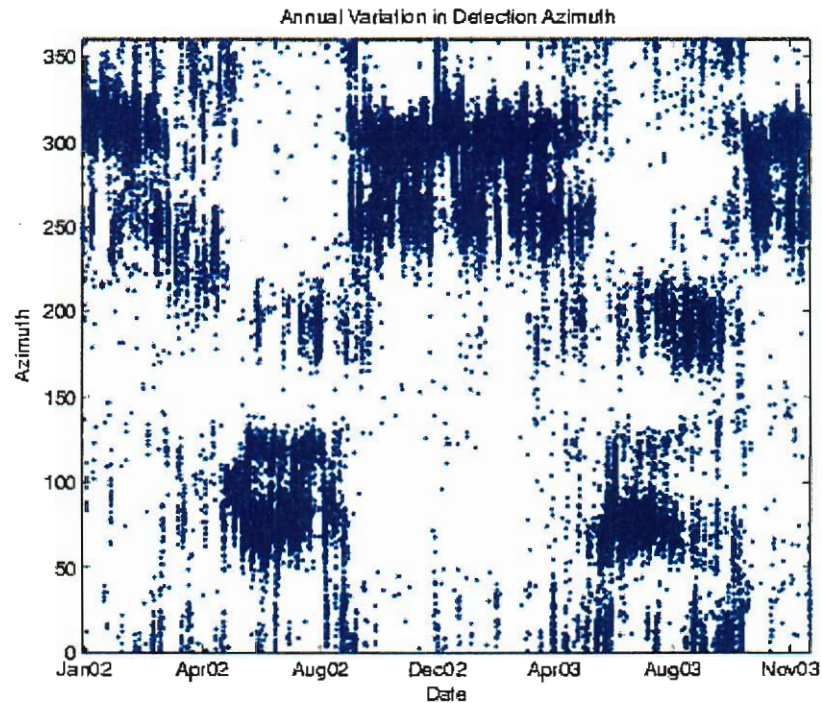
Figure 21. Plot of microbarom arrivals from January 2002 to December 2003, showing seasonal repetition of the azimuth trends shown in Figure 20.
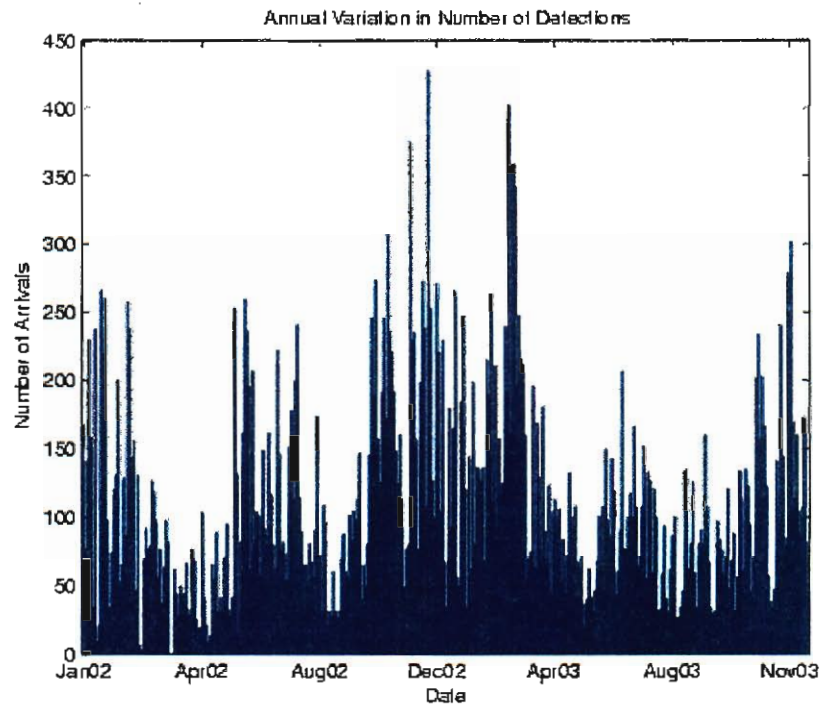
Figure 22. Histogram of microbarom arrivals showing strong activity in winter months, less strong activity in summer, and relative calm in spring and early autumn. This reflects normal seasonal storm trends, with heavy North Pacific storms in winter and tropical storms in summer.

25
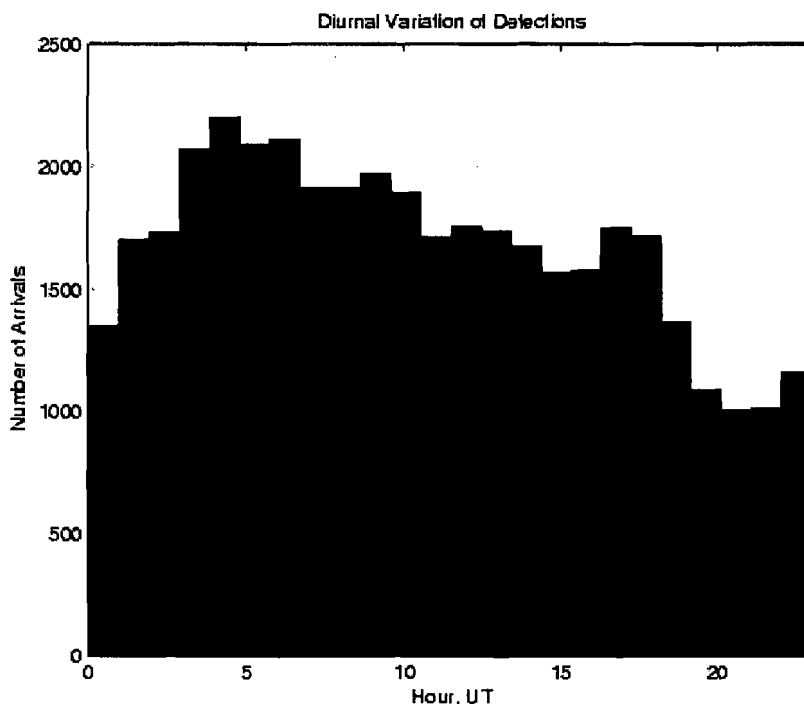
Figure 23. Histogram showing diurnal variation in microbarom arrivals.

Microbarom signals recorded at I59US have been used to locate and follow several storms in the central and eastern Pacific, including Hurricanes Daniel (2000) and Jimena (2003) and Tropical Storm Barbara (2001).

On July 23, 2000, approximately two months after the initiation of operations of IMS array I59US in Hawaii, Hurricane Daniel formed in the eastern Pacific and steadily moved towards Hawaii, passing by on July 31st (Figure 24). Daniel provided the first opportunity for ISLA to locate and follow storms using microbarom signals. Figure 25 shows the track history of Daniel, and the arrival azimuth of infrasonic signals detected by I59US. We see that infrasonic detection of Daniel started before it was designated a hurricane (Figure 24, red), and the detected azimuth matches the actual azimuth of Daniel up to August 1, when Daniel began to dissipate. Figure 26 shows the frequency content of the microbarom signals recorded by I59US. Most of the energy is in the 0.1-0.4 Hz band, and there is a bifurcation in the microbarom band from late July 30 to early August 1 which corresponds to a group of higher-frequency arrivals at that time (Figure 27); these may be generated by the interaction of direct ocean waves from the storm with reflections of those waves from the island chain.
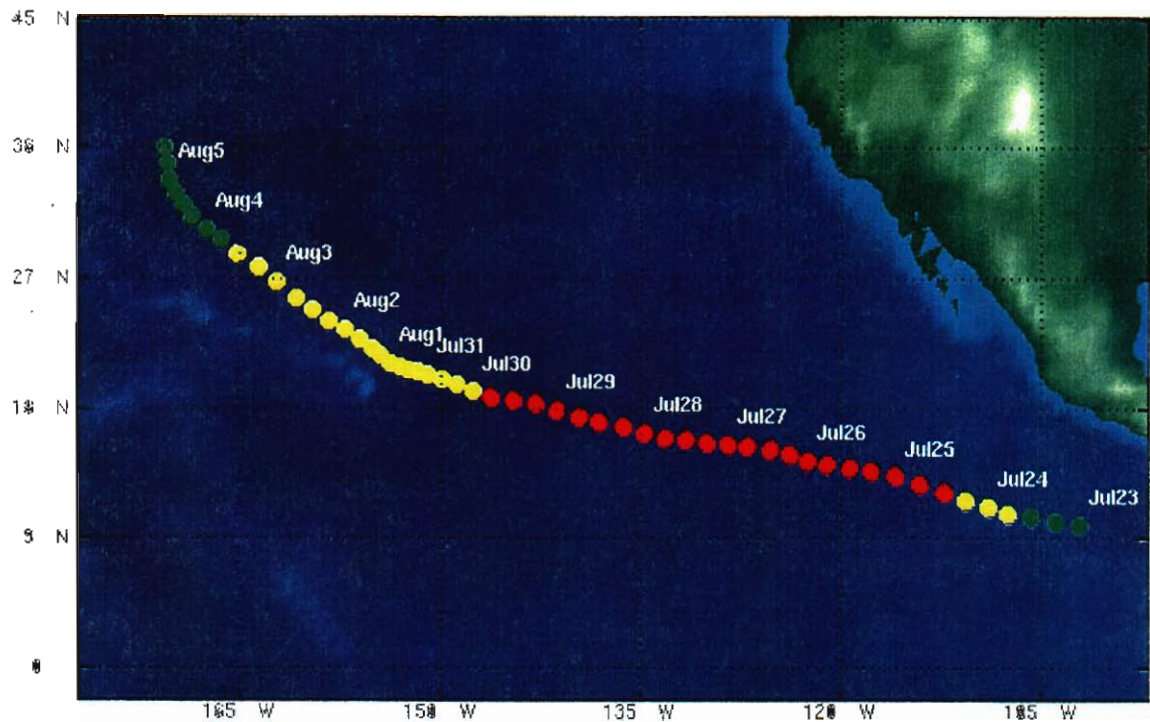
Figure 24. Map showing the track of Hurricane Daniel as a function of time and intensity. Green indicates tropical depression, yellow indicates tropical storm, and red indicates hurricane strength.
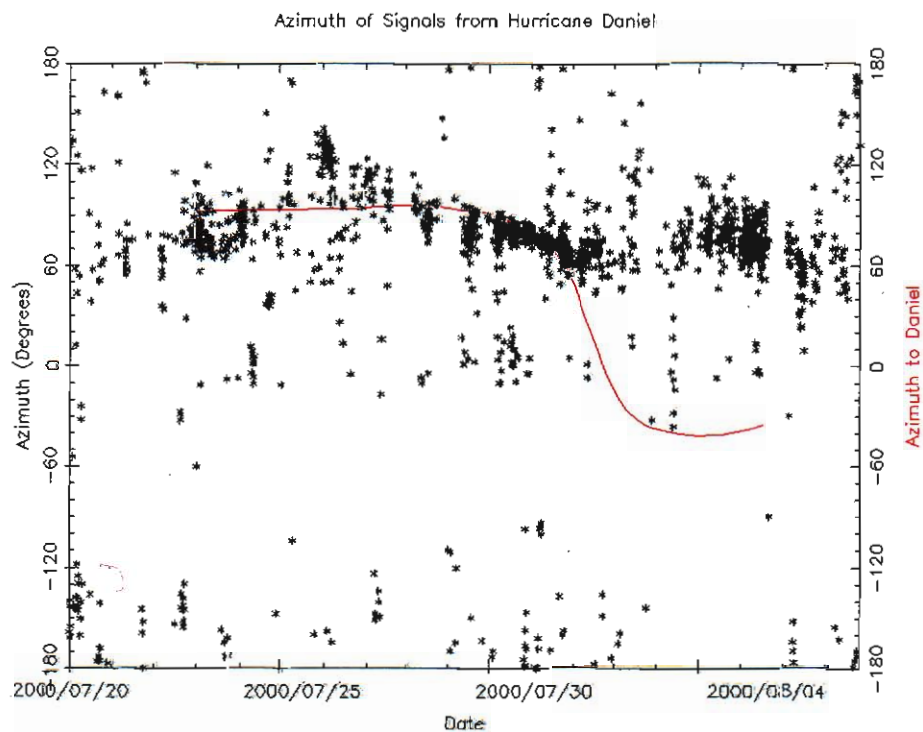
Figure 25. Observed microbarom signal azimuths (black) and the azimuth from I59US to the core of Hurricane Daniel (red).
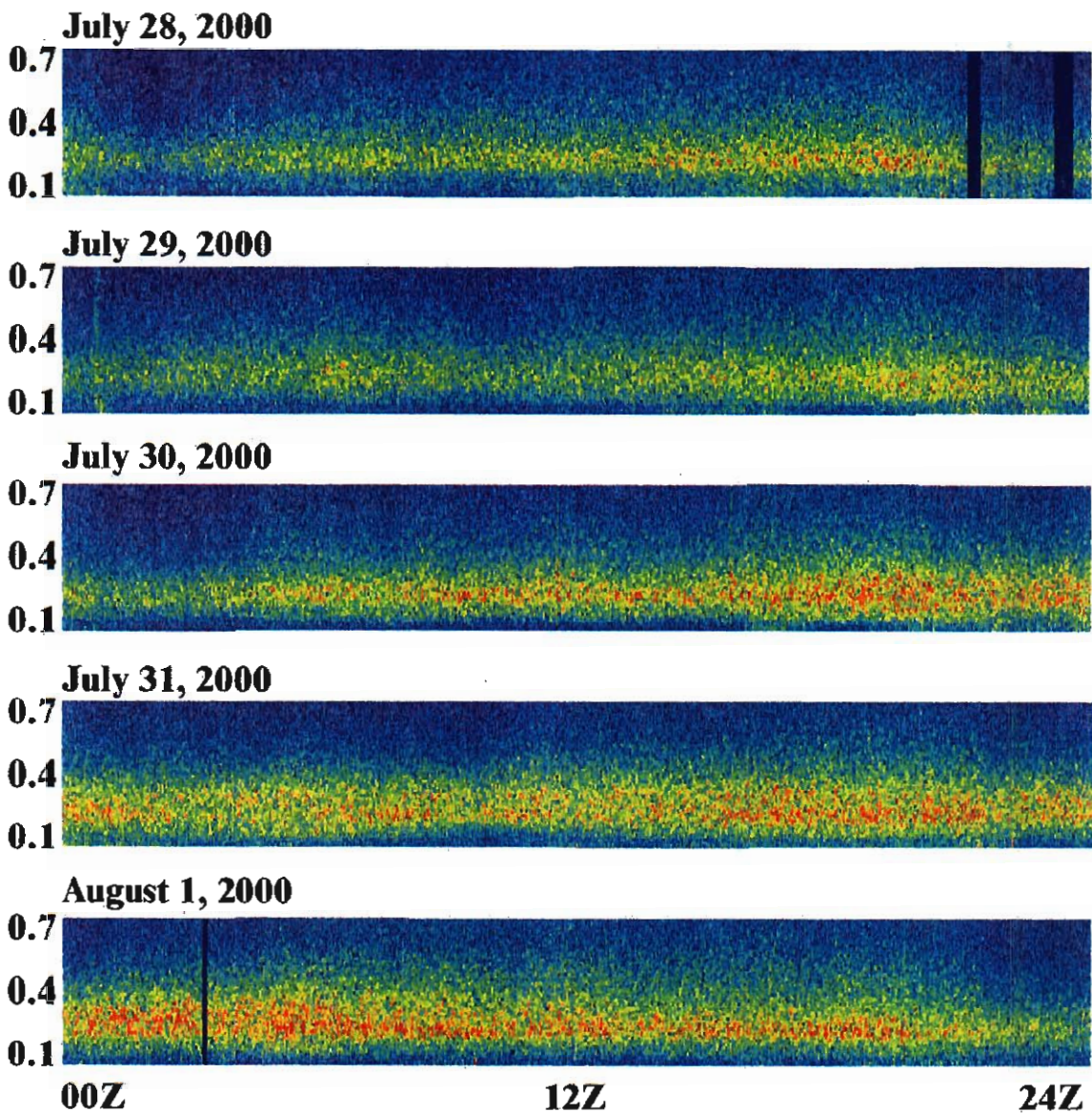
Figure 26. Spectrograms in the microbarom range for Daniel, showing initial diurnal fluctuations in the microbarom levels, which disappear as Daniel approached Hawaii. Note the frequency bifurcation starting after 12 Z on July 30 and ending around 12Z on August 1.
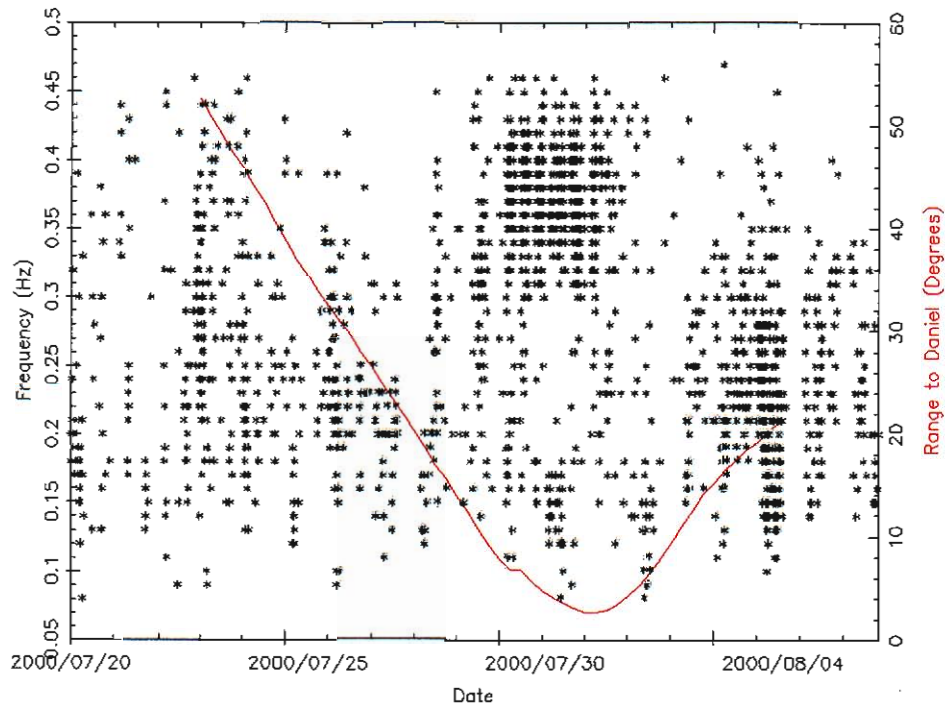
Figure 27. Mean frequency of microbarom arrivals as a function of time (black) and range from I59US to Daniel (red). A grouping of higher-frequency arrivals can be seen from July 30 to August 2, roughly corresponding to the times of the frequency bifurcation seen in Figure 26.

Tropical Storm Barbara developed as a tropical depression on June 20 2001 and was quickly upgraded to Tropical Storm status the same day (Figure 28). Microbarom signals from the general area, however, were visible as early as June 17 (Figure 29). It is possible that the signals were recorded from more proximal weather visible in the early satellite images, or the weather system that produced Barbara may have generated enough energy to be heard. Barbara's life as a tropical storm lasted for less than 48 hours, but infrasonic signals generated in her vicinity persisted for several days.
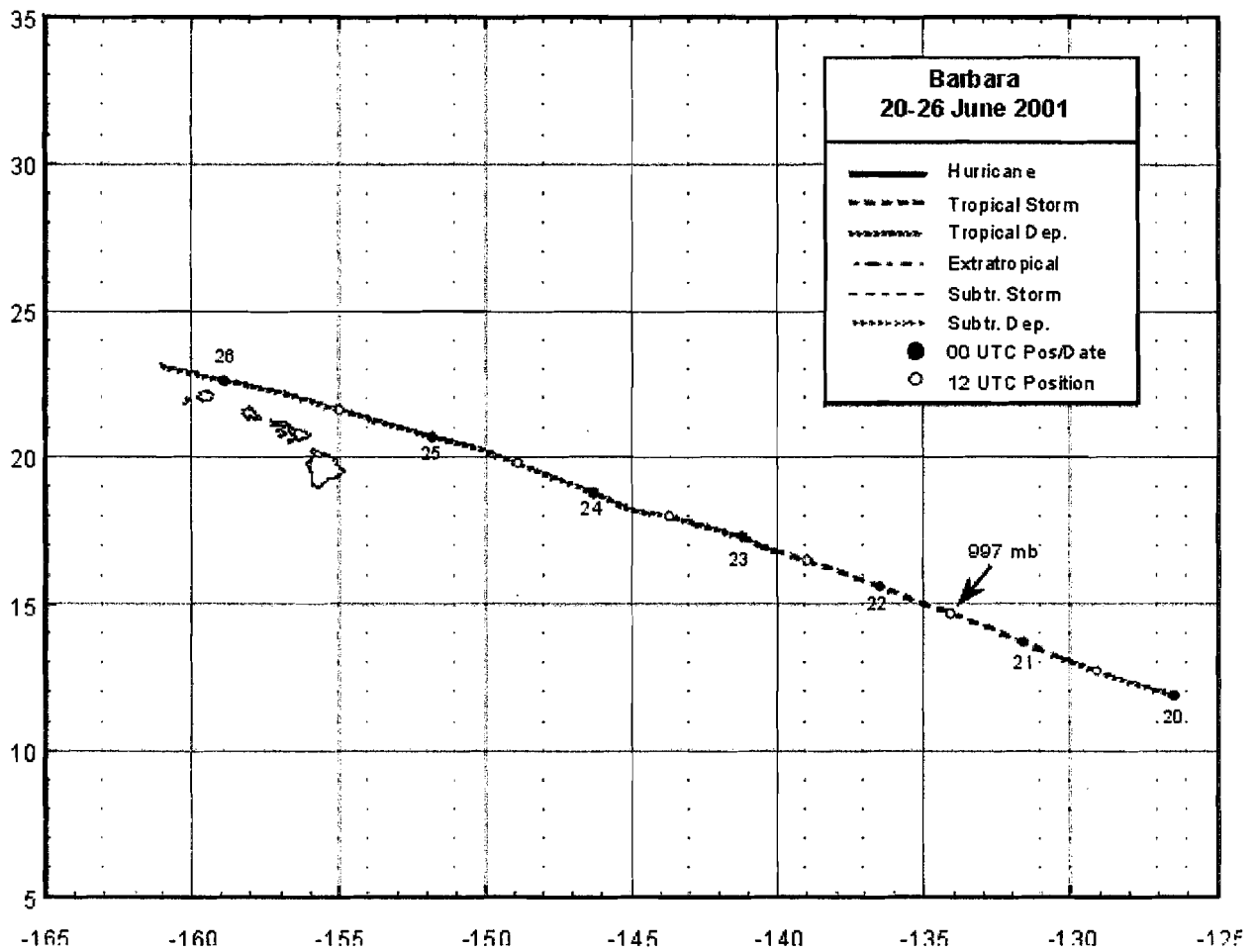
Figure 28. Track of Tropical Storm Barbara. From NOAA National Hurricane Center,
http://www.nhc.noaa.gov/2001barbara.html
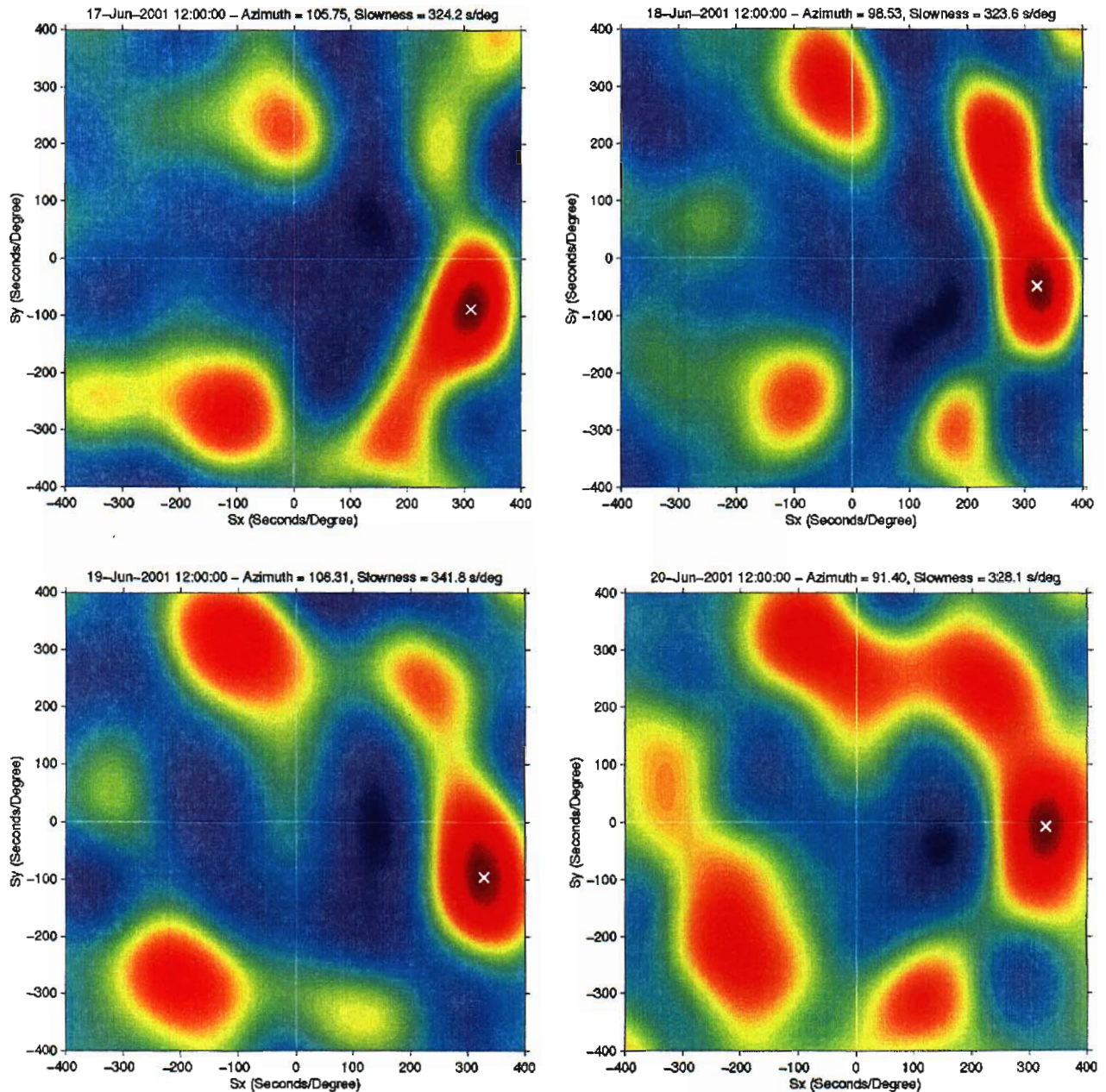
Figure 29. FK diagrams showing signal coming from the direction of Tropical Storm Barbara. Variation in calculated azimuth comes both from the size of the main lobe and the spatially-distributed source region.

Hurricane Jimena developed on August 28, 2003 and quickly reached its full Category 2 hurricane strength, with sustained winds measured at over 100 miles per hour on August 30. It passed south of Hawai'i Island on September 1, 2003 (Figure 30), by which time its winds had weakened to Category 1 strength. Signals recorded from Jimena illustrate not only that tropical cyclones can generate detectable microbarom infrasound, but also that the strong hurricane sounds can be drowned out by other, weaker events for which recording conditions are better. On August 31, when Jimena was approaching Hawai'i Island, bursts of microbarom activity are

visible from the east, in the direction of Jimena, but stronger signals are visible from the south and southwest as well (Figure 31). Wave height maps from that time show an area of elevated wave heights to the southwest of the Hawaiian Islands that could potentially generate microbarom energy (Figure 32). Although the wave heights are less than those of the Jimena system to the east, and although the distances from Hawaii to the approximate centers of the two wave regions are roughly equal, it is probable that the massive Mauna Loa volcano blocked enough energy from Jimena for the other wave region to be preferentially detected.

The utility of microbarom energy for monitoring storms was also demonstrated in a 4-hour segment of data from September 1, 2003, from 12:00 to 16:00 GMT. During this time an obvious westward azimuth trend is visible in the microbarom data as the center of the storm passes to the south of the island and continues its westward movement (Figures 33-35).
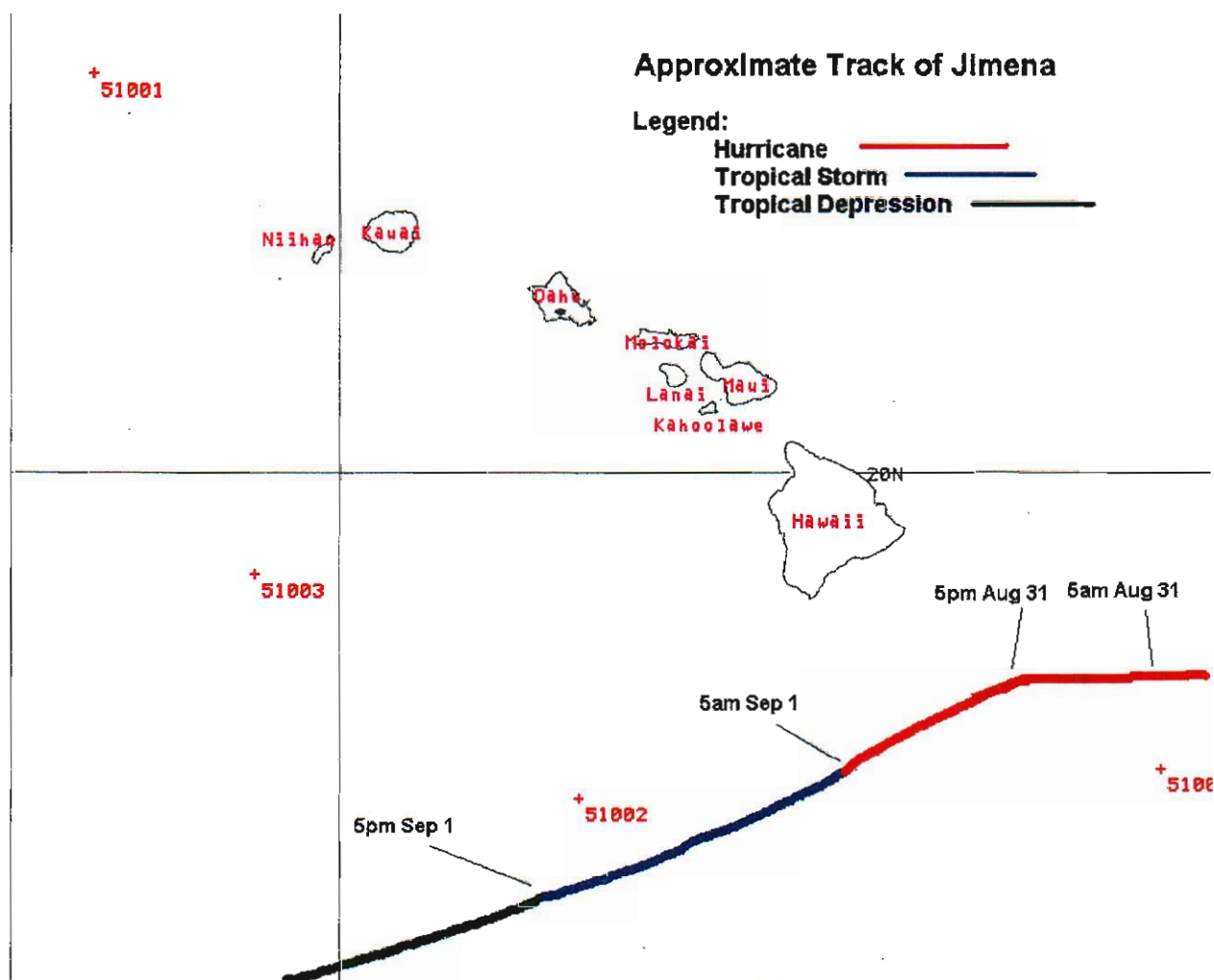
Figure 30. Approximate track of Hurricane Jimena, showing closest approach to Hawaii and storm classifications. Figure from NOAA National Weather Service Central Pacific Hurricane Center, http://www.prh.noaa.gov/cphc/summaries/2003/jimena/jimena.php.
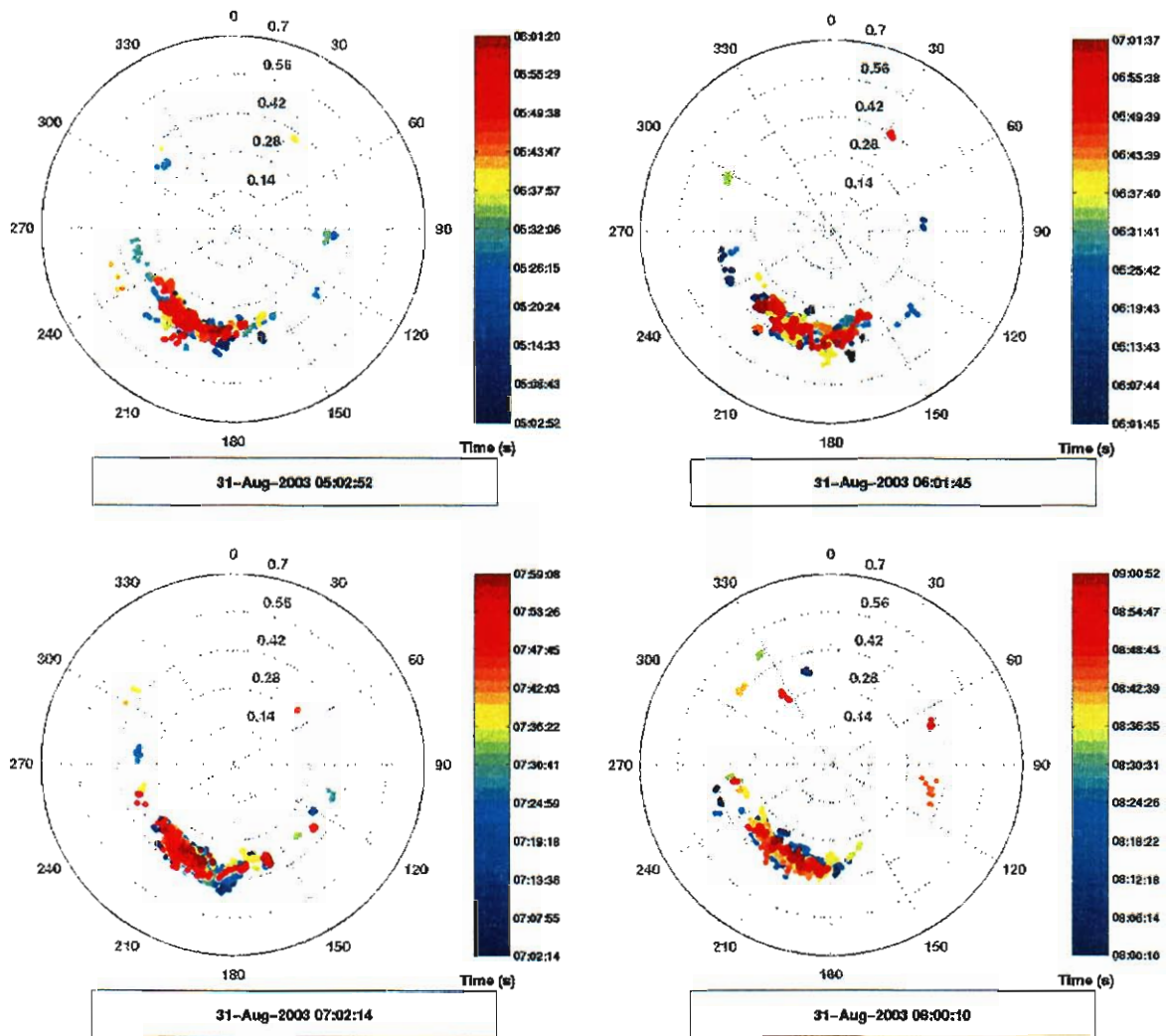
Figure 31. Polar plots from a 4-hour segment during the approach of Jimena showing preferential recording of a local, unshielded ocean wave system.
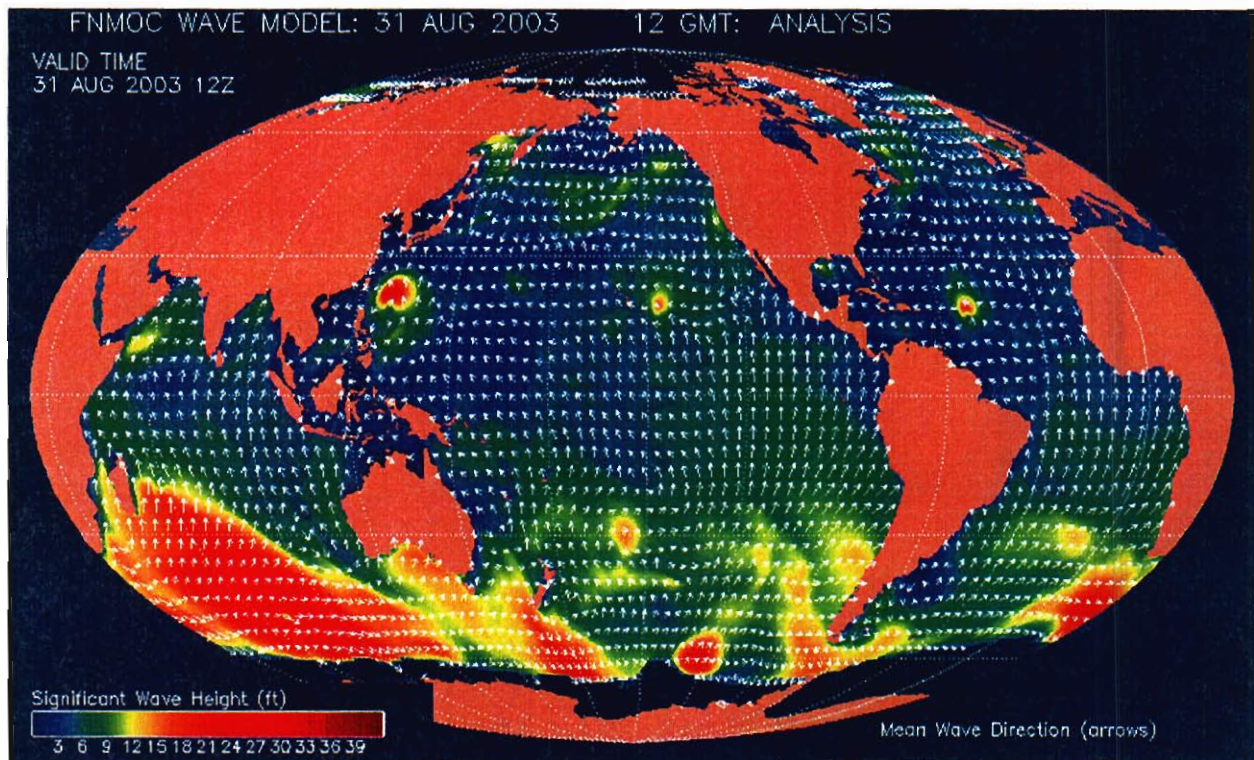
Figure 32. Global wave height map showing regions of elevated wave height from Jimena and a second wave system to the southwest of Hawaii that appears to be preferentially detected.
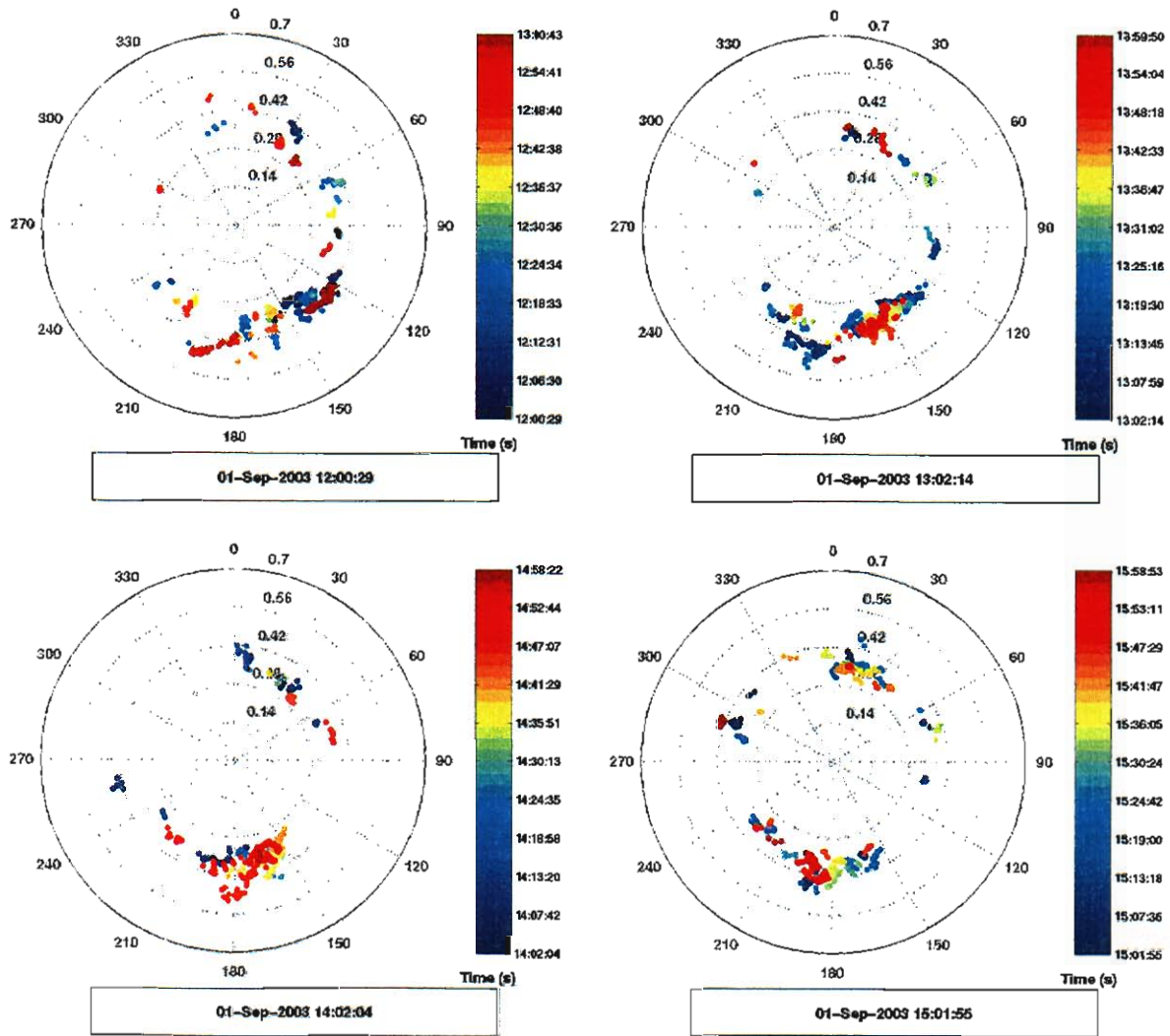
Figure 33. Polar diagrams for 4 hours showing strong westward trend in microbarom data as Jimena passes to the south of the island and continues westward.
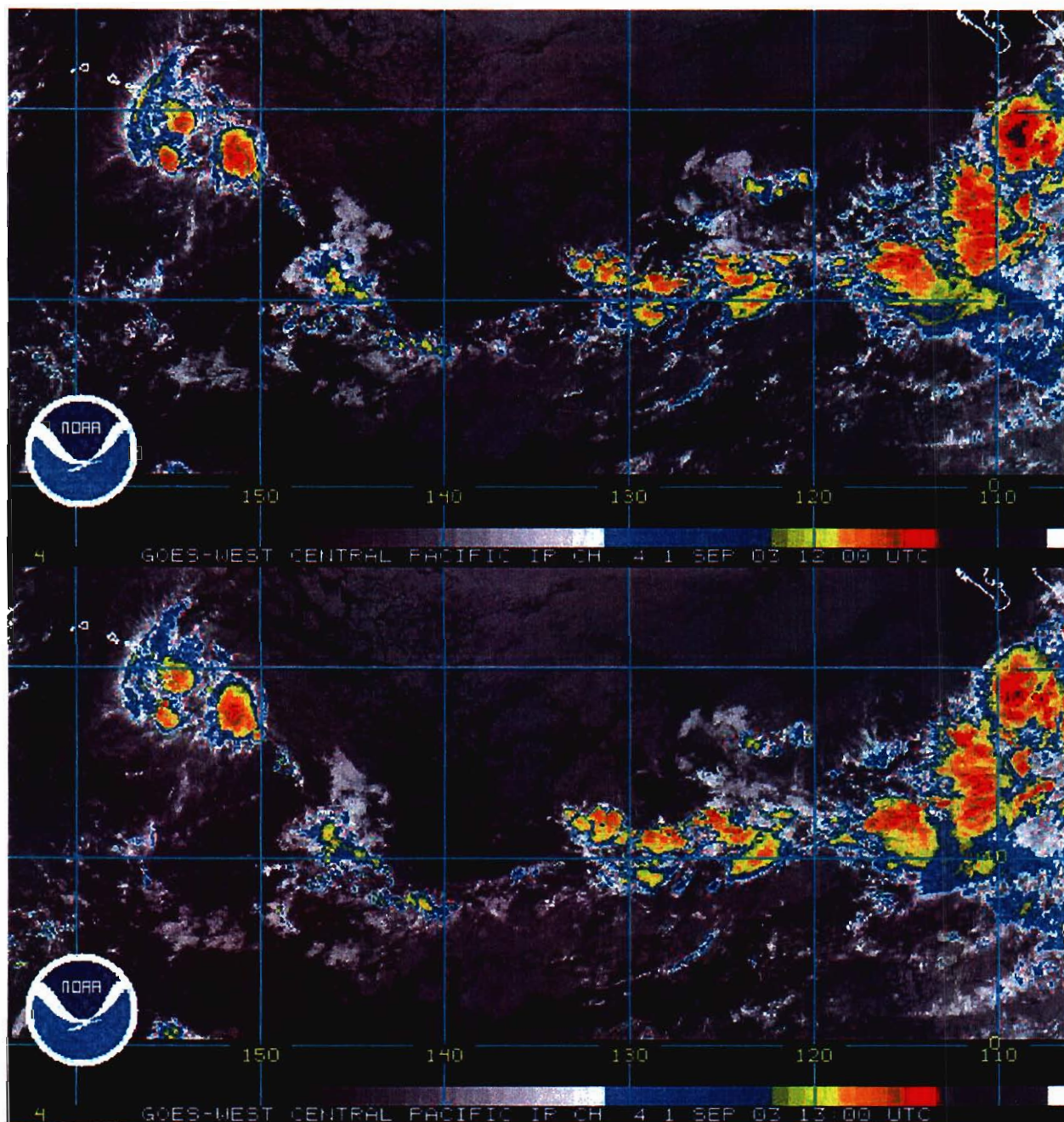
Figure 34. GOES Infrared satellite image showing position of Jimena storm system for the first two radar plots in Figure 33. Note that the system has split into several subsystems, each of which may be generating waves that can interact with each other and produce microbaroms.
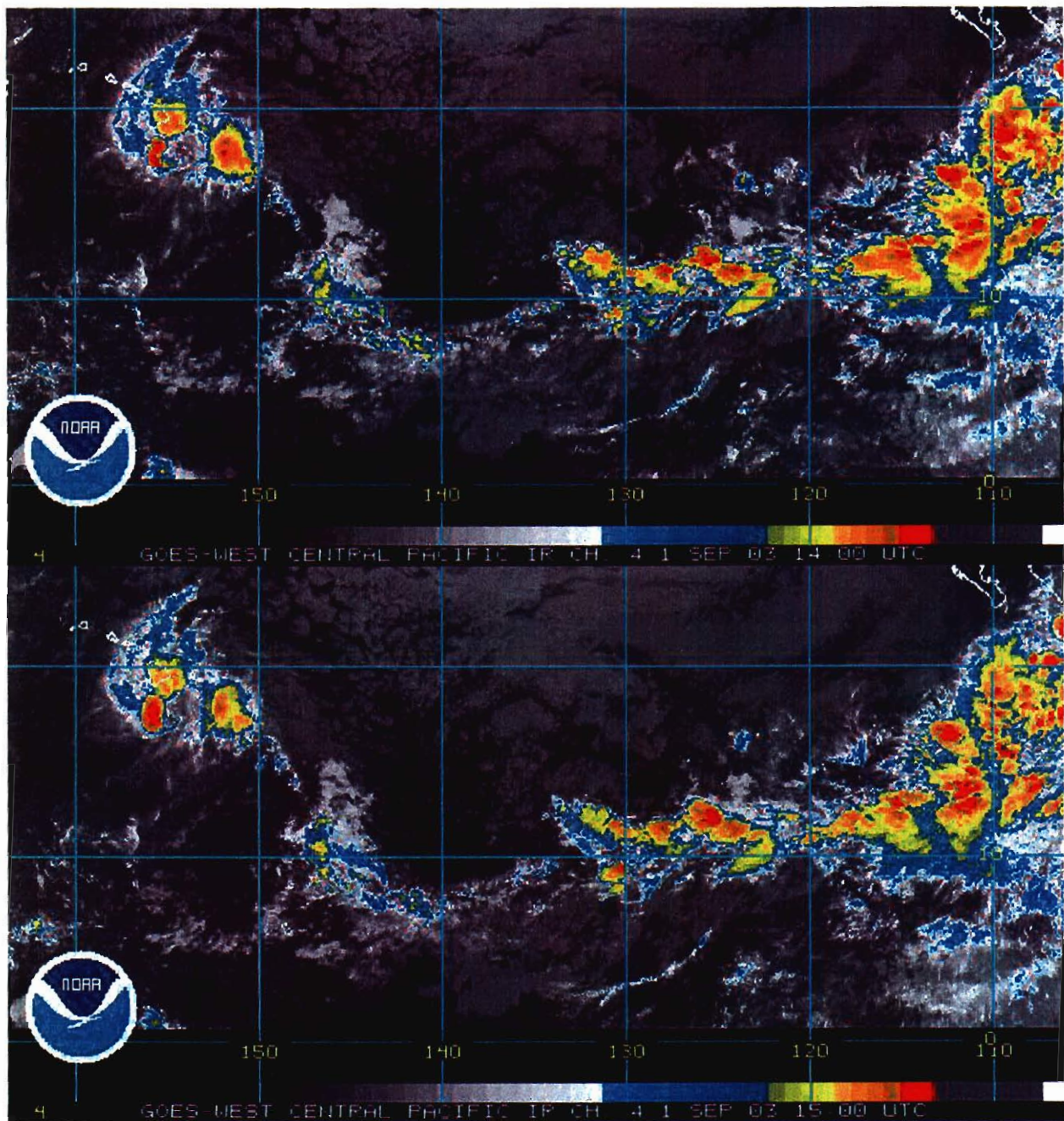
Figure 35. GOES Infrared satellite image showing position of Jimena storm system for the last two radar plots in Figure 33. Note that the system has split into several subsystems, each of which may be generating waves that can interact with each other and produce microbaroms.

Current microbarom research revolves around the prediction of microbarom intensity on a global scale. In order to accurately model microbarom generation, an accurate model of surface wave heights, periods, and directions must be available. The method of Arendt and Fritts (2000) has been adopted using input from the WaveWatch3 model of Tolman et al. (2002) to calculate the infrasonic source pressure at each point in a global grid. The WW3 model outputs the variance density, F, of the surface wave field as a function of frequency, f, and propagation direction, θ, at

each node of a global 1 degree grid. The variance density has units of $m^2/(rad*Hz)$ and it is a measure of the energy in the surface wave field. The phase of each wave component is assumed to be random. The infrasonic source pressure spectrum at each point (Figure 36) can be calculated from the variance density F using a method detailed by Garcés et al. (2003b). The source pressure can then be propagated to every other point on the global grid by calculating the distance R (km) to each target point and then using the pressure scaling relation of Stevens et al. (2002),

$$P = \frac{P_{ref}}{R^{1.36}} 10^{0.019v},$$ (2)

where the reference pressure P_{ref} is relative to the source location and the stratospheric wind speed v at 50 km along the propagation direction is given in m/s. For our initial tests of the process we have ignored the stratospheric winds, which will be eventually incorporated using Naval Research Laboratory (NRL) ground-to-space (G2S) atmospheric specifications. The infrasonic propagation is a computationally expensive process that we plan to implement at the Maui High Performance Computing Center.
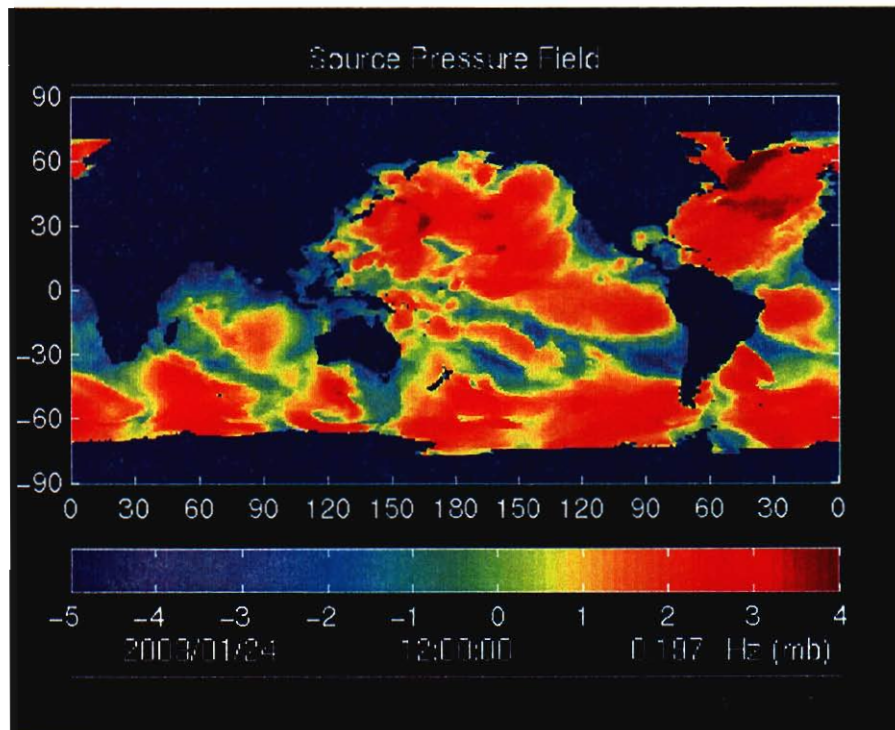
Figure 36. Example of an infrasonic source field calculated from the variance density of the oceanic wave field.

5. Distant and Large Event Detections

Since station I59US entered into operation a number of significant infrasonic events have been recorded by the array. This chapter will enumerate them and discuss the characteristics of the arrivals.

Bolides

Bolides are among the highest-energy sources that can be expected to be regularly recorded on infrasonic sensors. A recent bolide explosion in April, 2001, had an estimated energy release of 4.6×10^{12} Joules (Brown et al., 2001), which is the approximate equivalent of a 1-kiloton nuclear explosion (1 ton TNT = 4.184×10^9 J). Due to the potentially immense amount of energy released by these events, bolide signals are of great interest to the infrasound community, not just for scientific purposes but also as potential false alarm signals for test-ban-treaty monitoring. Numerous examples of bolide infrasound recordings exist (e.g. ReVelle et al., 1997 & 1998; ReVelle and Whitaker, 1999; Evers and Haak, 2001; Su and Su, 2001. Brown et al. (2002) estimate that an impact of about 5 kilotons equivalent yield occurs once per year on average, and a 10-megaton event such as that in Tunguska, Siberia in 1908 occurs about every 1000 years. Because of the coincidence in energy release between bolides and nuclear tests, and the frequency of bolide event occurrence, it is crucial to be able to positively and expeditiously identify a questionable arrivals as a bolide. However, without secondary supporting information such as a confirmed satellite detection (the ideal situation, as it gives fairly accurate estimates of the location and time of the explosion), radar observations, records from a CONCAM (Nemiroff & Rafert, 1999) or other photographic system, or detections on additional arrays, it can be very difficult to positively identify the signal.

The first large bolide recorded infrasonically in Hawaii was the *Acapulco* event of August 25, 2000 (Garces et al, 2001, 2002). This event had an estimated energy release of 1.4×10^{12} Joules, was located at 14.45° N, 106.13° W, and was recorded on current IMS infrasound stations in Hawaii (Figures 37 & 38), Alaska, Canada, Bolivia, and French Guiana, as well as the Los Alamos-operated station DLIAR in New Mexico.
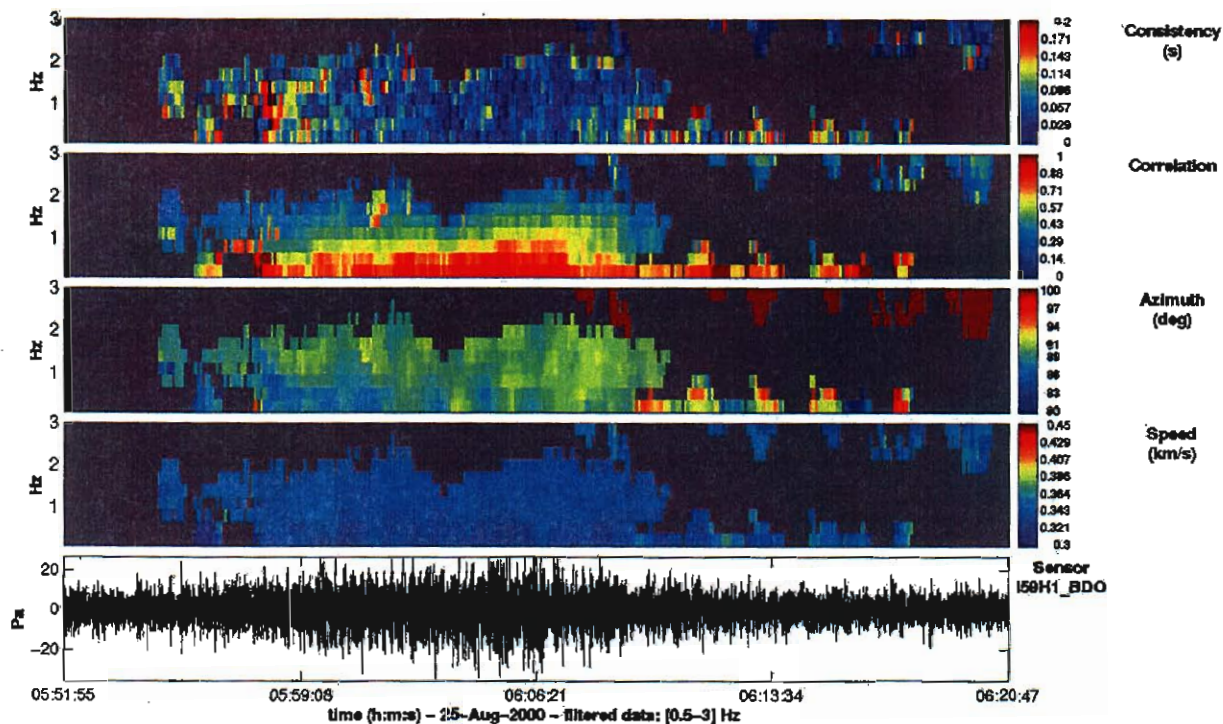
Figure 37. PMCC results showing the Acapulco bolide as recorded at station I59US.
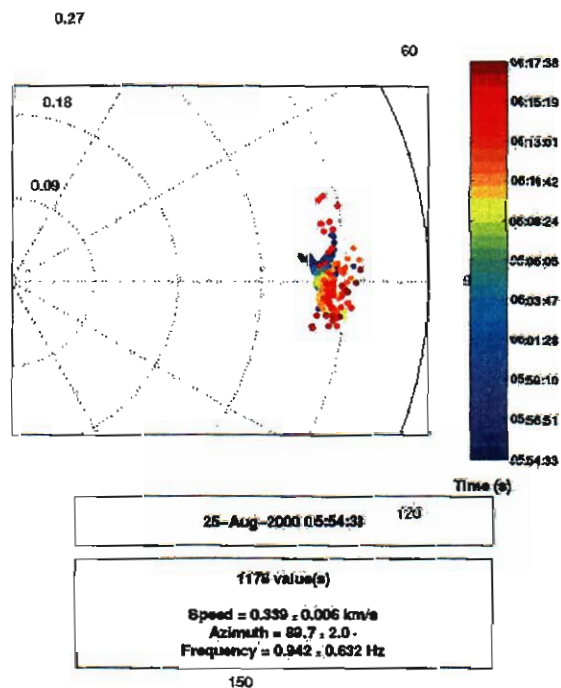
Figure 38. Polar diagram showing general southward
progression with time of signals from the Acapulco
bolide.

Much analysis was performed on the Acapulco bolide and a number of crucial conclusions were reached. It was found that for long propagation ranges, the time contribution from the source height to the ground or the source height to the upper waveguide boundary is negligible, multiple bounces produce overlapping travel time curves which begin to appear as a continuous curve, and shadow zones disappear. Due to the continuous appearance of travel time curves and the further degradation of shadow zones by scattering and diffraction, it was discovered that computing a range of celerities, or effective speeds, was an effective way to generalize a ray trace over long distances. Celerity, as the ratio of the horizontal range covered by one infrasonic "skip" (ground to refraction point in the atmosphere and back to the ground) to the time elapsed during the skip, is a function only of slowness for a given atmospheric profile, is independent of the actual number of skips taken by a given ray, and can be averaged over a long propagation path, making a generalized ray trace relatively simple to perform. This is important because ray tracing in a medium with acoustic properties that vary with range is a complicated procedure. In order to compute the celerity we used the Tau-P method of Garcés et al. (1998). In this method the slowness domain is divided into phases defined by the top and bottom turning heights of acoustic waves propagating with that slowness. Candidate phases are listed in Table 6, but for propagating ranges greater than a few thousand kilometers it is difficult to sustain the iw phases and the Iw, Is, and It phases are not applicable. For long ranges, is phases are also found to be unstable, as the stratospheric winds can vary significantly along a meridian. However, the it, itd, and isd phases are found to exist for almost all azimuths and geographic locations. Only when an is phase exists does the itd phase disappear. Once the signal onset time was determined, celerities for various phases were calculated and used to attempt to match the reported event times and locations. The best matches were obtained from solutions in which most first-arriving phases are itd or isd. These phases represent energy conducted through the atmosphere in elevated waveguides, never reaching the ground. These waveguides allow the energy to travel at high speeds with little attenuation; one must, however, invoke scattering or diffraction to explain the escape of the energy from the waveguide.

Tables 7-11 shows the infrasonic observations and analysis for the Acapulco bolide. Figure 39 shows the station locations and backazimuths, again showing a poor azimuth fit of some of the stations to the actual source location. In general, it appears that the worst azimuth deviations occur in stations with extreme topography along the propagation path, specifically IS53 (Alaska) and IS08 (Bolivia). From the seed locations, azimuths from the stations to the source were estimated and the celerity computed at each station. Table 8 shows the maximum celerity for each phase. We computed locations for various permutations of phase ID's for the first and second arrival times. An attempt was also made to separate the detections into two events, one recorded by the US stations and another by the South American stations. However, two-station locations are inherently unstable, and even the solution using the three US stations was unstable because of the near parallel alignment of the DLIAR and IS53 propagation paths from the source. Three solutions are shown in Table 9. The first solution, LA_DL1, assumes all first arrivals are isd phases, and yields a large error on the origin time estimate as well as in the time differentials for some of the stations (Table 10). The second solution, LA_DL2, assumed a combination of it, itd and isd phases (Table 11) and yielded a good fit to the origin time. A source location west of the satellite location (LO1) is consistent with the DLIAR observations. Further work is needed to determine whether this event consists of a single bolide or more than one bolide arriving at different times, as suggested by the infrasound detections from IS25.

Table 6. Arrival identification nomenclature for long-range infrasonic propagation

Arrival ID	Description	Typical celerity of first arrival, m/s
iw	Guided wave propagating between the tropopause and the ground.	330-340
is	Guided wave propagating between the stratopause and the ground.	310-330
isd	Guided wave propagating in elevated waveguide between stratopause and the troposphere, and diffracted or scattered to the ground. May have higher frequency.	310-330
it	Guided wave propagating between the lower thermosphere and the ground.	280-300
itd	Guided wave propagating in elevated waveguide between the lower thermosphere and the troposphere, and diffracted or scattered to the ground.	280-300
It, Is, Iw	Direct arrival from the source to the receiver. May have high apparent phase velocity	N/A

Table 7. First arrival observations of August 25, 2000 bolide by infrasound stations.

Station	Lat (N)	Lon (E)	Speed (m/s)	Azimuth	ETA (epoch)
IS08	-16.3	-68.1	340	298	967184490
IS25	5.2	-52.7	344	283	967187730
IS53	64.87	-147.84	355	144	967187230
IS59	19.59	-155.9	346	88	967182900
DLIAR	35.87	-106.33	360	180	967173900

Table 8. Predicted first arrival celerity (km/s) for select phases: August 25, 2000

	it	itd	isd
IS08	0.289		0.298
IS25	0.263	0.285	0.29
IS53	0.292	0.303	0.31
IS59	0.281	0.297	0.308
DLIAR	0.278		0.309

Table 9. Source location and errors relative to satellite location (LO1): August 25, 2000

Source	Lat (N)	Lon (E)	Origin Time (Epoch)	Lat error (deg)	Lon error (deg)	Time error (s)
LO1	14.45	-106.13	967165945	0	0	0
LA_DL1	13.68	-108.21	967166247	-0.77	-2.08	302
LA_DL2	13.37	-107.74	967165950	-1.08	-1.61	5

Table 10. First arrival phase selection and time error for LA_DL1 solution: August 25, 2000

Station	Selected Phase	Range to LA_DL1	X/T (km/s)	Predicted Arrival	Time Error / Travel Time	PA-ETA	PA-OT	Ratio (%)
IS08	isd	5513	0.298	967184747	1.63%	257	18500	1.39
IS25	isd	6149	0.290	967187450	1.39%	-280	21203	-1.32
IS53	isd	6432	0.310	967186995	1.42%	-235	20748	-1.13
IS59	isd	5110	0.308	967182838	1.78%	-62	16591	-0.37
DLIAR	isd	2464	0.309	967174221	3.80%	321	7974	4.03

Table 11. First arrival phase selection and time error for LA_DL2 solution: August 25, 2000

| Station	Selected Phase	Range to LA_DL2	X/T (km/s)	Predicted Arrival (PA)	Time error / Travel time	PA-ETA	PA-OT	Ratio (%)
IS08	it	5452	0.289	967184815	0.03%	325	18865	1.72
IS25	itd	6096	0.285	967187339	0.02%	-391	21389	-1.83
IS53	itd	6481	0.303	967187339	0.02%	109	21389	0.51
IS59	isd	5168	0.308	967182729	0.03%	-171	16779	-1.02
DLIAR	isd	2495	0.309	967174024	0.06%	124	8074	1.54
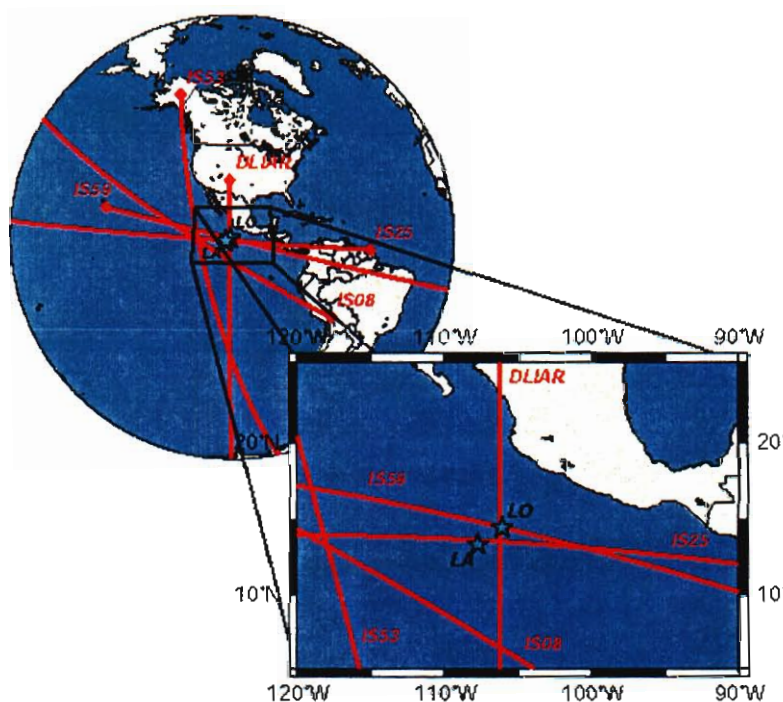
Figure 39. Map showing the locations of sensors that detected the Acapulco bolide, recorded backazimuths, and source locations provided by satellite records (LO) and inversion of the infrasound data (LA).

Another large bolide was recorded in Hawaii on April 23, 2001 (Figure 40, Garces et al, 2001, 2002)). The *North Pacific* event had an estimated energy release of 4.6 x 10^12 Joules and was located at 27.90° N, 133.89° W. This bolide was detected on current IMS infrasound stations in Hawaii, California, Alaska, Canada, and Germany, as well as DOE sensors in Nevada and New Mexico (Table 12). The size of this bolide, together with the large number of stations on which it was observed, make it one of the most spectacular events ever recorded by the IMS infrasound network.

It was observed that the high-frequency signal onset time at I59US, as measured by PMCC was as much as 4 minutes earlier

than as measured by InfraTool. This is an important result, as the first arrival time and the phase identification of that first arrival are essential to the location of infrasonic sources. As with the Acapulco bolide, the estimated times of arrival of the first or second arrival at the station were used to compute the residuals from a grid search around the seed source location and origin time, based on celerities calculated for each phase (Figure 41, Table 13). Various locations were made assuming different phase identifications for both first and second arrivals (when present), but only two solutions (with the minimal residuals) are shown in Table 14. The first solution, LA_S1, assumes all first arrivals correspond to isd phases, and produced a very good match to the origin time provided by the satellite observation (LO1). Although in seismic location an 8 s time differential is unacceptable, when scaled to the total travel time of the signal, the percent error is small and comparable to the best seismic location accuracies (Table 15). The difference in the source location between LO1 and LA_S1 (Figure 42) may be attributed to the high speed of the bolide and could correspond to a difference in where the peak sound and infrared energy are radiated. This result suggests that isd phases can be used to explain the arrival of signals in the upstream stratospheric direction, and the relatively higher frequency of the first arrivals suggest that scattering is an important factor. A second solution, LA_S2, assumed that the first arrival at IS53 was an isd phase, the second arrival at IS57 was an itd phase, and the second arrival at IS59 was an isd phase. These phases were selected in an attempt to match the source location at the expense of the origin time. However, we favor the first solution because of we believe the uncertainty in time (~10 s) may be less than the uncertainty in position for the satellite location LO1.
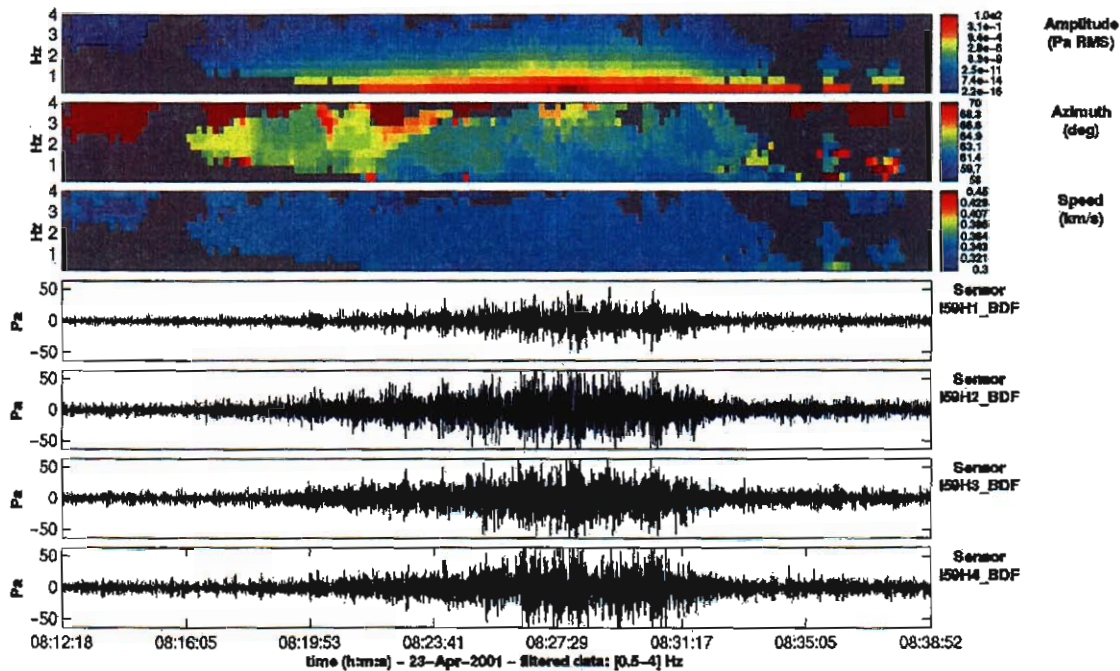
Figure 40. PMCC results showing the detection of the April 23, 2001 bolide at I59US. Note that coherent energy is detected by PMCC minutes before the signal is visible on the filtered traces.
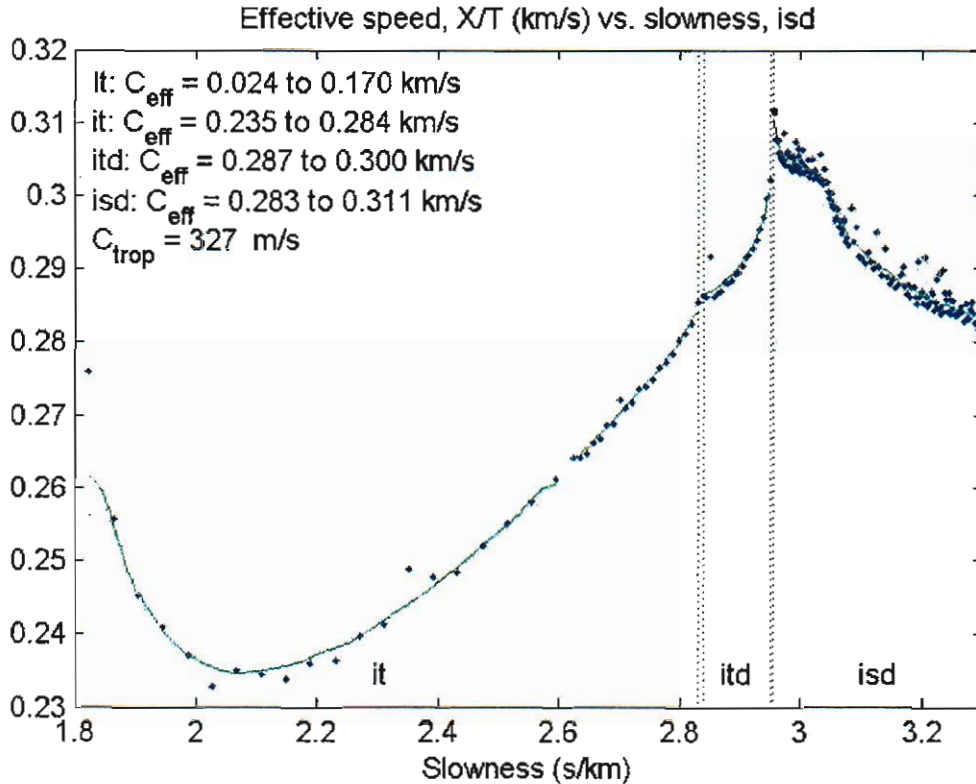
Figure 41. Graph of celerity (effective speed) as a function of slowness for the April 23 bolide as recorded at I59US. This graph shows that the highest effective speeds are for the isd, or diffracted stratospheric, and itd, or diffracted thermospheric, phases.

Table 12. First arrival observations of April 23, 2001 bolide by three nearest IMS infrasound stations

Station	Lat (N)	Lon (E)	Speed (m/s)	Azimuth	ETA (epoch)
IS53	64.87	-147.84	322	150.6	988020690
IS57	33.6	-116.5	349	256.1	988012060
IS59	19.59	-155.9	348	63.6	988013790

Table 13. Predicted first arrival celerity (km/s) for select phases: April 23, 2001

	it	itd	isd
IS53	0.268	0.284	0.292
IS57	0.278	0.292	0.328
IS59	0.284	0.3	0.311

Table 14. Source location and errors relative to satellite location (LO1): April 23, 2001

Source	Lat (N)	Lon (E)	Origin Time (Epoch)	Lat error (deg)	Lon error (deg)	Time error (s)
LO1	27.9	-133.89	988006355	0	0	0
LA_S1	28.07	-135.09	988006347	0.17	-1.2	-8
LA_S2	27.79	-133.42	988006145	-0.11	0.47	-210

Station	Selected Phase	Range to LA_S1	X/T (km/s)	Predicted arrival	Time Error /Travel Time	PA-ETA	PA-OT	Ratio (%)
IS53	isd	4191	0.292	988020700	-0.06%	10	14353	0.07
IS57	isd	1877	0.328	988012070	-0.14%	10	5723	0.17
IS59	isd	2313	0.311	988013784	-0.11%	-6	7437	0.08
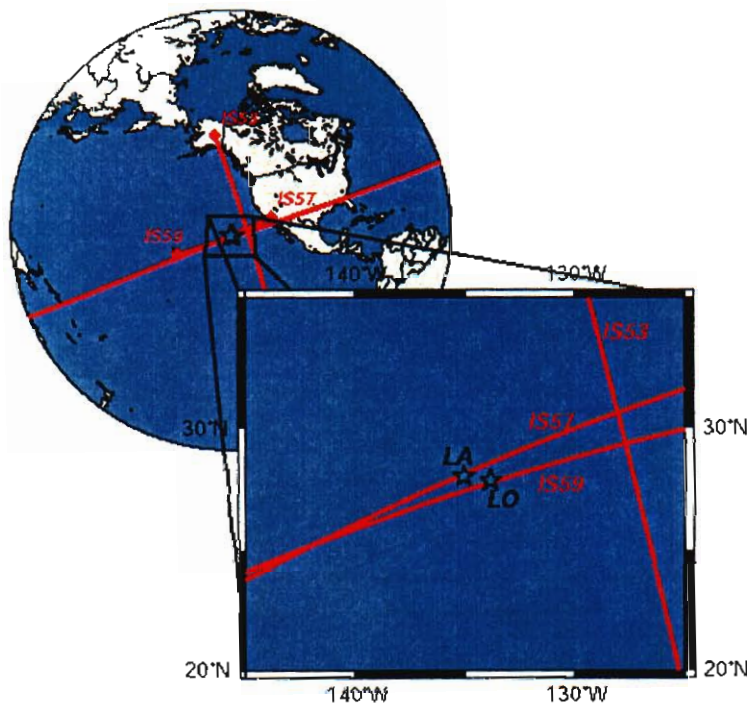
Figure 42. Map showing the locations of sensors that detected the April 23, 2001 bolide, recorded backazimuths, and source locations provided by satellite records (LO) and inversion of the infrasound data (LA).

Several smaller bolides were recorded in Hawaii, with independent confirmation from other sources. Following eyewitness accounts of a spectacularly bright fireball during the annual Leonid meteor shower, a short, impulsive signal was found recorded at I59US on November 18, 2001 at around 10:18:09 UT (Figure 43). The pulse had a peak amplitude of ~40 mPa, an apparent horizontal phase velocity of 455 m/s, and an arrival azimuth of 151.8 degrees from North. The eyewitness accounts were corroborated by a photographic observation made by the Mauna Kea CONCAM (Figure 44), which allowed the event time to be constrained to 10:14:00 ± 60 s (P. Jenniskens, personal communication), yielding a travel time of ~250 ± 60 s from the midpoint. The arrival backazimuth is nearly perpendicular to the meteor path, as would be expected for radiation from a cylindrical Mach surface associated with hypersonic sources. The observed low slowness suggests a steep angle of incidence and a direct sound path. Using atmospheric profiles for Hawaii at 12 GMT of November 18, 2001 and a corrected slowness of 2.1 s/km, a travel time of 250 ± 60 s corresponds to a source height of 60 ± 10 km. The mean angle subtended along the plane of incidence (measured from the vertical axis) would be ~40 degrees (corresponding to a range of ~45 km), which is consistent with the angular distance observed in the CONCAM photograph. Using a relationship given in Le Pichon et al. (2002), the diameter of the bolide was estimated to be about 10 cm, with a maximum yield equivalent of 0.24 tons of TNT.

Figure 43. The arrival believed to be generated by the Leonid bolide of November 18, 2001. The bright green line is the beam created by the other four dimmer lines.
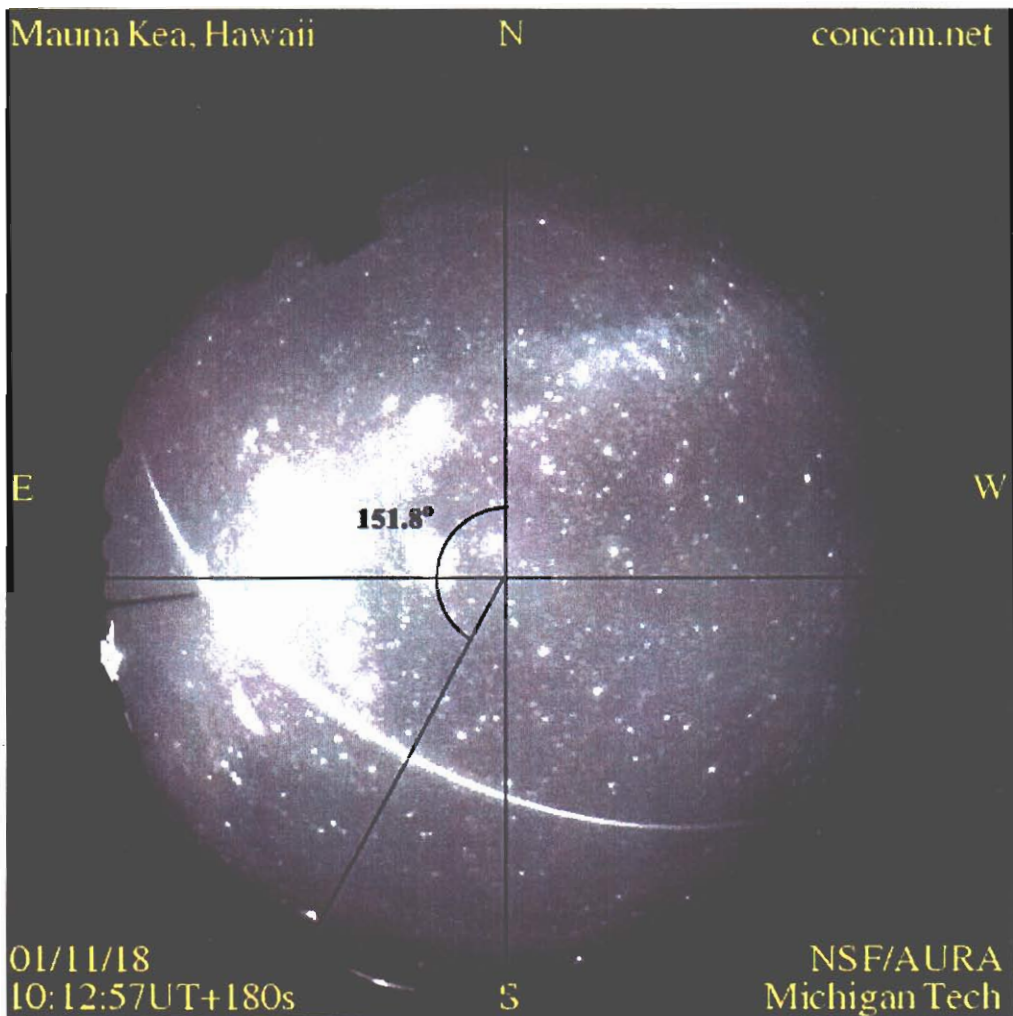
Figure 44. Mauna Kea CONCAM image showing the bright fireball believed to be the source for an infrasonic signal. The black line marks the approximate position of the bolide when it radiated the sound pulse.

Several other possible bolides have been recorded at I59US (Table 16; Figure 45). Most of these were identified using confirmation from satellite or other stations, but two remain unconfirmed. The March 9, 2002 bolide was initially missed by the analyst, illustrating the need for effective automatic detection routines that can notify an analyst of interesting arrivals.

Table 16. Confirmed and suspected bolide arrivals at station I59US

Date	Confirmation
2000-Aug-25	I53US, DLIAR, satellite
2001-Apr-23	I57US, I53US, SGAR, DLIAR, I10CA, I26DE, satellite
2001-Jul-26	None
2001-Nov-18	CONCAM
2002-Mar-09	I57US, I10CA
2003-Jun-21	Visual, satellite
2003-Jun-30	None

Rockets

On March 16 2002 at 02:11 GMT a modified Minuteman ICBM was launched from Vandenberg AFB in California. At 02:32 GMT a prototype interceptor was launched from Kwajalein Atoll in the Marshall Islands. Neither of these events was observed in Hawaii. The two missiles collided at about 02:42, but as the collision took place at an altitude of about 225 kilometers, no infrasonic signals were expected to propagate to the ground. However, an event with family starting time of 03:41:28 was detected that may be related to the reentry of part of the target or the interceptor into the atmosphere (Figure 46).

The signal is broadband, containing energy up to about 6 Hz, impulsive with no prelude or coda visible above noise, and the total family duration is 30 seconds, suggesting both a short source duration and a short propagation path. As the interception is believed to have taken place almost directly above Hawaii, these characteristics are consistent with possible debris reentry and burnup. Arrival backazimuth and trace velocity were estimated to be 301.2 degrees and 346 m/s. Conventional FK analysis from 2-5 Hz results in an azimuth of 302.83 degrees with a trace slowness of 295.13 s/deg (~370 m/s), the inaccuracy of which is most likely due to the spatial aliasing common at such high frequencies; when the frequency range of the FK analysis is extended down to 0.5 Hz, the results of azimuth 300.96, slowness 326.53 (~340 m/s) are much closer to the PMCC results.

Another pair of events was observed before the announced times of the launches, arriving at about 01:37 and 01:40 (Figure 47). The observed signals resemble other signals typically associated with aircraft.
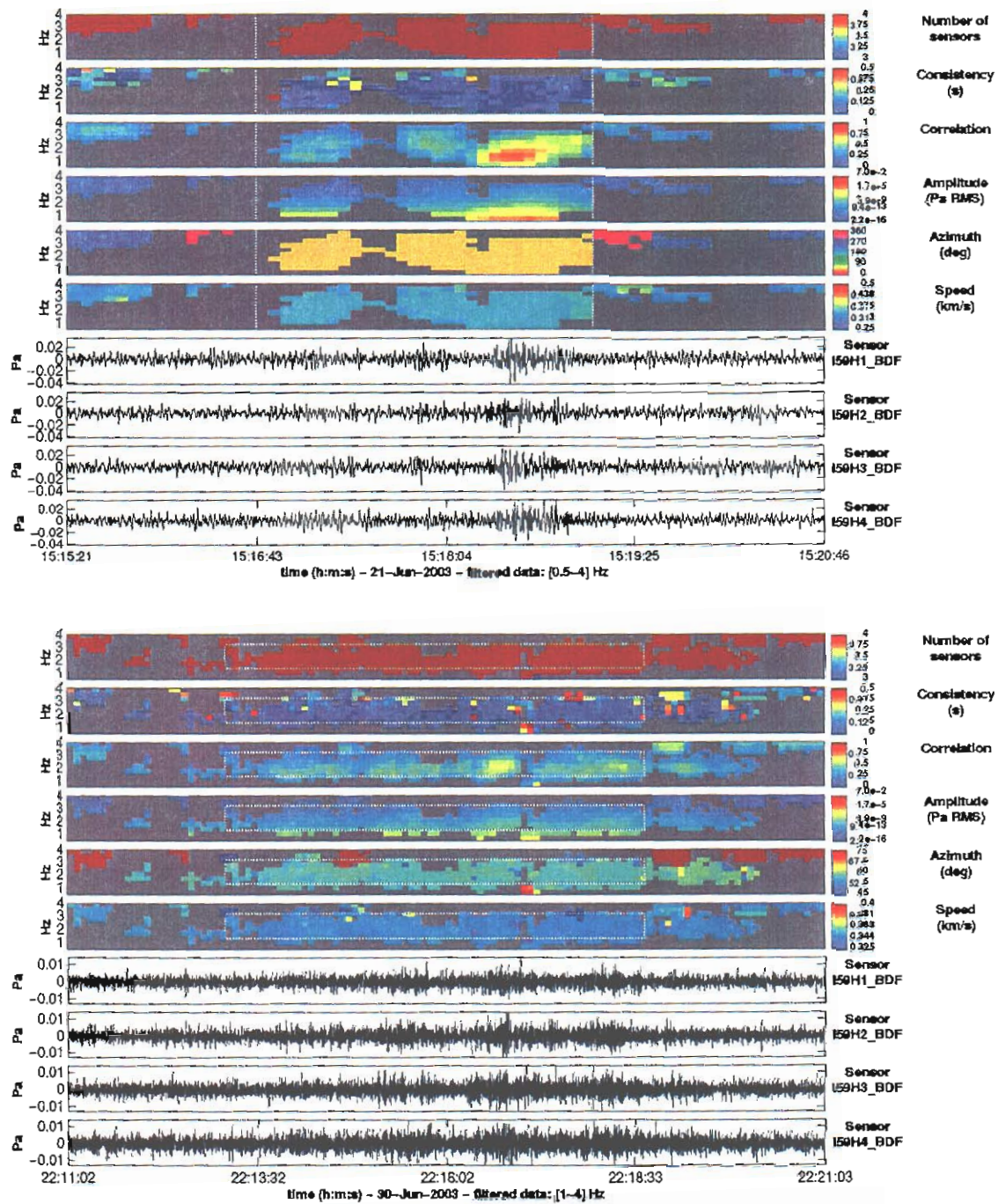
Figure 45. Possible bolides observed at I59US but outside the detection range of other IMS stations. The June 21 bolide was observed visually and by the DOD/DOE satellite monitoring system.
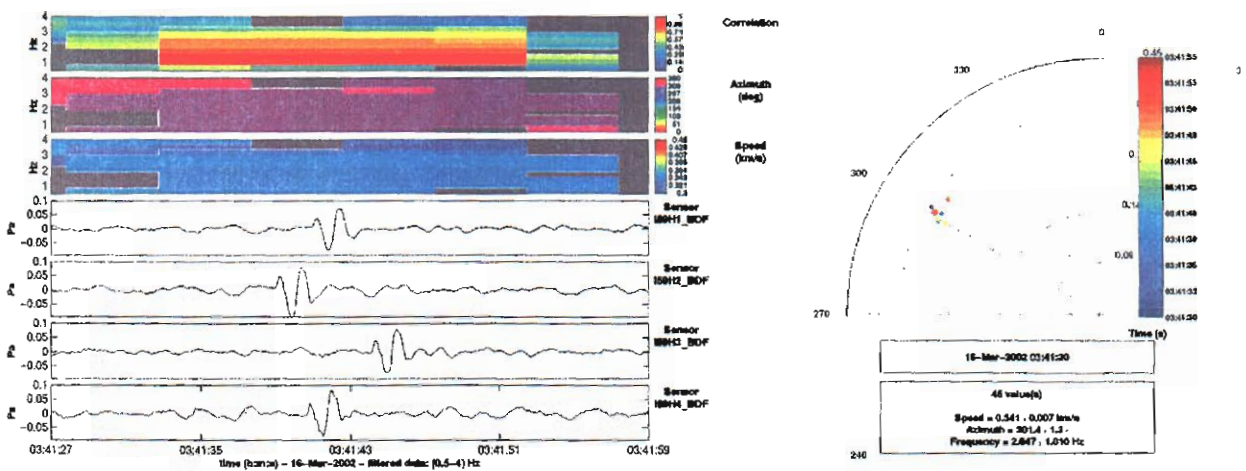
Figure 46. PMCC results (left) and polar diagram (right) showing signal that may be related to the reentry of debris from a missile collision test over Hawaii.
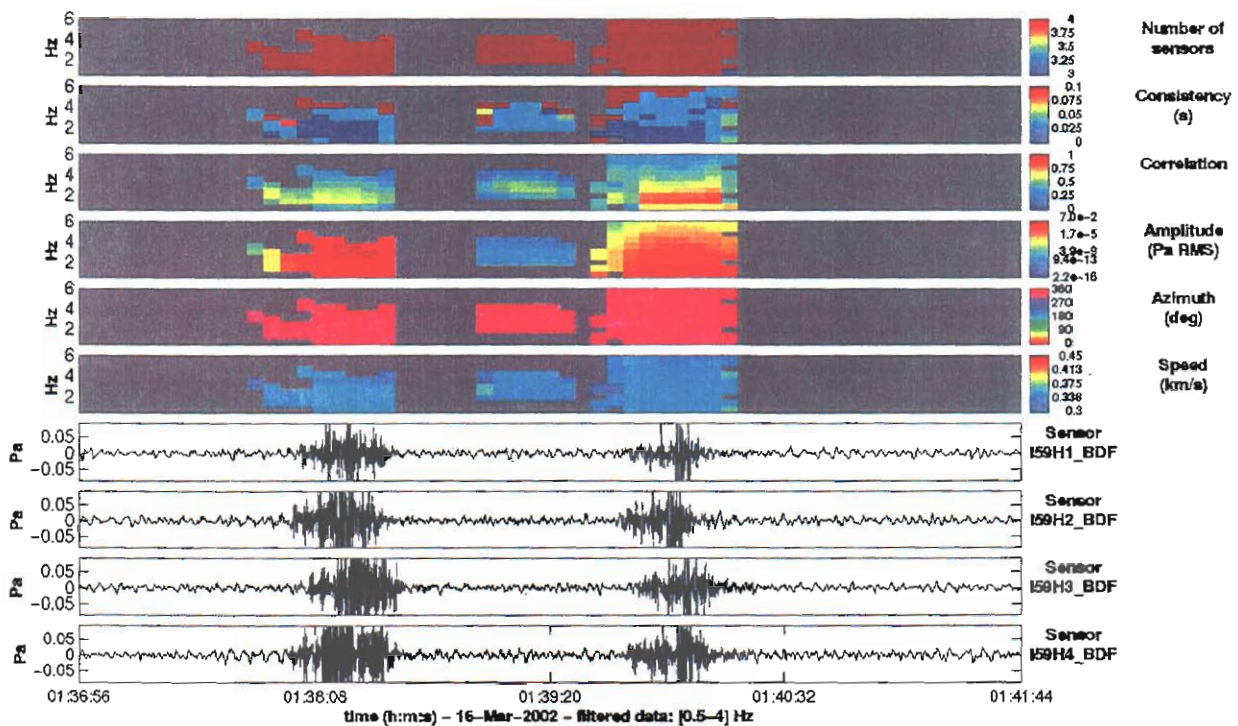
Figure 47. PMCC results showing events possibly related to aircraft. These events cannot be directly related to the rocket launches as they occur too early.

The signals arrive from an azimuth of 321.2±1.5 degrees with a trace velocity of 348±7 m/s. A signal with this azimuth could originate from a northbound takeoff trajectory from Kona International Airport (azimuth from airport to station is ~305 degrees) or from an airport on a neighbor island. The high signal-to-noise ratio of the signal suggests the former. The signals are roughly spindle-shaped and broadband; the strong high-frequency signal content also suggests a local (i.e. on-island) source.

On June 10, 2003, Sea Launch successfully launched the Thuraya-2 satellite, one of the heaviest commercial satellites ever launched, into orbit from its equatorial floating launch platform at 154° west longitude. The Sea Launch Zenit-3SL rocket lifted off from the Odyssey Launch Platform at 06:55:59 am PDT (13:55:59 GMT) at the opening of the launch window. Signals from this launch were observed at I59US (Figures 48 & 49) as well as at the French IMS station I24FR in Tahiti. Other launches from this location have not been observed at I59US, but this may be related either to differences in launch trajectories (not available for most launches) or seasonal wind patterns.
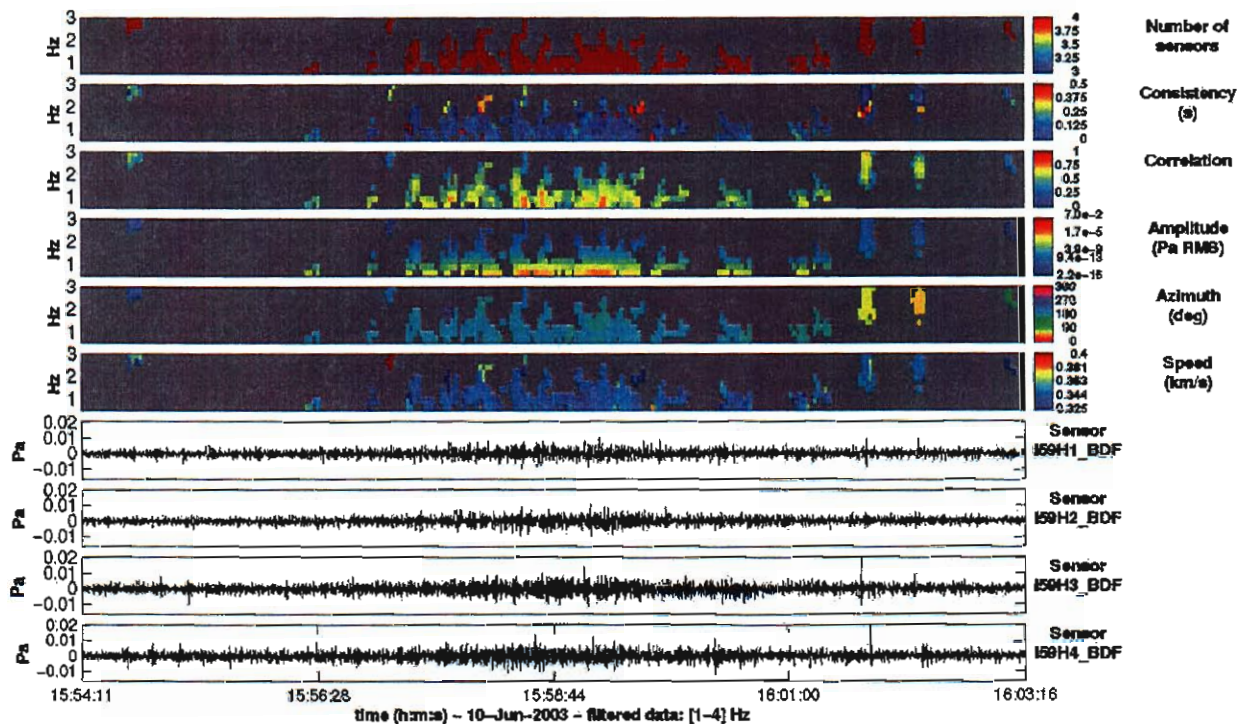
Figure 48. PMCC results showing signal from the Sea Launch rocket of June 10, 2003.
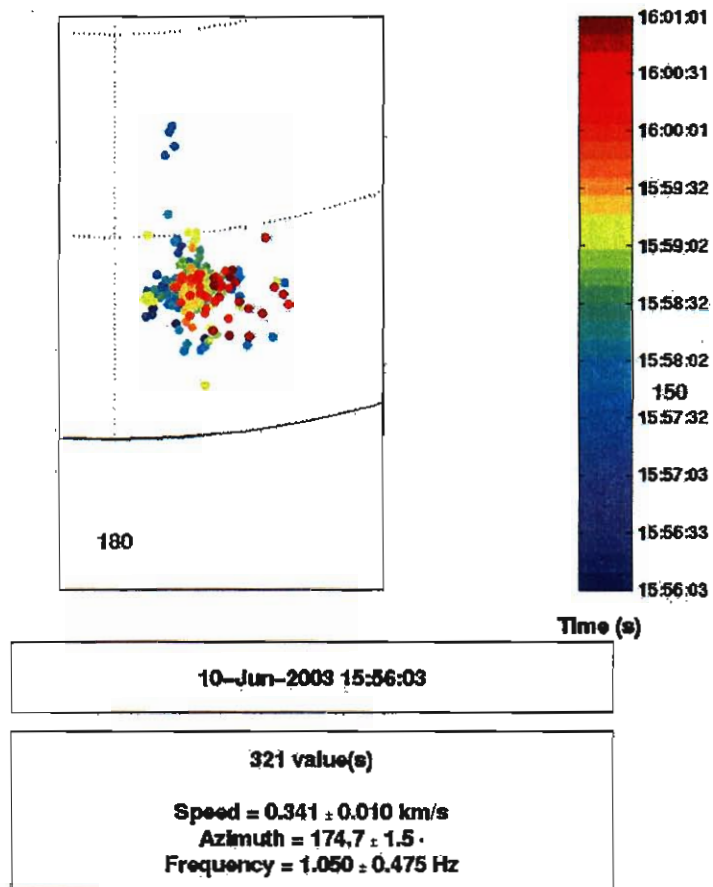
Figure 49. Polar diagram showing arrival azimuth and trace velocity of signals from the Sea Launch rocket.

Notable Non-Detections

Although it was recorded at a number of continental U.S. infrasound stations, the tragic re-entry of space shuttle mission STS-107, Columbia, was not recorded in Hawaii (Figure 50). Numerous sets of detection parameters were used to analyze the data and try to extract some coherent signal, to no avail. We speculate that a combination of the range and the altitude of the shuttle at the point of closest approach were both too great for infrasonic signal to propagate to the I59US array. Nonetheless, much of the forensic infrasound analysis carried out for the investigation of the disaster was performed by ISLA, and provided much valuable information. It was demonstrated that the shuttle was observed almost continuously from the time that it crossed the California coast to the point of its disassembly over Texas. It was also shown that tuning of the PMCC detection parameters was necessary for obtaining as much useful data as possible. Details of the analyses can be found in the official reports written by ISLA and attached as Appendices B through F. There reports used the expertise in signal processing and detector tuning developed at I59US to optimize the PMCC algorithm for all the arrays in the North American infrasound network. Characterization of the prominent features observed at all other arrays allowed us to return to the I59US and I53US (Alaska) arrays and confirm that indeed no detections were associated with the Columbia at these stations.
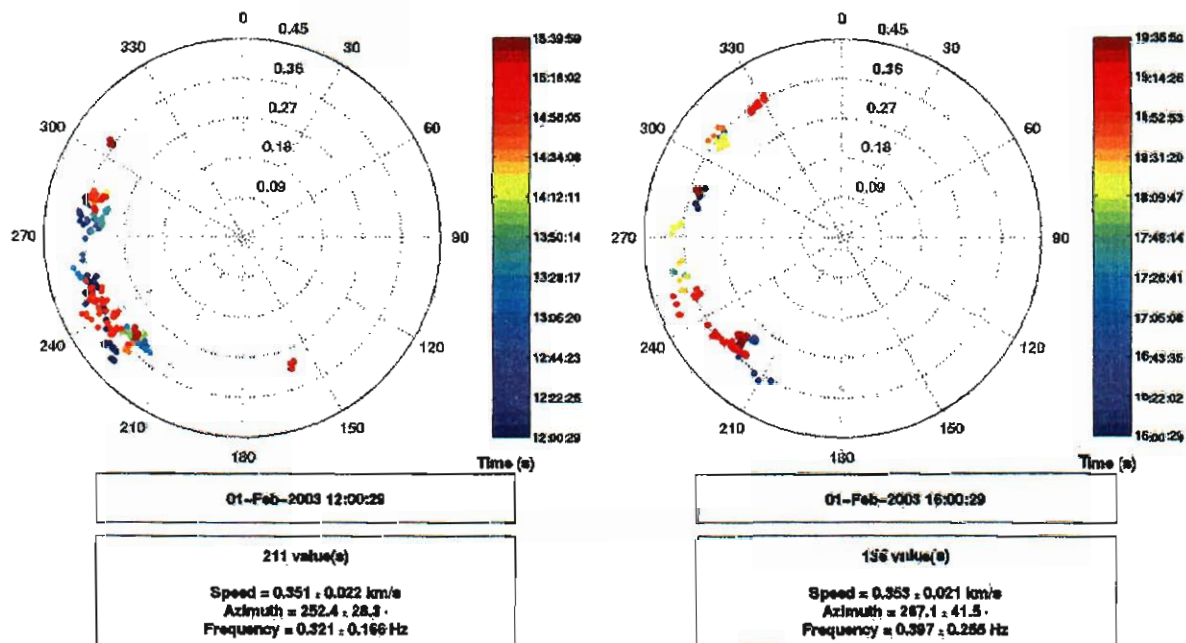
Figure 50: Polar diagrams showing arrivals for 8 hours bracketing the expected arrival time for signals from the space shuttle Columbia re-entry. No arrivals from the expected arrival direction (north) can be seen.

6. Arrivals from Local Events

This chapter will discuss local (i.e. on-island source) arrivals detected in Hawaii, both transient and ongoing. While not necessarily a significant part of the overall ambient infrasonic field, they are of interest because similar events can be expected to be found at other stations; if similar arrival features are observed at a new station, then a similar source mechanism can be inferred.

Chemical Explosions

A number of chemical explosions have been detected on the I59US array. Since they all (presumably) originate on Hawaii Island, they share similar characteristics: impulsive character, short duration, and relatively high frequency content. Unlike surf events, which also have similar characteristics, they either occur only once, or they may repeat but appear irregularly spaced in time. The following sources are believed to have been observed in Hawaii.

- Construction Blasting
- Munitions
- Fireworks

A well defined source of construction blasting was the preparation of the site for a new Lowe's Home Improvement Warehouse. Over the course of about 1½ months in early 2002, 14 separate chemical explosions were detected by the I59US array, all from the same backazimuth and similar in appearance to the waveform shown in Figure 51. On April 13, 2002, a rock from the blasting fell through the roof of a nearby house (Marshall, 2002), apparently bringing the major blasting to an end; no similar events were recorded after this date.
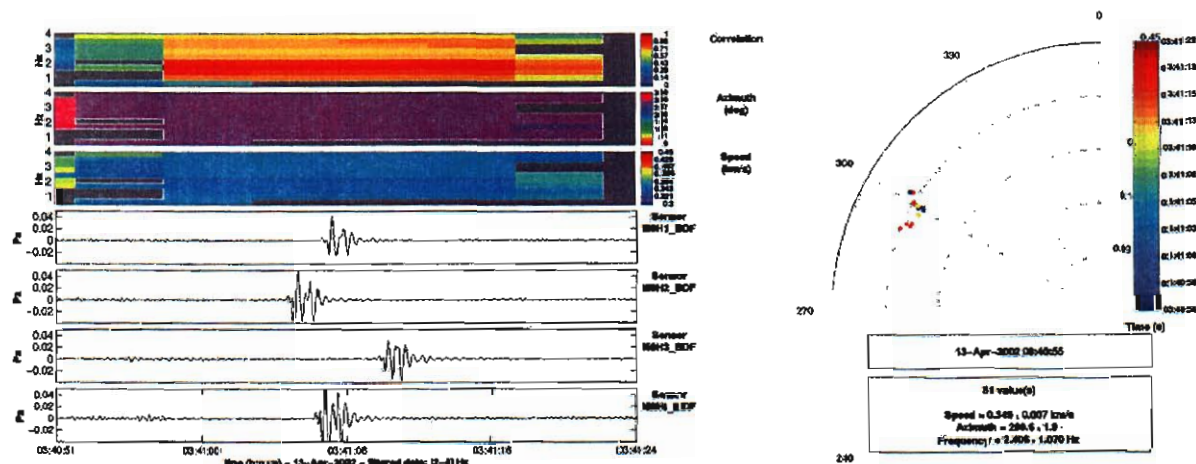
Figure 51. PMCC results (left) showing the signal from the construction explosion that cast a rock through the roof of a nearby house. The azimuth of the signal (right) points directly toward downtown Kailua-Kona, where the blasting was taking place.

Another source of chemical explosion signals is the Pohakuloa Training Area in the center of Hawaii Island. These arrivals tend to be short and impulsive, with high signal-to-noise, and they tend to arrive in short-duration groups of sharp, irregularly-spaced arrivals (Figure 52), although some arrivals from that azimuth range are emergent. Pohakuloa arrivals are not detected constantly, suggesting that the source from which they are generated is not active at a constant year-round rate.
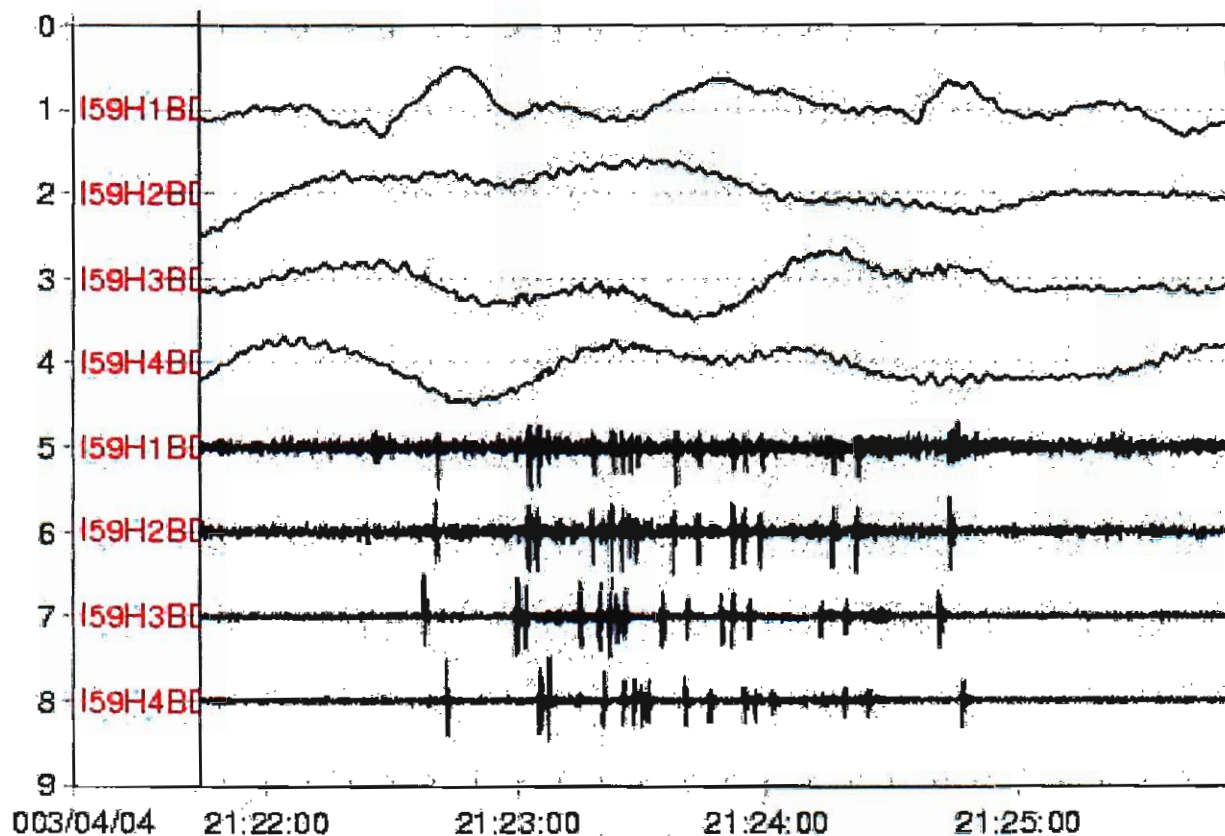
Figure 52. Filtered waveforms showing typical signals from the Pohakuloa Training Area.

On August 19, 2002 at 05:57 GMT, a series of irregularly-spaced impulsive arrivals were observed over the course of about 11 minutes (Figure 53). These arrivals coincided with a private party that had been held west of the array and included a large fireworks display. A grand finale can be observed (Figure 54).
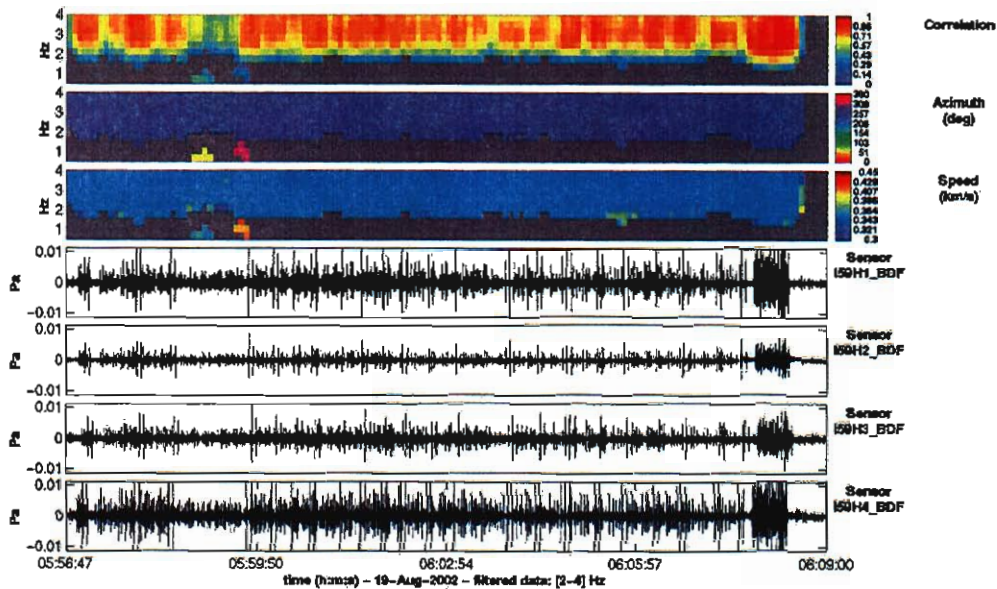
Figure 53. PMCC results showing signals from a nearby fireworks display. This is also an excellent illustration of PMCC's tendency to concatenate families associated with adjacent events into large, multi-arrival families.
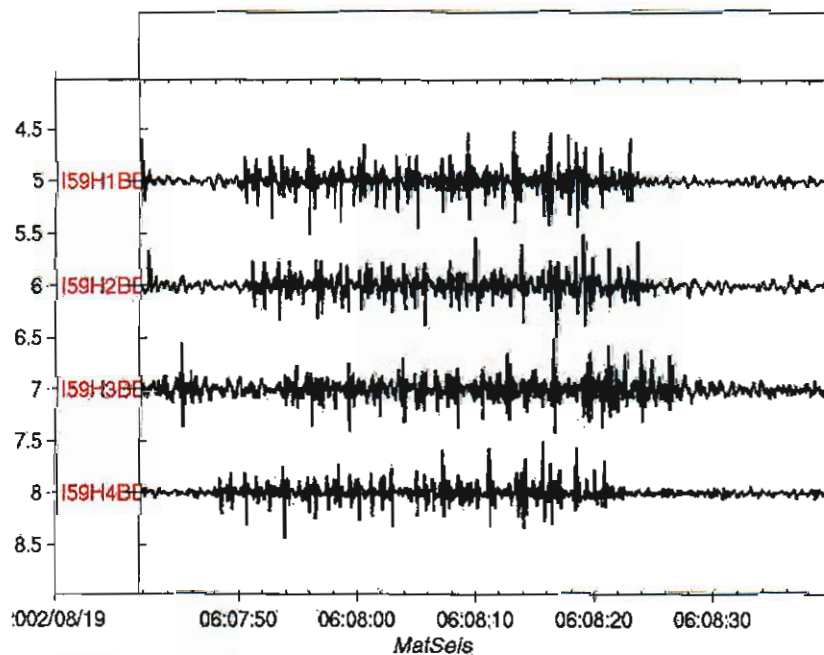
Figure 54. Filtered waveforms showing the grand finale from the firework signals shown in Figure 53.

Thunder

Although thunderstorms are rare on Hawaii Island, on occasions where they have occurred a series of sharp, irregularly-spaced arrivals have been observed (Figures 55 & 56). This irregular spacing, combined with arrival azimuths that indicate inland sources, serve to distinguish them from surf, as does the tendency for pulse amplitudes to remain high and relatively constant over long periods of time, whereas surf amplitudes tend to be cyclical on a scale of minutes. The time between successive pulses is also longer for lightning than for surf. They can also be distinguished from Pohakuloa signals by a different arrival azimuth and a tendency to last for longer periods at a time. They generally arrive from the east, which is uphill from the array, because the local thunderstorms tend to occur at higher altitudes. During periods of thunderstorm activity on the windward (eastern) side of the island, similar arrivals are occasionally seen from the southeast, in the direction of Mauna Loa summit, and migrating towards Hilo, on the northeastern side of the island. It is also possible some detections off the western coast may be caused by lightning storms offshore or over Maui.
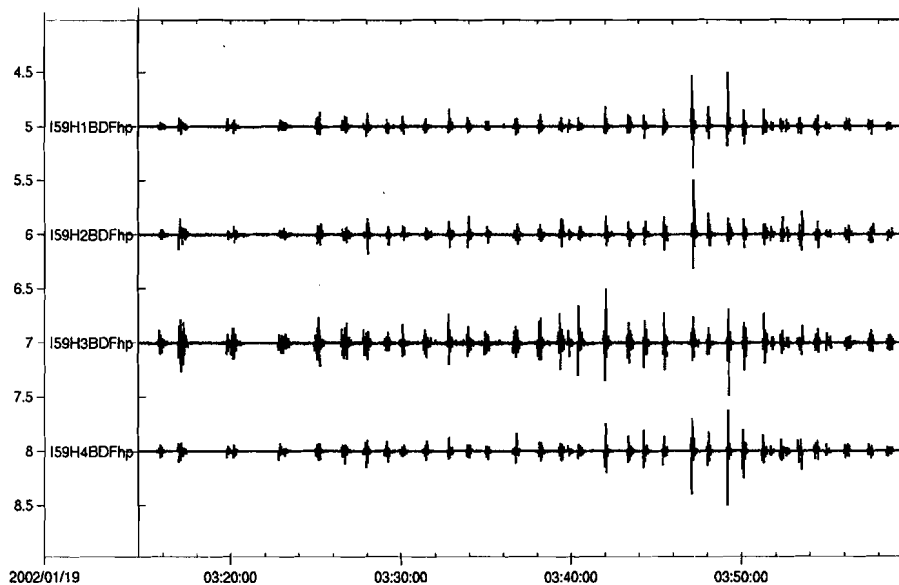
Figure 55. Filtered waveforms showing irregularly-spaced arrivals interpreted to be related to thunder.
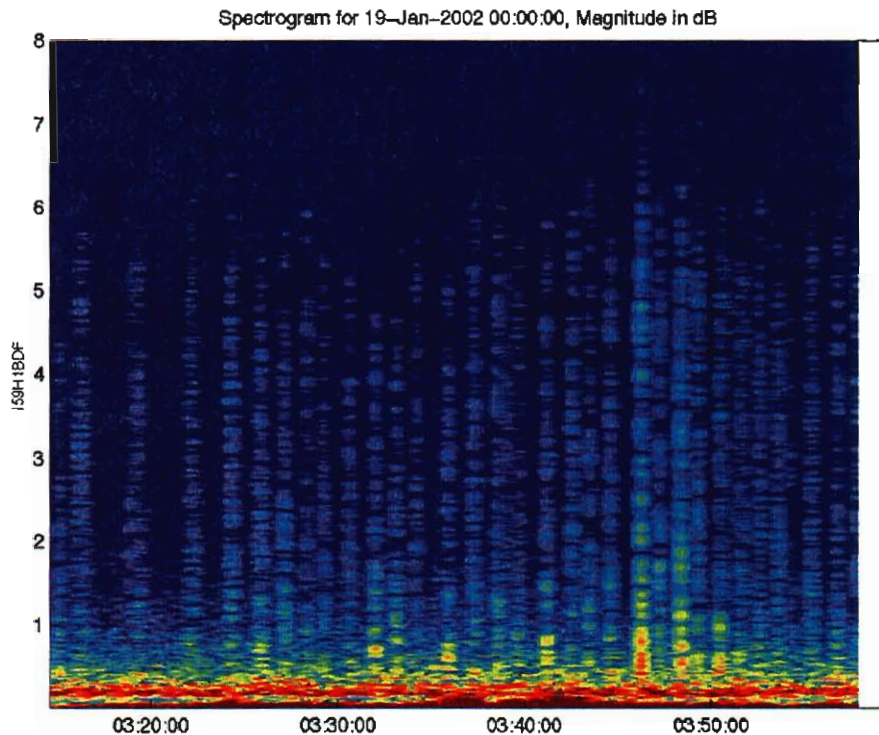
Figure 56. Spectrogram showing frequency content of signals interpreted to be from thunder.

Aircraft

Signals arriving from the direction of Keahole International Airport have been observed on I59US since its installation. Aircraft signals are generally extended, emergent events with durations between 30 and 120 seconds, and can have bursts of increased pressure within the overall tapered shape. They are identified based on these waveform characteristics and a backazimuth corresponding to Keahole Airport. However, observations have not been constant and consistent as would be expected from a busy airport with dozens of takeoffs and landings per day. Currently we speculate that a specific kind of aircraft or unusual approach or departure trajectory may be responsible for the observed signals. Installation of a sensor array close to the airport would provide much more consistent aircraft recordings (see Chapter 7).
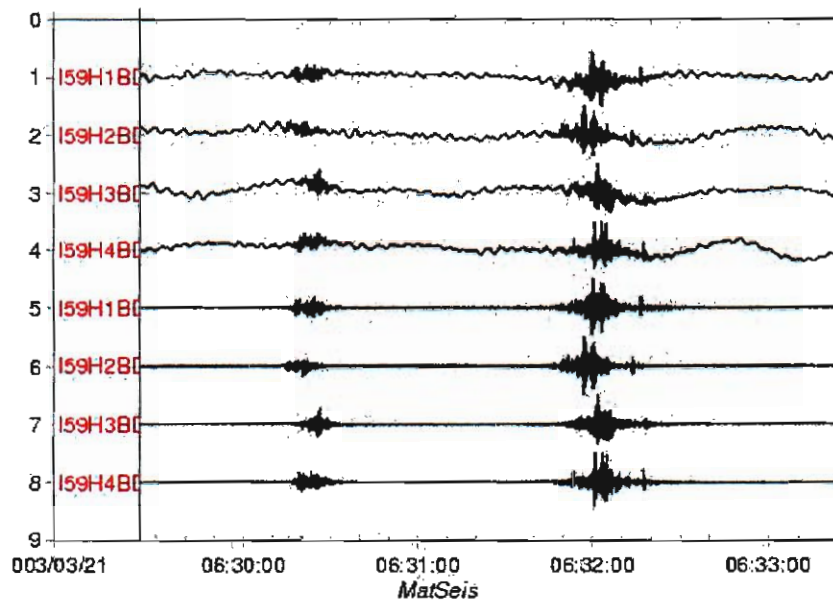
Figure 57. Raw (top) and filtered (bottom) waveforms for signals interpreted to be related to aircraft.

Earthquakes

Although Hawaiian earthquakes are not infrasonic sources per se, in that the ground displacements associated with seismic arrivals do not appear to couple significant energy into acoustic waves, they are recorded by the sensors due to the physical movement of the ground (Figure 58; De Bremaecker, 2003). They can be easily distinguished from infrasonic arrivals by the extremely high trace velocity, appearing to arrive almost simultaneously across the array. I59US has recorded earthquakes with magnitudes as low as $M_L = 2.6$ and as high as $M_L = 5.0$. Deep (>20-30 km) earthquakes may be preferentially recorded, probably because P-waves from these earthquakes tend to displace the sensor vertically.
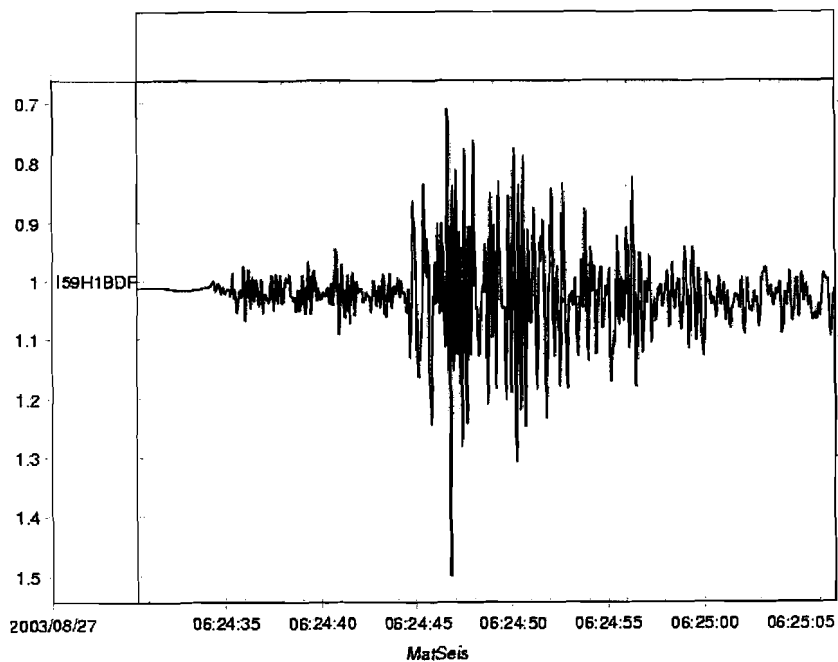
Figure 58. Waveform of local earthquake recorded at I59US. The quake was of magnitude $M_L = 5.0$ and was centered about 75 km from the array.

7. Portable Array Deployments and Results

To facilitate recording and analysis of low-magnitude local signals and to aid in source location, a portable infrasound data acquisition system has been designed. The specifics of the system are described by Garcés et al. (2003a). Two field deployments are described in this document.

Kilauea Deployment

The first major test of the portable system was at Kilauea Volcano. Both systems were deployed near the volcano, with one system set up as a 4-element array in a small grove of trees ~2 km from the active vents and the other system set up with two sensors on the crater rim about 100 m from the vents. Although some low-intensity sound from the lava tube system was audible to the human ear, the volcano appeared to be fairly quiet. It was discovered upon analysis of the data that there is significant infrasonic tremor in the 1-10 Hz band, distributed in space and apparently originating from a shallow source near the active crater complex and extending into the lava tube system. The deployment also demonstrated that at times of high wind the distal, sheltered source recorded the signals much more reliably than the proximal, exposed source (Figure 59). This demonstrates that site selection and minimization of wind exposure is a crucial step in the deployment process for infrasonic arrays.
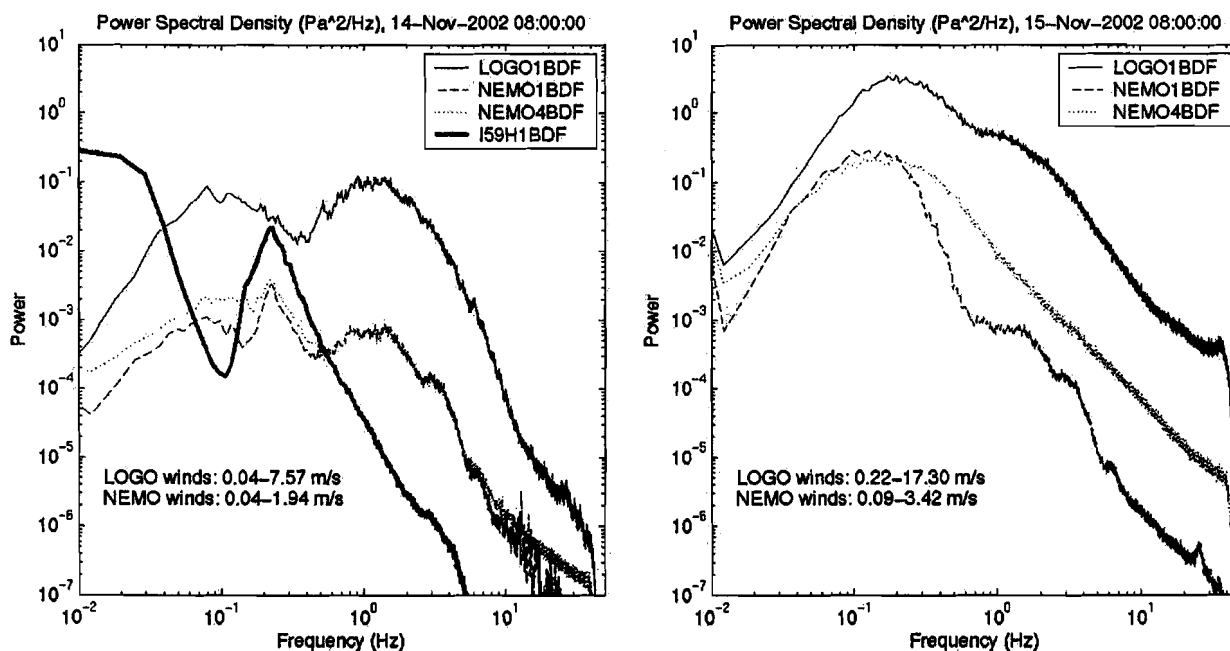
Figure 59. Power Spectral Density of infrasonic pressure for three microphones deployed temporarily near the Pu'u 'O'o crater under relatively low (left) and high (right) wind conditions. The minimum and maximum winds are shown in the figure. The closest sensor was LOGO1 located at the exposed crater rim and ~0.1 km from the active vents. NEMO1 was located ~2km from the vent within a forested section. NEMO4 was on the outskirts of the forested patch and more vulnerable to wind. The tremor signal coexists with wind noise as a broad peak with maximum between 1 and 2 Hz. For reference, the background noise levels observed at I59US (range of ~80 km) are shown. Under high wind conditions (>10 m/s) at the crater, only NEMO1-3 could consistently observe the tremor peak.

Keahole Point Deployment

The portable array was subsequently deployed at Keahole Point, the westernmost point on Hawaii Island. The deployment coincided with an epic set of ocean swells that generated several episodes of high surf along the west coast of the island. A single breaking wave front may generate multiple pressure pulses as it collapses into multiple sections or interacts with different segments of the reef or adjacent cliffs. However, each of these pulses will have a different arrival direction, thus permitting the identification of specific regions of wave action. If the array is relatively far from the coast, as with I59US, then the observed infrasonic field provides a measure of the swell energy distribution along a large portion of the shoreline. However, if an array is close to the shore, it is possible to identify smaller, distinct regions of wave action (Figure 60). Infrasound arriving from an azimuth of 330 and 10 degrees appeared concentrated in a narrow beam, whereas arrivals from 260-300 degrees and 220-240 degrees appeared to have a broader spatial distribution. Further studies are needed to relate the sound directivity to swell direction, bathymetry, and wave breaking dynamics. However, a clear relationship between ocean wave height and infrasonic amplitude could be observed (Figure 61), where the rates of growth and decay observed in the infrasonic data roughly matches those of the ocean buoy observations (Figure 14). No relationship was seen between wave height and the number of arrivals recorded on the portable array, unlike on I59US where the number of surf arrivals has been correlated to incoming swells. This suggests that the sound is constantly being generated by the waves, and it is only the higher-amplitude signals generated by large swell events that can propagate all the way to I59US.

Figure 60. Azimuth plot showing the distribution of arrival angles for surf events during January 10-14 from the portable array deployment at Keahole Point. Distinct areas of wave action can be identified. The radial distance denotes apparent horizontal wave slowness in 100 s/degree intervals.

Since the Keahole Point deployment was close (<1 km) to Kona International Airport, several aircraft were also observed taking off and landing (Figure 62). Some of these signals were also detected at I59US (Figure 63).

Figure 61. Infrasonic amplitude (in millipascals) for the January 10-14 swell as calculated from the portable array deployment at Keahole Point. The rate of growth and decay observed in the acoustic amplitudes for this swell roughly match those observed in the wave buoy data. The gaps in the detections correspond to periods of high wind noise.
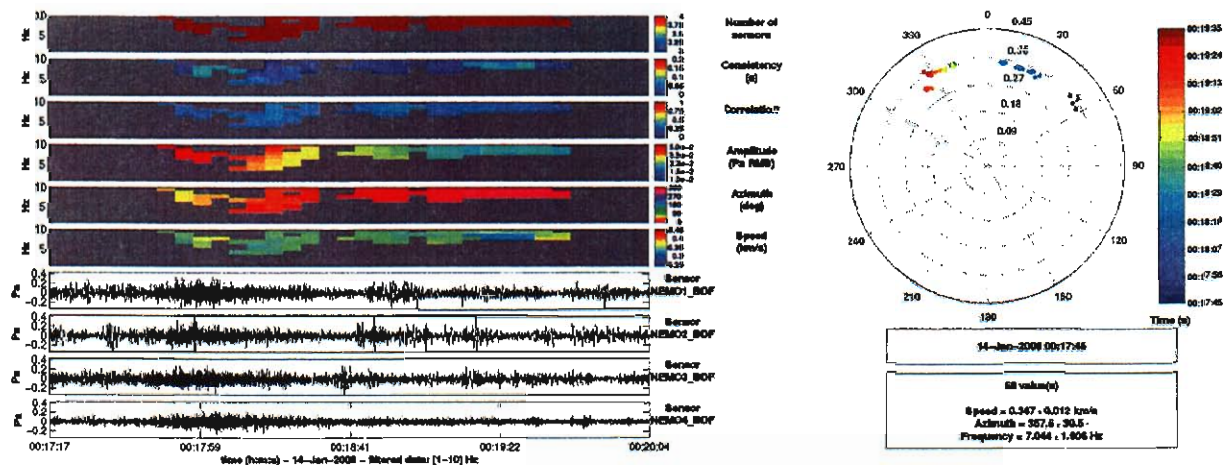
Figure 62. The right panel shows PMCC families for an aircraft recorded by the portable array at the Keahole Point deployment. The right panel shows a polar diagram showing azimuth and trace velocity as a function of time (blue=early).
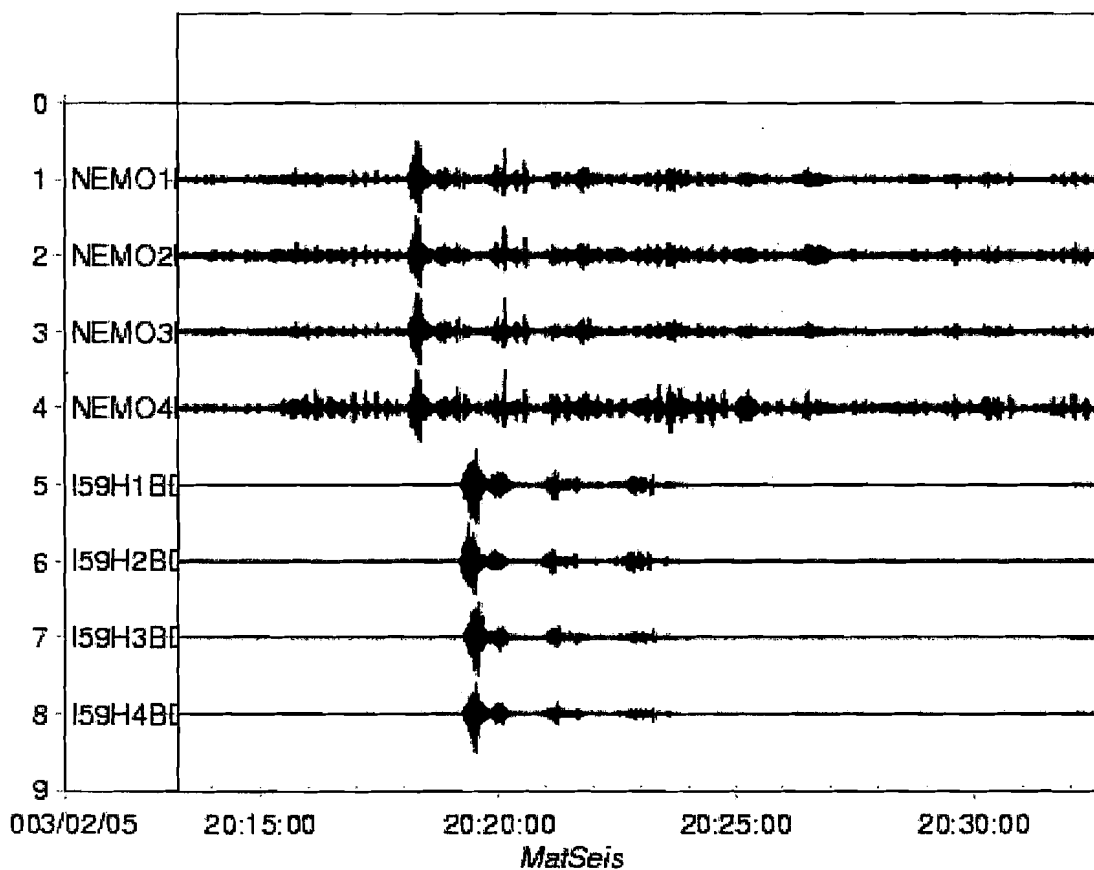
Figure 63. Waveform showing aircraft recorded at both the portable array (NEMO1-NEMO4) and I59US. The apparent increased signal-to-noise at I59US is probably due to attenuation of the surf signals seen on the portable array data as well as the more sheltered location of I59US. The small pulses observed in the portable arrays correspond to surf.

8. Conclusion

The infrasonic field of the central Pacific Ocean has been well characterized by three years of study. It has been determined that above 1 Hz the vast majority of coherent infrasonic signals are related to surf, either through sound generated directly by breaking waves, or through resonance set up by waves trapped in coastal bays. These sounds are present to some degree at all times, but incoming swells can boost amplitudes to the point where they propagate farther inland and can be recorded even by sensors that are not close to the shoreline. Further research will be conducted relating the characteristics of surf arrivals with swell direction, local bathymetry, and the dynamics of breaking waves. Integration of ocean buoy measurements with land-based infrasonic sensors may also be used to facilitate the testing and validation of global and near shore mesoscale ocean wave propagation models.

Microbarom arrivals also make up the dominant portion of the infrasonic field in the 0.1-0.7 Hz band. While signals appear to be present almost constantly, the array geometry and low number of elements appears to degrade coherence such that they are recorded in discrete bursts. Microbarom arrivals have been shown to be related to ocean storms on several occasions and can propagate thousands of kilometers while retaining sufficient coherence to be recorded even on 4-element IMS arrays. Future research will focus on using microbarom signals from multiple arrays to locate storm systems in near-real time.

A number of confirmed and suspected bolide events have been recorded in Hawaii. Apart from their natural scientific interest, they provide excellent surrogates for nuclear test explosions to evaluate the detection thresholds of IMS arrays. Analysis of the larger bolide signals has demonstrated the need for accurate atmospheric models in order to locate the source events. It is also apparent that, in order for the signals of interest to be quickly identified and separated from background clutter, a set of identification criteria needs to be developed that can be applied by an automatic system to eliminate the possibility of analyst oversight. As independent confirmation of the origins of these events is necessary for positive identification, it would be desirable to have an automatic system that would be queried when an signal of interest was detected, collect and associate the queries, and issue timely reports of apparent multi-station detections or coincident satellite detections.

Over the past three years several arrival detection methods have been developed and tested, including visual detection, STA/LTA, InfraTool, and PMCC. PMCC has emerged as the best performer of the group, and has recorded over 115,000 arrivals since January 2002. Its advantages include the ability to detect coherent energy even when signal-to-noise is close to unity. A number of persistent local sources of infrasound have been identified, most of which are related to surf. A strong relationship between ocean wave heights and surf infrasound has been found; future work will begin to relate signal features with characteristics of the nearshore wavefield and physical aspects of the shoreline and ocean bottom. Studies of microbaroms have confirmed their generation by interacting ocean waves and their association with oceanic storm systems; future work in this area will focus on predicting microbarom recordings from ocean wave models, and the verification and improvement of those models. Numerous confirmed and suspected bolides have been recorded in Hawaii, with several recorded by multiple stations. Rocket signals from a sea-based launch platform have also been recorded, as have many local

explosive and weather-related events. Additionally, a number of productive and informative studies have been carried out using a portable infrasound array, which has allowed the exploration of infrasound fields on a more local scale and in less accessible parts of the island.

Finally, a large amount of work has gone into the validation of the PMCC software as an effective infrasound detector, superior in many ways to other widely-used software packages. The extensive ISLA forensic analysis of infrasound from the tragic space shuttle Columbia re-entry is an excellent demonstration of PMCC's capabilities and flexibility.

9. Acknowledgements

10. References

Arendt, S. and D.C. Fritts, Acoustic radiation by ocean surface waves, *J. Fluid Mech.* 415, 1-21, 2000.

Bass, H., Report to the Department of Defense on infrasonic re-entry signals from the Space Shuttle Columbia (STS-107), March 31, 2003.

Bhattacharyya, J., C.H. Hetzer, M.A. Garcés, and V. Oancea, Description and analysis of infrasound signals recorded from the North Pacific event of February 22, 2003, presented at the *2003 Infrasound Technology Workshop*, La Jolla, California, October 27-30, 2003.

Brown, D.J., A.K. Gault, R. Geary, P. Caron and R. Burlacu, The Pacific infrasound event of April 23, 2001, presented at the *23rd Annual Seismic Research Review*, Jackson Hole, Wyoming, October 2-5, 2001.

Brown, P., R.E. Spalding, D.O. ReVelle, E. Tagliaferri, and S.P. Worden, The flux of small near-Earth objects colliding with the Earth, *Nature* 420, 294-296, 2002.

Cansi, Y., An automatic seismic event processing for detection and location: The P.M.C.C. method, *Geophys. Res. Lett.* 22, 1021-1024, 1995.

De Bremaecker, J.-C., Barometric pressure oscillations in Houston caused by the 1964 Alaska earthquake, *Seismol. Res. Lett.* 74, 39-40, 2003.

Donn, W.L. and B. Naini, Sea wave origin of microbaroms and microseisms, *J. Geophys. Res.* 78 (21), 4482-4488, 1973.

Donn, W.L. and E.S. Posmentier, Infrasonic waves from the marine storm of April 7, 1966, *J. Geophys. Res.* 72 (8), 2053-2061, 1967.

Evers, L.G. and H.W. Haak, Listening to sounds from an exploding meteor and oceanic waves, *Geophys. Res. Lett.* 28, 41-44, 2001.

Garcés, M.A., R.A. Hansen, and K.G. Lindquist, Traveltimes for infrasonic waves propagating in a stratified atmosphere, *Geophys. J. Int.* 135, 255-263, 1998.

Garcés, M.A. and C.H. Hetzer, Infrasonic signals detected by the KONA array, Hawaii, presented at the *23rd Annual DTRA/NNSA Seismic Research Review*, Jackson Hole, Wyoming, October 2-5, 2001.

M. Garces, C. Hetzer, K. Lindquist, R. Hansen, J. Olson, C. Wilson, D. Drob, and M. Hedlin, Infrasonic Source Location of the April 23, 2001, Bolide Event, presented at the 23rd Seismic Research Review: Worldwide Monitoring of Nuclear Explosions, Jackson Hole, Wyoming, 2-5 October, 2001.

Garcés, M.A. and C.H. Hetzer, Evaluation of infrasonic detection algorithms, presented at the *24th Annual DTRA/NNSA Seismic Research Review*, Ponte Vedra Beach, Florida, September 17-19, 2002.

M. Garces, C. Hetzer, K. Lindquist, and D. Drob, Source Location Algorithm for Infrasonic Monitoring, presented at the 24th Seismic Research Review: Nuclear Explosion Monitoring: Innovation and Integration, Ponte Vedra Beach, Florida, 17-19 September, 2002.

Garcés, M.A. and C.H. Hetzer, Optimizing the Progressive Multi-Channel Correlation detector for the discrimination of infrasonic sources, presented at the *25th Annual DTRA/NNSA Seismic Research Review*, Tucson, Arizona, September 23-25, 2003.

Garcés, M., A. Harris, C. Hetzer, J. Johnson, S. Rowland, E. Marchetti, and P. Okubo, Infrasonic tremor observed at Kīlauea Volcano, Hawaii, *Geophys. Res. Lett.* 30 (20), 2023, doi:10.1029/2003GL018038, 2003 (a).

Garcés, M.A., C.H. Hetzer, M. Willis, and S. Businger, Integration of infrasonic models with ocean wave spectra and atmospheric specifications to produce global estimates of microbarom signal levels, presented at the *25th Annual DTRA/NNSA Seismic Research Review*, Tucson, Arizona, September 23-25, 2003 (b).

Garcés, M., C. Hetzer, M. Merrifield, M. Willis, and J. Aucan, Observations of surf infrasound in Hawai'i, *Geophys. Res. Lett.*, in press.

Goerke, V.H. and M.W. Woodward, Infrasonic observations of a severe weather system, *Monthly Weath. Rev.* 94, 395-398, 1966.

Hasselmann, K., A statistical analysis of the generation of microseisms, *Rev. Geophys. Space Phys.* 1, 177-210, 1963.

Johnson, D.H. and D.E. Dudgeon, *Array Signal Processing: Concepts and Techniques*, Upper Saddle River, New Jersey: PTR Prentice Hall, 533 pp, 1993.

Le Pichon, A., J.M. Guérin, E. Blanc, and D. Reymond, Trail in the atmosphere of the December 29, 2000 meteorite as recorded in Tahiti: characteristics and trajectory reconstitution, *J. Geophys. Res.*, 1029/2001JD001283, 2002.

Longuet-Higgins, M.S., A theory of the origin of microseisms, *Philos. Trans. Roy. Soc. London, Ser. A, Math. Phys. Sci.* 243 (857), 1-35, 1950.

Marshall, C., Rock crashes through roof of home, *West Hawaii Today*, April 24 2002, http://www.westhawaiitoday.com/daily/2002/Apr-14-Sun-2002/news/news2.html.

Nemiroff, R.J. and J.B. Rafert, Towards a continuous record of the sky, *Pub. Astr. Soc. Pacific* 111, 886-897, 1999.

Ponomaryov, E.A., A.G. Sorokin, and V.N. Tabulevich, Microseisms and infrasound: a kind of remote sensing, *Phys. Earth Planet. Inter.* 108, 339-346, 1998.

Posmentier, E., A theory of microbaroms, *Geophys. J. Roy. Astron. Soc.* 13, 487-501, 1967.

ReVelle, D.O. and R.W. Whitaker, Infrasonic detection of a Leonid bolide: 1998 November 17, *Meteoritics Planet. Sci.* 34, 995-1005, 1999.

ReVelle, D.O., R.W. Whitaker, and W.T. Armstrong, *Infrasonic observations of bolides on October 4, 1996*, Los Alamos National Laboratories Report LA-UR-972481, 1997.

ReVelle, D.O., R.W. Whitaker, and W.T. Armstrong, *Infrasound from the El Paso super-bolide of October 9, 1997*, Los Alamos National Laboratories Report LA-UR-98-2893, 1998.

Rind, D., Heating of the lower thermosphere by the dissipation of acoustic waves, *J. Atmos. Terres. Phys.* 39, 445-456, 1977.

Stevens, J., I. Divnov, D. Adams, J. Murphy, and V. Bourchik, Constraints on infrasound scaling and attenuation relations from Soviet explosion data, *Pure Appl. Geoph.* 159, 1045-1062, 2002.

Su, F. and X. Su, Infrasonic observation of meteor shower from Leo on November 17 in 1998, *J. Univ. Petrol. China, Nat. Sci. Ed.* 25, 118-122, 2001.

Tolman, H., B. Balasubramaniyan, L. Burroughs, D. Chalikov, Y. Chao, H. Chen, and V. Gerald, Development and Implementation of Ocean Surface Wave Models at NCEP, *Weath. Forec.* 17, 311-333, 2002.

Appendix A: Comparison of PMCC and InfraTool for Specific Events

The 4-element I59US array has a 2km aperture, which causes spatial aliasing above ~0.5 Hz. This is not a problem for high S/N ratios - in that case even visual analysis can be performed. The results of this study would probably be quite different if I59US had a 3 or 4-element subarray that would reduce aliasing in the 1-4 Hz band.

Events can be most easily detected in InfraTool via a series of consistent values of azimuth and velocity/slowness, or via an increase in waveform correlation. The azimuth criterion is most useful for long-duration events, while the correlation criterion appears to be most useful in cases of high signal-to-noise. InfraTool and PMCC were compared using three situations that vary the duration and signal-to-noise of events. Each event was tested both in the 1-4 Hz and 3-4 Hz frequency bands; the narrower band was selected because two of the three situations contain signals that are strongest above 2 Hz.

It should be noted that the version of InfraTool used in these tests is that developed by ISLA based on the original SNL/LANL version. The ISLA InfraTool carries out the same calculations but adds an F-statistic calculation and converts velocity to slowness based on a conversion factor of 108.0773 km/deg. The controls were also moved into a separate frame to allow easier expansion of the main window when new tools are added. The two versions are cosmetically dissimilar but functionally equivalent.

Situation 1: Impulsive event, high signal-to-noise

The event chosen for this test is believed to be a construction-related chemical explosion. It was chosen to provide a signal that would test the response to elevated signal-to-noise in the absence of increased duration. It can be seen from Figures 1 and 2 that the correlation waveform shows an obvious spike during the event, and the F-statistic shows a less-obvious increase in the 1-4 Hz band. It should also be noted that the azimuth readings for the two frequency bands differ by approximately 18 degrees (Figure 3).

The PMCC results (Figures 4 and 5) also show a clear and unambiguous arrival across both frequency bands, although some gaps are present in the 3-4 Hz band. The azimuth values computed using this method vary by less than two degrees, and lie within a standard deviation of one another (Figure 6). This improvement in precision is most likely due to the lesser effects of spatial aliasing in the PMCC detector.

In this situation Infratool is adequate for detection, but the variation in arrival azimuth for the two frequency bands suggests that spatial aliasing is a problem even in the case of high S/N, potentially making event location via backazimuth unreliable.

Situation 2: Pervasive Impulsive Events, moderate signal-to-noise

The event chosen for this test is a series of surf-related arrivals. The individual arrivals that make up the event are lower-amplitude than that in the previous situation, but still are easily

visible above noise on both frequency bands (Figures 7 and 8). This event was chosen so that both the correlation and consistent azimuth criteria could be fulfilled; although surf events are short-duration, in this case they are so pervasive that they can theoretically be macroscopically treated as a single long-duration event.

The results shown in Figures 7 and 8 demonstrate that in this situation the high signal-to-noise causes the correlation waveform to show definite detections, while the azimuth trend is messy but obvious. Results are practically identical in the 1-4 Hz and 3-4 Hz frequency bands, presumably because the energy in the 3-4 Hz band is strong enough to dominate the 1-4 Hz band. Aliasing will be less of a problem in this case because an average value over a number of points will most likely be used instead of a single point.

PMCC analysis shows a similarly strong set of detections (Figures 9 and 10). The upper displays clearly show the energy concentrated above 2 Hz, demonstrating the reason for the similarity between the 1-4 Hz and 3-4 Hz band results in the InfraTool analysis. One advantage of the PMCC method is apparent in this figure: the surf events can be separated into discrete arrivals and further analyzed individually if desired. The display technique used by InfraTool of continuous waveforms makes this, although possible, somewhat more difficult.

This situation is probably ideal for analysis using InfraTool, as both detection techniques are valid. This is a similar situation to the analysis of superbolide signals, in that we have high signal-to-noise along with an extended duration. Other differences between PMCC and InfraTool in the analysis of superbolide signals can be found on the Tau-P CD from the 2002 Infrasound Technology Workshop in Deelen.

Situation 3: Pervasive Impulsive Events, low signal-to-noise

The event chosen for this test is another series of surf arrivals, but with lower signal-to-noise than that in Situation 2. This was chosen to make the test more difficult for the correlation detector but still give the consistent azimuth detector a chance. As can be seen in Figure 11, there is very little to be seen in the 1-4 Hz band. Not until the end of the waveform segment can some correlation spikes be seen (these events are surf arrivals from a different direction, with energy at a lower frequency), and without them the azimuth grouping is too ambiguous to constitute a definite arrival. When the 3-4 Hz band is considered the results improve (Figure 12); the filtering removed some of the lower-frequency noise, allowing the signal to emerge. The correlation waveform is similar to that in Situation 2, and there is once again a messy but definite trend in the azimuth waveform.

The PMCC detector, in contrast, appears to have performed equally well in both Situation 2 and Situation 3, and comparably well in both frequency bands (although the events at the end, which occur primarily below 3 Hz, are sparsely represented in the 3-4 Hz analysis) (Figures 13 & 14). This demonstrates that, because PMCC functions by subdividing its analysis passband and analyzing each subband individually, noise in one part of the band has little effect on detection of signal in another part of the band. It thus can perform adequately in cases of low signal-to-noise, as long as there is coherent signal in some part of the passband.

Conclusion and Summary

The InfraTool detector has shown that it can be quite useful under certain circumstances, such as when signal-to-noise is high or the event has a long duration. However, the PMCC detector has demonstrated the ability to deal with some adverse situations in which InfraTool has difficulty. Also, the PMCC detector provides information about the frequency content of a signal as a matter of course, and allows the analyst to view frequency-dependent trends in the analysis as well as time-dependent trends. With all of the additional information generated by PMCC, more sophisticated event thresholds can be set up for automatic processing (another advantage of PMCC; it can easily be run automatically with no user input and no graphical front-end).

InfraTool has one advantage over PMCC, in that PMCC requires specific trace velocity bounds to be set. Although this feature allows PMCC analysis to be more focused on particular types of events, it limits the ability to detect high-speed or low-speed events. Also, the fact that InfraTool is integrated with the excellent array-processing capabilities of MatSeis provides an advantage over PMCC in that all necessary analysis can be done in a single package. The ISLA version of InfraTool has expanded on the connections between MatSeis and InfraTool.

In summary, although InfraTool is quite adequate for a number of analysis situations, it lacks some of the versatility and flexibility of PMCC, and suffers in situations of low signal-to-noise. The ability to run as a non-graphical executable is also an advantage to the PMCC software, and its user interface is excellent. InfraTool's main advantage is its integration into MatSeis, which can be improved and expanded upon by anyone conversant with Matlab GUI programming.
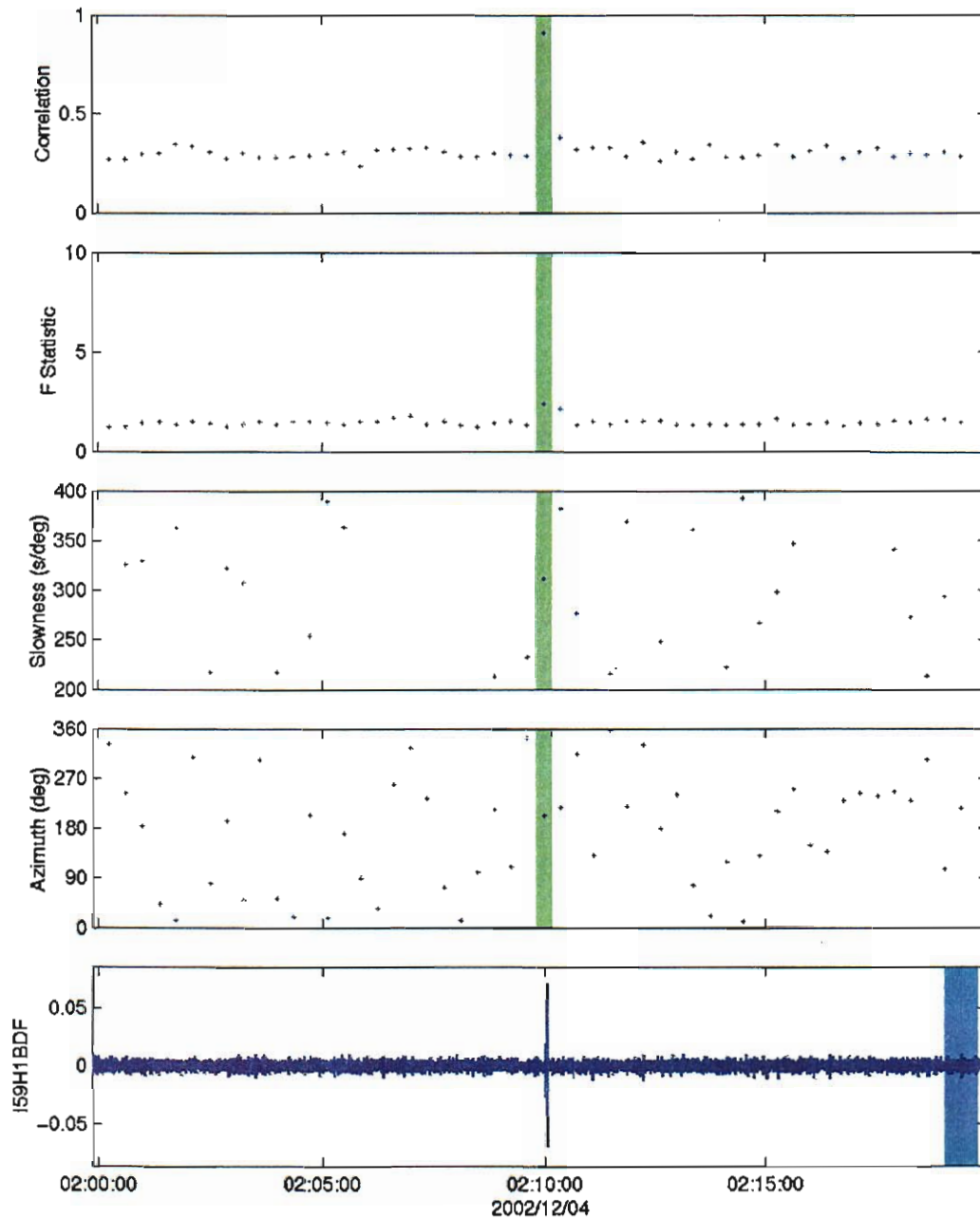
Figure 1. InfraTool window showing the response of the detector over the 1-4 Hz band when analyzing a short-duration, high signal-to-noise event.
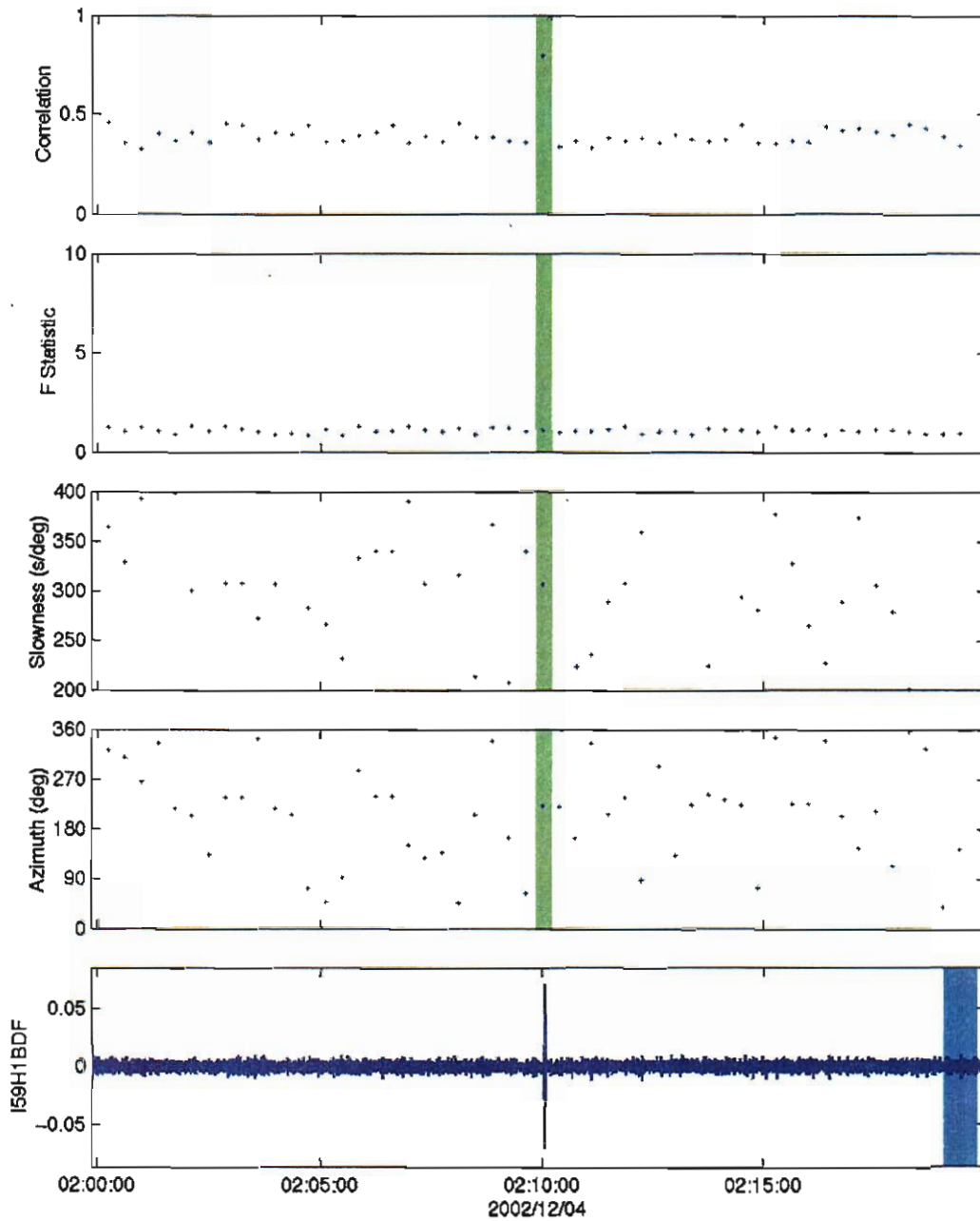
Figure 2. InfraTool window showing the response of the detector over the 3-4 Hz band when analyzing a short-duration, high signal-to-noise event.
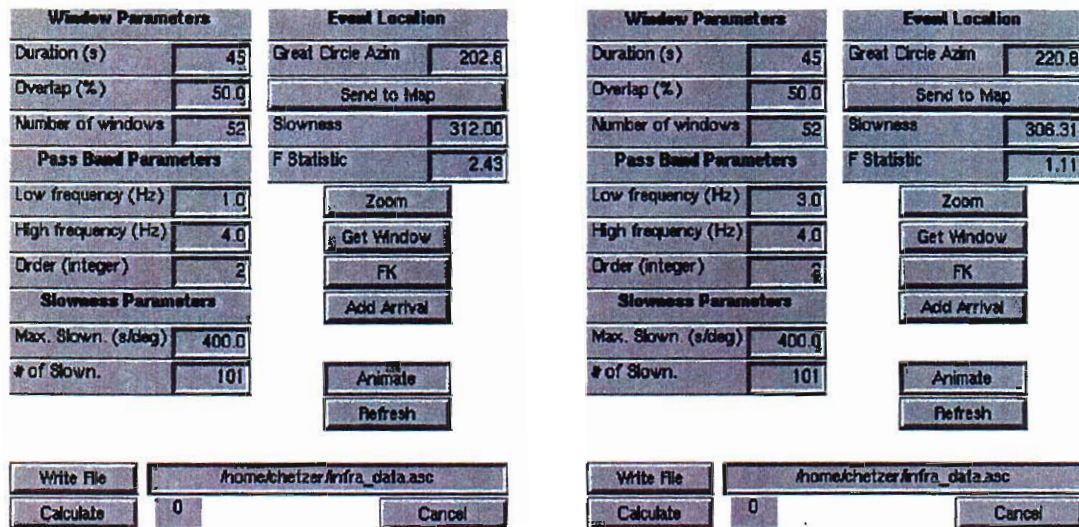
Figure 3. InfraTool control panels showing the parameters used for the 1-4 Hz (left) and 3-4 Hz (right) bands, and the variation in azimuth detected between the two.
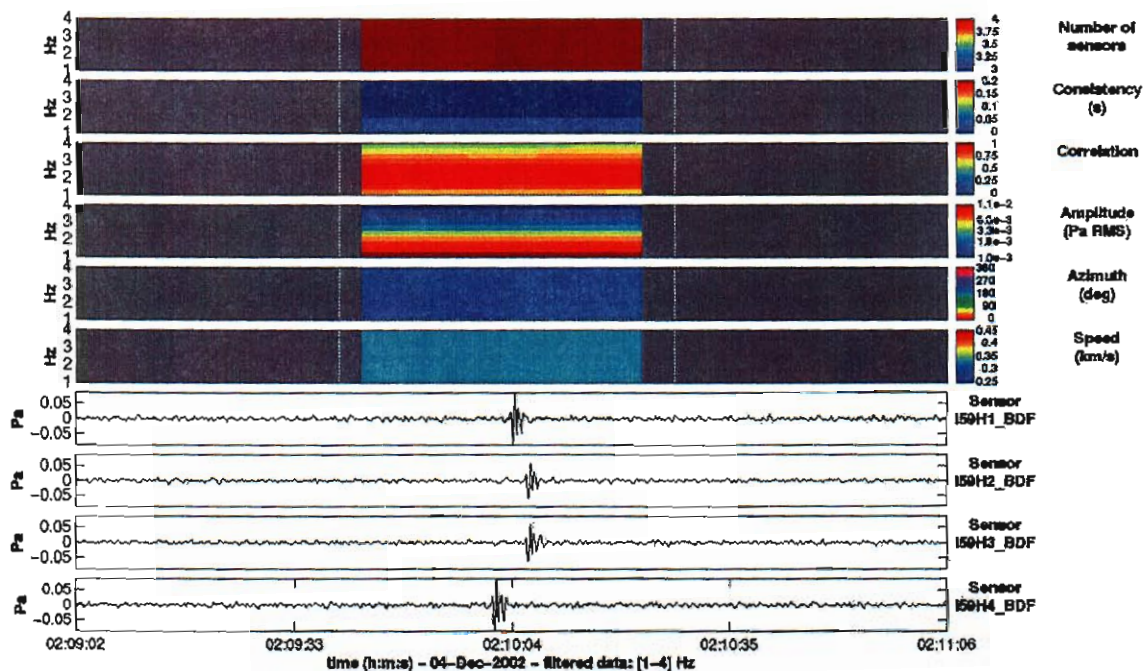
Figure 4. PMCC main analysis window showing the detection in the 1-4 Hz band.
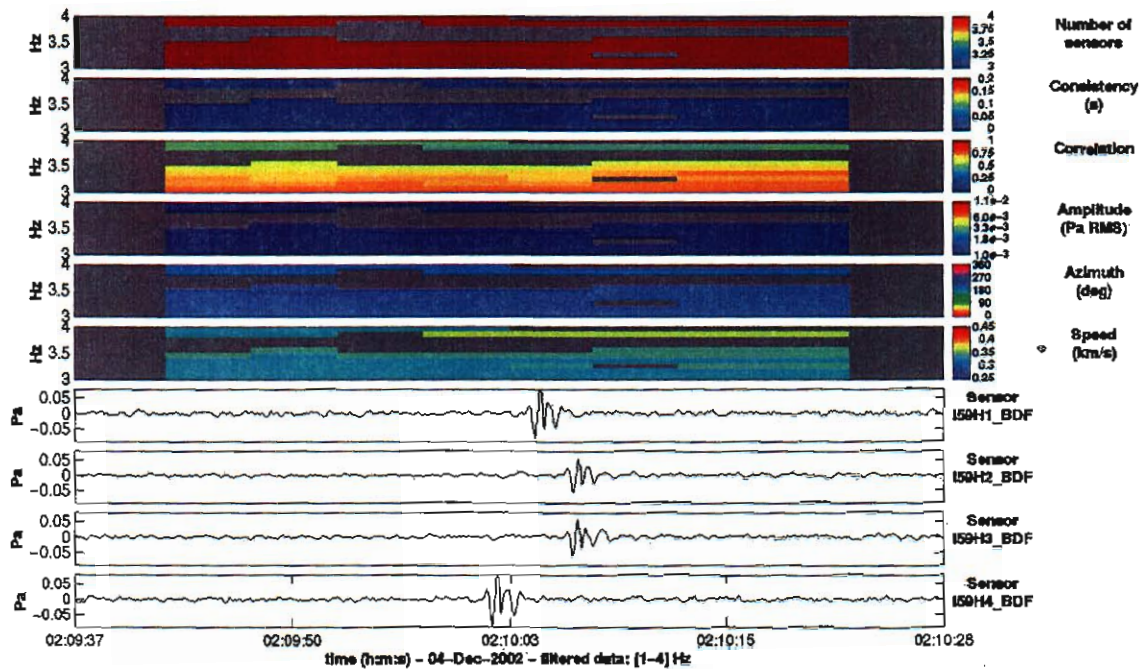
Figure 5. PMCC main analysis window showing the detection in the 3-4 Hz band.
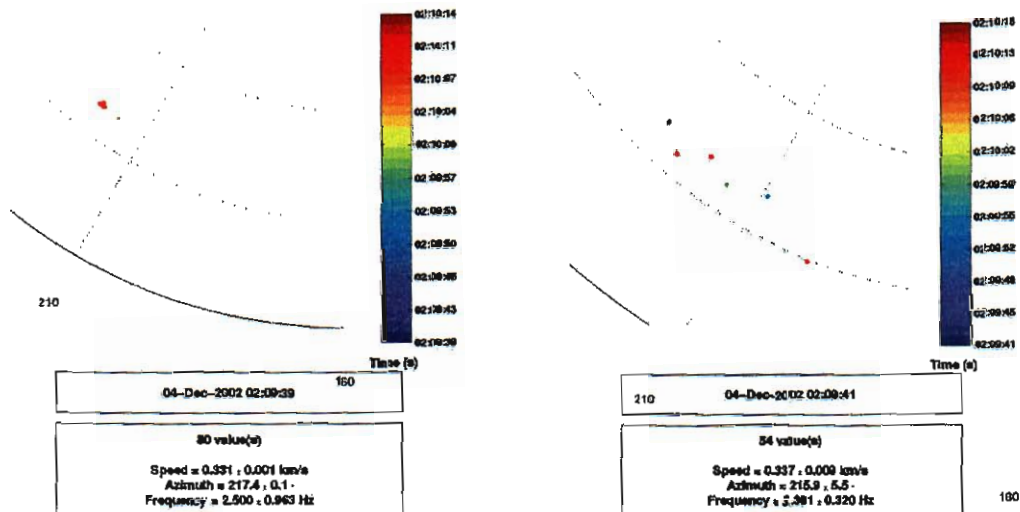
Figure 6. PMCC polar plot windows showing the azimuth and velocity analysis of the event in the 1-4 Hz (left) and 3-4 Hz (right) bands.
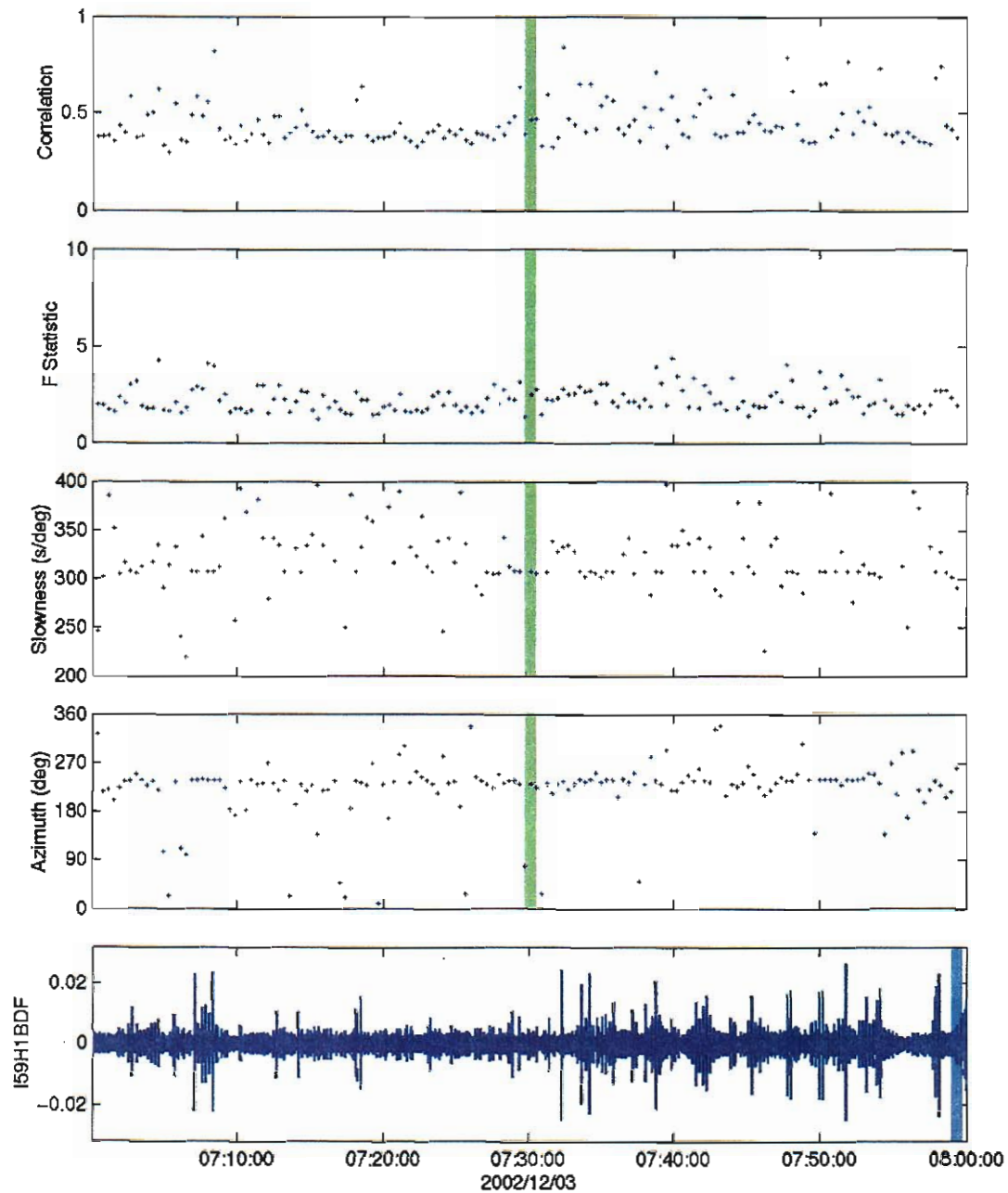
Figure 7. InfraTool window showing high signal-to-noise surf events and the analysis results in the 1- 4 Hz band.
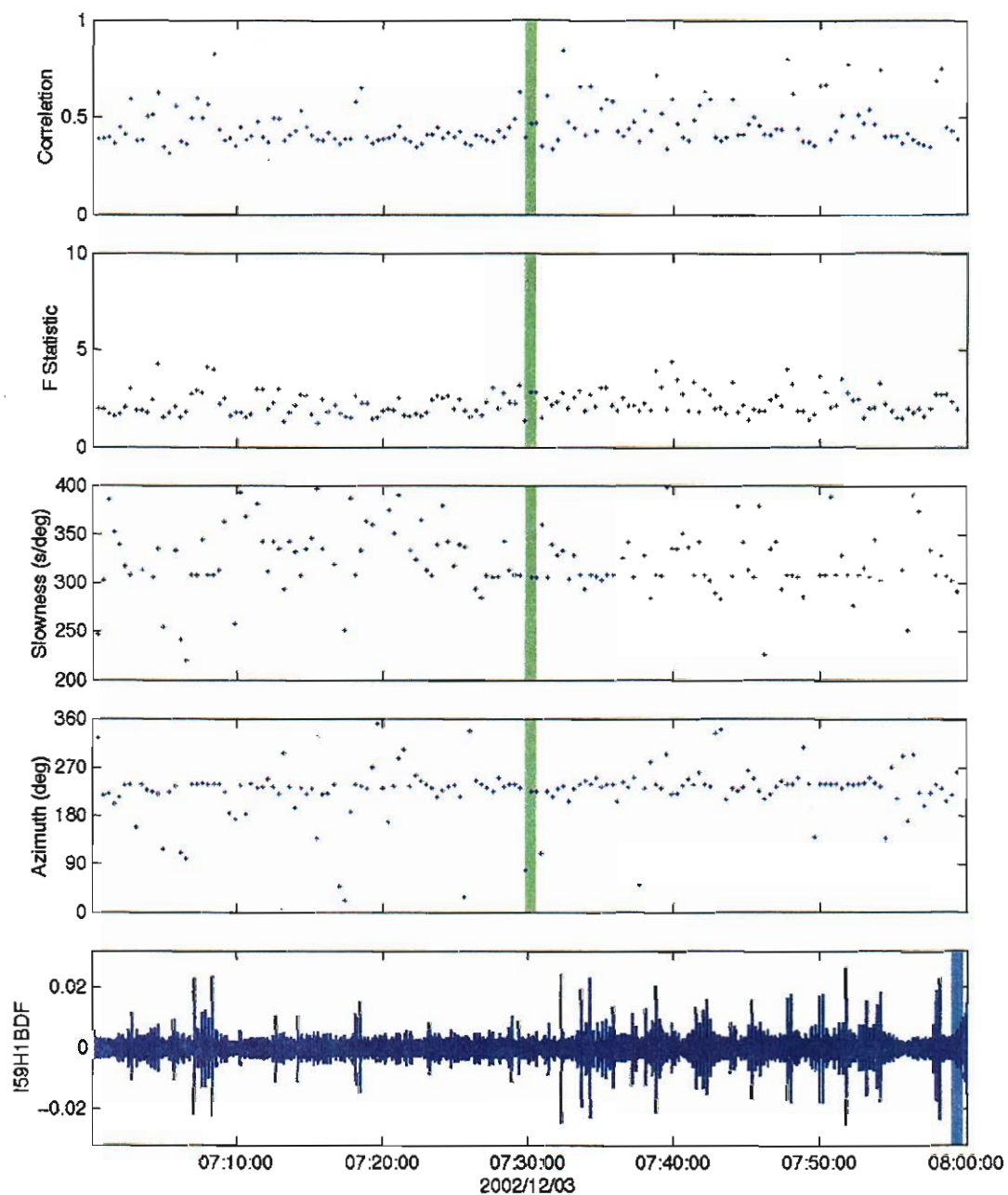
Figure 8. InfraTool window showing high signal-to-noise surf events and the analysis results in the 3-4 Hz band.
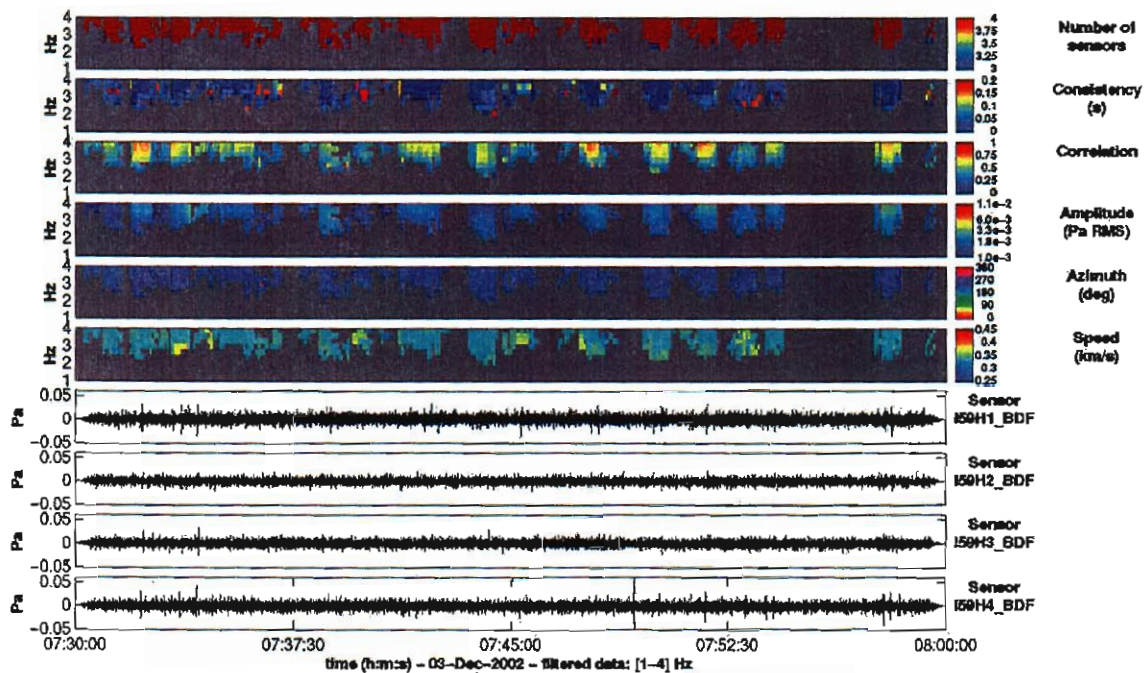
Figure 9. PMCC analysis window showing the results of the calculation in the 1-4 Hz band. Note the relatively high frequency content of the surf signals.
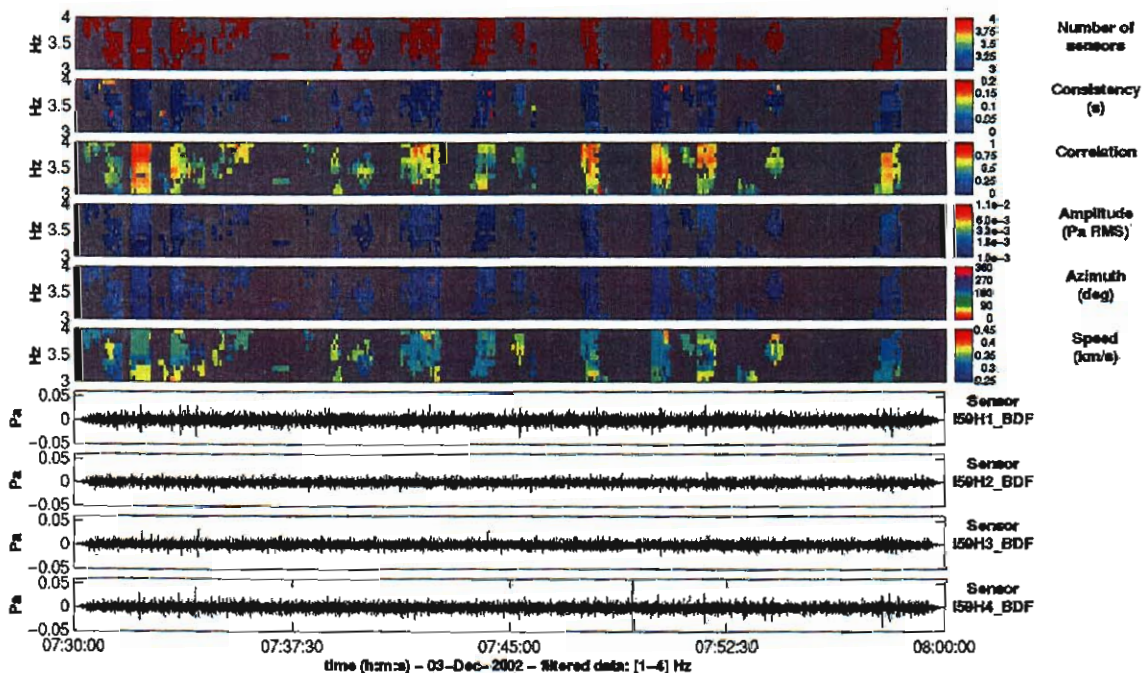
Figure 10. PMCC analysis window showing the results of the calculation in the 3-4 Hz band.
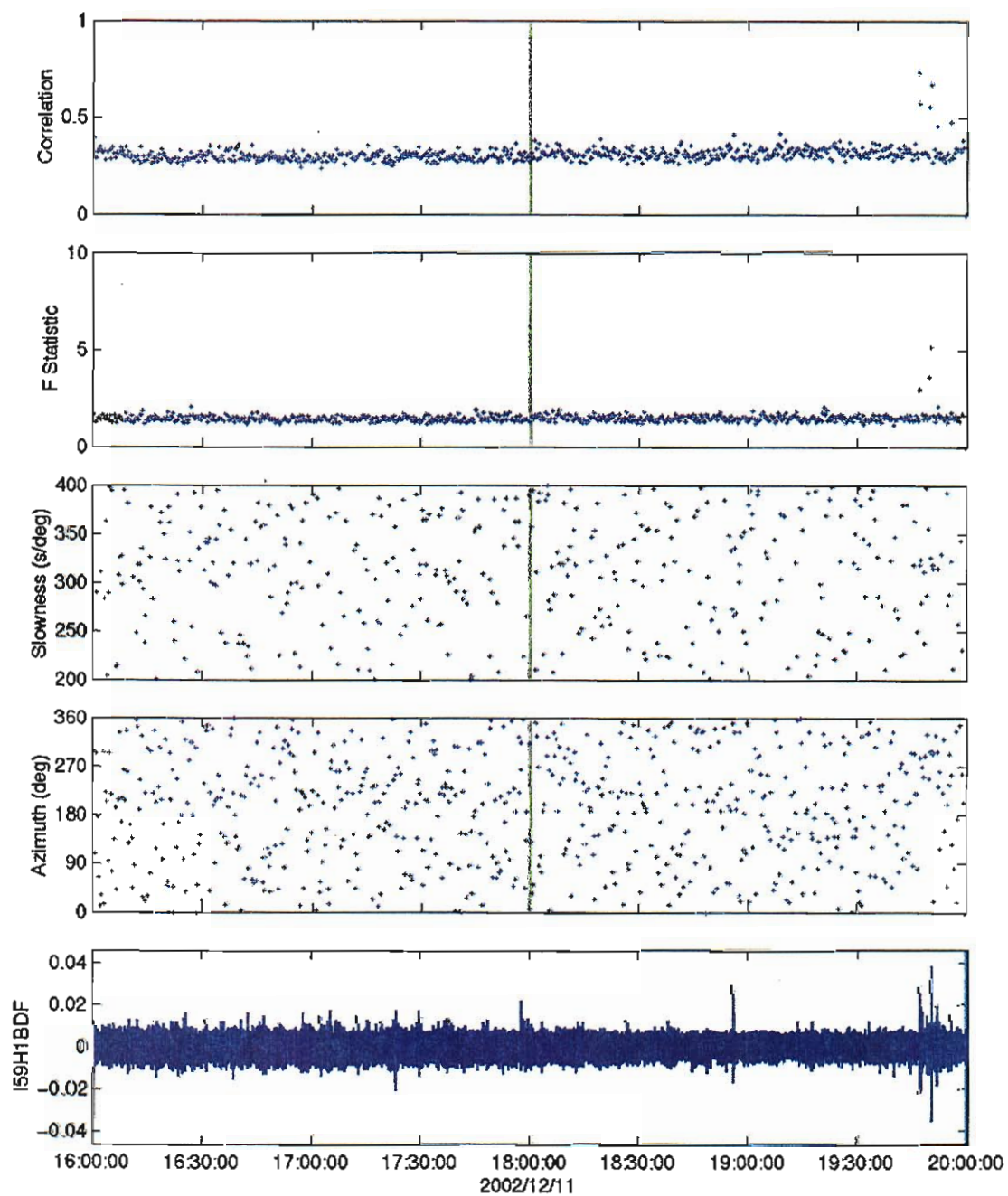
Figure 11. InfraTool window showing low signal-to-noise surf events and the analysis results in the 1-4 Hz band.
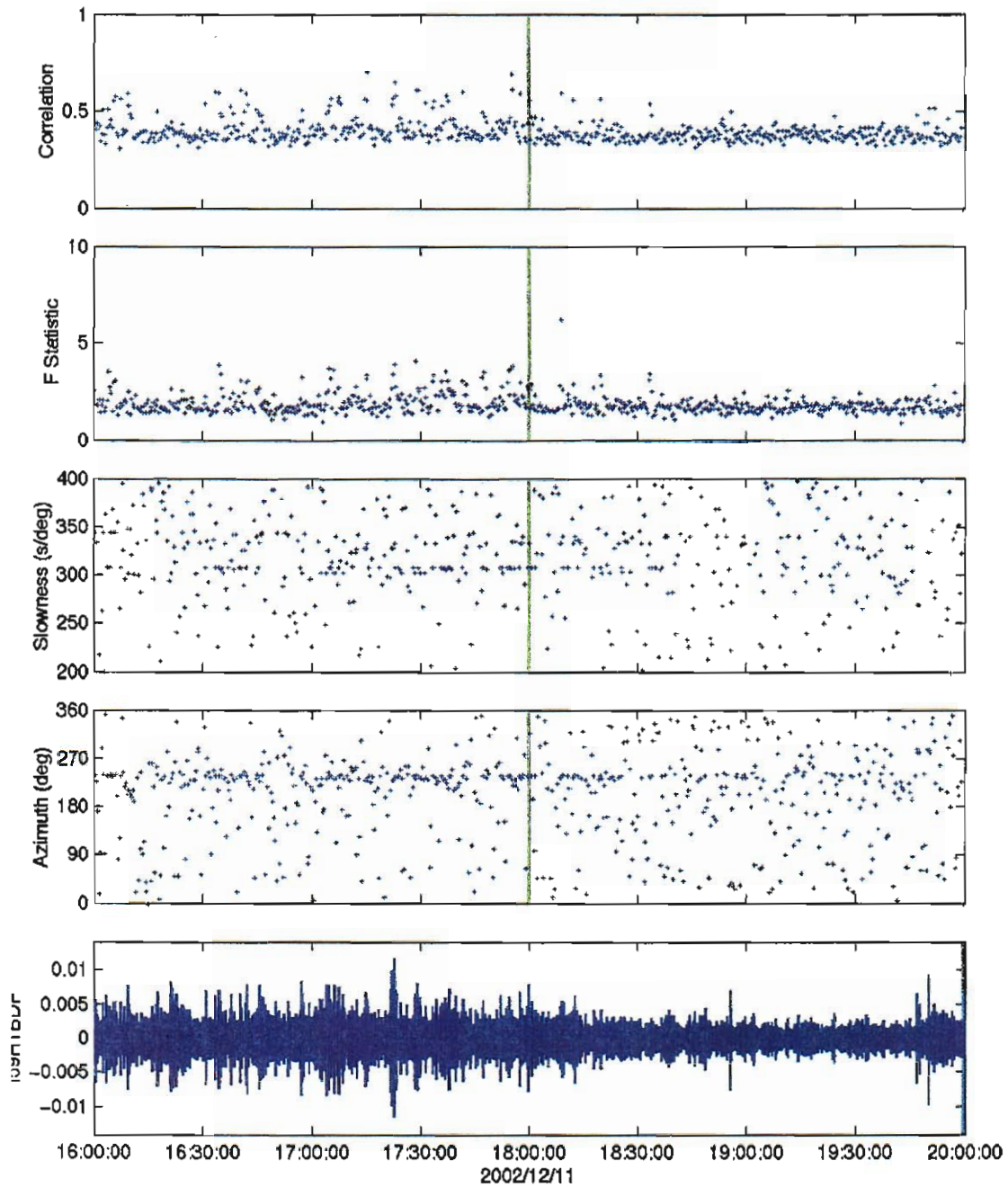
Figure 12. InfraTool window showing low signal-to-noise surf events and the analysis results in the 3-4 Hz band.
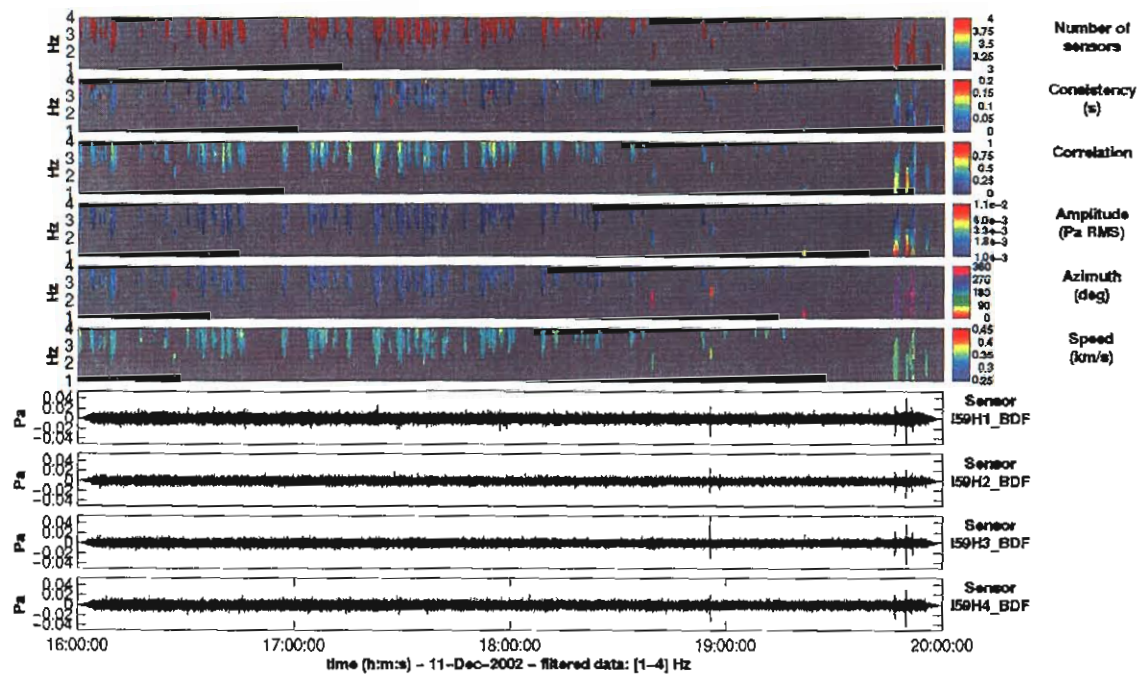
Figure 13. PMCC analysis window showing the results of the calculation in the 1-4 Hz band. Again, note the relatively high frequency content of the surf signals.
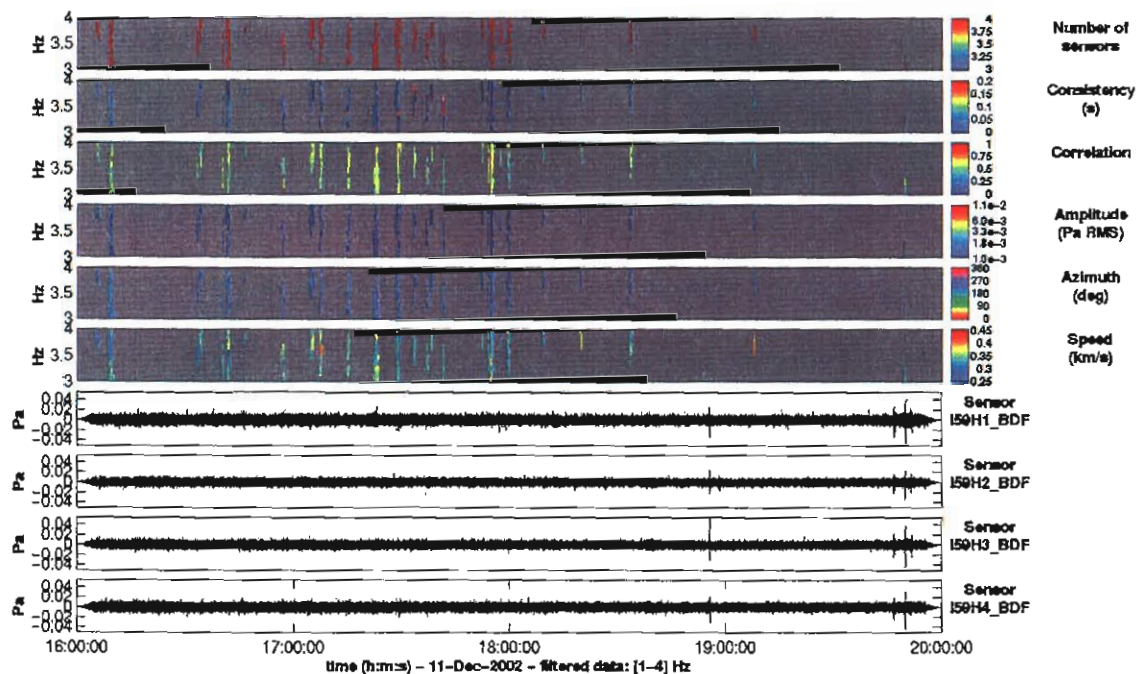
Figure 14. PMCC analysis window showing the results of the calculation in the 3-4 Hz band.

82

Appendix B

Infrasonic Investigations of the Columbia Re-Entry
Part 1. Preliminary analysis of infrasound data associated with the Columbia disaster of February 1, 2003

February 11, 2003
Revision 5

Milton Garcés and Claus Hetzer
Infrasound Laboratory, University of Hawaii, Manoa
Michael Hedlin
Laboratory for Atmospheric Acoustics
IGPP, Scripps Institution of Oceanography
Henry Bass
NCPA, University of Mississippi

1. Introduction

The Space Shuttle Columbia exploded on February 1, 2003, killing its crew of seven. Infrasound stations in the continental United States and Canada observed the entry of the Columbia into the atmosphere, its approach along the western US, and its unscheduled disassembly near Texas. The following discussion uses PMCC to analyze some of the presently available infrasound data. Appendix A provides available trajectory information. The Center for Monitoring Research (CMR) can provide more detailed track information.

2. Infrasonic Array Detections

With the following exceptions, CSS data was downloaded from the CMR data server. I56US data were provided by Michael Hedlin, UCSD. I59US data were obtained from ISLA's local CSS database. I53US, PDIAR, and NVIAR data were provided by Joydeep Bhattacharyya, CMR. All array detections were performed with PMCC. Some DSP and array processing was done with Matseis.

2.1. I57, California

Very good detection, interesting sequence. Only used outside 4 elements (L1-L4).

Figure 1. Closeup of detections at I57US associated with the entry of the Columbia. There is a clear arrival to what might correspond to the passing of the shuttle (14:25:46), with a bit of energy arriving before (14:23:08) and after (~14:27:52, 14:29:08, and 14:42). All later arrivals appear to correspond to the landing approach. The arrival preceding the bow wave is very intriguing, as the shuttle speed is probably over 6 km/s at that point and thus should overtake any sound waves. Mach "cone" should be nearly cylindrical.

Figure 2. Three hour segment showing microbaroms detections near 0.5 Hz originating from the NW, where high winter surf is ongoing.

Figure 3. Three hour segment showing background noise from microbaroms in the 0.1 – 0.5 Hz band.

Figure 4. Closeup of detection in 0.1 – 0.5 frequency band.

2.2. I10, Canada
Detections associated with the Columbia reentry did not have much energy above 1 Hz (Figure 5). Complex first arrival after 15:24 has most coherent energy between 0.5 –1 Hz (Figure 6). Some progression towards higher apparent horizontal phase speeds with time.

2.3. DLIAR, New Mexico
Possible bow wave with relatively high horizontal phase speed (Figure 7). Coda shortly after first arrival appears to lose coherence in the 0.5- 4 Hz band.

2.4. SGAR, Utah
Possible bow wave with very high horizontal phase speed (717 m/s, Figure 8). Coda shortly after first arrival appears to lose coherence in the 0.5- 4 Hz band.

2.5. NVIAR, Nevada
Possible bow wave with very high horizontal phase speed (991 m/s, Figure 9). Secondary detection after first arrival may be related to coda, but marked deviation from first arrival azimuth makes the association questionable.

2.6. TXIAR, Texas
We have no access to this data. This discussion is taken from
http://www.geology.smu.edu/%7Edpa-www/columbia/index.html

"The following data (Figure 10) was recorded by the TXAR array, about 500 miles south of Dallas, as the Columbia passed over north Texas. The N wave would not normally be seen at this distance.
The signal was recorded at about 14:30 GMT. It shows a gradual ramp up of signal, interpreted by the seismologists as some sort of severe turbulence, followed by a series of sharp events that appear to be explosions as the shuttle came apart, somewhere between 7 and 12 separate events, with one widely spaced small event near the end. It took the sound wave about 40 minutes to arrive at the infrasound array in Lajitas, Texas."

A press release, with some azimuth information, is given in Appendix B.

2.7. I56, Washington
Only three elements were available at this array (H3 was down). Figures 11 and 12 shows a series of detections at I56 with relatively stable azimuth and slowness. Multiple arrivals may be attributed to multiple propagation paths.

2.8. PDIAR, Wyoming

Complex arrival with some variation in azimuth over time (Figure 13). The general trend of the azimuth variation is to the west, suggesting the later arrival of signals from earlier in the shuttle's re-entry. The coda of the signal continues the westward trend. Some background noise is present at the observed azimuths, but the signal displayed is more coherent than most of the noise observed (Figure 14).

2.9. I59US, Hawaii (No Detections):

Figure 15 shows the detections in the 0.1-1.0 Hz frequency band at I59US for over 7 hours, starting at 12 GMT. There are no clear associations to the Columbia reentry. At I59US longitude, the closest approach occurred near156.54 W, 34.871 N, 98 km height, 13:46:40 GMT.

2.10. I53US, Alaska (No Detections):

Figure 16 shows the detections in the 0.1-1.0 Hz frequency band at I59US for 8 hours, starting at 12 GMT. There are no clear associations to the Columbia reentry.

Synopsis

Our results are in agreement with CMR's February 4 release entitled "Space Shuttle Columbia Accident, 1 February 2003, Preliminary Analysis of Center for Monitoring Research Data Assets". The waveforms at I57 and I10 appear more complex than those at SGAR and DLIAR, possibly due to multipath propagation. The main signal at most stations appears to be primarily due to the shock wave of the Shuttle during reentry. A graphical summary of the detections is shown in Figure 17. The track information is obtained from CMR's February 7, 2003 release.

From Figure 17, the earliest detections appear to occur when the shuttle was at 38.465 N, 120.822 W, 70.4 km height, and at a time of 13:54 GMT. This time almost coincided with the arrival of the shuttle over NVIAR, and signals from that sector of the reentry were observed at I56 and I57. Clear N waves were observed at SGAR and DLIAR as the shuttle flew almost overhead. Before the final catastrophic disassembly there are two groups of detections at I10, and the final detections appear to occur at TXIAR at ~32.351 N, 97.179 W, 60.3 km height at a time of ~14:00 GMT. The final time is consistent with the track information provided in Appendix A.

References

Cansi, Y, An automatic seismic event processing for detection and location: The P.M.C.C. method, *Geophys. Res. Lett., 22*, 1021-1024, 1995.

Cansi, Y., and Y. Klinger (1997). An automated data processing method for mini-arrays. Newsletter of the European-Mediterranean Seismological Center, 11, 2-4.

Garcés, M. and C. Hetzer, Evaluation of Infrasonic Detection Algorithms, Proceedings of the 24th Annual DTRA/NNSA Seismic Research Review, Ponte Vedra, FL, 17-19 September 2002.
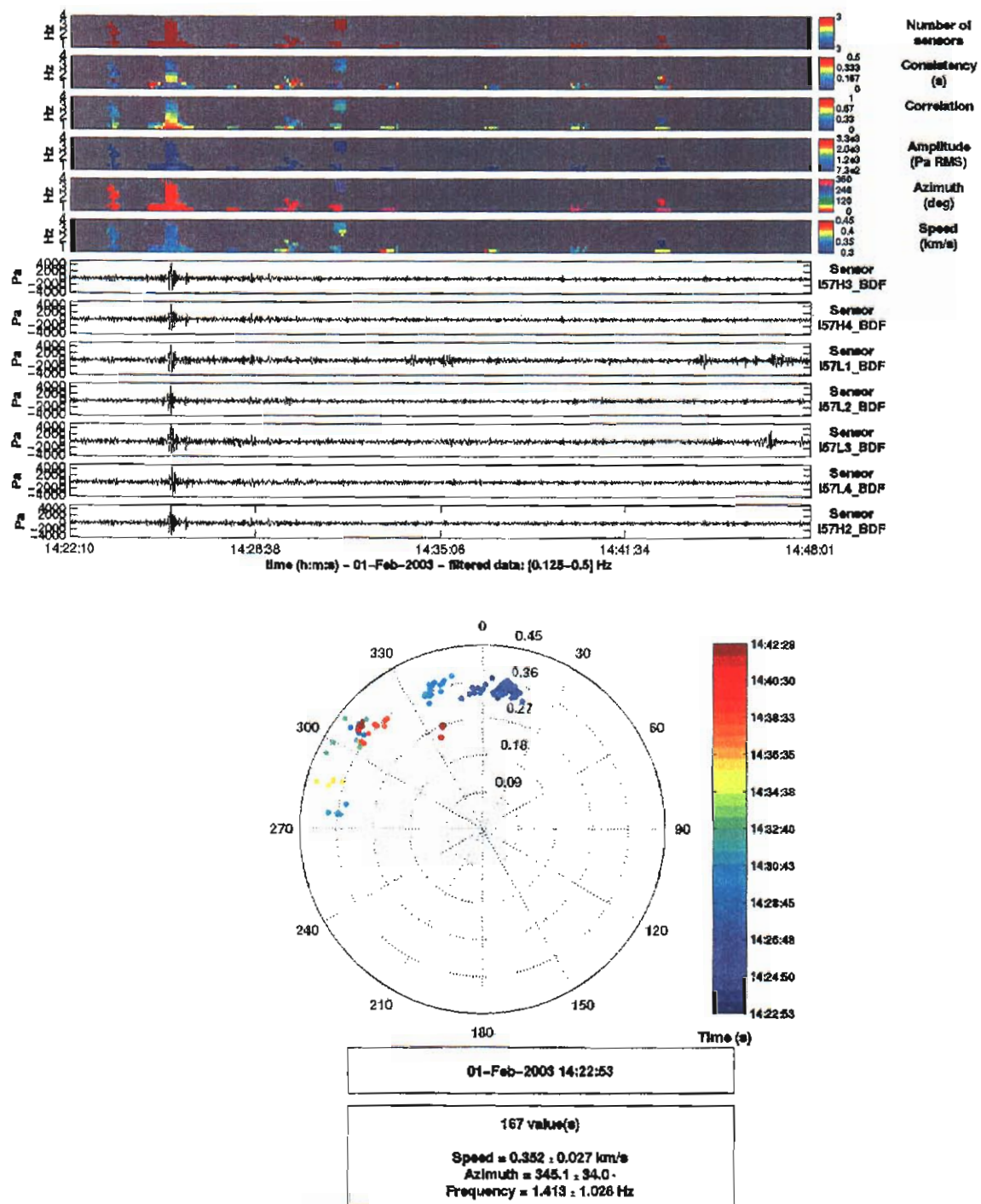
Figure 1. Main Columbia arrival at I57US. Frequency band of 0.5 – 4 Hz.
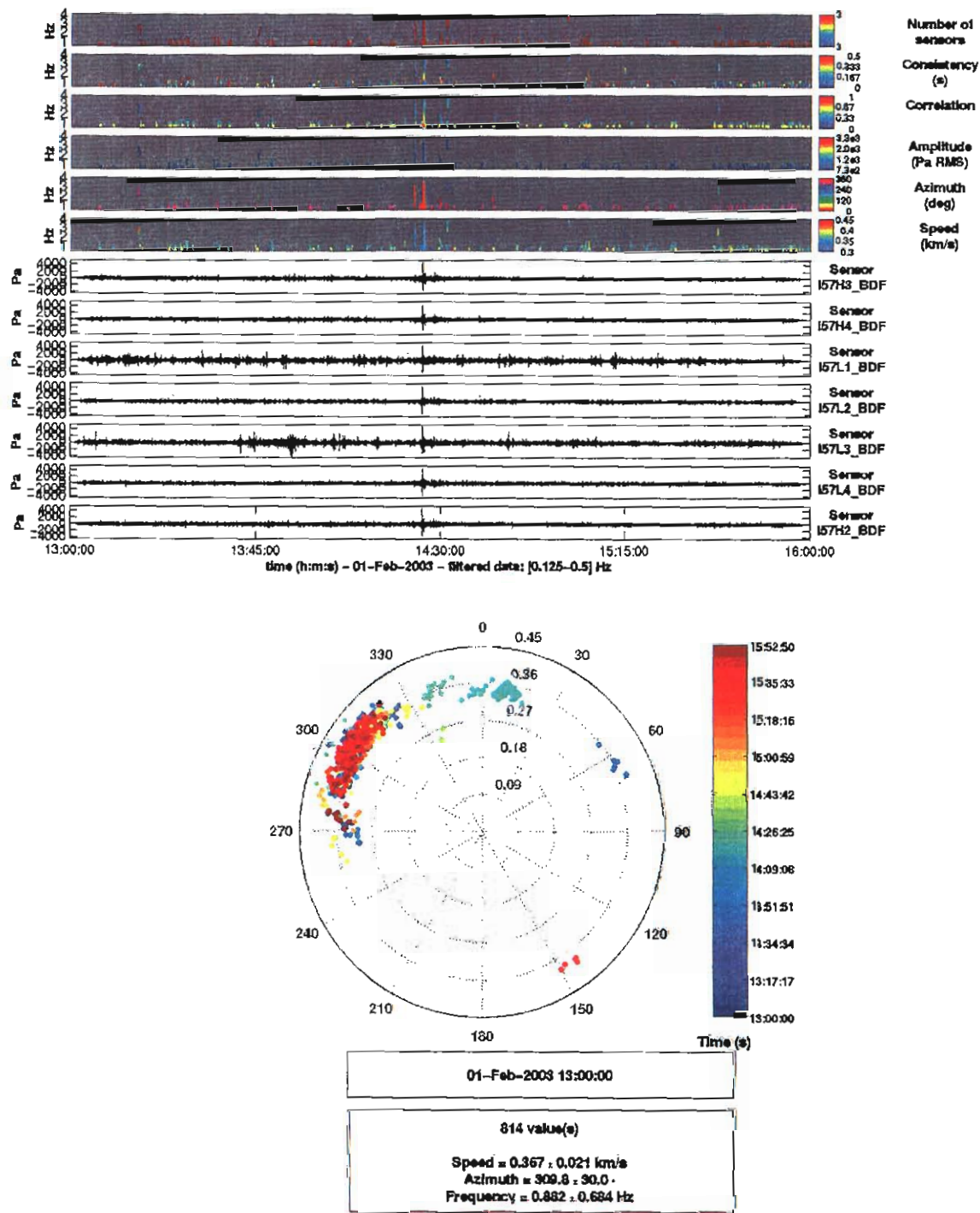
Figure 2. Three hour segment in the frequency band of 0.5 – 4 Hz showing noise source in the 270-330 azimuth segment corresponding to energy leakage from microbaroms.
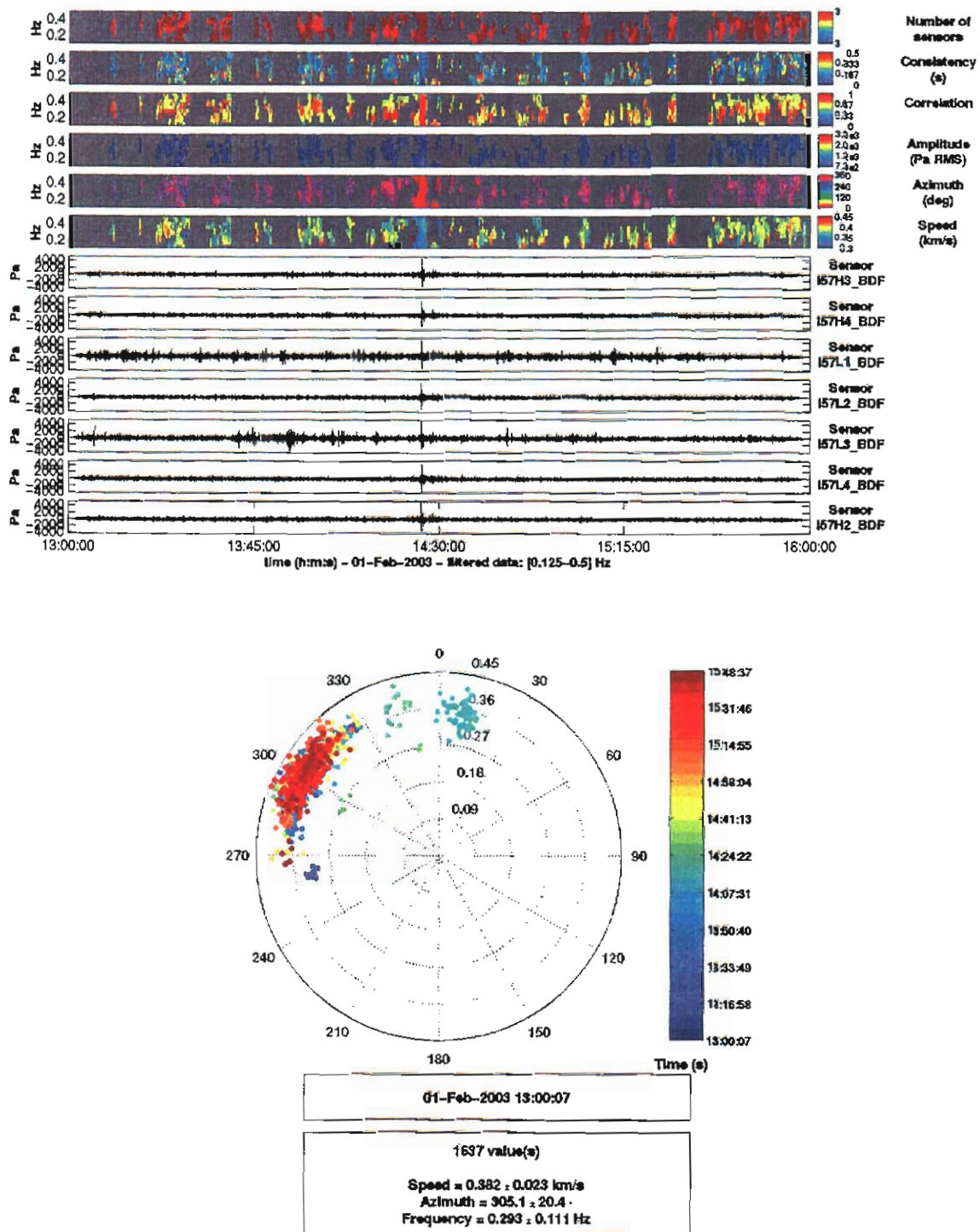
Figure 3. Three hour segment in the frequency band of 0.1 – 0.5 Hz showing noise source in the 270-330 azimuth segment corresponding to microbaroms.
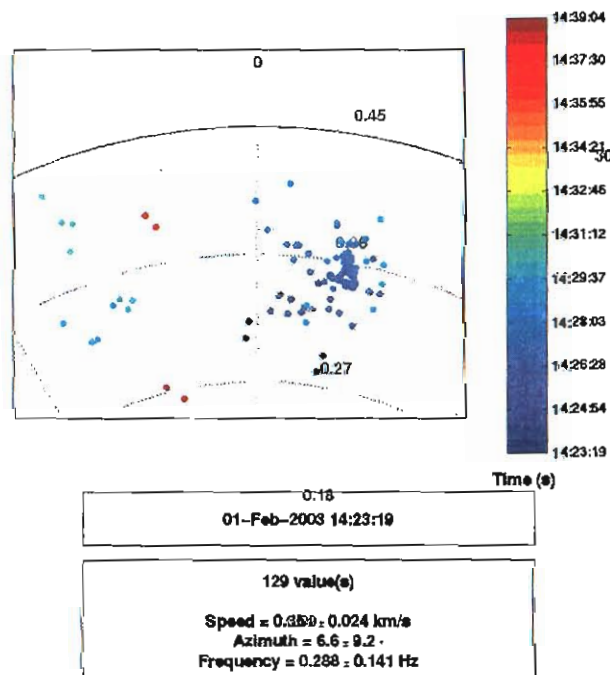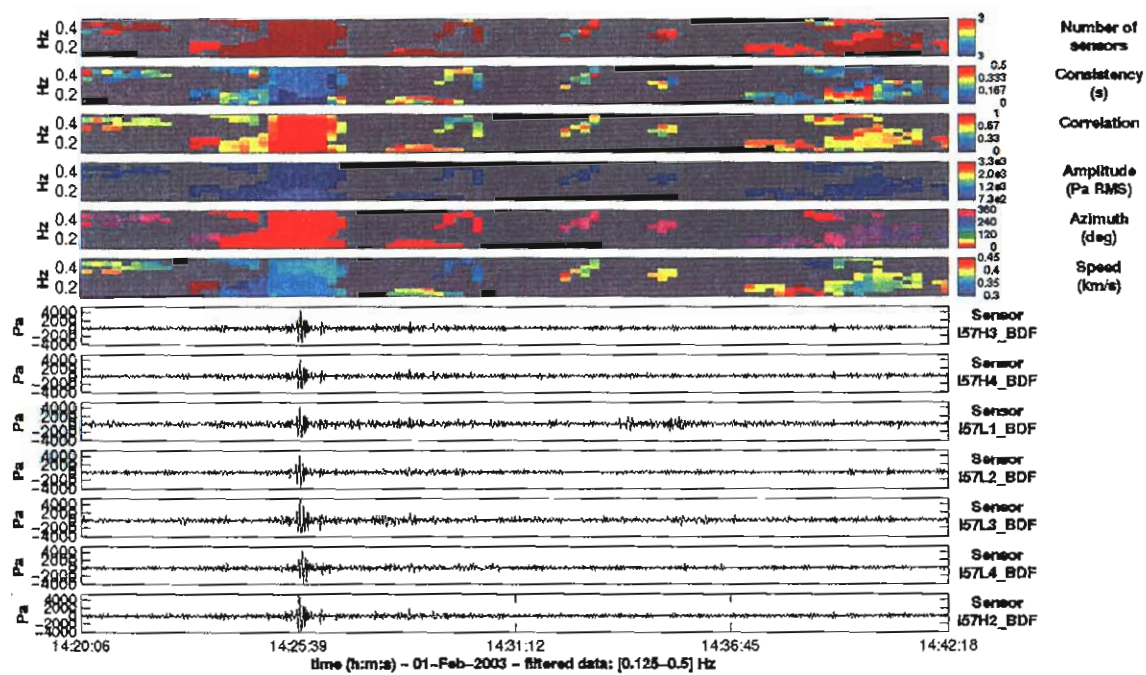
Figure 4. Main Columbia arrivals at I57US. Frequency band of 0.1-0.5 Hz.
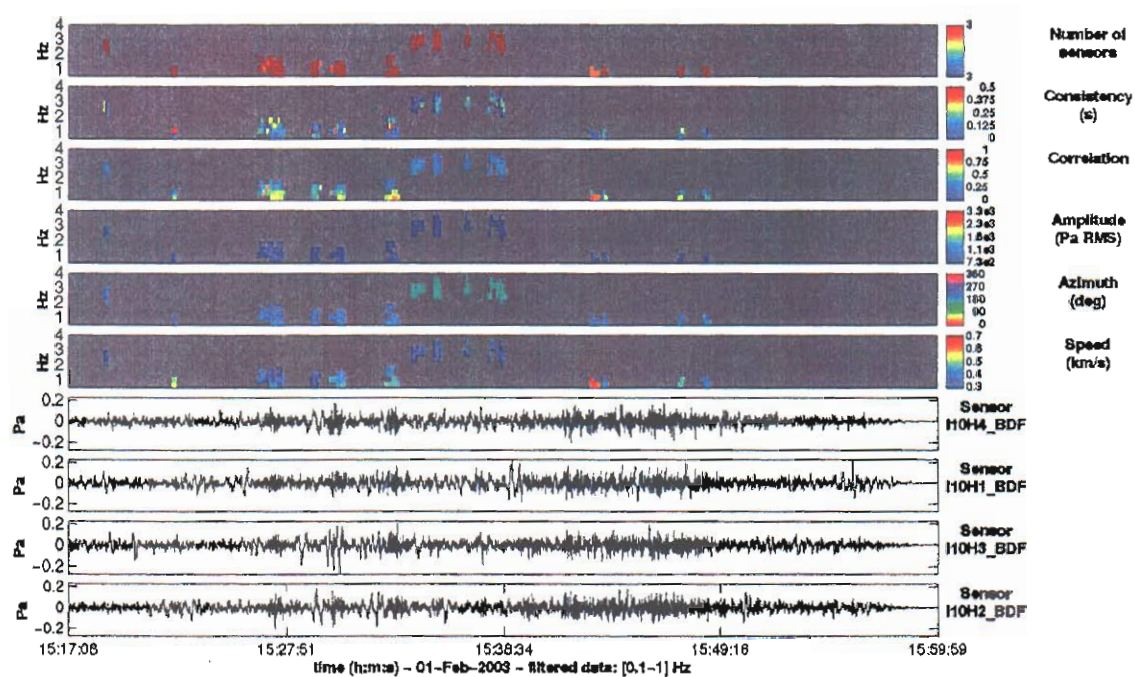
Figure 5. Columbia arrivals at I10, Canada, in the frequency band of 0.5-4 Hz. There is not much energy in the higher frequency bands.
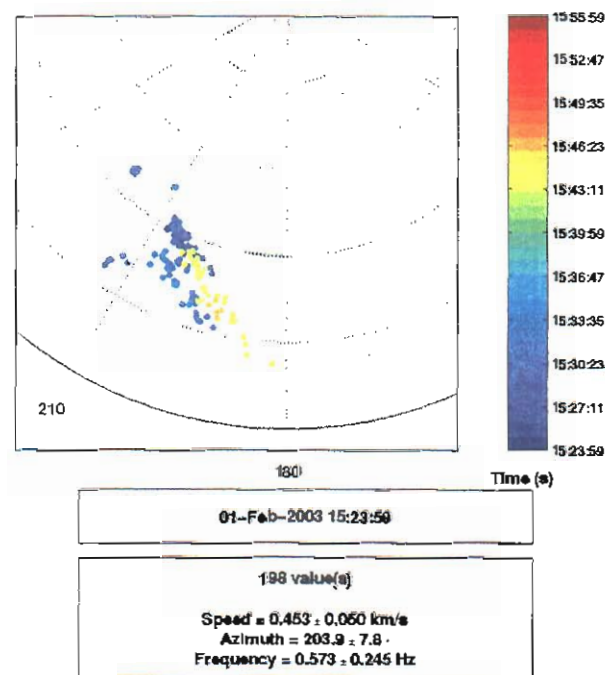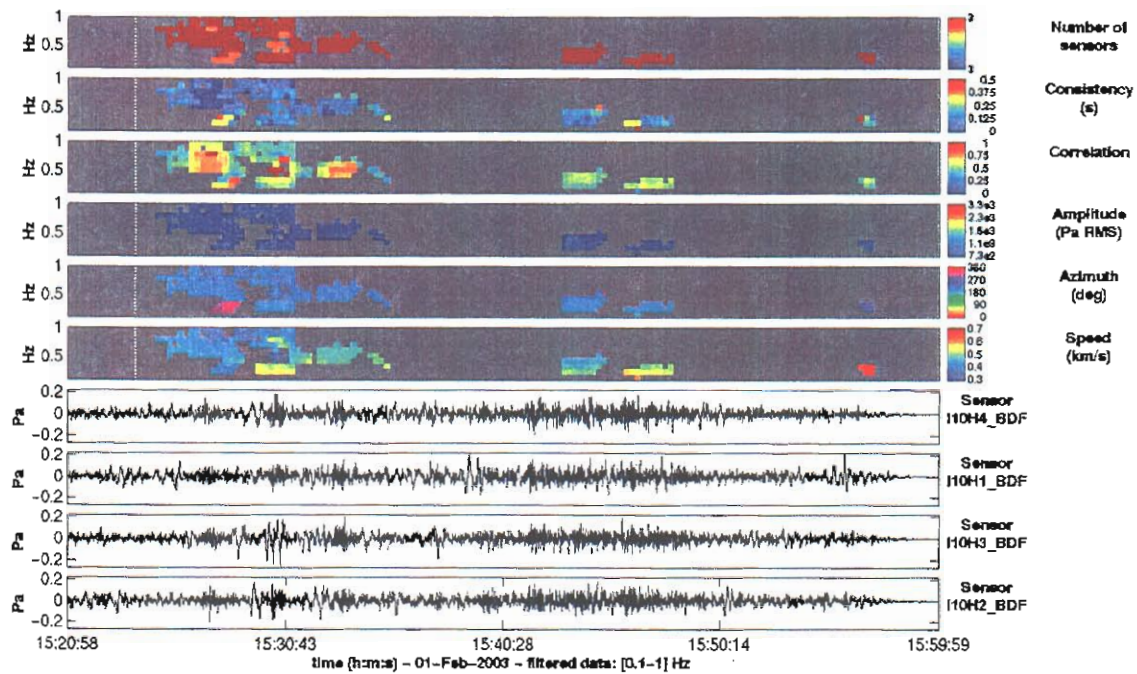
Figure 6. Columbia arrivals at I10, Canada, in the frequency band of 0.1-1 Hz.
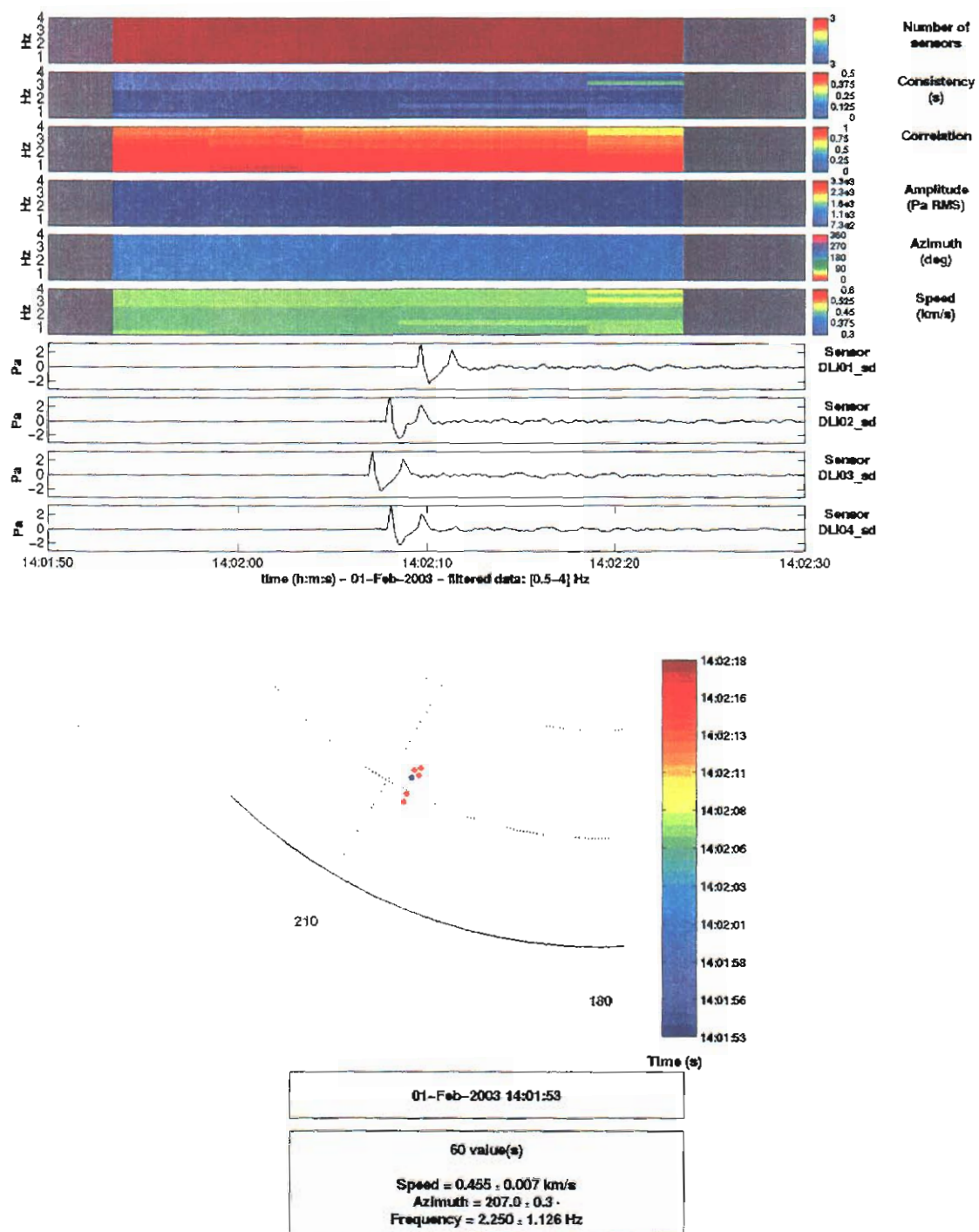
Figure 7. Possible bow wave observed in the 0.5- 4 Hz band at DLIAR and associated with the Columbia reentry.
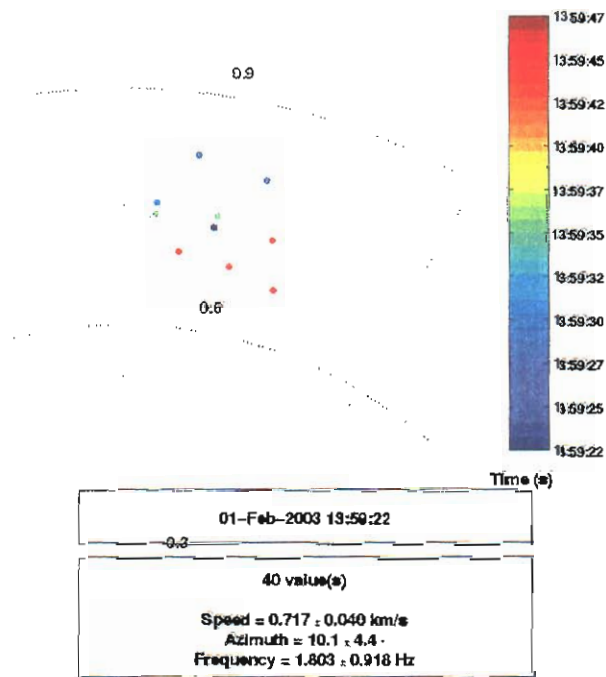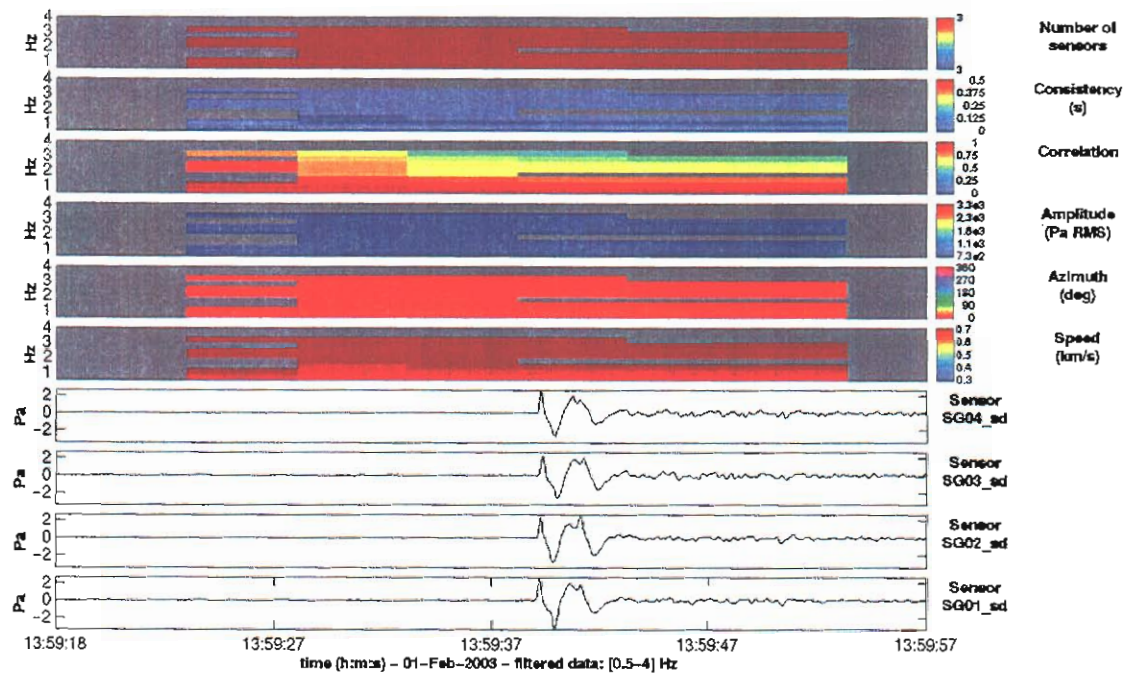
Figure 8. Possible bow wave observed in the 0.5- 4 Hz band at SGAR and associated with the Columbia reentry.
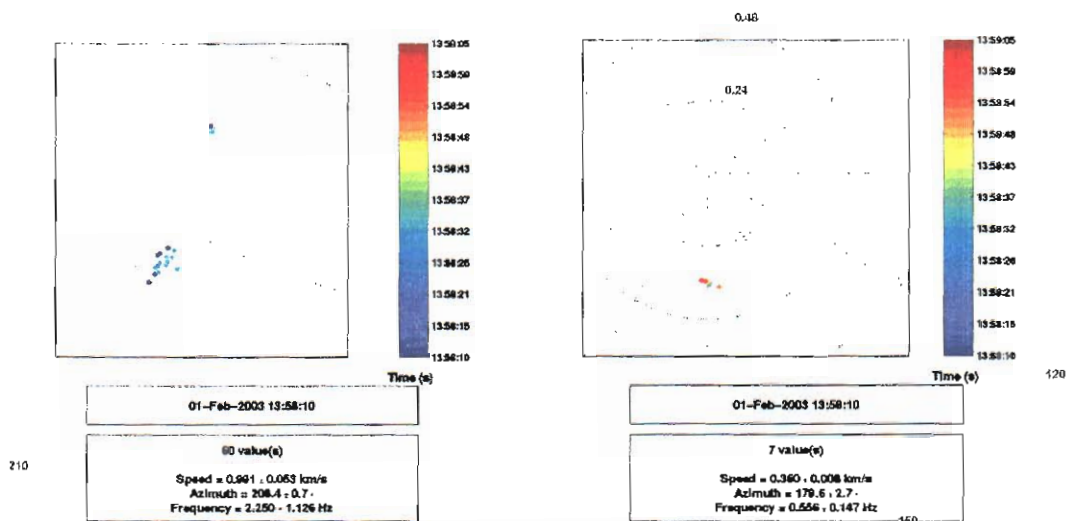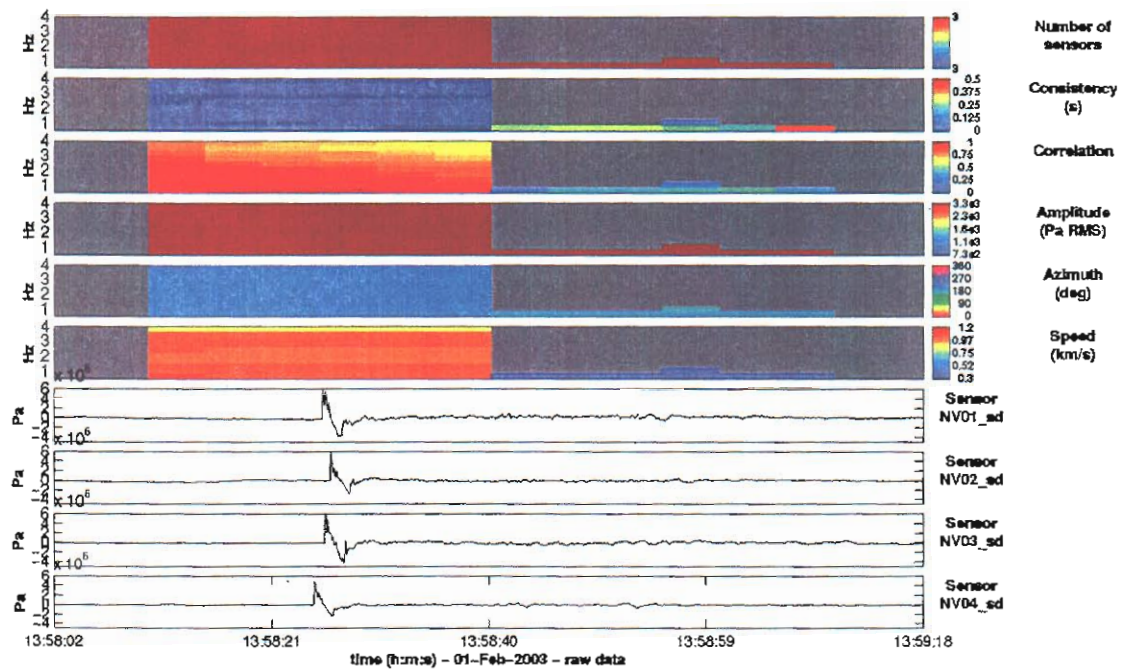
Figure 9. Possible bow wave observed in the 0.5- 4 Hz band at NVIAR and associated with the Columbia reentry. Bottom panel shows arrival azimuth and horizontal phase velocity of the main arrival (left) and possible coda (right).
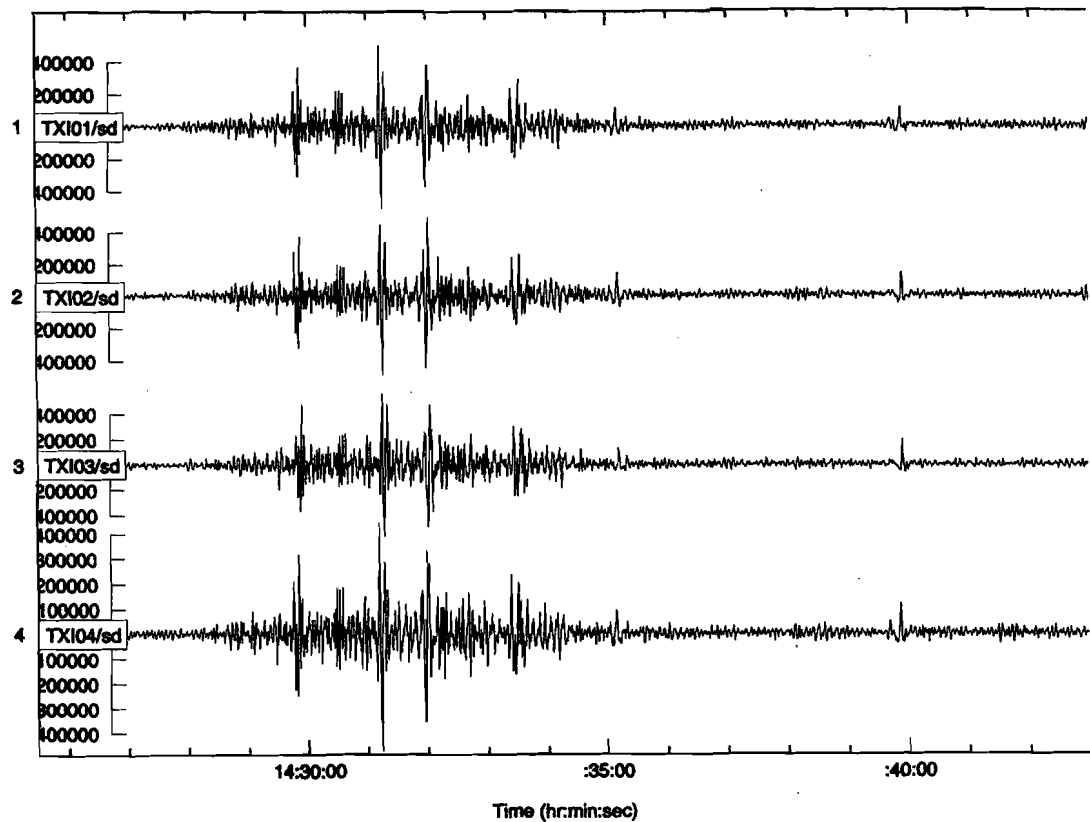
Space Shuttle Columbia Explosion, fromTXAR infrasound array in Lajitas, Texas, 01 February 2003 — Southern Methodist University

Figure 10. Waveform observed in Texas, near the time of the shuttle's catastrophic disassembly. At the time of this writing, we have no access to these data. Image was downloaded from the SMU web page.
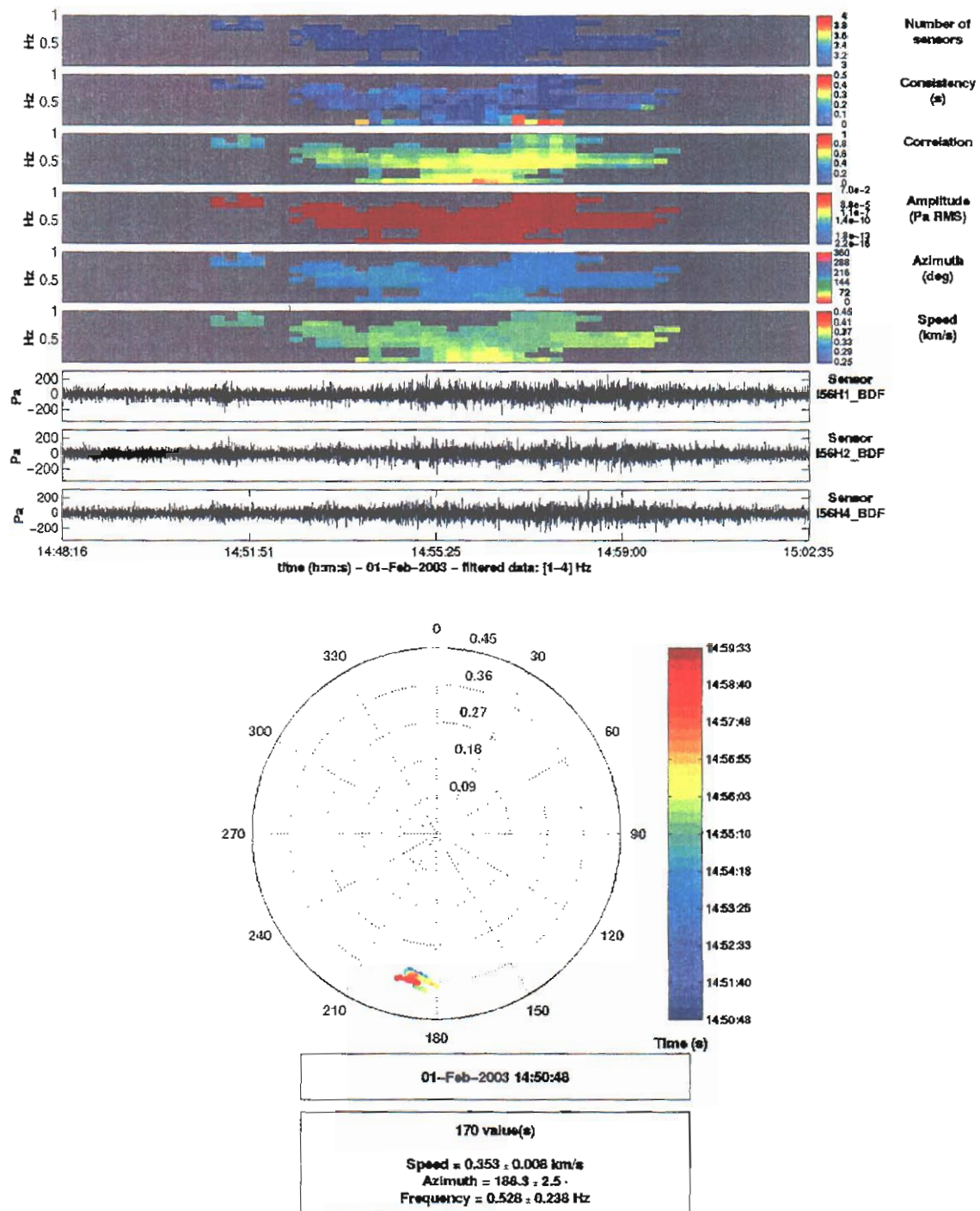
Figure 11. Main Columbia arrival at I56US. Frequency band of 0.1 – 1 Hz. Most of the energy appears concentrated at an azimuth of ~188 degrees.
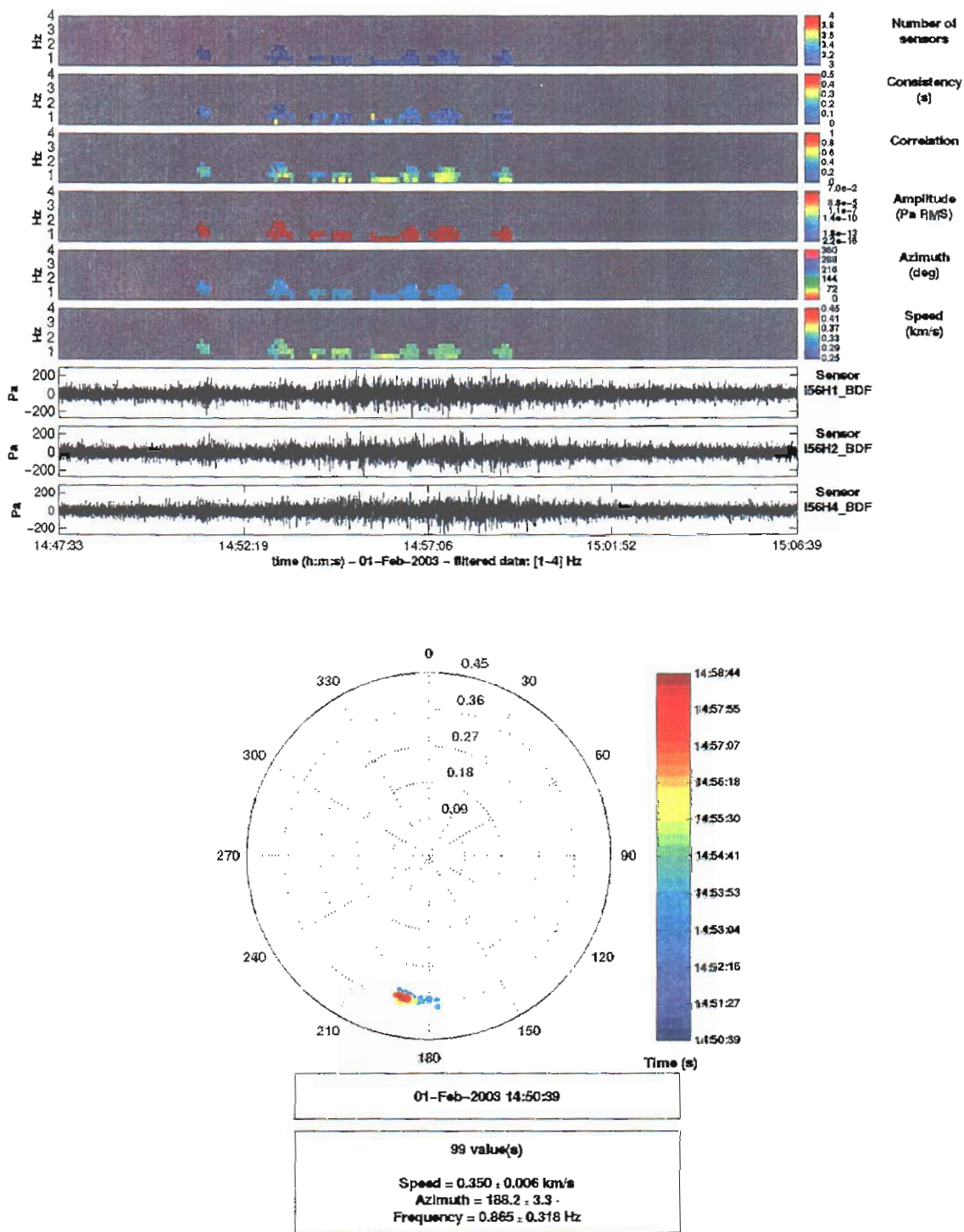
Figure 12. Main Columbia arrival at I56US. Frequency band of 0.5-4 Hz. There is not much energy above 2 Hz.
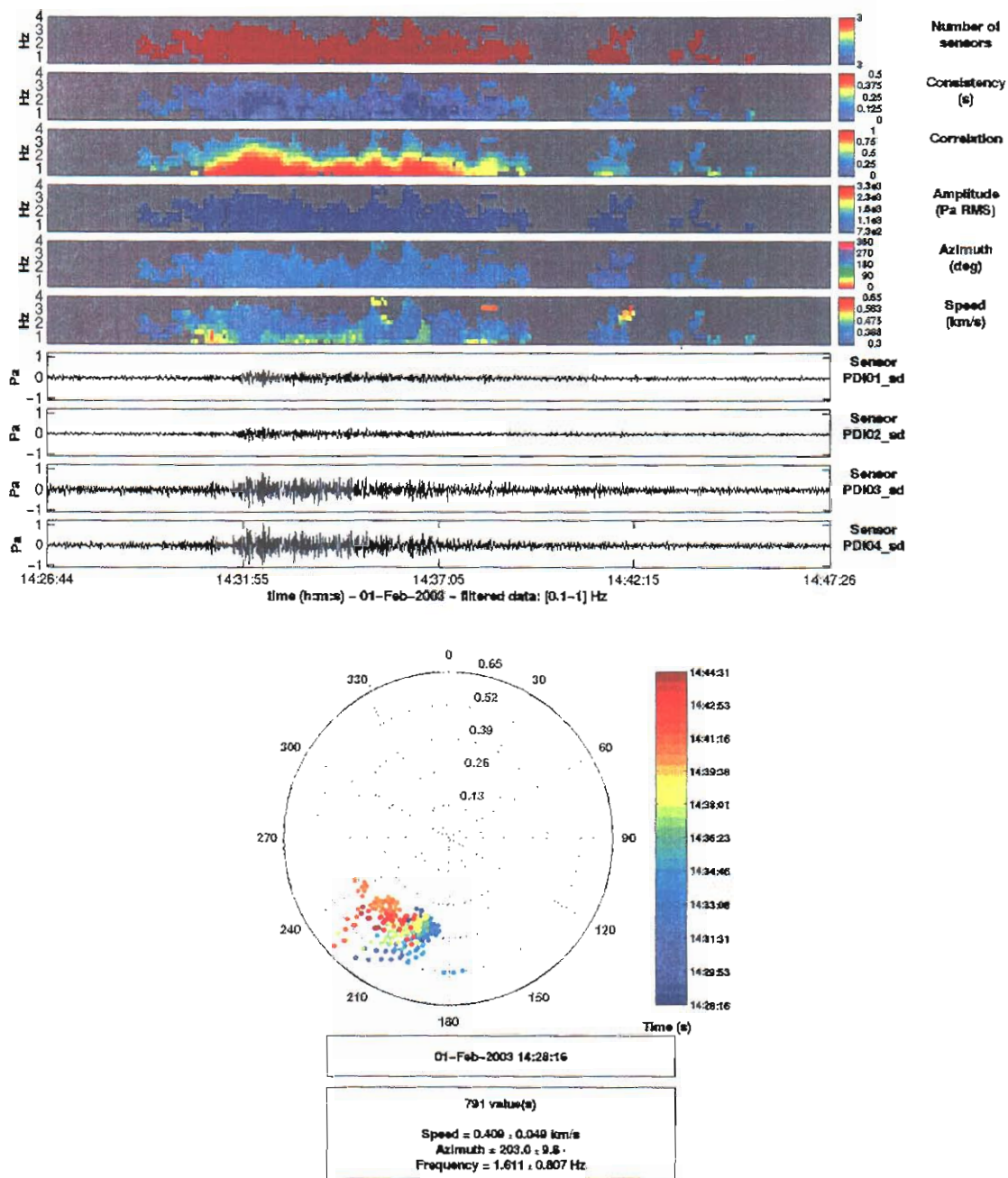
Figure 13. Main Columbia arrival at PDIAR. Frequency band of 0.5–4 Hz. Most of the energy in the main arrival appears concentrated at an azimuth of ~200 degrees, with energy in the coda appearing progressively more to the west.
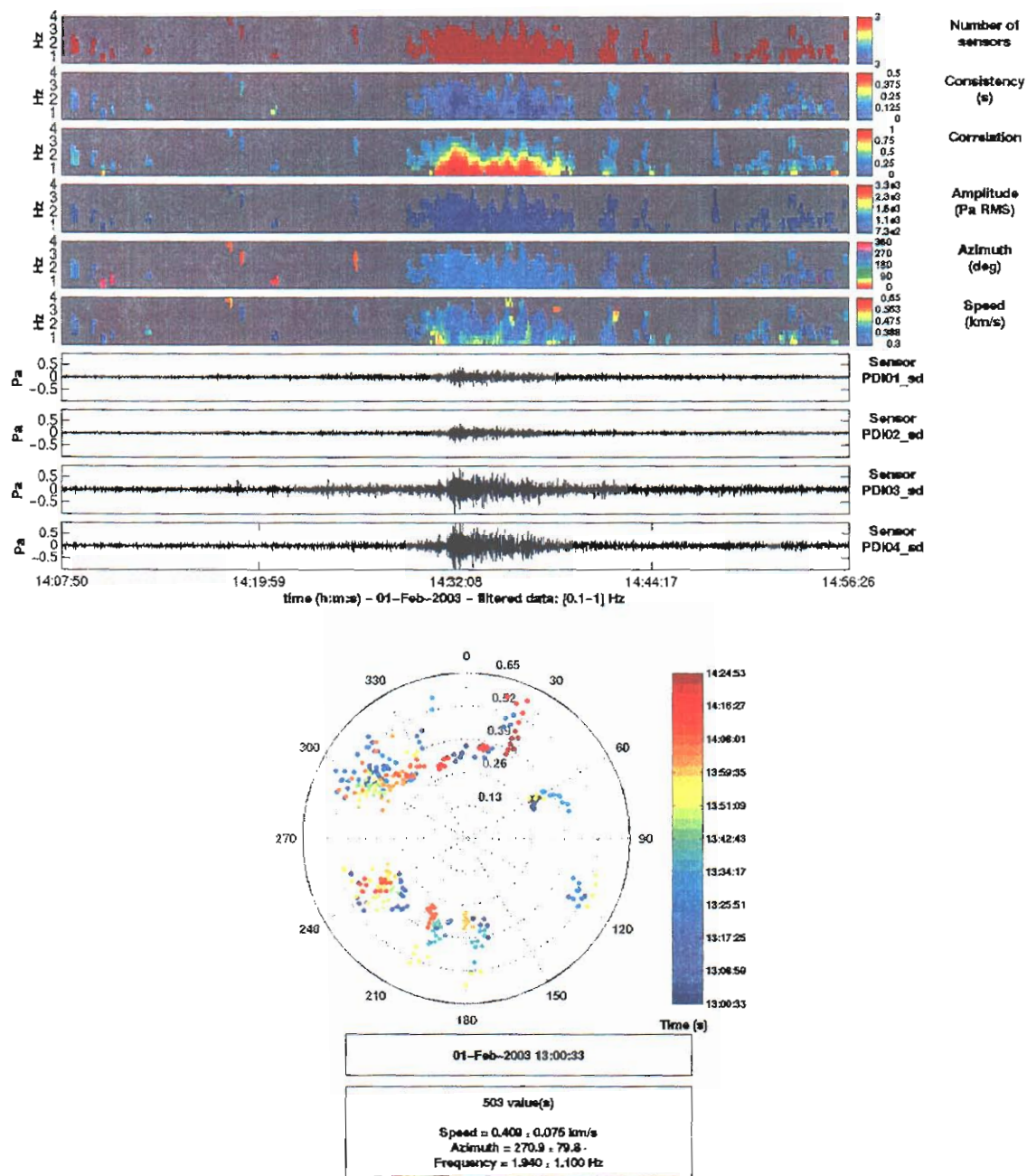
Figure 14. Background noise immediately preceding Columbia arrival at PDIAR. Note the difference in appearance between the arrivals preceding and following the main arrival. Polar diagram depicts the noise field for 90 minutes immediately preceding the main Columbia arrival.
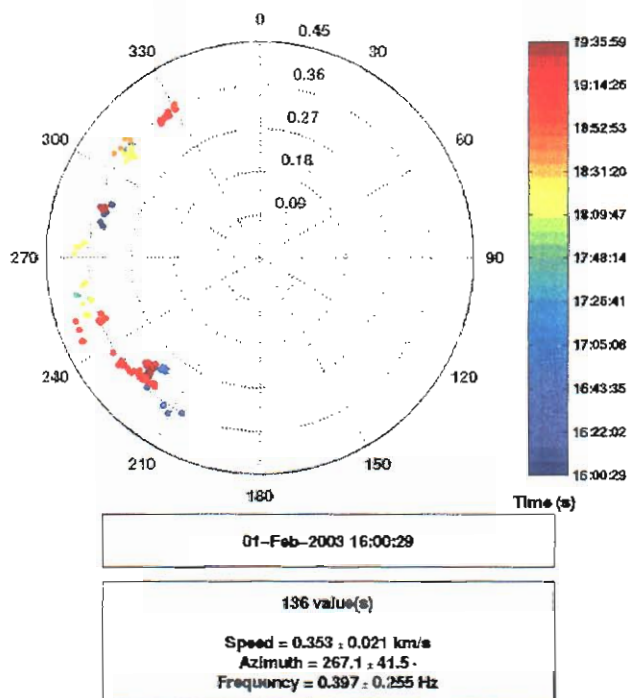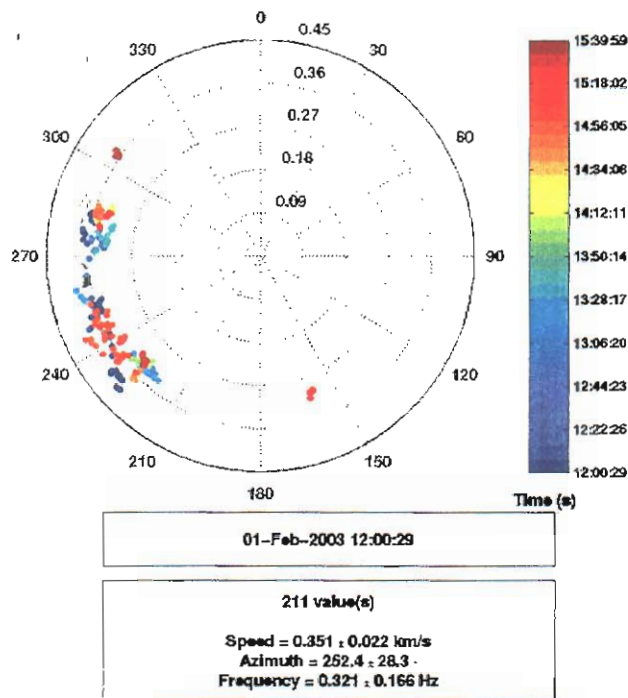
Figure 15. Detections for I59US in the 0.1-1 Hz band for the time period of 12 to 19:40 UT. There are no clear detections from the Columbia approach.
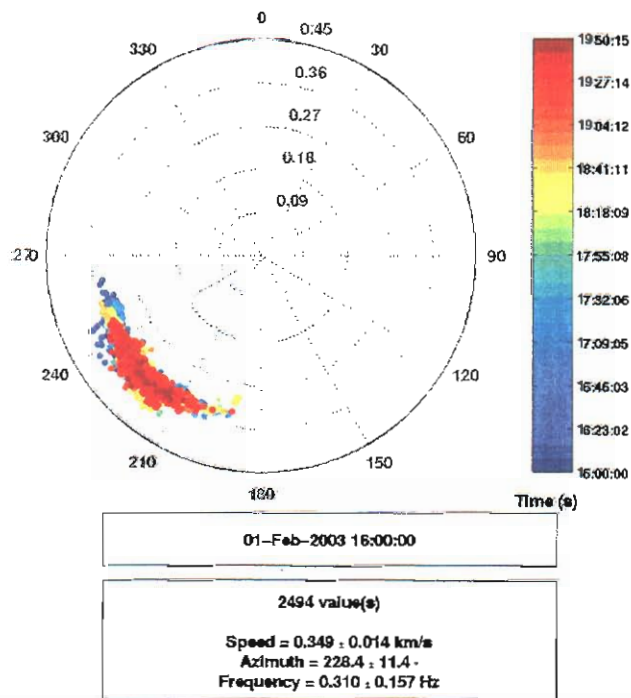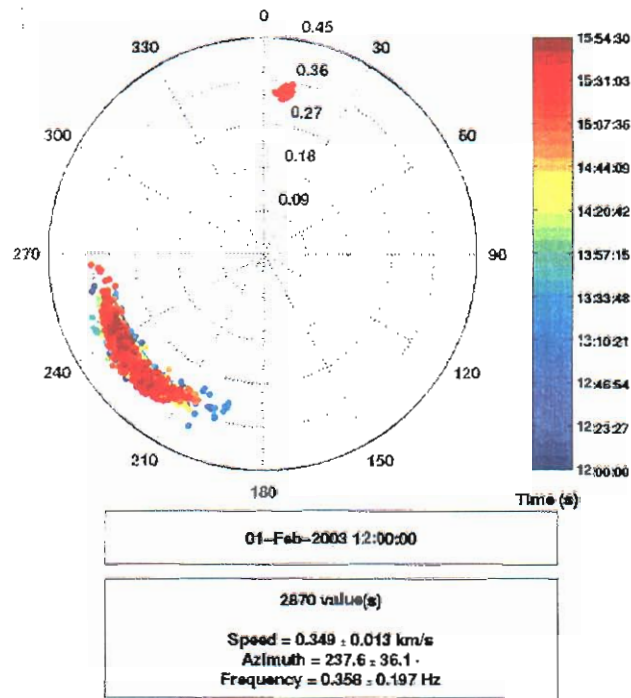
Figure 16. Detections for I53US in the 0.1-1 Hz band for the time period of 12 to 20:00 UT. There are no clear detections from the Columbia approach.

Infrasonic Arrivals from Columbia

Figure 17. Projected track, altitude, time GMT, and infrasonic detections for the Columbia reentry.

Timeline of Events Leading to Columbia Disaster
By Jim Banke
Senior Producer, Cape Canaveral Bureau
posted: 01:00 pm ET
04 February 2003

CAPE CANAVERAL, Fla. -- Here is a timeline of events, as released by NASA, that begins with the de-orbit burn and ends with the last understanding of telemetry received from Columbia. This information is expected to change from day to day as some facts are added, others adjusted.

Last updated as of 7 a.m. EST (1200 GMT) Tuesday, Feb. 4:

8:15:18 a.m. EST (1315.18 GMT) -- Columbia's twin orbital maneuvering engines, each capable of generating 6,000 pounds of thrust, were fired for two minutes and 38 seconds, slowing the shuttle by 176 mph. At the time it was over the Indian Ocean roughly 5,000 miles away from the Kennedy Space Center. Columbia's orbital path required only about 14 miles of crossrange flight toward the right.

8:43:53 a.m. EST (1343.53 GMT) -- Columbia reaches entry interface, the official point about 75 miles (120 km) high that NASA defines as the place where the vehicle first begins to encounter traces of Earth's atmosphere. It's at this time the vehicle begins to slow from orbital velocity of 17,500 mph (28,000 kph ~ 7.8 km/s) and the crew begins to feel the first tugs of gravity. Outside the first hints of re-entry heat start.

8:49:26 a.m. EST (1349.26 GMT) -- Because Columbia is a glider and has only one shot at landing, the shuttle enters the atmosphere with excess altitude and speed, or with too much "energy." To dissipate that energy so the shuttle doesn't overshoot the runway, the shuttle flies a couple of sweeping S-turns. The first of these starts now, with Columbia rolling onto its right wing at an angle of 23 degrees.

At this same time the shuttle's nose is up about 40 degrees, the crew have long since been strapped into their seats and the onboard computers are flying the re-entry profile with the help of inputs from sensors and other guidance and navigation equipment located all over the spaceplane.

8:51 a.m. EST (1351 GMT) -- Columbia crosses the California coast north of San Francisco and is seen on the ground.

8:52 a.m. EST (1352 GMT) -- The first indication that something is going wrong is recorded when three left main landing gear brake line temperature sensors detect a rise. The shuttle is flying over California.

1353 GMT -- Two more sensors in the left-hand wheel well (left brake line strut actuator and uplock actuator temperature sensors) detect an increase in temperature of 30 to 40 degrees Fahrenheit in five minutes. At the same time, four sensors near the elevon at the back of the wing failed off, suggesting their wiring was severed somewhere.

1354 GMT -- Sensors on the outside wall of Columbia's fuselage above the left wing shows a 60-degree rise in temperature in five minutes, while the sensors on the right side showed a more normal 15-degree rise – an indication that a significant heating problem was taking place on the left side. Temperatures inside the cargo bay are normal. The shuttle was over eastern California and western Nevada.

1355 GMT -- Another main gear brake line temperature sensor shows an unusual temperature rise.

1357 GMT -- Two sensors on the left wing's upper and lower skin failed off. The shuttle is flying over Arizona and New Mexico.

1358 GMT -- The elevon flaps on the left wing began moving to steer the shuttle on course after computers detected the shuttle was beginning to fly off course due to increased drag on the left wing. At the same time, wheel well sensors measuring temperature and pressure of the left main-landing gear failed. The shuttle is over New Mexico.

1359 GMT -- Two of Columbia's nose steering jets automatically fired for 1.5 seconds to help the shuttle counteract the rapidly increasing drag on the left wing. The shuttle is over west Texas.

1359.22 GMT -- Loss of signal happened at 15 days, 22 hours, 20 minutes and 22 seconds after launch. Columbia was 207,000 feet (62.7 km) high and moving 18 times the speed of sound, or more than 12,000 mph (19,200 kph ~ 5.3 km/s)

Appendix B. Seven large subsonic explosions detected from shuttle

http://abclocal.go.com/ktrk/news/20403_nat_infrasoundblast.html

By The Associated Press

(2/04/03- DALLAS) — Seven large subsonic explosions erupted the shuttle Columbia as it broke apart above Texas, according to data from a university's high-tech listening post.

The blasts, although below the level of human hearing, were detected and relayed to Southern Methodist University researchers Saturday morning from an array of very-low-frequency sound detectors near Big Bend National Park.

Professor Eugene Herrin said Monday that the instrument array's detection of the explosions coincided with breakup of the shuttle, which was 39 miles over Texas and experiencing maximum re-entry heat of 3,000 degrees at the time.

"Over a period of about six minutes, it picked up seven fairly large explosions and we are able, since we have four detectors, to determine the azimuth of the explosions," said Herrin, who directs SMU's geophysical laboratory. *"We found the explosions from west of Wichita Falls to east of Dallas."*

The data from the seismic array northwest of Terlingua, operated by SMU for the Air Force, was relayed by satellite to Dallas and surprised researchers, said Herrin.

"We conclude, and I think there is no other conclusion, that these were explosions on the shuttle and that it was coming apart, perhaps beginning in eastern New Mexico," he said. "We cannot see it come apart but we can see explosions as a result of it coming apart."

All seven astronauts perished. Searchers recovered thousands of debris fragments and some body parts as separate NASA and independent investigations began. Sounds at very low frequencies, also called infrasound, travel hundreds of miles while higher-pitched noises are absorbed by the atmosphere, said Herrin. He said the shuttle explosions were like blasts detected from some meteors as they burn up and explode after entering the earth's atmosphere.

"We see very few explosions in the atmosphere of that size," said Herrin, "and we've never before seen seven in a row."

The shuttle's normal signature, which includes periodic sonic booms, was detected by another infrasound station operated by SMU near Carson City, Nev., and a listening post at Los Alamos National Laboratory in New Mexico.

Very low frequency sounds range from one-half to four Hertz, the basic unit of frequency, Herrin said. He said the best stereo sound systems reproduce sound down to 20 Hertz.

The SMU data was posted on the Web, where seismologist Petru Negraru was shown analyzing the infrasound signals with Herrin. Negraru declined to comment on the research Monday to The Associated Press.Herrin said researchers are analyzing the data in cooperation with the Air

Force, but some results may be classified."We are analyzing the data and trying to quantify the yield of these explosions in (comparison to) tons of high explosive," he said.

Appendix C

<u>Infrasonic Investigations of the Columbia Re-Entry</u>
<u>Part 2. Preliminary analysis of arriving phases associated with the Columbia Disaster of February 1, 2003</u>

<u>February 10, 2003</u>
<u>Revision 1</u>

Milton Garcés and Claus Hetzer
Infrasound Laboratory, University of Hawaii, Manoa
Douglas Drob
Naval Research Laboratory

1. Introduction

The aim of this manuscript is to characterize infrasonic arrivals associated with the Columbia disaster. We use the tau-p method of Garcés et al. (1998, 2002) to compute estimates of the apparent propagation speed and azimuth deviation of propagating phases. For the propagation medium we use the Naval Research Laboratory (NRL) near real time Ground to Space (GTS) climatological specification (GTS RT V0.5) which are automatically transferred to the Infrasound Laboratory (ISLA) data server. The GTS files provide wind vectors and sound speed in a global grid. Figure 1 shows a graphical summary of the infrasonic detections discussed in Revision 4 of Garcés et al. (2003).

2. Ray Tracing Method Overview

Although ray tracing should be restricted to high-frequency interpretations, we find rays to be of value for rapidly estimating travel times and azimuth deviations for propagating phases. The results presented in this manuscript are preliminary and could be used as starting points for more sophisticated and precise propagation models. To provide our initial propagation estimates, we use ISLA's Tau9.1 ray tracing software (Garcés et al., 2002a,b) to read the NRL GTS global grid for 12 UT of February 1, 2003.

Figure 2 shows the zonal wind speed along the great circle route roughly corresponding to the shuttle reentry route between the first and last points of infrasonic detection. Figure 3 shows the meridional winds and Figure 4 shows the sound speed for the same great circle path. To look at possible multipath propagation, atmospheric profiles were extracted at each array location from the global grid to estimate the celerity (X/T) and azimuth deviation for a single skip of a predicted arrival. Since in a range independent environment these two parameters do not change with the number of skips, we find them useful for initial assessments of the propagating phases that can be observed at an array. Although there is a range-dependent version of Tau9.1, we defer that work to future revisions of this document.

3. Observations

Below are tabulated distinct arrivals observed at each array, with the exception of TXIAR, whose arrivals are determined from a figure and a press release (Garcés et al., 2003). The arrival time is taken from the PMCC arrivals of *Part 1*, the track time is taken from the CMR distribution of the shuttle trajectory and corresponds to the closest point to the backazimuth intercept in Figure 1, dt is the time difference between the first two columns, BAZ is the observed PMCC backazimuth measured clockwise from North, the speed is the observed apparent horizontal phase speed computed by PMCC, the slowness is the inverse of the speed, the range corresponds to the track time, and the celerity is ratio of the range and dt.

Station	Arrival Time	Track Time	dt (s)	Baz (deg)	Speed (m/s)	p (s/km)	Range (km)	Celerity (km/s)
I56US	14:51:08	13:54:02	3426	187.7	344	2.907	1130.5	0.3300
I56US	14:52:37	13:54:02	3515	188.3	353	2.833	1130.5	0.3216
DLIAR	14:02:08	13:57:33	275	207	456	2.193		
I10CA (1)	15:25:09	13:58:12	5217	203.4	431	2.320	1871.5	0.3587
I10CA (1)	15:29:24	13:58:12	5472	202.7	490	2.041	1871.5	0.3420
I10CA (1)	15:32:09	13:58:12	5637	204.5	477	2.096	1871.5	0.3320
I10CA (2)	15:41:09	13:58:50	6139	195.4	515	1.942	1895.3	0.3087
I10CA (2)	15:43:08	13:58:50	6258	198.4	473	2.114	1895.3	0.3029
I10CA (2)	15:45:54	13:58:50	6424	191	529	1.890	1895.3	0.2950
I57US (2)	14:23:27	13:55:00	1707	7.5	342	2.924	467.29	0.2737
I57US (2)	14:24:52	13:55:00	1792	10.4	343	2.915	467.29	0.2608
I57US (2)	14:27:37	13:55:00	1957	5.9	330	3.030	467.29	0.2388
I57US (1)	14:29:37	13:54:02	2135	341.3	362	2.762	668.15	0.3130
I57US (1)	14:31:13	13:54:02	2231	337.2	358	2.793	668.15	0.2995
I57US (1)	14:42:42	13:54:02	2920	336.7	259	3.861	668.15	0.2288
SGAR	13:59:40	13:55:38	242	9.8	714	1.401		
TXIAR (1)	14:28	13:59:28	1712				582.7	0.3404
TXIAR (2)	14:40	14:00:02	2398				705.4	0.2942
NVIAR	13:58:25	13:54:40	225					

4. Predicted Arrivals

In this document, a positive azimuth deviation corresponds to a angle correction at the array to the right of the arrival backazimuth.

4.1. Direct Arrivals

The waveforms observed at NVIAR, SGAR, and DLIAR appear like typical N-waves and may be associated with the bow wave of the shuttle passing within ~30 km of the arrays. Figures 5-7 provide travel time curves for the direct ray at each of the three arrays, respectively, and shows that the ray tracing results are consistent with the observed delay times. With an interpolated trajectory it would be possible to obtain a better estimate of the ray launch time corresponding to the observed azimuth to compute a more precise estimate of range for each array.

4.2. Multipath Arrivals

Arrivals at all the other arrays probably correspond to multiply reflected and refracted rays. Along its flight of the Continental US, the shuttle kept a height of 60-70 km. This height would effectively deposit energy onto elevated waveguides in the stratosphere and thermosphere. The lower part of these waveguides may leak energy into the ground through scattering and diffraction. Although scattering and diffraction are not incorporated into Tau9.1, it is still possible to estimate the celerity and azimuth deviation of phases trapped in these waveguides. We only consider phases where the bottom of the waveguide either reaches the ground or is less than 10 km from the ground. Table 2, taken from Garcés et al. (2002b) reviews the phase nomenclature used in this document. Although apparent horizontal phase speed estimates obtained from array processing are used in the identification of phases, we believe the celerity is a more robust parameter for phase ID.

Table 2. Preliminary phase identification nomenclature for long-range infrasonic propagation

Phase ID	Description	Typical celerity of first arrival, m/s
iw	Guided wave propagating between the tropopause and the ground.	330-340
is	Guided wave propagating between the stratopause and the ground.	310-330
isd	Guided wave propagating in elevated waveguide between stratopause and the troposphere, and diffracted or scattered to the ground. May have higher frequency.	310-330
it	Guided wave propagating between the lower thermosphere and the ground.	280-300
itd	Guided wave propagating in elevated waveguide between the lower thermosphere and the troposphere, and diffracted or scattered to the ground.	280-300
It, Is, Iw	Direct arrival from the source to the receiver. May have high apparent phase velocity	N/A

4.2.1. I56US, Washington

Figures 8 and 9 show the celerity and azimuth deviation for the predicted phases. Although energy ducted in the troposphere is vulnerable to topography and regional effects, we assign an azimuth deviation of ~+3 degrees to these arrivals.

4.2.2. I10CA, Canada

For an arrival azimuth of 203 degrees, Figures 10 and 11 show the existence of a very tenuous tropospheric phase with a very small azimuth deviation. We use the *iw* phase ID with some reservations – no other phase appears to explain the fast arrival. For an arrival azimuth of 194 degrees, Figures 12 and 13 show the stratospheric arrivals with an azimuth deviation of ~ +5 degrees would be consistent with the observed celerities.

4.2.3. I57US, California

As shown on Figures 14 and 15, for an incidence azimuth of 339 degrees *isd* phases with an azimuth correction of ~-2.5 degrees would match the fastest celerities, and the slowest celerity would be an *it* phase with an azimuth correction of ~-5 degrees. For an incidence azimuth of 7 degrees (Figures 16 and 17), the *itd* phases with an azimuth correction of ~ –4.5 degrees would yield the fastest celerities, and the slowest celerity would correspond to an *it* phase with an azimuth correction of ~ –5 degrees.

4.2.4. TXIAR, Texas

At the time of this writing, we do not have access to infrasound data from this array and thus do not feel we can perform travel time analysis. If indeed the first arrival azimuths are as stated in Table 1, then the first arrivals at TXIAR are propagating very fast.

5. Concluding Remarks

With the exception of NVIAR, SGAR, and DLIAR, who appear to have recorded a direct arrival, all other stations considered in this manuscript appear to have observed multiple arrivals corresponding to propagation in different layers of the atmosphere. We used atmospheric specifications for February 1, 2003 at 12 UT to perform azimuth corrections based on tentative phase identifications. The largest azimuth correction we performed was ~5 degrees, and placed the first observed energy just West of the California-Nevada border.

In terms of infrasound forensics, the signal captured by I56 and I57 that points to the California-Nevada border seems to be the most pertinent of this document, as the main arrival at I57 and the detections at I10 appear to correspond to multipath propagation from Columbia's Mach cylinder. However, it could be argued that the arrival at I56 was also generated by the Mach cylinder, so the interesting question is: why did I57 capture an arrival from this location?

We hope that a future revision of this document will include TXIAR data and any other relevant information that might shed some light on the nature of this tragedy.

6. Works Cited

Garcés, M., C. Hetzer, M. Hedlin, and H. Bass (2003). *Part 1. Preliminary analysis of infrasound data associated with the Columbia disaster of February 1, 2003.* Release 4, February 10, 2003, Internal document of the US Infrasound Group.

Garcés, M, C. Hetzer, D. Drob, R. Woodward, H. Bass, D. McCormack, L. Evers, M. Hedlin, A. LePichon, L. Liszka, C. Wilson, R. Whitaker (2002a). *Progress in the development of a ground truth database of infrasonic events.* Infrasound Technology Workshop, De Bilt, Netherlands, October 28-31, 2002. CD with Tau9.1 distributed to workshop attendees.

Garcés, M., C. Hetzer, K. Lindquist, and D. Drob. *Source Location Algorithm for Infrasonic Monitoring* (2002b). 24[rt] Annual DTRA/NNSA Seismic Research Review, Ponte Vedra, FL, 17-19 September 2002.

Garcés, M. A., R. A. Hansen, K. Lindquist (1998). *Travel times for infrasonic waves propagating in a stratified atmosphere.* Geophys. J. International, 135, 255-263.
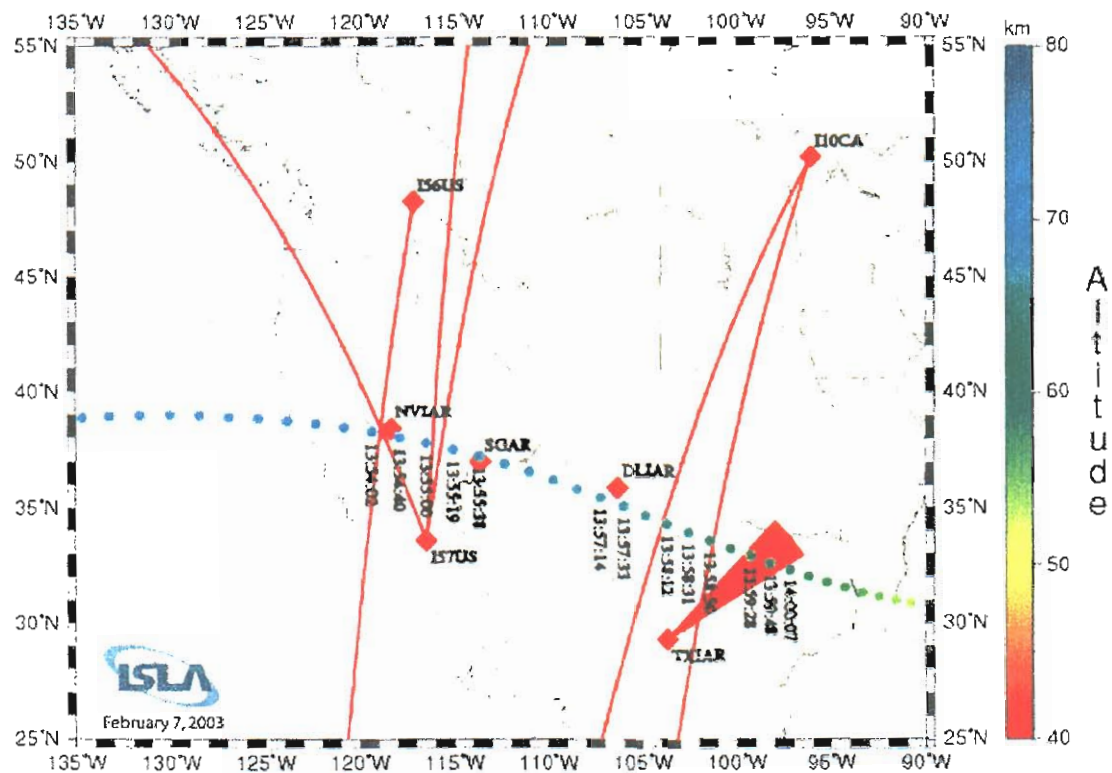
Figure 1. Spacecraft altitude, time GMT, and infrasonic detections for the Columbia reentry.
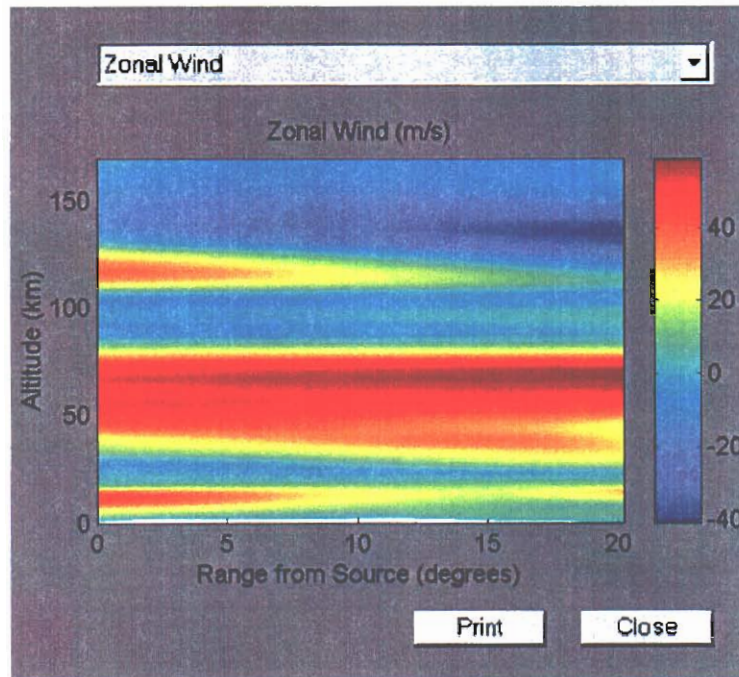
Figure 2. Zonal wind speed along the great circle path from 38.465 N, 120.822 W to 32.351 N, 97.179 W at 12 GMT. Positive speed is towards the East. This path roughly corresponds to the Columbia approach between the first and last detections shown in Figure 1.
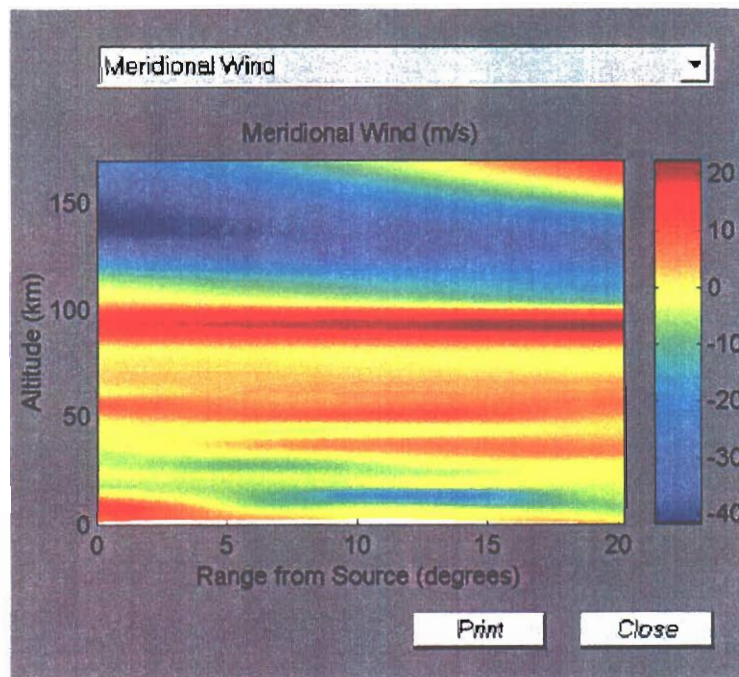
Figure 3. Meridional wind speed along the great circle path from 38.465 N, 120.822 W to 32.351 N, 97.179 W at 12 GMT. Positive speed is towards the North.
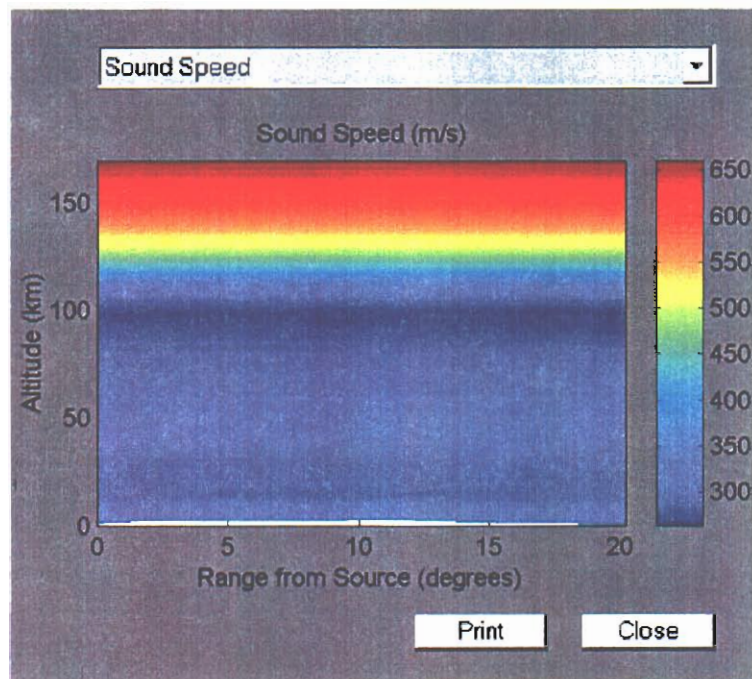
Figure 4. Sound speed along the great circle path from 38.465 N, 120.822 W to 32.351 N, 97.179 W at 12 GMT.
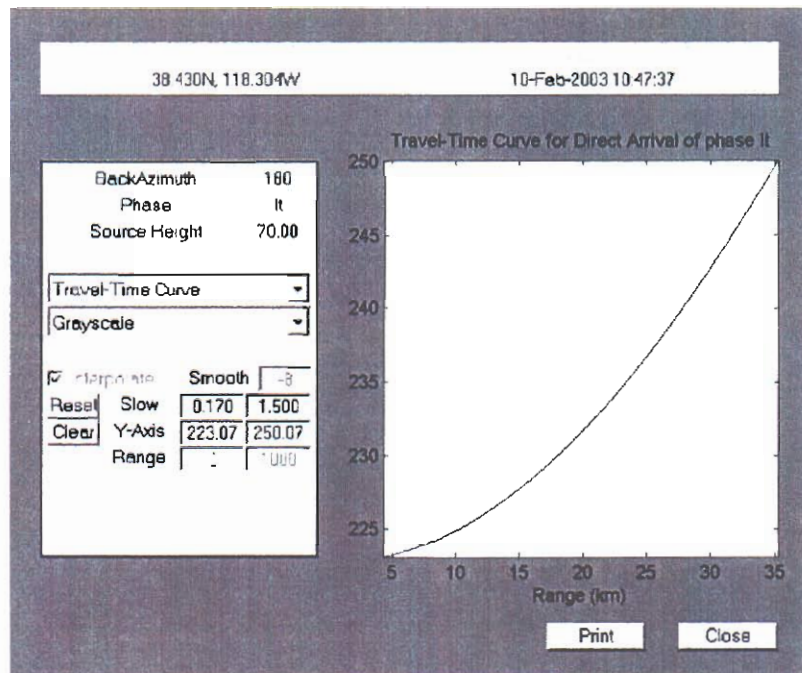
Figure 5. Travel time for the direct arrival at NVIAR for a source south of the array at a height of 70 km.
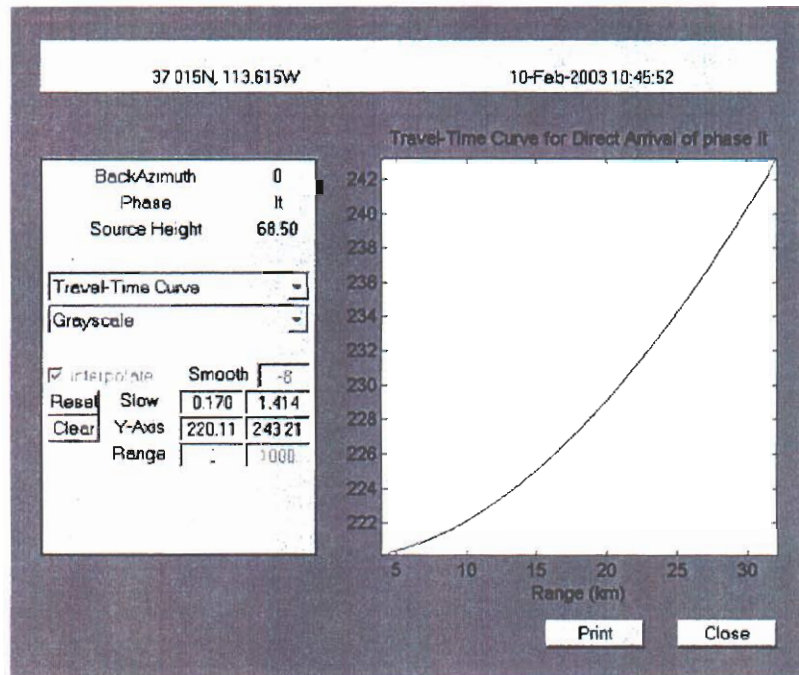
Figure 6. Travel time for the direct arrival at SGAR for a source north of the array at a height of 68.5 km.
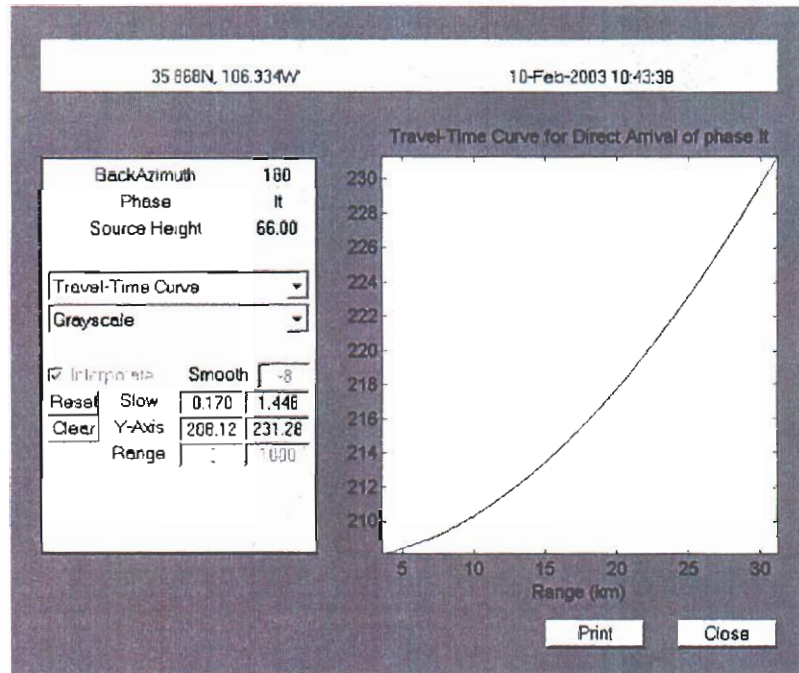
Figure 7. Travel time for the direct arrival at DLIAR for a source south of the array at a height of 66 km.
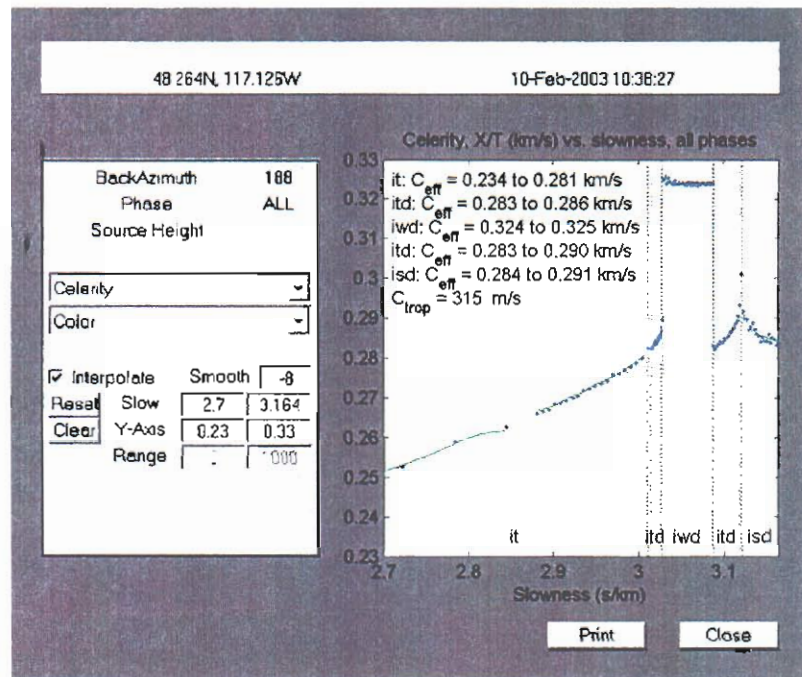
Figure 8. Predicted celerity for arrivals at I56US with an azimuth of 188 degrees. Note the presence of a tropospheric duct, which may yield the observed celerities.
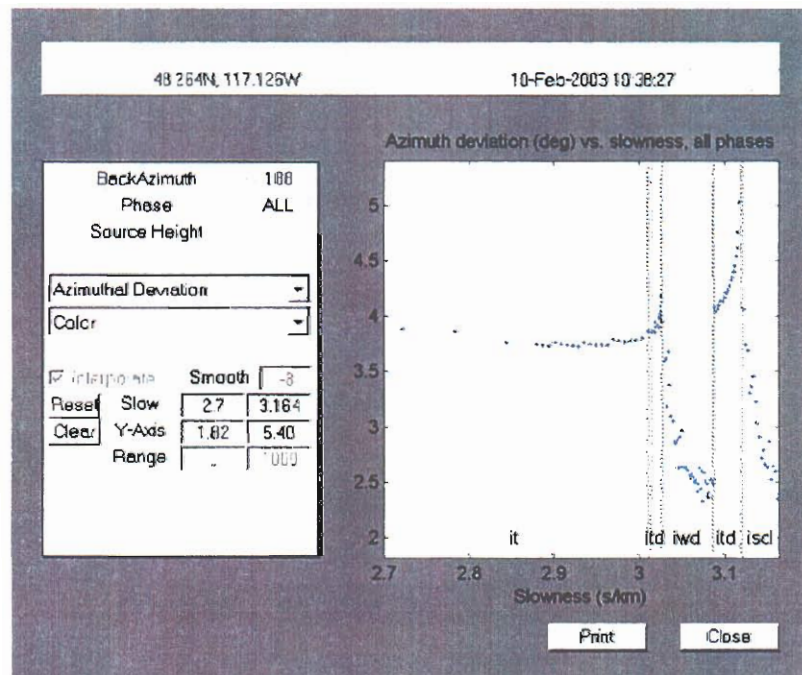
Figure 9. Predicted azimuth deviations for arrivals at I56US with an azimuth of 188 degrees. For the tropospheric phases, we pick a mean azimuth deviation of 3 degrees.
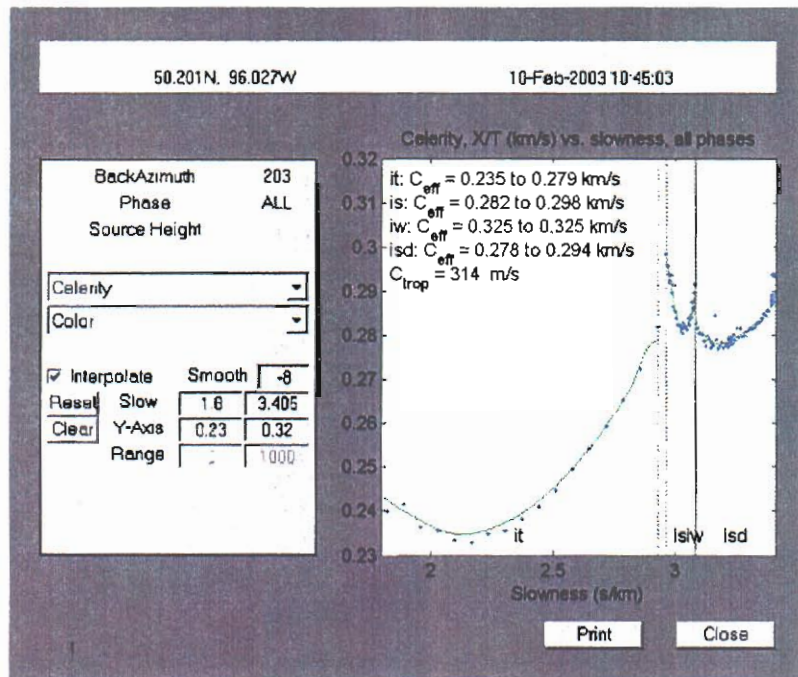
Figure 10. Predicted celerity for arrivals at I10CA with an azimuth of 203 degrees. Note the presence of a very small tropospheric duct, which would be consistent with observed celerities. However, for long range propagation such ducts may not be stable.
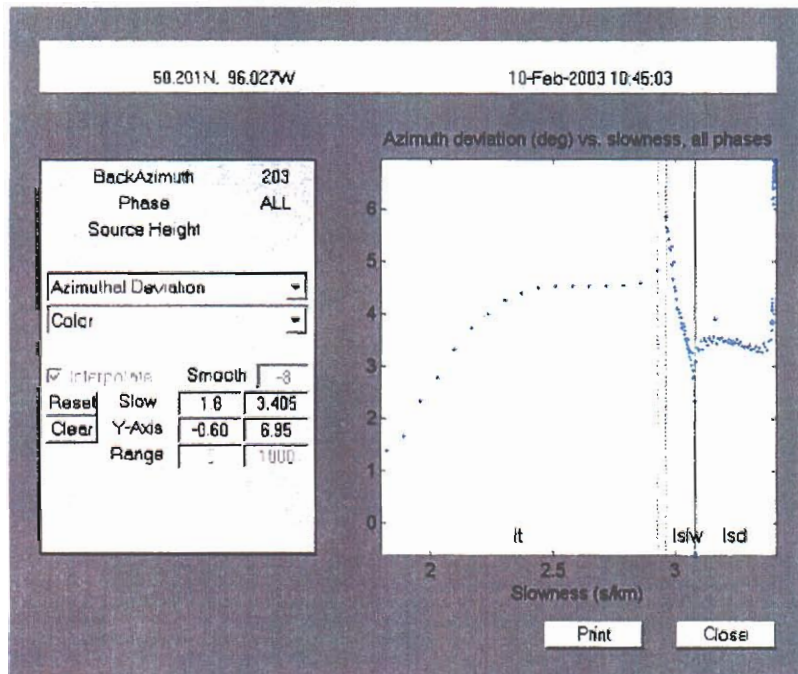
Figure 11. Predicted azimuth deviation for arrivals at I10CA with an azimuth of 203 degrees. The tropospheric phase shows a small azimuth deviation.
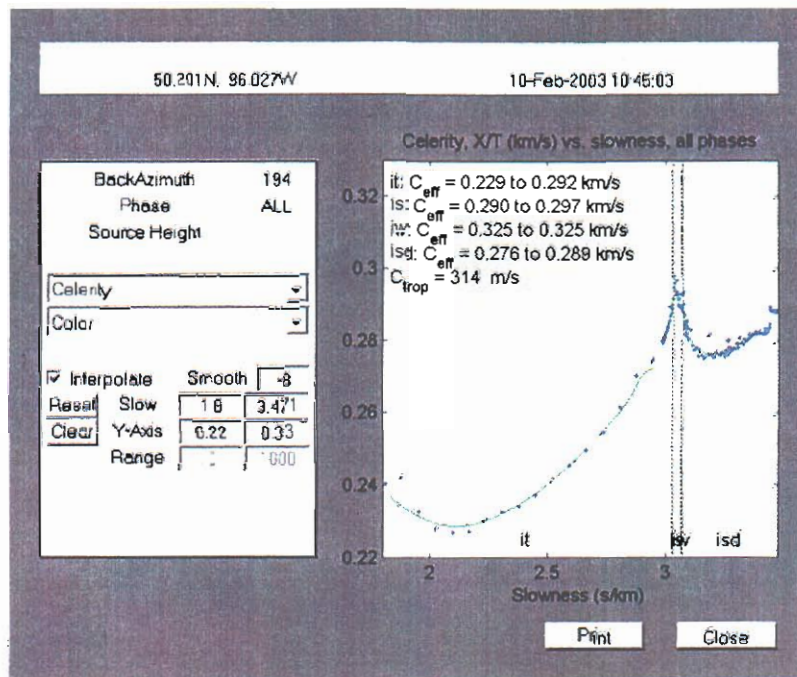
Figure 12. Predicted celerity for arrivals at I10CA with an azimuth of 194 degrees. Stratospheric phases would be consistent with observed celerities.
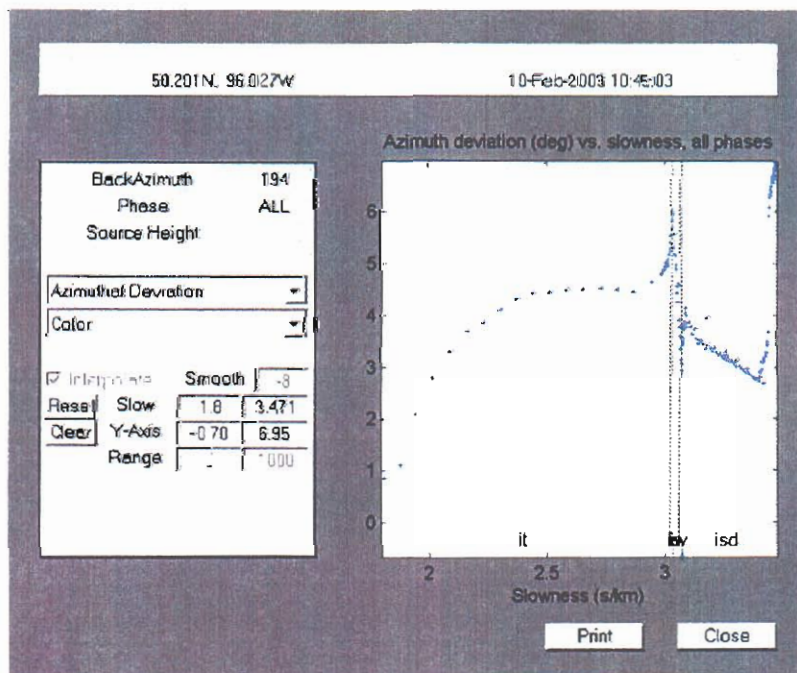
Figure 13. Predicted azimuth deviations for arrivals at I10CA with an azimuth of 194 degrees. For the stratospheric phases, we pick a mean azimuth deviation of 5 degrees.
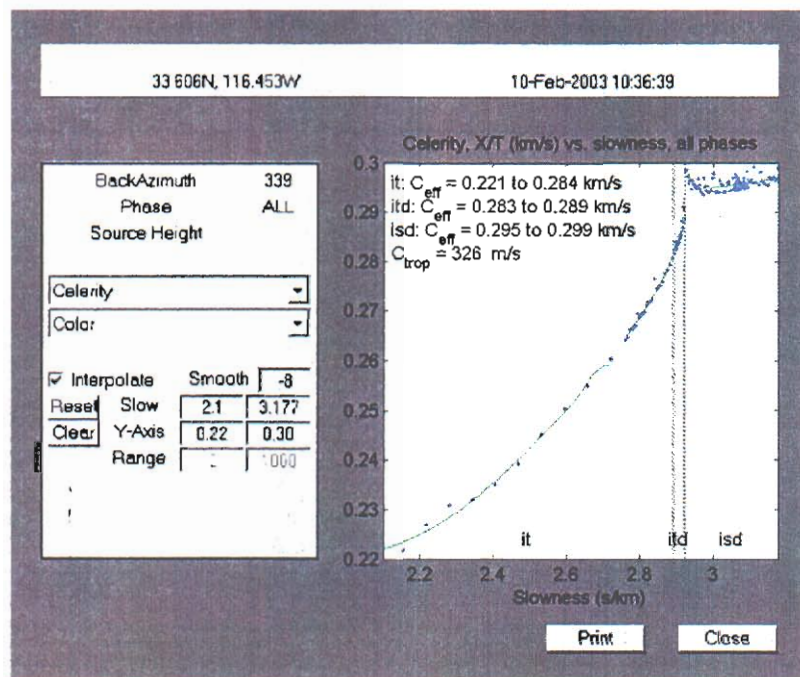
Figure 14. Predicted celerity for arrivals at I57US with an azimuth of 339 degrees. The *isd* phases are the closest to the fastest celerities, and the slowest celerity would be an *it* phase.
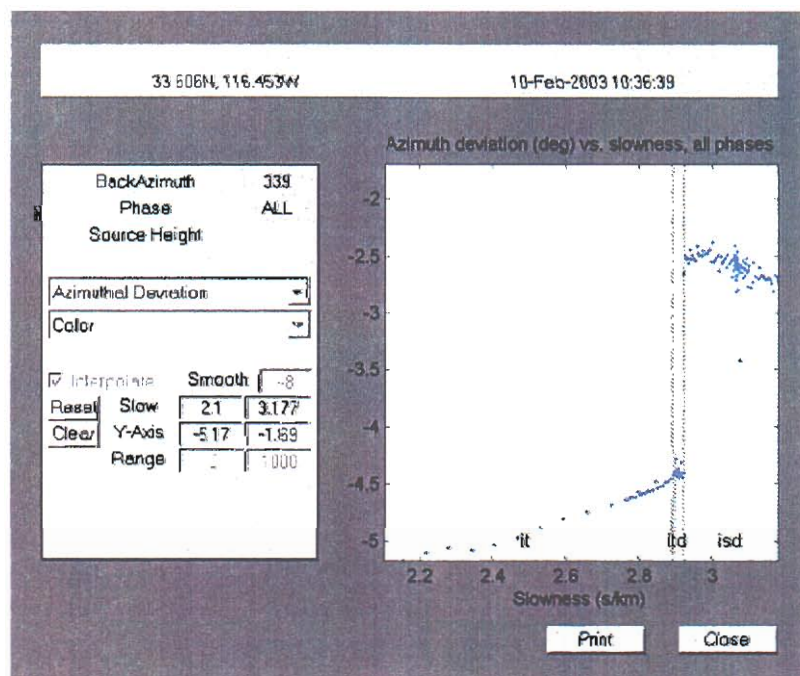
Figure 15. Predicted azimuth deviations for arrivals at I57US with an azimuth of 339 degrees. For the *isd* phases, we pick a mean azimuth deviation of –2.5 degrees, and for the *it* phase it would be –5 degrees.

120
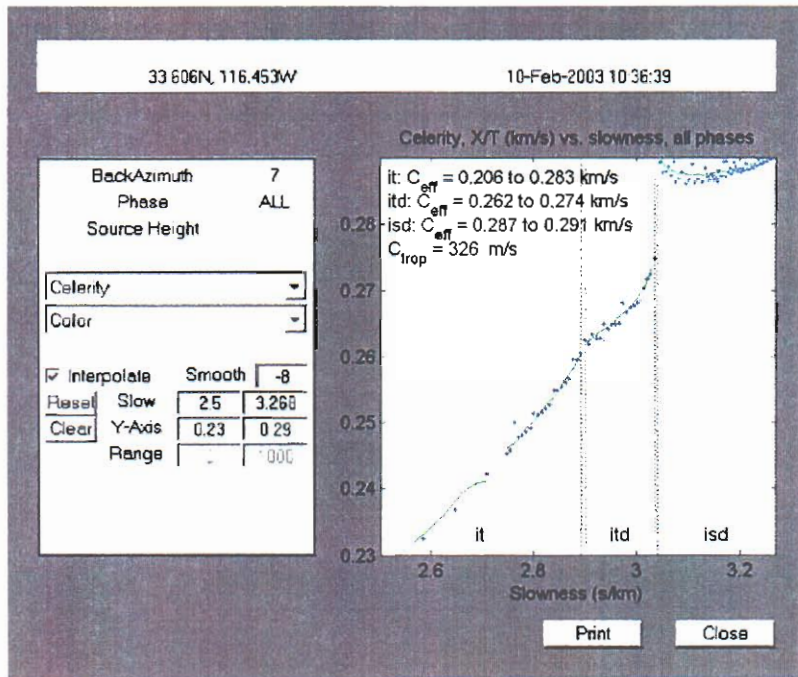
Figure 16. Predicted celerity for arrivals at I57US with an azimuth of 7 degrees. The *itd* phases are the closest to the fastest celerities, and the slowest celerity would be an *it* phase.
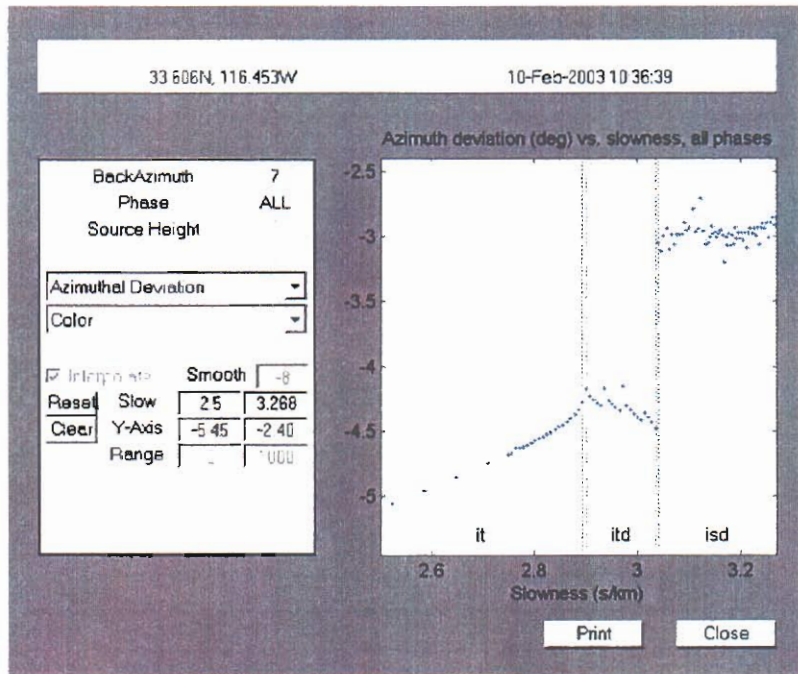
Figure 17. Predicted azimuth deviations for arrivals at I57US with an azimuth of 7 degrees. For the *itd* phases, we pick a mean azimuth deviation of –4.5 degrees, and for the *it* phase it would be –5 degrees.
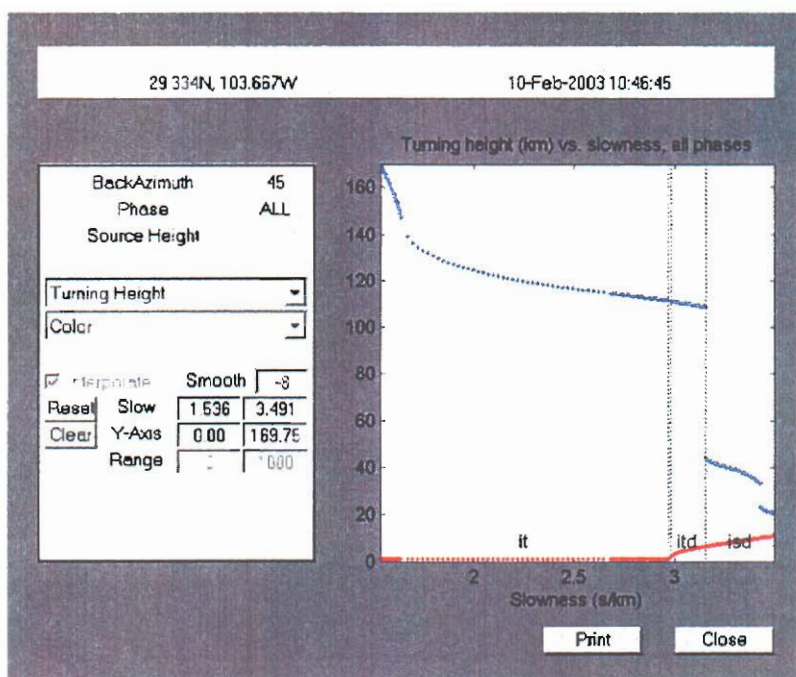
Figure 18. Waveguide boundaries for all propagating phases arriving at TXIAR from an azimuth of 45 degrees. Note from Figures 1 and 2 that the wind shear in the upper atmosphere increases as we approach Texas.
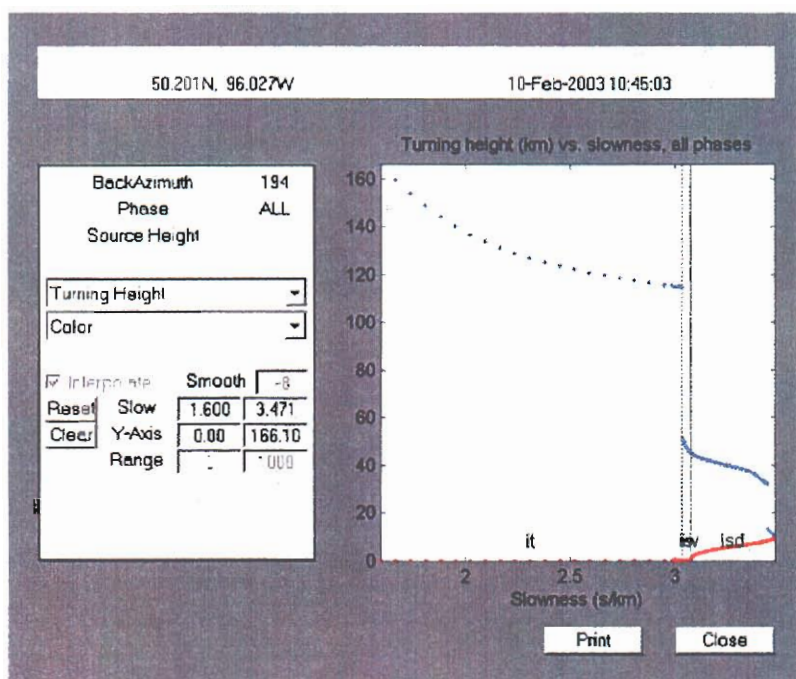
Figure 19. Waveguide boundaries for all propagating phases arriving at I10CA from an azimuth of 194 degrees. This figure is presented for comparison with the one above.
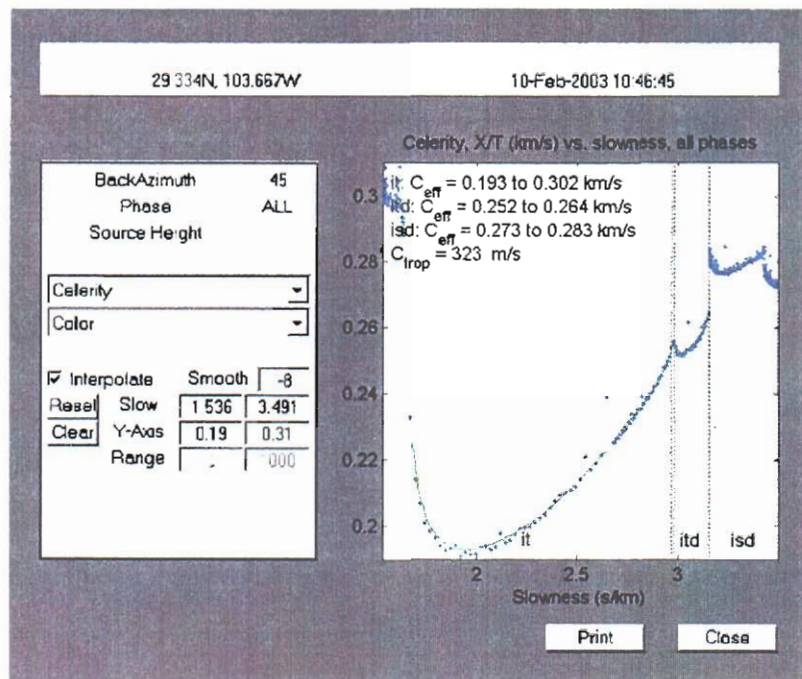
Figure 20. Predicted celerity for arrivals at TXIAR with an azimuth of 45 degrees. We do not feel we have sufficient information to use this station data, so this figure is placed here for future reference.
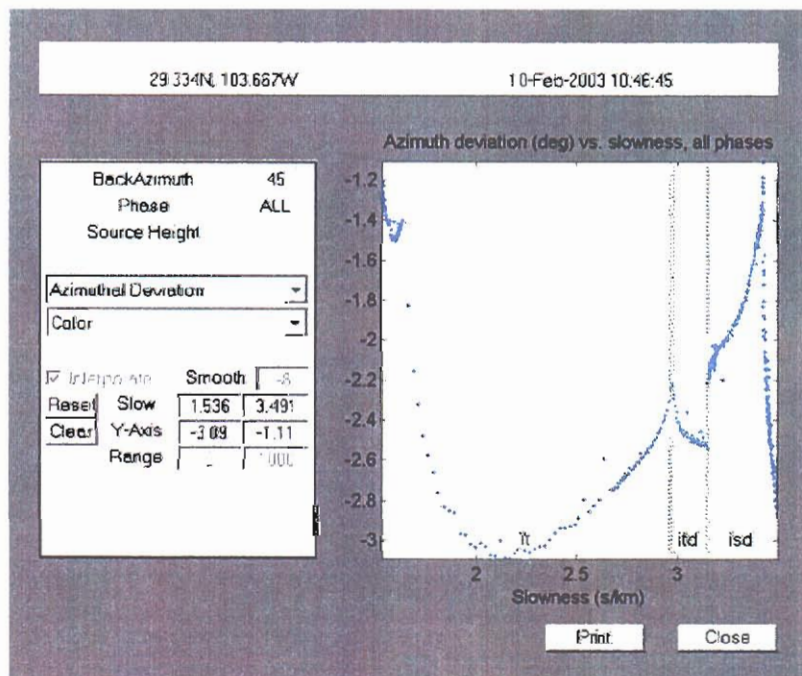
Figure 21. Predicted azimuth deviations for arrivals at at TXIAR with an azimuth of 45 degrees.

Infrasonic Arrivals from Columbia
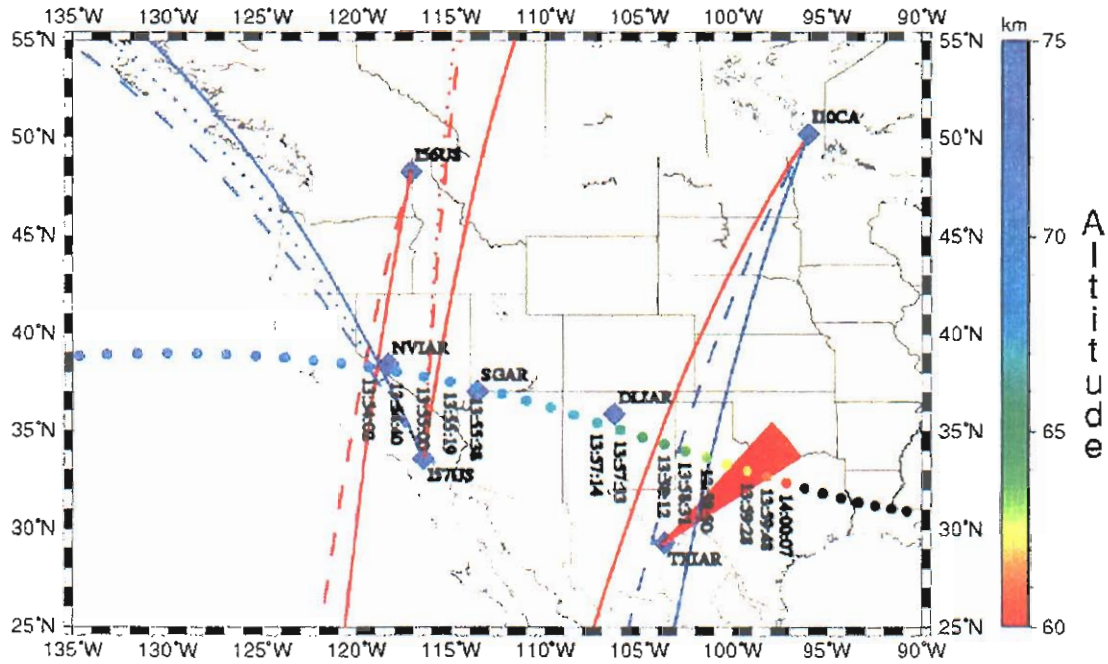
Figure 22. Revised map of observed arrivals, with corrected azimuths (dashed lines). For California, dotted lines are *it*, dashed are *itd/isd*. The shift in the azimuths brings the celerity estimates even closer to those of Table 1, with the exception of I10CA (dashed blue line), where the celerity decreases slightly.

Appendix D

Infrasonic Investigations of the Columbia Re-Entry
Part 3. The search for short energy bursts in the coda of infrasonic signals associated with the Columbia reentry

March 5, 2003
Revision 4

Milton Garcés and Claus Hetzer
Infrasound Laboratory, University of Hawaii, Manoa

1. Introduction

Part 1, Preliminary analysis of infrasound data associated with the Columbia disaster of February 1, 2003, Revision 5, released on February 11, 2003, ran detections on all available infrasound array data for (1) a window length of 30s, 25s overlap, and consistency of unity in the 0.5-4 Hz range and (2) a window length of 90s, 75s overlap, and consistency of unity in the 0.1-0.5 Hz range. At the suggestion of Al Bedard during a visit to the NOAA Labs on February 15, 2003, we initiated a more careful analysis of the coda following the first arrivals associated with the Columbia reentry. We used smaller time windows as well as overlap and consistency thresholds tailored for each array, and intended to look for brief bursts of energy associated with the approach path. The new results provide a more detailed description of the infrasonic fingerprint of the Columbia reentry. Figure 1 shows the detections provided in Revision 5 of Part 1, and Figures 12a and 12b shows the azimuth ranges obtained from the revised analysis presented herein.

2. Infrasonic Array Detections

All array detections were performed with PMCC. Some DSP and array processing was done with Matseis.

2.1.1. NVIAR, Nevada

The narrower window allows better resolution of brief bursts of infrasonic energy in the coda following the main arrival (Figure 2). The later arrivals have a lower apparent horizontal phase speed and the latest arrival points almost due West. Dropping the speed tolerance to 0.2 km/s did not improve the detections. The backazimuth ranges from 206.5 to 268 degrees.

2.1.2. I57US, California

The narrower window shows a clear progression Westward with increasing time (Figure 3a). The backazimuth ranges from 310.8 to 15 degrees, apparently extending the Westward range beyond the California coast. Figure 3b shows an abundance of coherent noise arriving from the 270-325 degree sector. This high pre-existing ambient noise field may preclude the identification of

Columbia signals with low signal to noise ratios arriving from that sector, and would certainly make waveform feature extraction quite challenging. Figure 4 shows the subarrays used for the PMCC detections. Following the approach of D'Spain et al. (2003) we tried different subarray configurations with the removal of the central element at L1, but the results were essentially unchanged from those presented herein.

2.1.3. I56US, Washington
Due to the large aperture of the array and the missing element, analysis of higher frequencies did not yield any additional information, presumably because higher frequency signals lose coherence along the relatively large aperture. This highlights the value of seven or eight element arrays over four element, large aperture arrays. The azimuth range is 180.5 to 194.6 degrees (see Part 1).

2.1.4. SGAR, Utah
The trail immediately following the main arrival appears incoherent across the array, but ~5 minutes afterwards there is an abundance of late-arriving energy. However, some of the arrivals in the coda point South of West, with is unexpected given the Columbia trajectory. This southwards diversion may be due to the effects of meriodional winds along the acoustic propagation path. Figure 5 shows the detections as well as the backazimuth range of 245 to 321 degrees for the coda. The first arrival is shown in the lower panel of Figure 5 as blue detections at ~9 degrees.

2.1.5. PDIAR, Wyoming
With the narrower window, much of the clear time progression observed with the 30s wider window processing is now absent (Figure 6). Some of the arrivals that used to come in at ~14:42 (Part 1, Figure 13) are not picked up by the shorter time windows. The backazimuth ranges from 184.3 to 220.7 degrees, narrower than for the wider window detections.

2.1.6. DLIAR, New Mexico
Two distinct energy bundles, arriving over five minutes apart, can be observed. Figure 7 shows the backazimuth ranges from 207.0 to 269.4 degrees. The large time difference between these two packets coming from similar azimuths (lower panels of Figure 7) makes them suspect, although time travel analysis (Part 4) suggests some of the last set of arrivals may correspond to energy launched from Arizona sector of the approach.

2.1.7. White Sands, New Mexico
Processing was restricted to frequencies below 5 Hz because of an abundance of ambient noise above that frequency. A clear Westward progression with increasing time can be seen in Figure 8 for the detections at the short-aperture (40 m) White Sands array. The azimuth ranges from 317.4 to 27.8 degrees. The multiple values of speed at each azimuth are puzzling, and can also be observed in the InfraTool analysis (Figure 9).

2.1.8. TXIAR, Texas
Multiple arrivals were observed at TXIAR (Figure 10) corresponding to the approach and violent unscheduled disassembly of the Columbia. As can be inferred by the range of times and apparent

horizontal phase speeds, many of the arrivals may be associated with multipath propagation. The azimuth ranges from 333.1 to 25.6 degrees.

2.1.9. IS10CA, Canada

As in I56US, due to the large aperture of the array and the relatively long range, analysis of higher frequencies did not yield any additional information. The azimuth range is 186.4 to 222.7 degrees (see Part 1), with the backazimuth tracking *Eastwards* with increasing time. This trend is the reverse of all the other stations.

2.1.10. I59US, Hawaii

No clear detections associated with the Columbia were observed in Hawaii with smaller window lengths. A variety of window lengths and passbands were tried. One reason for the null detection (Figure 11) may be the relatively large aperture of the array. A second reason may be hinted by the pattern of microbaron detections at I59US, which suggests possible blocking of infrasonic energy by the tall peaks of Mauna Kea and Mauna Loa.

2.1.11. I53US, Alaska

No clear detections associated with the Columbia were observed in Alaska. A detection from the expected azimuth was observed at ~15:19 UT, but for a range of ~3000 km the signal would have had to travel at an effective speed of 560 m/s to arrive at Fairbanks at the observed time. Other pulses with the same azimuth were found at unrelated times in the same I53 data set, suggesting a noise source in that sector.

3. Synopsis

Narrowing the time windows worked well for smaller aperture arrays at relatively short ranges to the shuttle trajectory. For I57US, with its smaller subarray, it was possible to detect infrasonic energy pointing to the Columbia approach into the California coast. Similarly, late arrivals at SGAR pointed south of west, stressing the need to correct for the effects of the wind on the propagation path. Figures 12a and 12b shows a summary of the observed azimuth ranges using narrower time windows for the analysis. No improvement was observed for I56US and I10CA, so for these arrays the results of Garcés et al. 2003, Part 1, are plotted in Figure 12. Both range and array geometry were critical in the detection parameter selection for each array, suggesting that each array should be calibrated for optimum detections of specific signals. Based on the backazimuth windows shown in Figure 12a, the flash reported in Appendix A could, in principle, have been observed by I56, I57, NVIAR, and SGAR. However, careful analysis of the propagation paths to these arrays is required for a better assessment of the feasibility of this association.

4. References

D'Spain, G., J. Murray, G. Rovner, M. Hedlin (2003). *Bearing/Time Plots in the 1-3 Hz Band from I57US data during the Shuttle Columbia Re-Entry on JD 32, 2003.* Revision 1, February 28, 2003, Internal document of the US Infrasound Group.

Garcés, M., C. Hetzer, M. Hedlin, and H. Bass (2003). *Part 1. Preliminary analysis of infrasound data associated with the Columbia disaster of February 1, 2003.* Revision 5, February 11, 2003 (Rev 1, February 5), Internal document of the US Infrasound Group.

Garcés, M., and C. Hetzer (2003). *Part 2. Preliminary analysis of arriving phases associated with the Columbia Disaster of February 1, 2003.* Revision 1, February 10, 2003, Internal document of the US Infrasound Group.

Tenney, Stephen (2003). *ARL Infrasonic Detections of the Columbia Incident from WSMR.* February 26, 2003, Internal document of the US Infrasound Group.

Infrasonic Arrivals from Columbia
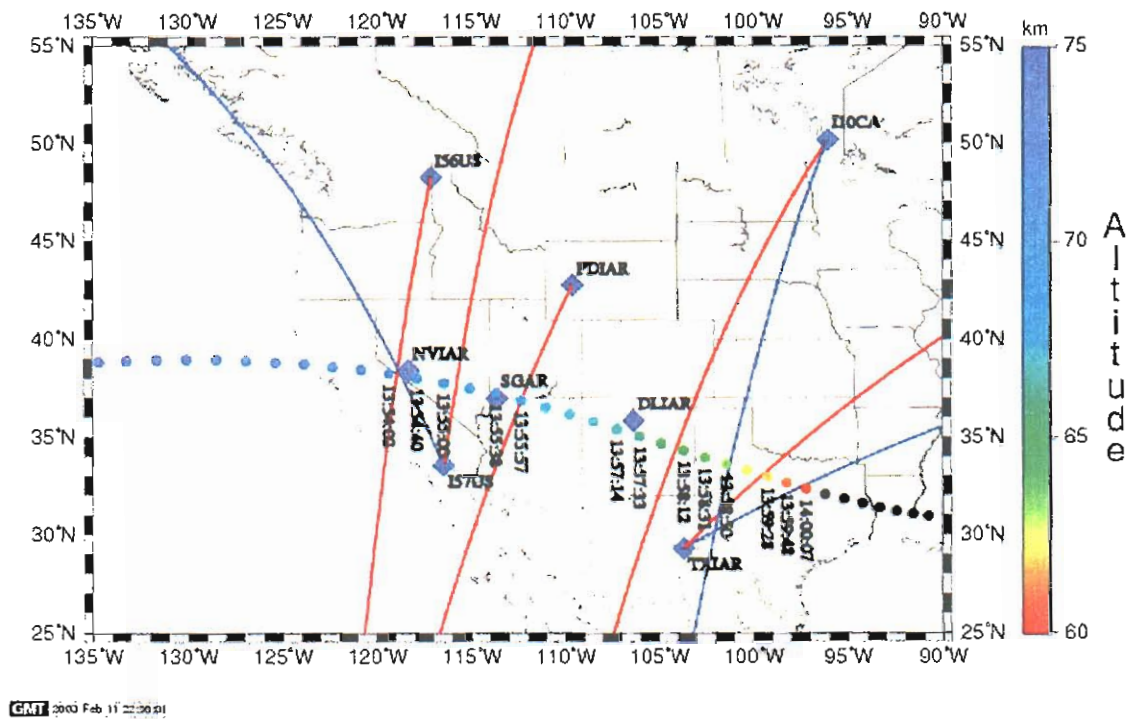
Figure 1. Projected track, altitude, time GMT, and infrasonic detections for the Columbia reentry based on time windows greater than 30 s. (Garcés et al. 2003, Part 1). No corrections are made for the wind deflection. Note that the TXIAR azimuth range plotted on this figure are based on a statement issued on a press release, and is known to be incorrect.
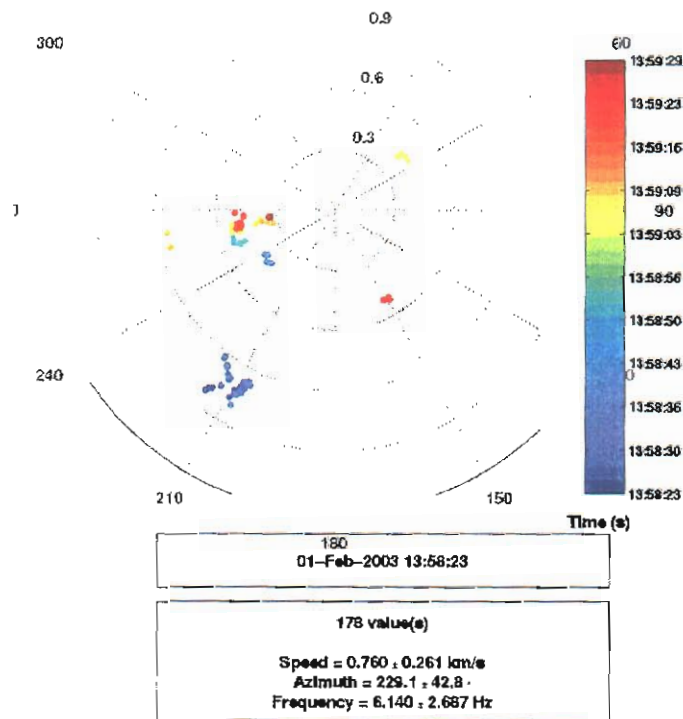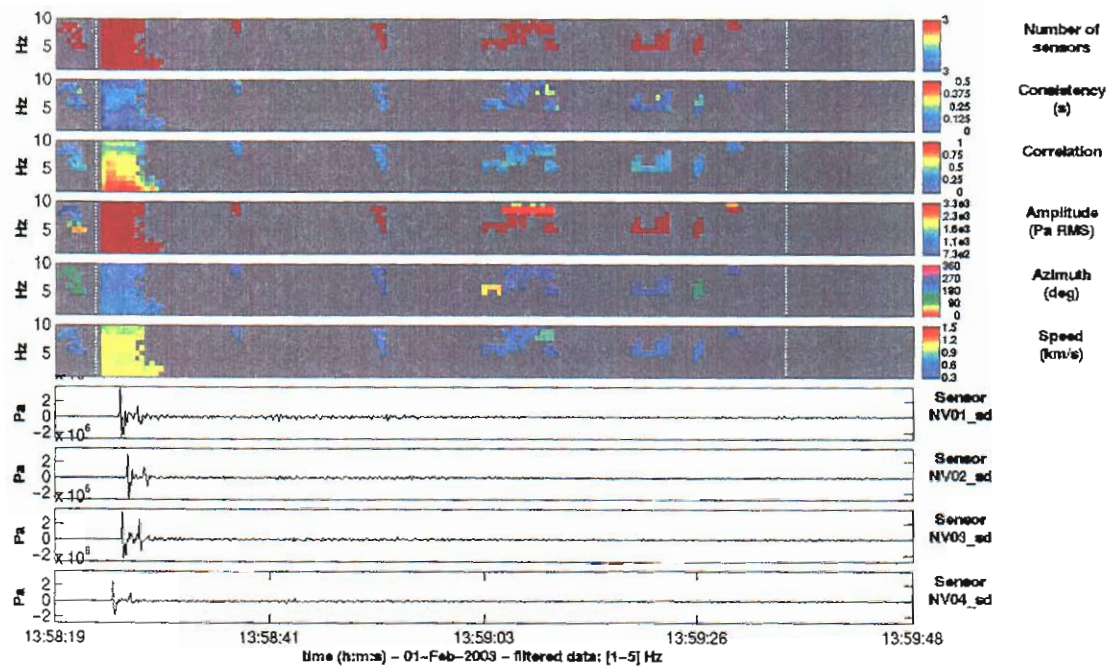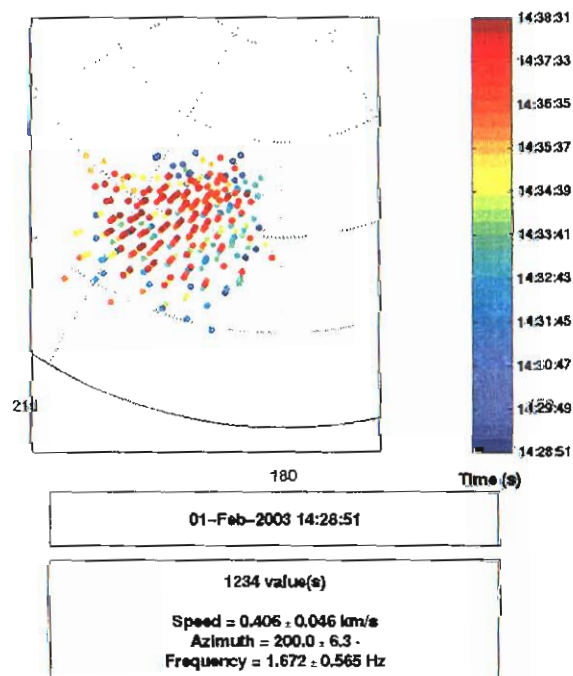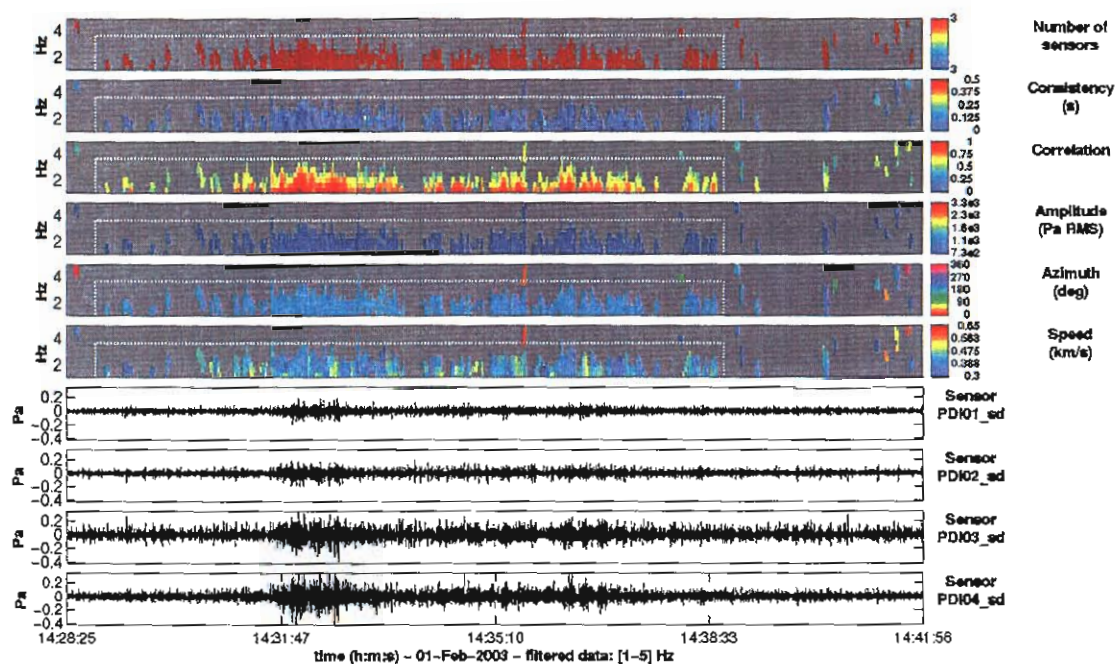
Figure 2. Detections and polar diagram at NVIAR for the Columbia reentry. The detection parameters are: time window of 5s, 4.5s overlap, passband of 1-10 Hz, 0.5 s consistency, speed range of 0.3-1.5 km/s.
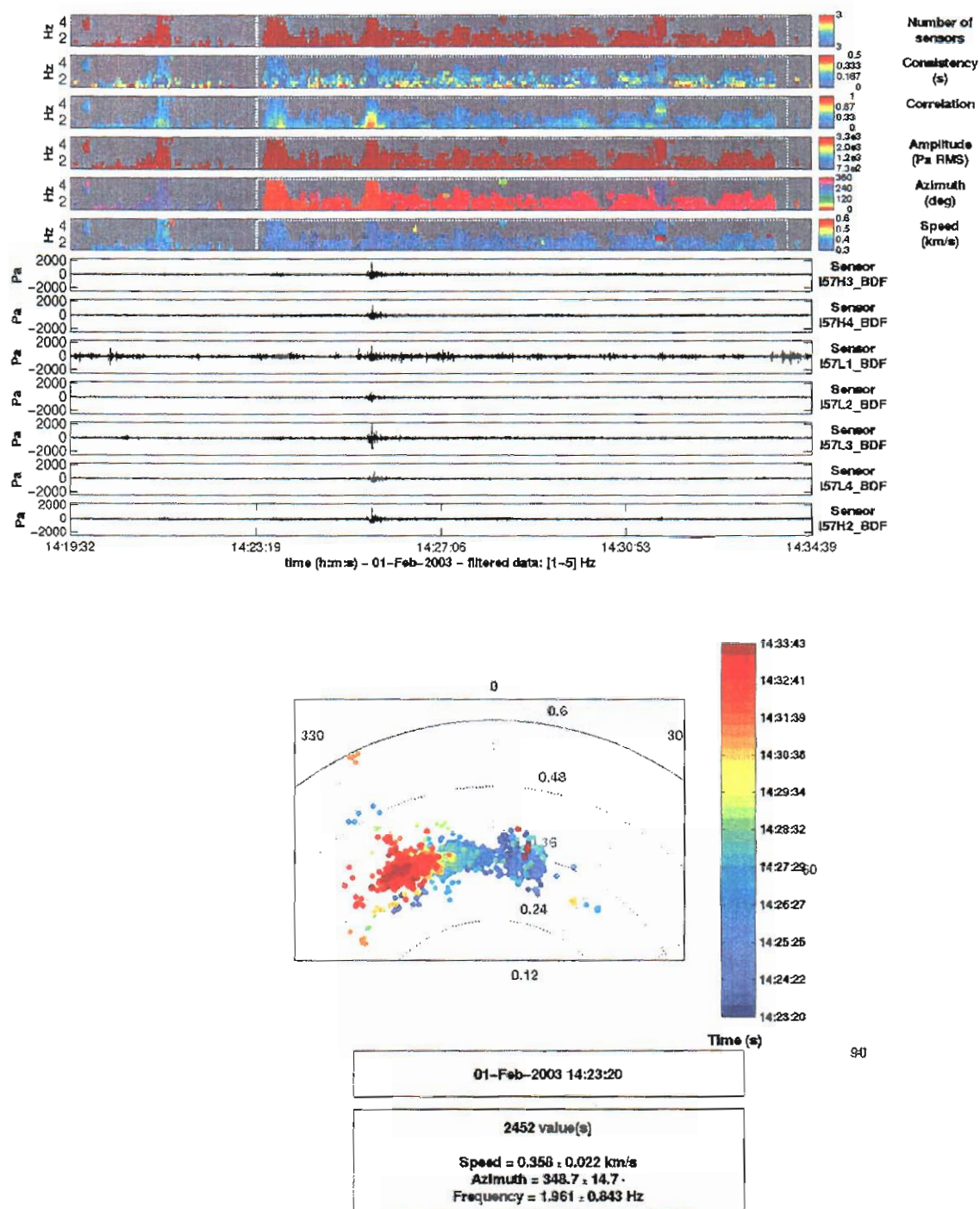
Figure 3a. Main detections and polar diagram at I57US for the Columbia reentry. The detection parameters are: time window of 15s, 14s overlap, passband of 1-5 Hz, 1 s consistency, speed range of 0.3-0.7 km/s.
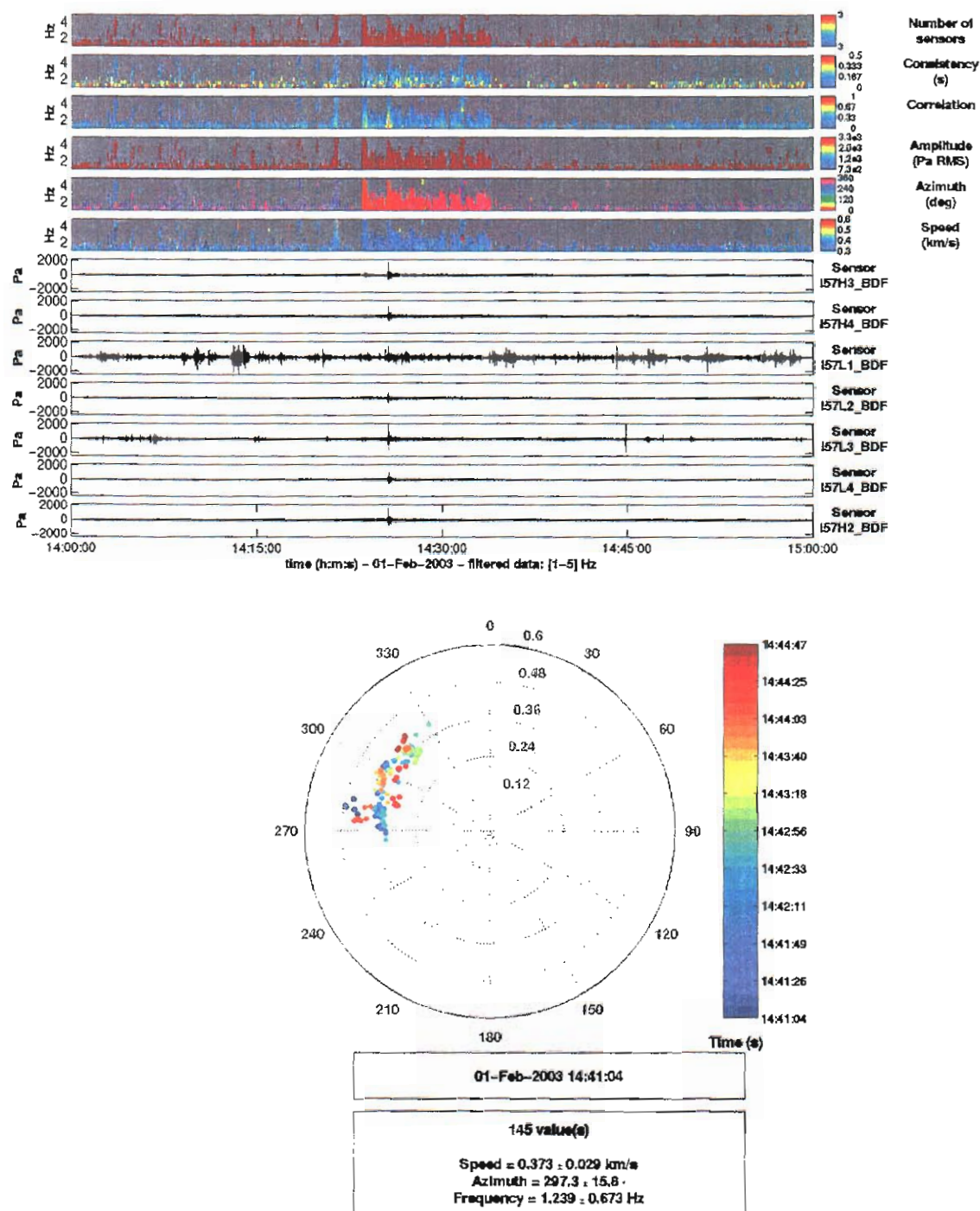
Figure 3b. Visualization of ambient noise field at I57US in the 1-5 Hz band. The upper panel shows that there is an abundance of background noise in the 270-325 degree sector, the lower panel shows the arrival detection azimuth and speed in the 14:41:04-14:44:47 time window. If weak signals from the Columbia arrive from this sector, they would be difficult to distinguish from the coherent background signals.
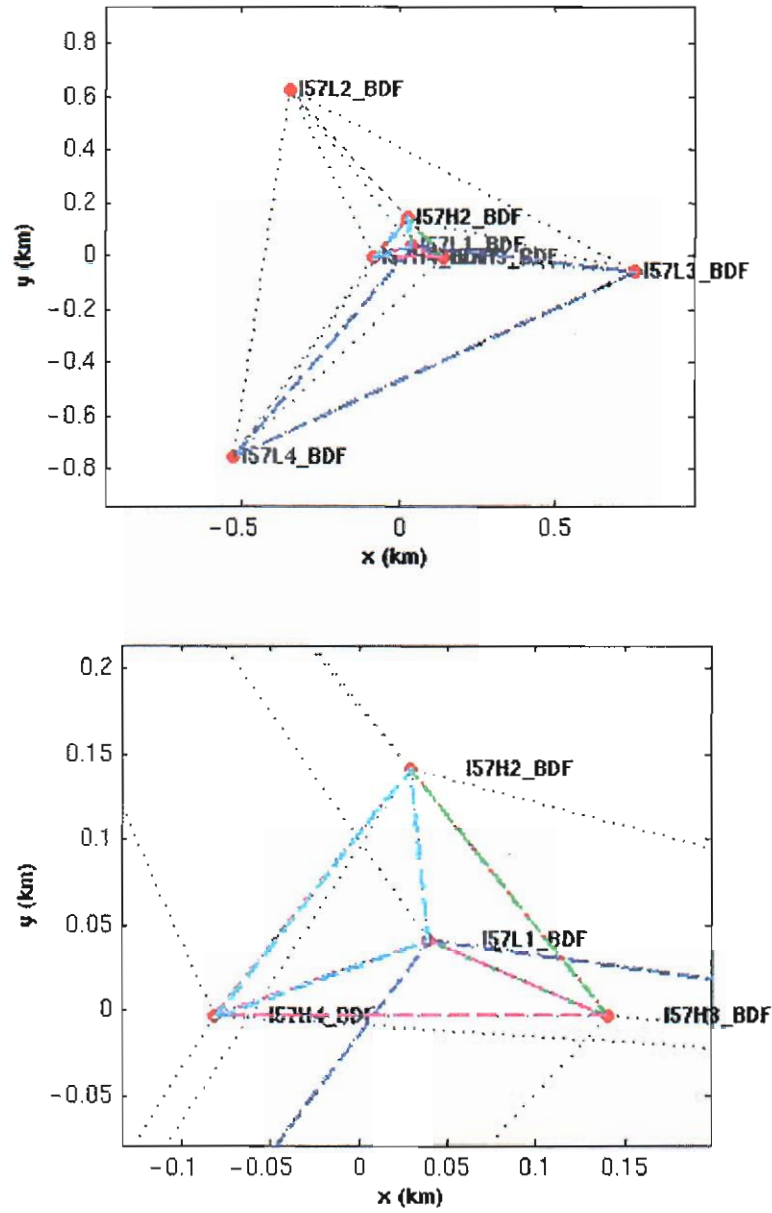
Figure 4. Sets of three-element subarrays defined at I57US for the PMCC progressive search algorithm during the higher frequency, narrow window analysis. The larger subarray was selected to optimize the azimuth resolution.
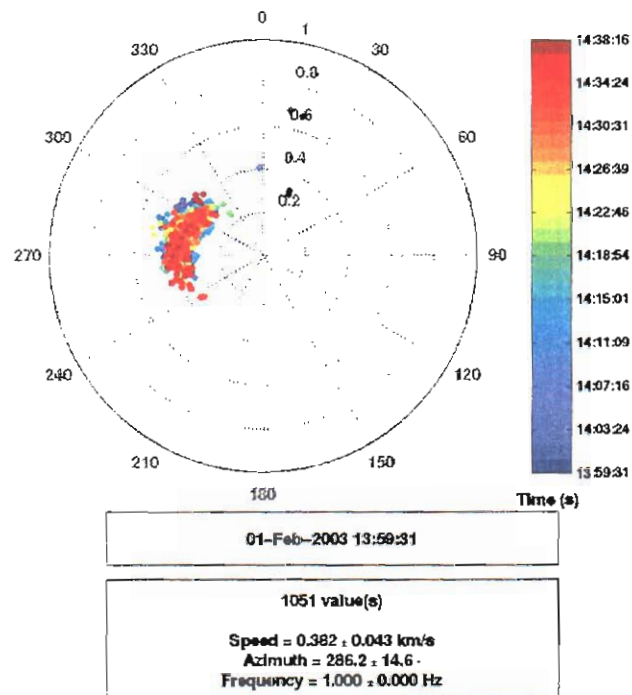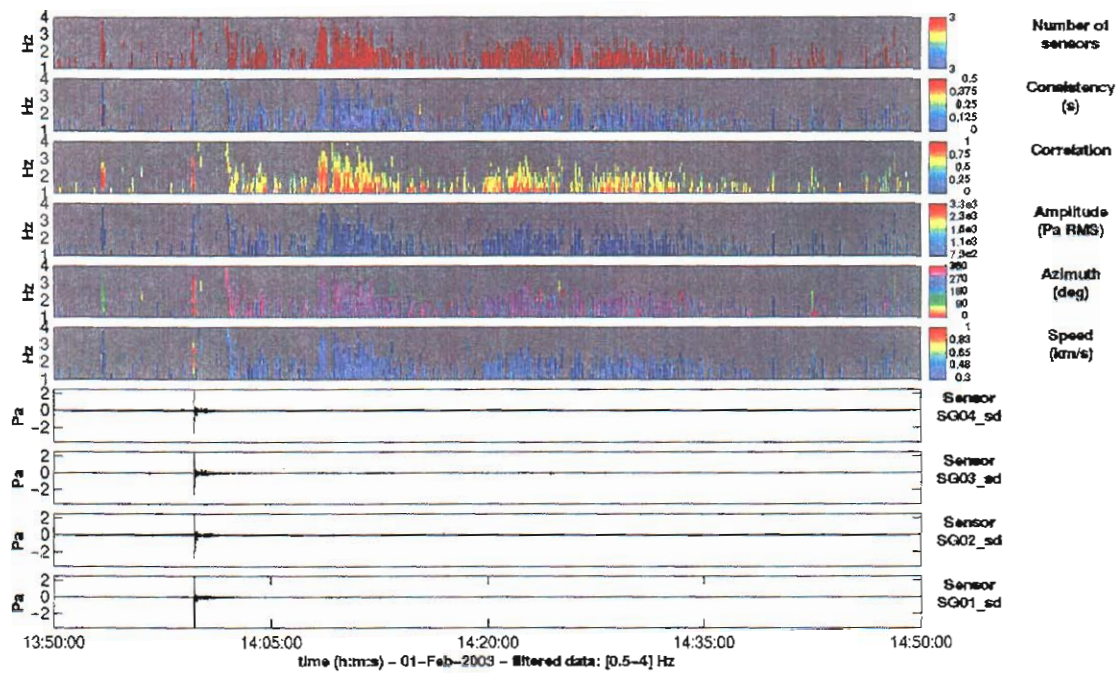
Figure 5. Detections and polar diagram at SGAR for the Columbia reentry. The detection parameters are: time window of 5s, 4s overlap, passband of 1-4 Hz, 1s consistency, speed range of 0.2-2.0 km/s.
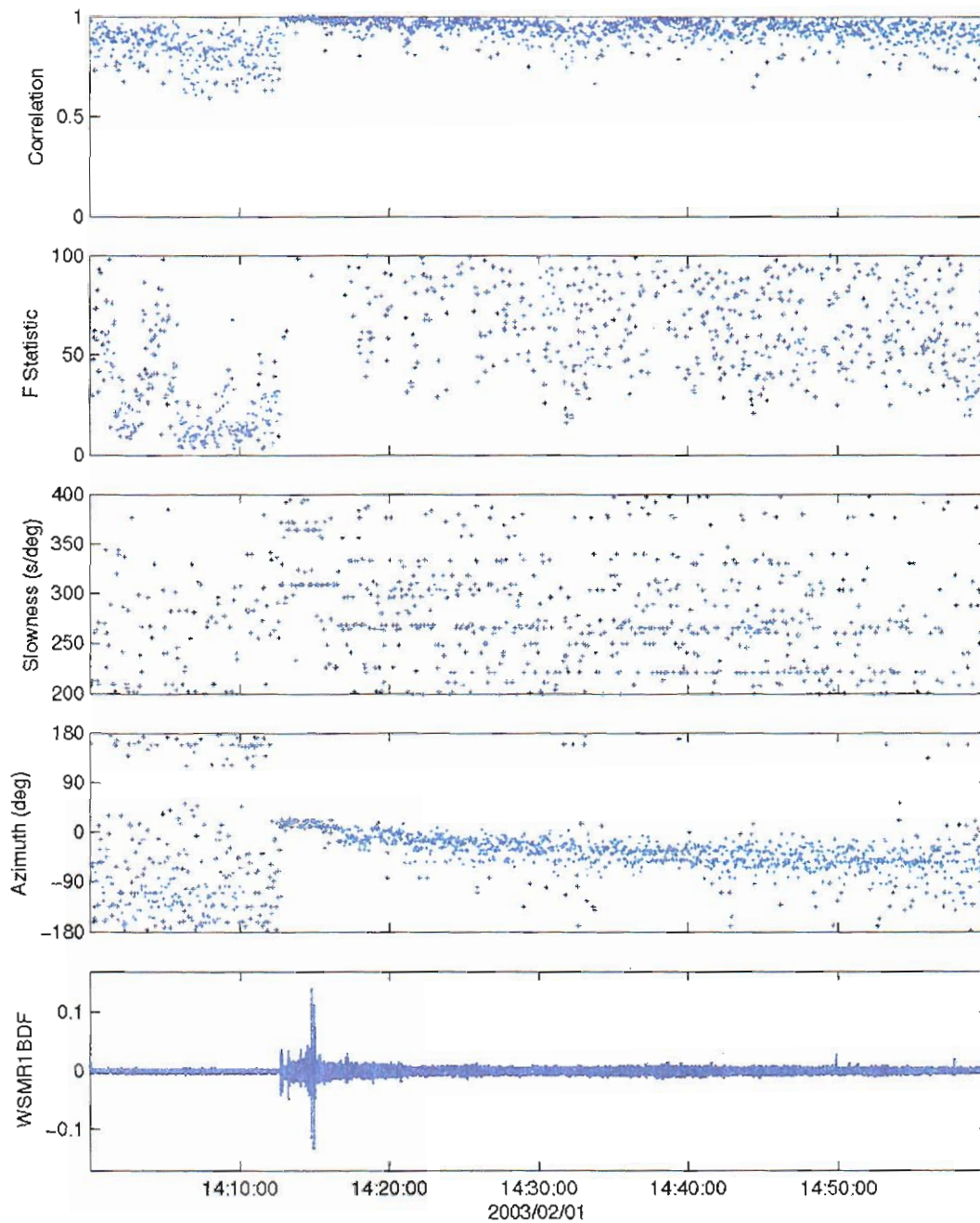
Figure 6. Detections and polar diagram at PDIAR for the Columbia reentry. The detection parameters are: time window of 5s, 4s overlap, passband of 1-5 Hz, 1 s consistency, speed range of 0.2-0.7 km/s.
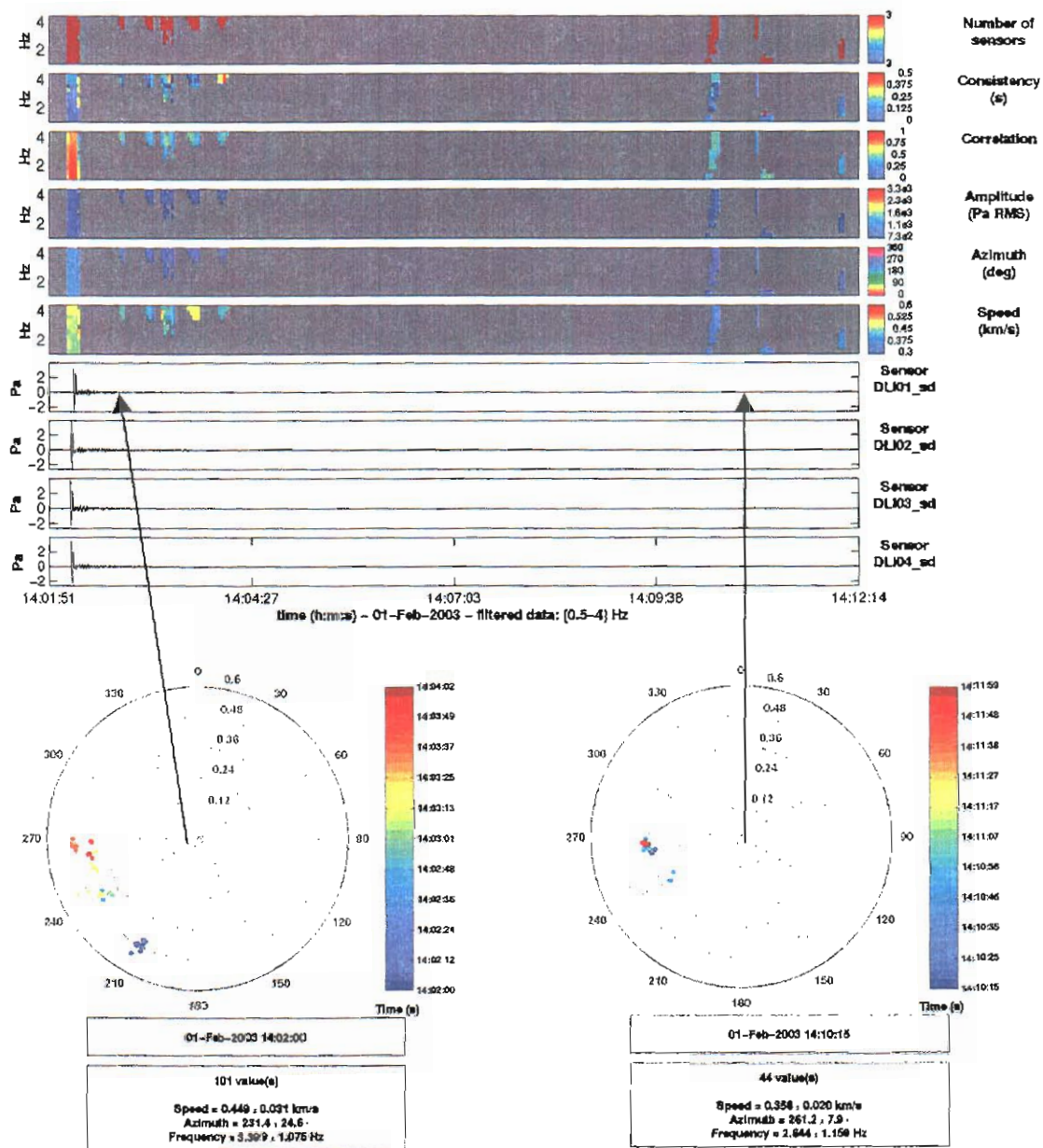
Figure 7. Detections and polar diagram at DLIAR for the Columbia reentry. The detection parameters are: time window of 10s, 8s overlap, passband of 1-4.5 Hz, 1 s consistency, speed range of 0.3-0.6 km/s.
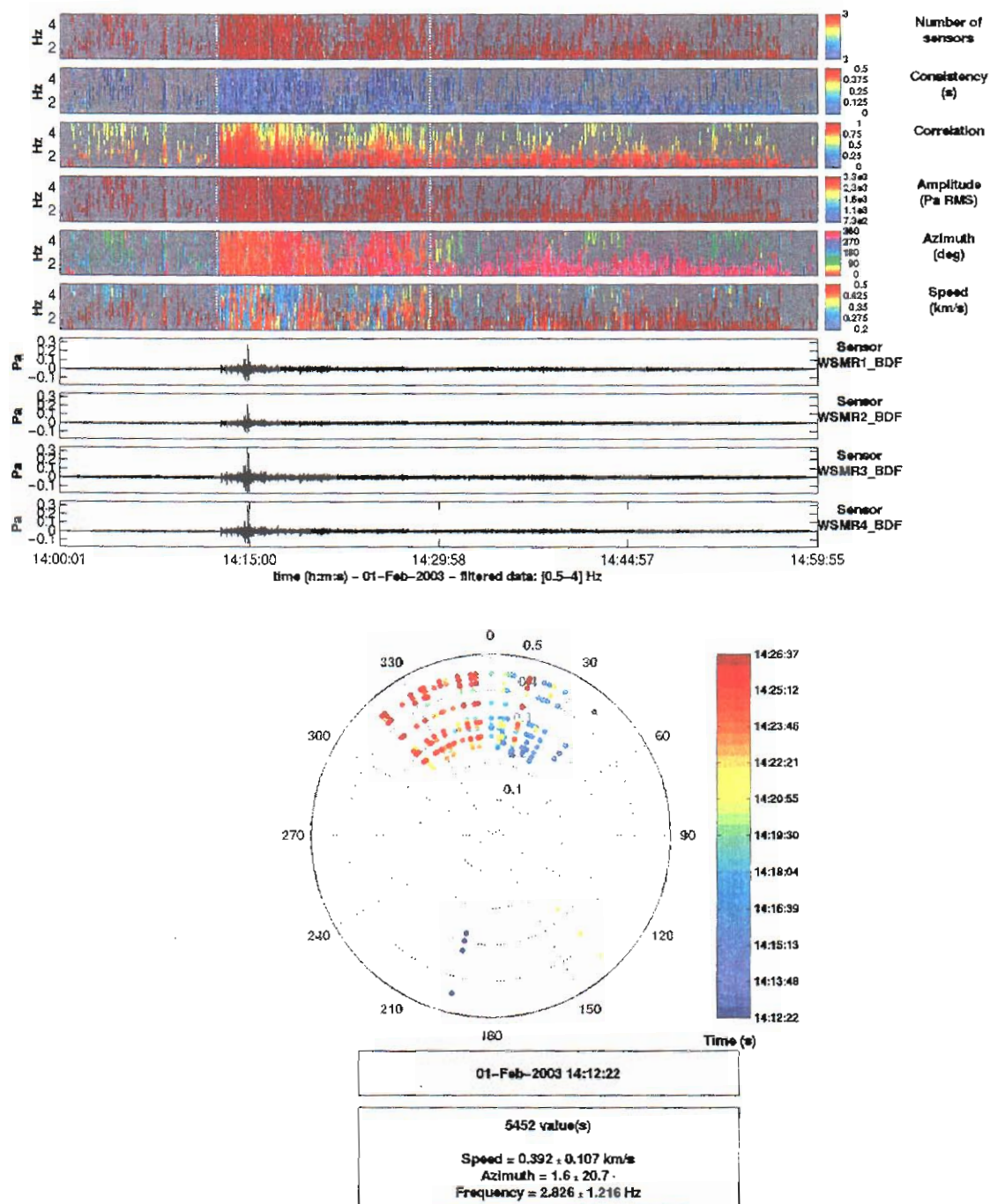
Figure 8. Detections at White Sands Missile Range showing a clear progression Westward with increasing time. The multiple values of speed at each azimuth may be due to phase mismatch between sensors. The detection parameters are: time window of 5s, 4s overlap, passband of 1-5 Hz, 1 s consistency, speed range of 0.2-0.7 km/s.

**Figure 9**. InfraTool results for the White Sands data. The westward progression and banding in the slowness plane are evident. The infratool detection parameters are selected to be consistent with the ARL report by Tenney (2003): time window of 5s, 2s overlap, passband of 1-8 Hz, 1 s consistency, max slowness of 400, 101 slowness values.

138
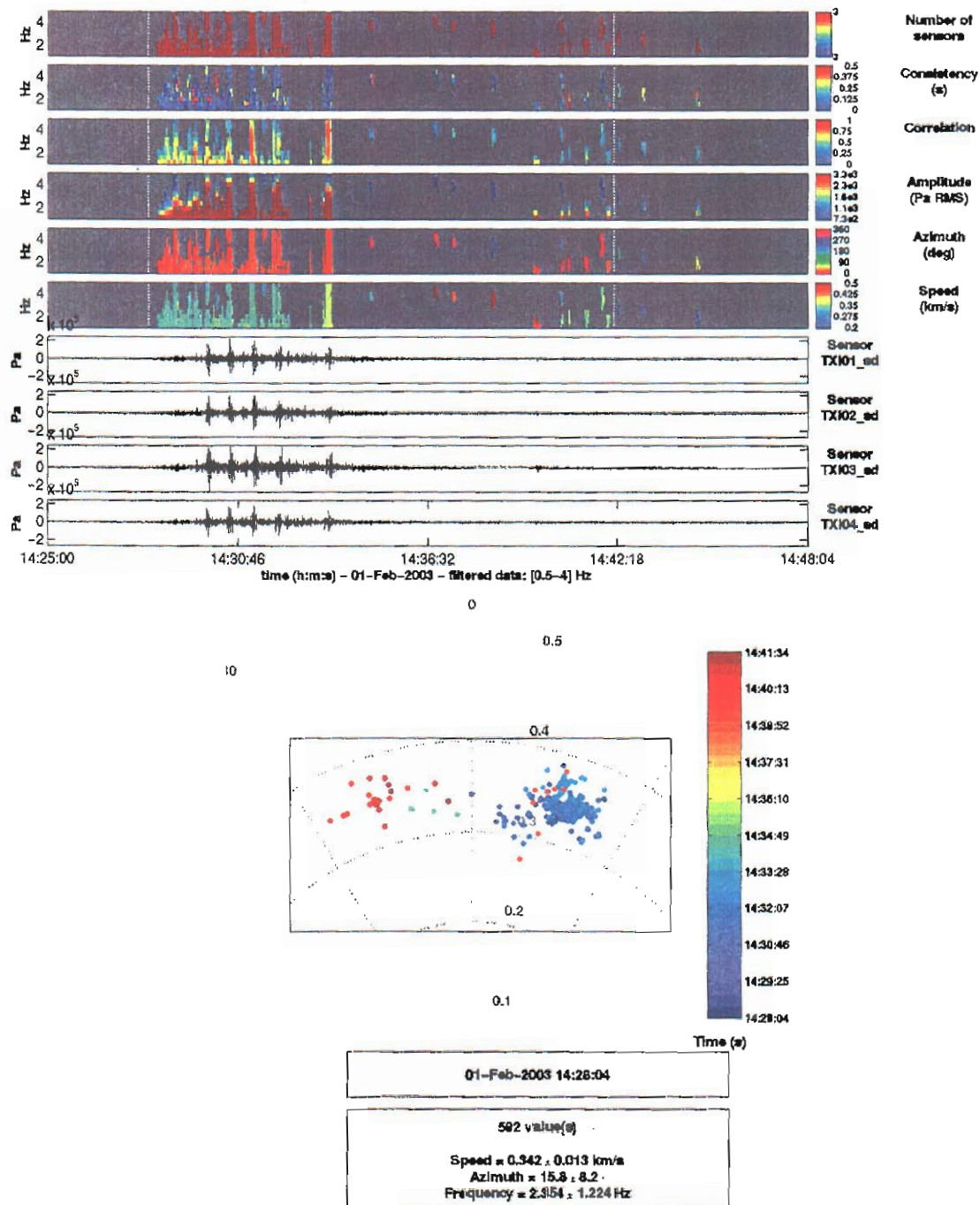
Figure 10. TXIAR detections showing an emergent signal followed by energetic multiple pulses and later northwesterly arrivals corresponding to the approach path. The detection parameters are: time window of 10s, 8s overlap, passband of 1-5 Hz, 1 s consistency, speed range of 0.2-0.7 km/s.
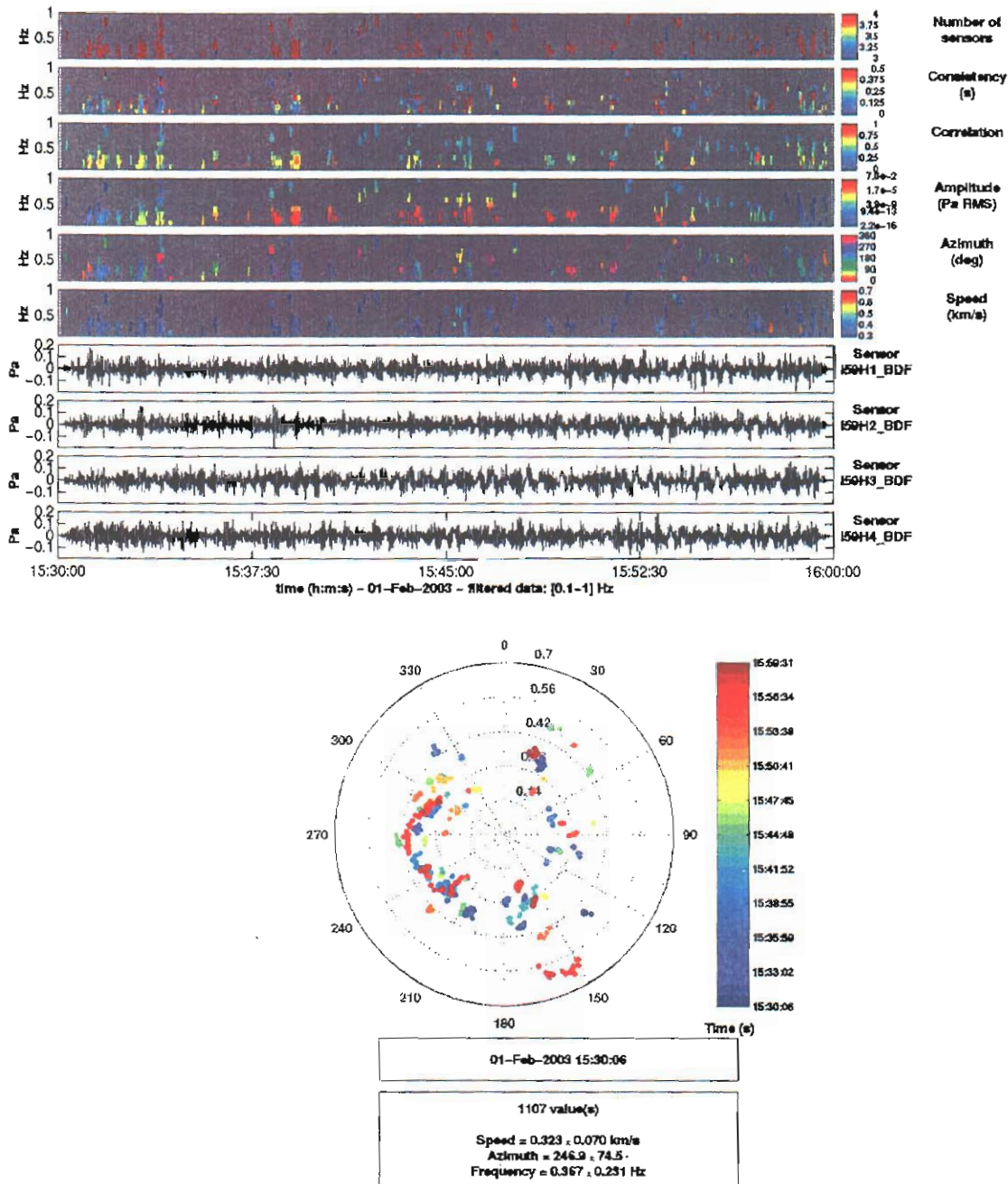
Figure 11. Detections and polar diagram at I59US, Hawaii, during the expected first arrival of the Columbia reentry. The detection parameters are: time window of 30s, 29s overlap, passband of 0.1-1 Hz, 1 s consistency, speed range of 0.2-0.7 km/s. There are no clear associations to the Columbia, possible arrivals near 330 degrees propagate too slowly.
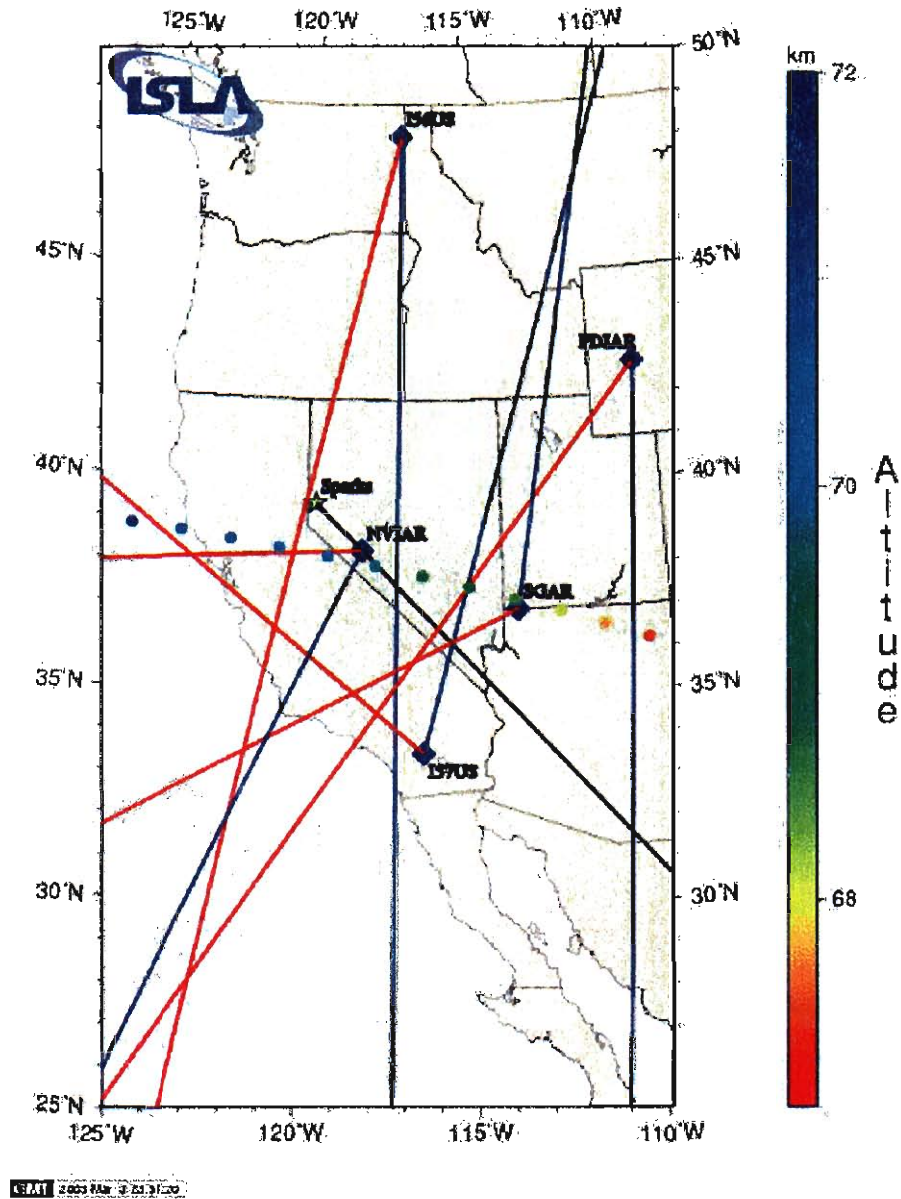
Figure 12a. Detected azimuth ranges for the easternmost arrivals (blue) and westernmost arrivals (red) for the Columbia approach to the US (color dots on the map) West of the Arizona-New Mexico border. The star denotes the location of Sparks, Nevada, and the black line is the 134 degree bearing relevant to the video reported in Appendix A. These azimuths are not corrected for the wind deflection.
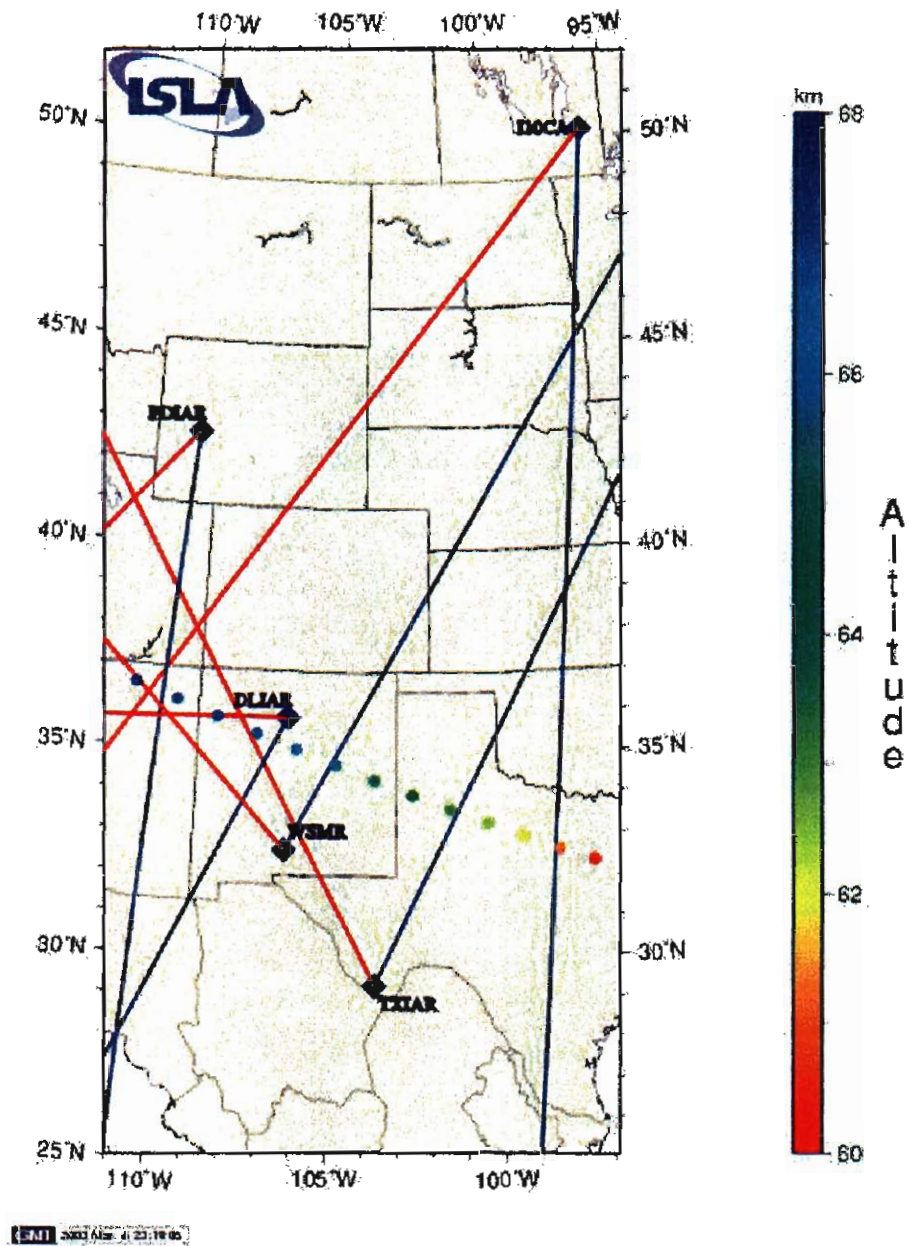
Figure 12b. Detected azimuth ranges for the easternmost arrivals (blue) and westernmost arrivals (red) for the Columbia approach to the US (color dots on the map) East of central Arizona. These azimuths are not corrected for the wind deflection.

Appendix A. The Flash

Lawson's shuttle video on its way to NASA
David E. Vieser

RENO GAZETTE-JOURNAL
2/3/2003 11:06 pm

A video by a Sparks amateur astronomer should arrive at NASA, possibly one of the first sightings of a problem aboard space shuttle Columbia before it broke apart, a Fleischmann Planetarium official said Monday.

Jay Lawson, 45, pointed his camera to the Western sky a few moments before 6 a.m. PST on Saturday. His videotape shows a burst of light as Columbia streaked across the Nevada sky.

"That was weird," Lawson can be heard saying on the tape.

It appears that Lawson's video is one of only a few amateur videotapes of the shuttle shot on the West Coast, said Mike Mewhinney, a spokesman for the National Aeronautics and Space Administration.

Also, the Ames Research Center, a NASA facility in Mountain View, Calif., has received no reports of shuttle remains falling in the Pacific Time Zone, Mewhinney said.

Keith Johnson, associate director of the Fleischmann Planetarium at the University of Nevada, Reno, said Lawson's tape might be among the first to catch sight of trouble on Columbia.

On Monday, Johnson sent a copy of Lawson's tape to investigators at the Johnson Space Center in Houston. Lawson asked for Johnson's help after he realized he might have a key piece of visual evidence.

Johnson said the tape might hold evidence of a problem just before sensors detected trouble.

"If something did happen, it would be quite a bit west of Texas, and this information could be helpful," Johnson said.

Based on a revised timeline from NASA, the flash of light appears just as heat sensors started to record a rapid rise in temperature.

According to NASA documents released Monday, the first sign of trouble came from heat sensors along the underbelly of the left wing. For 2 minutes, from 5:52 to 5:54 a.m. PST, the temperature rose unusually quickly in the brake lines and the landing gear's left wheel well. At that moment, a bright light can be seen on the videotape shot by Lawson from his home in Sparks.

NASA animation and data indicate the shuttle was over central California,

moving quickly across Nevada, well south of the Reno area.

During a media briefing Monday, Ron Dittemore, manager of the space shuttle program, said the agency is particularly interested in any debris, especially tiles from the bottom of the shuttle that might have landed "upstream" of the explosion over Texas.

Dittemore said if the tiles didn't burn up completely in the atmosphere, they likely might be found in Arizona or New Mexico.

In the wake of the disaster, Johnson had a difficult time reaching the right people at NASA to report the tape. Once contacted, NASA investigators asked that a copy of the original be sent immediately to the Johnson Space Center.

The rush to get the video to the government and the media has kept Lawson busy over the past three days. For him, little time has been left to mourn.

"I am fairly emotional when it comes to the astronauts, and I was pretty shaken up," said Lawson, who will watch the memorial services on television today.

National media are beginning to pay attention to his video. He has received a call from a reporter with the New York Times, and was scheduled to appear on "CBS This Morning" today in segment from the planetarium.

Lawson decided to tape the shuttle after getting an e-mail from Brian Webb, an amateur astronomer in California. Webb runs a Web site that keeps tabs on missile launches from the Vandenberg Air Force Base. Many times those missiles cause streaks of light in the Nevada sky, prompting thousands of calls to police and fire departments across the state.

Subject:
    Time of Flash from Quicktime movie (Sparks Video)
Date:
    Thu, 20 Feb 2003 15:16:43 -0800 (PST)
From:
    James Murray <james@mpl.ucsd.edu>
  To:
    gld@mpl.ucsd.edu, glr@mpl.ucsd.edu, milton@isla.hawaii.edu, chetzer@isla.hawaii.edu, joydeep@cmr.gov,
    hedlin@epicenter.ucsd.edu
  CC:
    james@mpl.ucsd.edu

Gerald,

I roughly calculate the flash to occur at 13:54:33 Z. If the bright stationary object in the video is Venus and the shuttle passes in front of it about 5 seconds after the flash, then we should be able to calculate the time of the flash by getting the position of Venus relative to Sparks Nevada.

According to mapquest.com, Sparks Nevada is at 39.535839 deg N and 119.751556 deg W. Plugging those coordinates into www.stargazing.net with an approximate time of 13:50:00 Z, gives us an azimuth of 134 deg East of North. By using a protractor on the trajectory map, an azimuth of 134 deg from Sparks puts the time at 13:54:38. Five seconds before that is 13:54:33Z.

Like I said, its a rough calculation.

James Murray

Marine Physical Laboratory
Scripps Institution of Oceanography
(858) 534-5384
(858) 534-5255 (fax)
james@mpl.ucsd.edu

Appendix E

Infrasonic Investigations of the Columbia Re-Entry
Part 4. Summary of infrasonic detections and propagation modeling estimates associated
with the Columbia reentry of February 1, 2003.

Milton Garcés and Claus Hetzer
Infrasound Laboratory, University of Hawaii, Manoa
March 18, 2003, *Revision 3*

1. Introduction

Various research groups have been collaborating on the interpretation of infrasonic signals observed during the reentry and violent disassembly of Shuttle Columbia (STS-107) on February 1, 2003. This document seeks to integrate the results of various reports issued to date, with the aim of providing a better characterization of the approach of the Columbia to the Western United States. An overview of some of the available seismic data is also presented.

2. Comparison of observed infrasonic detections and model predictions

Figures 1-8 show a comparison of the HARPA ray-tracing results presented by Gibson and Norris (2003b) and the infrasonic detections presented by Garcés et al. (2003, Parts 1 and 3). Figure 9 with the detections for WSMR is provided for reference. Many of the main propagation features are captured by ray tracing, namely the Westward progression of the detections with increasing time in I57, NVIAR, and SGAR, the first and subsequent arrivals at IS57 and PDIAR, as well as the Eastward progression with increasing time at I10. Some of the details in the detections are not captured. Except for the bow wave arrivals at the nearest station, the predicted arrivals are generally too slow in comparison with the observations. As discussed in Garcés et al. (2003, Part 2) and Garcés et al. (2002a,b), it may be possible to have relatively fast arrivals propagating in elevated ducts, and we use the tau-p method to estimate the propagation speed and azimuth deviations of selected phases at each array. The term *effective sound speed* usually refers to the algebraic sum of the wind speed and the sound speed along the propagation direction. To avoid confusion, in this document we use the term *celerity* to refer to the apparent speed of propagation of a wave, or the range divided by the travel time. Using the same procedure and climatological models described in Garcés et al. (2003), Part 2, we produced the tabulated theoretical values shown in Appendix A. Figures 10 and 11 show the backazimuth windows at each array for the Western and Eastern sector of the Columbia approach. The left hand panel of each plot shows the detected backazimuth windows at each array including the sonic boom arrival and uncorrected for the wind. The panels on the right show the backazimuth windows at each array after exclusion of the N-wave and after azimuth corrections due to the wind component transverse to the propagation direction.

3. Theoretical maximum ranges for detections at each array

Although the azimuth corrections help narrow down the areas of interest for the late-arriving energy, there is still quite a bit of ambiguity in how far Westward the detections can be projected. Array backazimuth estimates may be unreliable (Appendix D) and it is often necessary to rely on travel time estimates to refine source locations. Appendix A provides theoretical celerities (c_j) for selected arrivals (t_j), which are used to determine the theoretical maximum and minimum ranges of arrivals detected at each array. Note that Appendix A excluded the first arrivals at NVIAR, SGIAR, and DLIAR from the sonic boom. Using the Columbia GPS trajectory provided in the CMR CD releases, we used the time (t_i) and range (r_i) to a station from each point along the trajectory to estimate the minimum residual time difference between the propagation time ($t_i - t_j$) and the theoretical travel time (r_i/c_j). Only minimum residuals smaller than 400 s were retained for the plots shown in Figures 12 and 13. We also used the known backazimuths to eliminate solutions that were too far outside the allowed azimuth windows shown in Figures 10 and 11 (with the exception of SGAR, see Appendix D). The gaps in the azimuth in Figures 12 and 13 are for the most part artifacts of the distinct arrival times selected in Appendix A, and the lines are only intended to show the theoretical minimum and maximum detection ranges. For stations that exhibit detections with a continuous progression Westward with time, acoustic energy may have been launched along the whole path between the bounding lines.

Of particular note is the green line for I56US. Green lines denote acoustic energy that may be trapped in the troposphere and thus travel with relatively fast speeds. These tropospheric phases may be particularly vulnerable to topographic and boundary layer effects. The Westernmost extent of detections for I56US denoted by the green line in Figures 12 and 13 exceeds the boundaries of the detection backazimuths, which makes this solution suspect. However, a similar overreaching can be observed in WSMR, where the predicted phases are more robust.

Although there is some evidence to suggest PDIAR, and WSMR may have also detected arrivals from the California-Nevada border, a more careful analysis of these distant detections is necessary. The arrivals corresponding to the longer ranges are often buried in a fairly complex coda, and inferring flight perturbations from these sections of the data may require waveform extraction and modeling resources presently beyond ISLA's capabilities.

Figure 14 shows the detections observed by the infrasound station in Erie, Colorado (Bedard et al., 2003). The arrivals corresponding to the approach path appear to swerve North of the expected trajectory. As in I10CA, there are also some arrivals Eastward of the point of closest approach. This in an interesting data set which shows some unique features, such as detections from both East and West of the sonic boom arrival azimuth.

Figure 15 shows the PMCC backazimuths for impulsive bursts observed at NVIAR, Nevada, and I57US, California, and mentioned in Appendix B of Bedard et al. (2003), as well as a precursory detection observed at I56US, Washington. The I56US detection appears to be unrelated to the other two or to the Columbia approach. The range from I57US and NVIAR to the point of intersecting backazimuths is approximately the same. The arrival time of the precursory event at I57US is ~14:20, and the arrival time of the selected phase for NVIAR is ~13:59. The large time

discrepancy (as well as amplitude considerations) between the two arrivals suggests that they were not generated at the same origin time.

4. Preliminary assessment of uncertainty in the azimuth, time, and location estimates

Because we have used various arrays with different geometry, number of elements, and site-specific effects, we do not have an estimate of the azimuth errors associated with each array. The array with the smallest aperture (White Sands) would have the largest azimuth uncertainties in its detection. A measure of the scatter in the detection can be observed in the PMCC plots, which provides a standard deviation. Wind may produce a significant azimuth deflection, and attempts have been made to correct for this deviation. The uncertainties in the theoretical corrections depend on the atmospheric conditions and selected phases, and may be as much as a few degrees. The onset time uncertainty is determined by the detection algorithm, the sliding window size and the sensitivity parameters of detection algorithm. We have experimented with various PMCC setting to optimize the detection sensitivity. A 30s window may start picking up an impulsive arrival at the very tail of the window, thus leading to an error as large as 25 s on the onset time. However, a 5s window would have a relatively small error of a few seconds. For propagation times of tens of minutes on some of the more distant arrivals, errors on the order of seconds are not very significant. We use the short window detections described in Part 3 of Garcés and Hetzer (2003) for our onset time estimates. The location uncertainties are determined by the atmospheric models as well as the assumed phases and onset times for the observed arrivals. The estimated azimuth ranges shown in Figures 12 and 13 are intended to provide the shortest and largest range of observed detections for each station along the entry trajectory, and are in themselves rather generous uncertainties estimates in range.

5. Overview of some of the available seismic data

Appendices B and C provide reports by David Oppenheimer and James C. Pechmann on detections of the Columbia by seismic stations in California, Nevada, and Utah. Figure 16 shows the vertical component on a small portion of the available seismic stations South of the CA-NV border, where there appears to be a crossing of backazimuths from the Westernmost infrasonic arrays. Figure B1 of Appendix B shows as circles available seismic stations that were utilized for the determination of the travel times across the seismic network. Dr. Oppenheimer observed that the sonic boom propagates faster towards the North than towards the South, which would be consistent with the Northwards stratospheric and thermospheric winds along the Columbia trajectory (Garcés et al., 2003, Part 2). Dr. Pechmann also observed that one of the stations (ICU) in Utah received multiple arrivals. These seismic arrivals are consistent with the infrasonic arrivals at SGAR. Thus is may be possible to use the much denser seismic network to look in more detail at regions of interest identified from the infrasonic data, although care must be taken to account for widely varying station quality, site effects, sensor characteristics, and dynamic range. If the analysis of seismic data is to be pursued, it is recommended that it is coordinated through a central agency such as CMR or University of Mississippi to prevent duplication of effort by the various research groups involved in the Columbia effort.

6. Conclusions and Recommendations

Infrasound stations in the US detected the Columbia as far Westward as the approach to the California coast, with apparent continuous coverage of the trajectory over the continental US. Multipath propagation in the atmosphere complicates the analysis of the later-arriving energy at

most of the stations. All analyses performed to date point to the California-Nevada border as a region where higher than usual pressure levels may have been generated during the Columbia approach, although this could have been caused by a change in the angle of attack or trajectory of the spacecraft. With the notable exception of NVIAR detections, infrasound corresponding to this and earlier parts of the trajectory may be buried within the coda of the waveforms. It may be possible to infer information about changes in the structural integrity of the Columbia by looking at the sonic boom and later arrivals of the NVIAR data, as well as by inspecting selected seismic waveforms in the California-Nevada region.

References

Bedard, A., R. Nishiyama, and A. Gasiewski (2003). *Infrasound originating from the 1 February 2003 reentry of the Space Shuttle Columbia: A summary of sub-audible sound bursts detected near Boulder, Colorado for use by NASA and others studying this accident.* Draft V1.1, March 11, 2003, Internal document of the US Infrasound Group.

Center for Monitoring Research (CMR), 2003. Preliminary Results of Infrasonic Data Collection and Analysis for the Columbia Disaster of February 1, 2002. Distributed on February 26, 2003.

D'Spain, G., J. Murray, G. Rovner, M. Hedlin (2003). *Bearing/Time Plots in the 1-3 Hz Band from I57US data during the Shuttle Columbia Re-Entry on JD 32, 2003.* Revision 1, February 28, 2003, Internal document of the US Infrasound Group.

Garcés, M., C. Hetzer, M. Hedlin, and H. Bass (2003). *Part 1. Preliminary analysis of infrasound data associated with the Columbia disaster of February 1, 2003.* Revision 5, February 11, 2003 (Rev 1, February 5), Internal document of the US Infrasound Group.

Garcés, M., and C. Hetzer (2003). *Part 2. Preliminary analysis of arriving phases associated with the Columbia Disaster of February 1, 2003.* Revision 1, February 10, 2003, Internal document of the US Infrasound Group.

Garcés, M., and C. Hetzer (2003). *Part 3. The search for short energy bursts in the coda of infrasonic signals associated with the Columbia reentry.* Revision 2, March 3, 2003 (Rev 1, February 20), Internal document of the US Infrasound Group.

Garcés, M, C. Hetzer, D. Drob, R. Woodward, H. Bass, D. McCormack, L. Evers, M. Hedlin, A. LePichon, L. Liszka, C. Wilson, R. Whitaker (2002a). *Progress in the development of a ground truth database of infrasonic events.* Infrasound Technology Workshop, De Bilt, Netherlands, October 28-31, 2002. CD with Tau9.1 distributed to workshop attendees.

Garcés, M., C. Hetzer, K. Lindquist, and D. Drob. *Source Location Algorithm for Infrasonic Monitoring* (2002b). 24[rt] Annual DTRA/NNSA Seismic Research Review, Ponte Vedra, FL, 17-19 September 2002.

Gibson, R., and D. Norris (2003a). *Preliminary Infrasound Propagation Modeling Analysis of Space Shuttle Columbia (STS-107) Reentry.* Revision 1, February 13, 2003, Internal document of the US Infrasound Group.

Gibson, R., and D. Norris (2003b). *Addendum #2 to: BBN Memorandum, dated 13 Feb 2003, entitled: Preliminary Infrasound Propagation Modeling Analysis of Space Shuttle Columbia (STS-107) Reentry.* Revision 3, March 14, 2003, Internal document of the US Infrasound.Group.

Tenney, Stephen (2003). ARL Infrasonic Detections of the Columbia Incident from WSMR. February 26, 2003, Internal document of the US Infrasound Group.

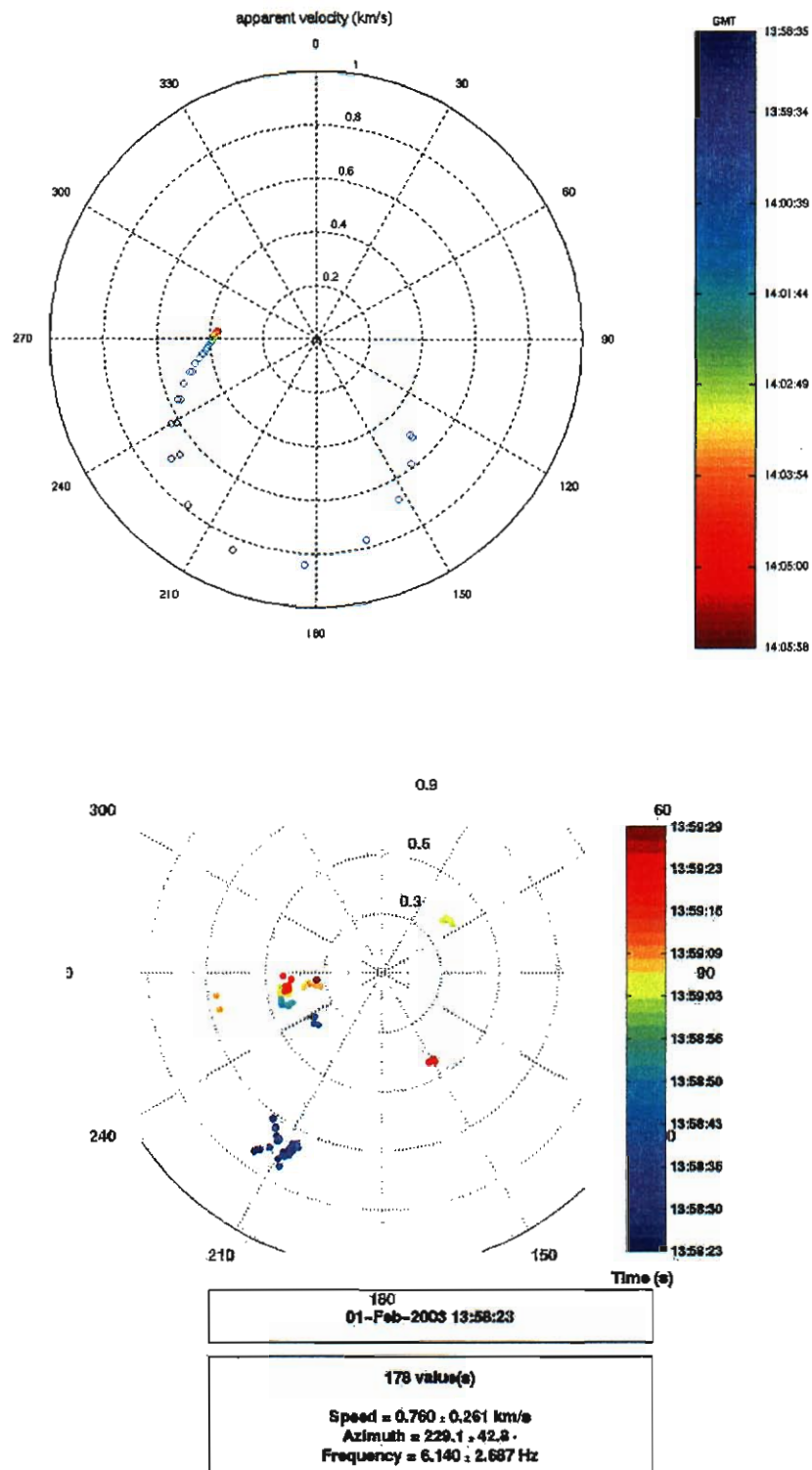SMU Web Page, *21 February 2003 Update of SMU NVAR and TXAR Infrasound of Explosion Event from Space Shuttle Columbia.* http://geology.heroy.smu.edu/~dpa-www/columbia/

Figure 1. HARPA predictions (upper panel, Gibson and Norris, 2003b) and PMCC observations (lower panel) for NVIAR.
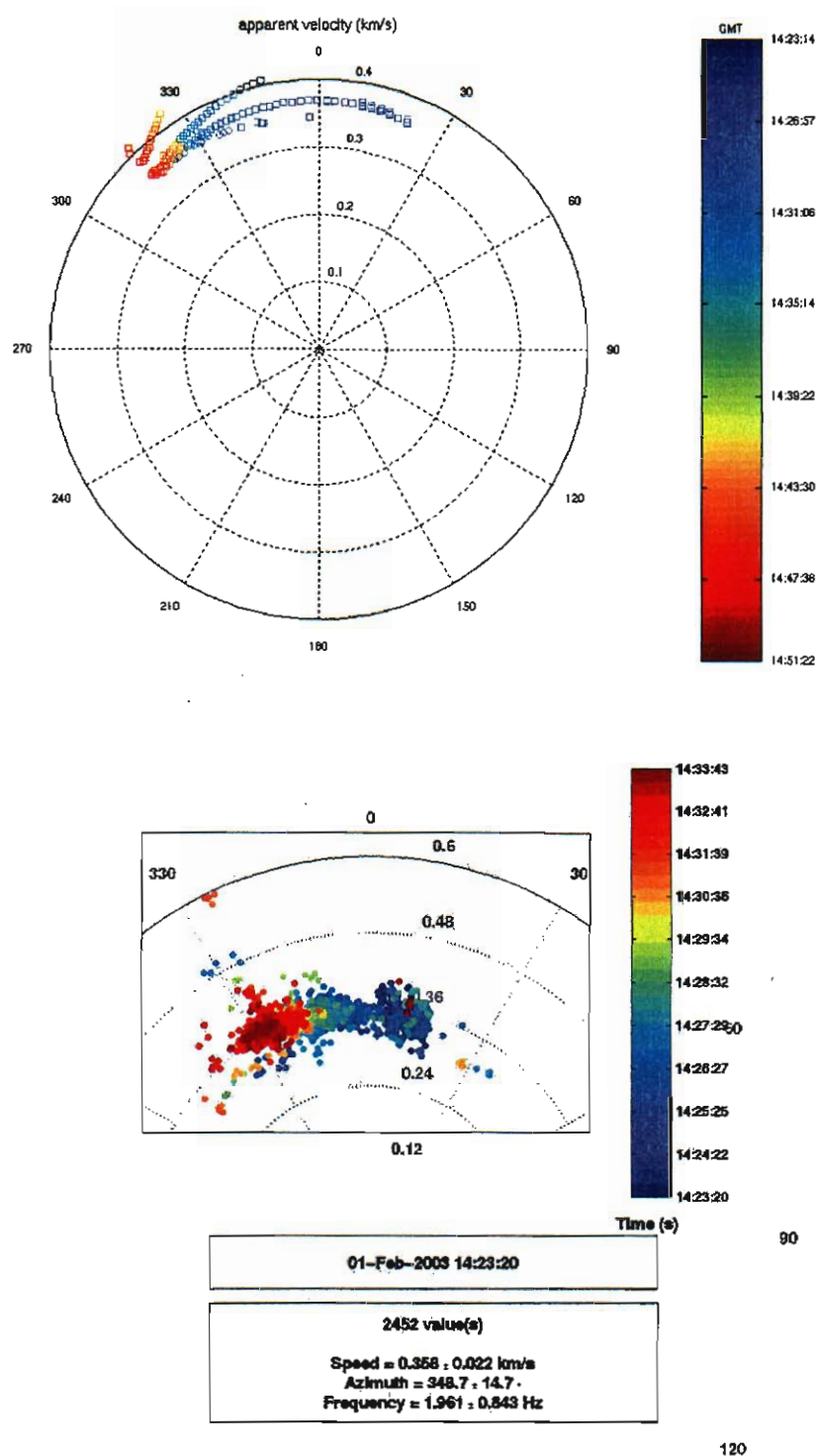
Figure 2. HARPA predictions (upper panel, Gibson and Norris, 2003b) and PMCC observations (lower panel) for I57US.
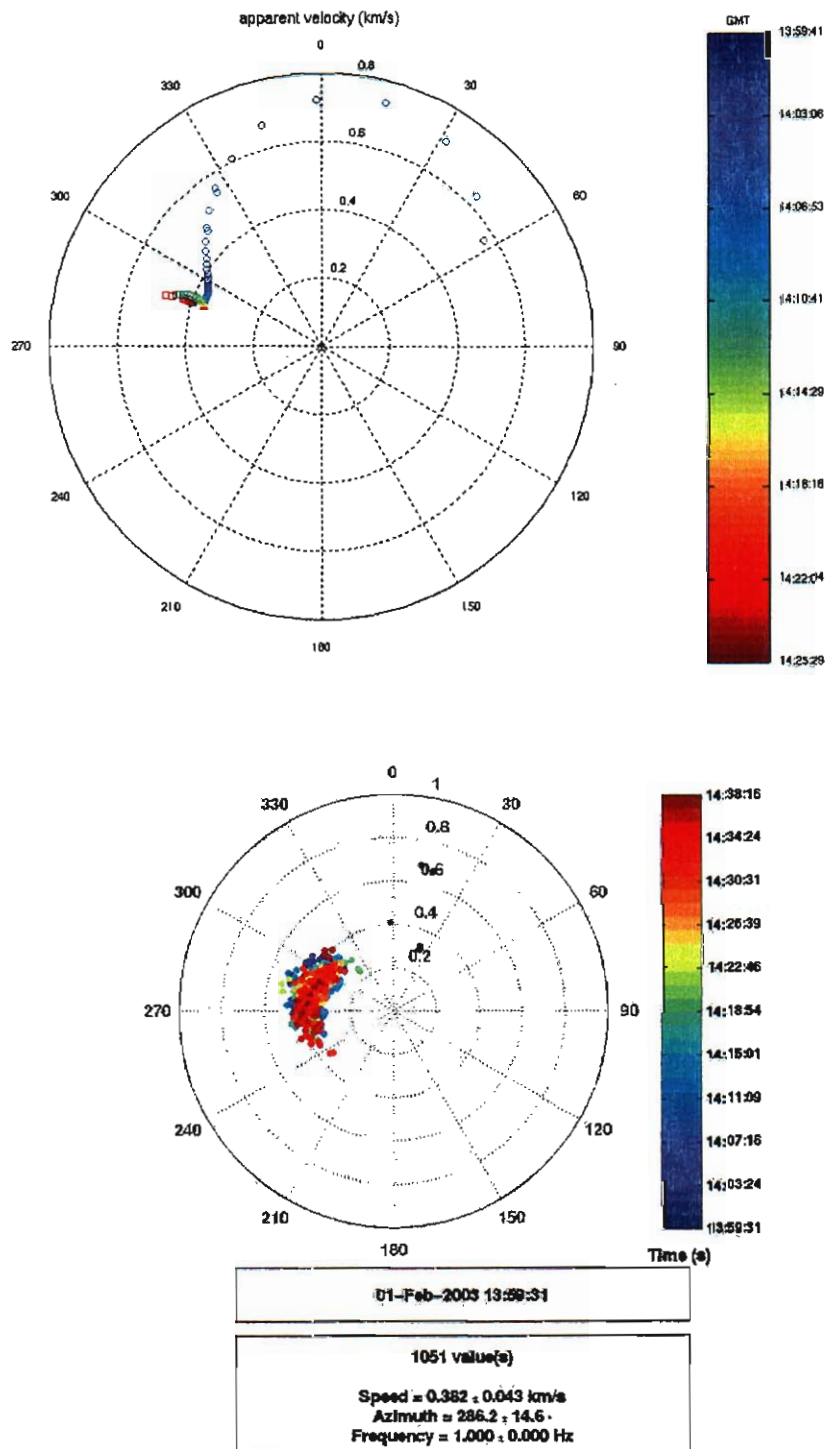
Figure 3. HARPA predictions (upper panel, Gibson and Norris, 2003b) and PMCC observations (lower panel) for SGAR
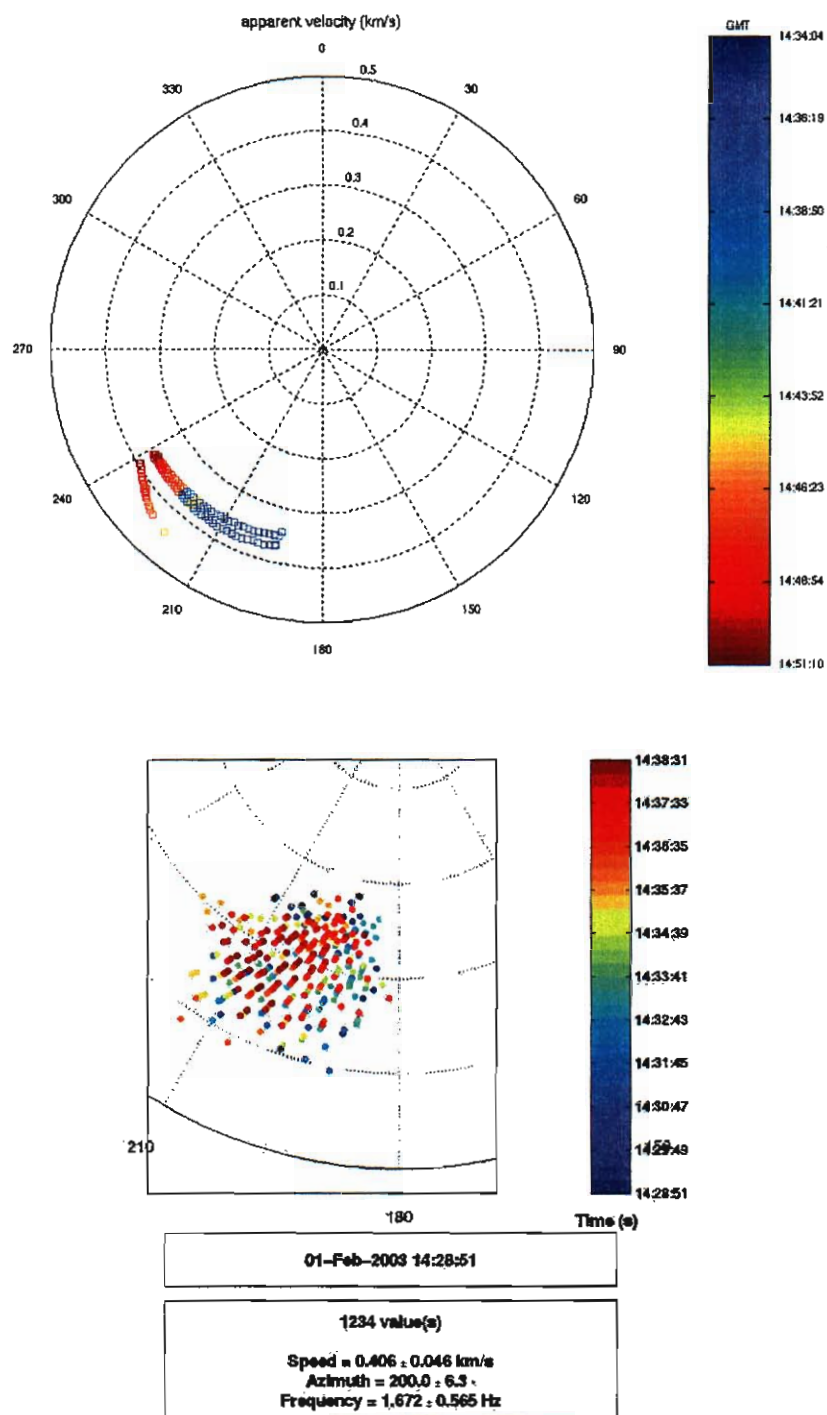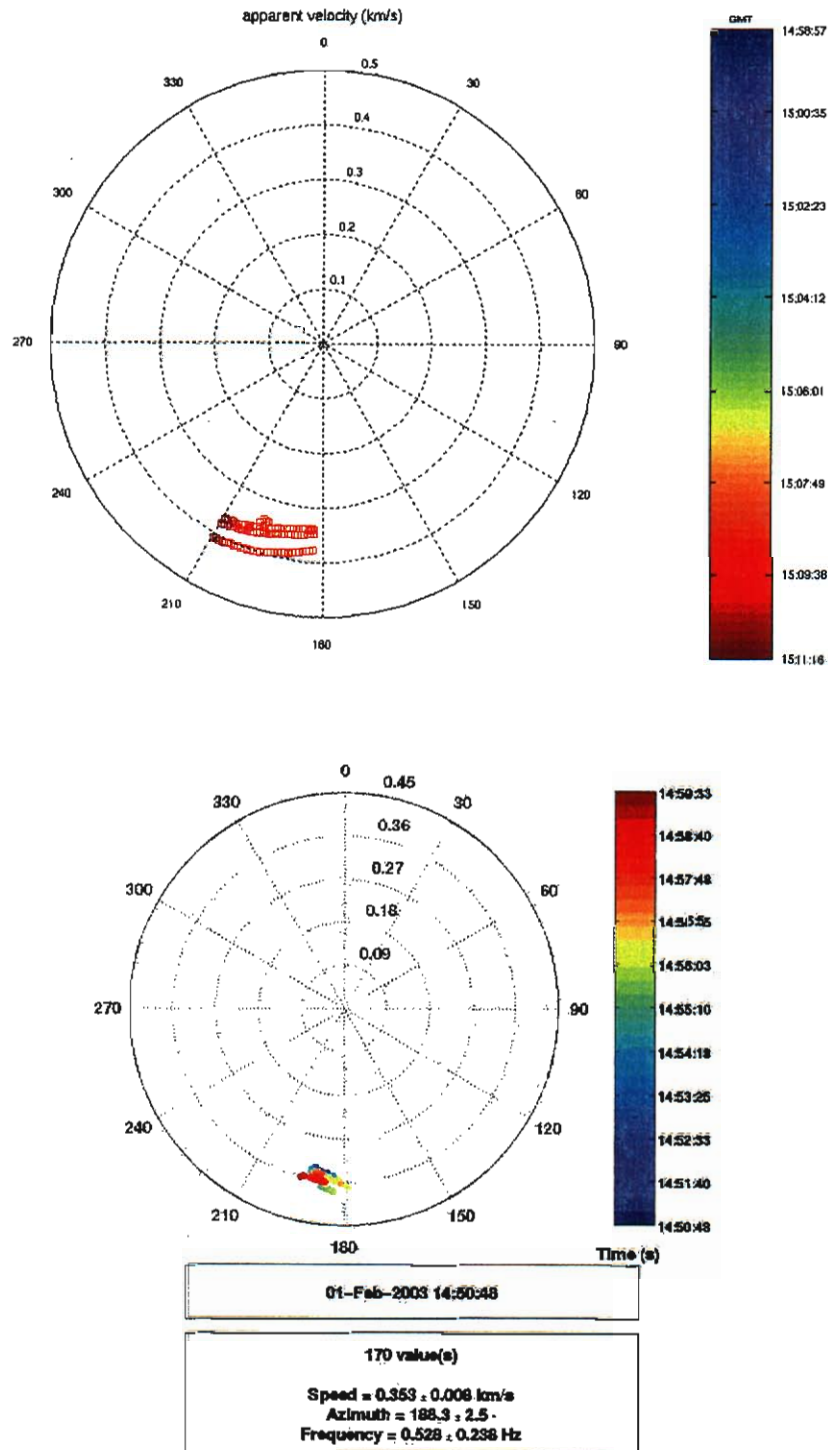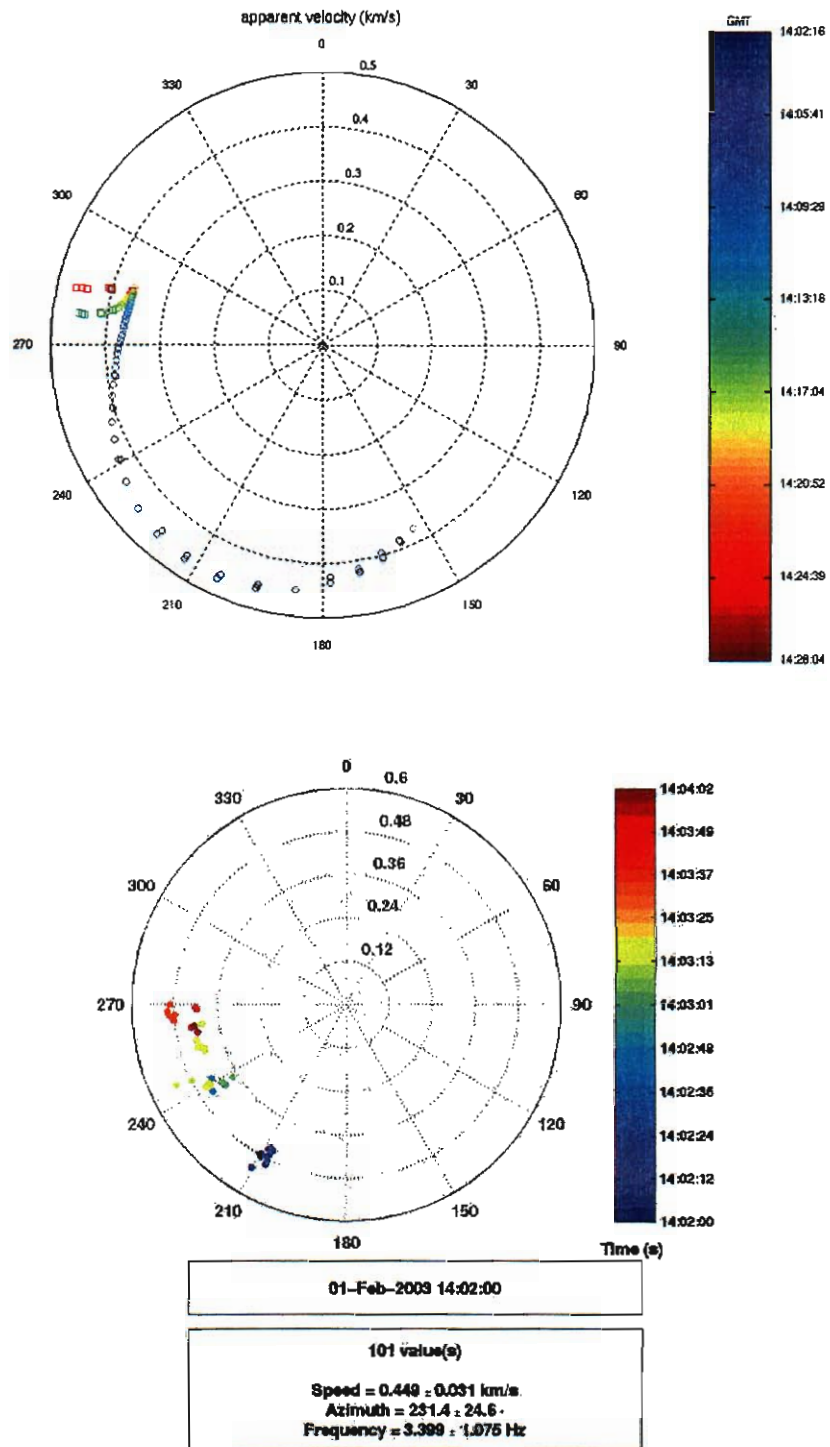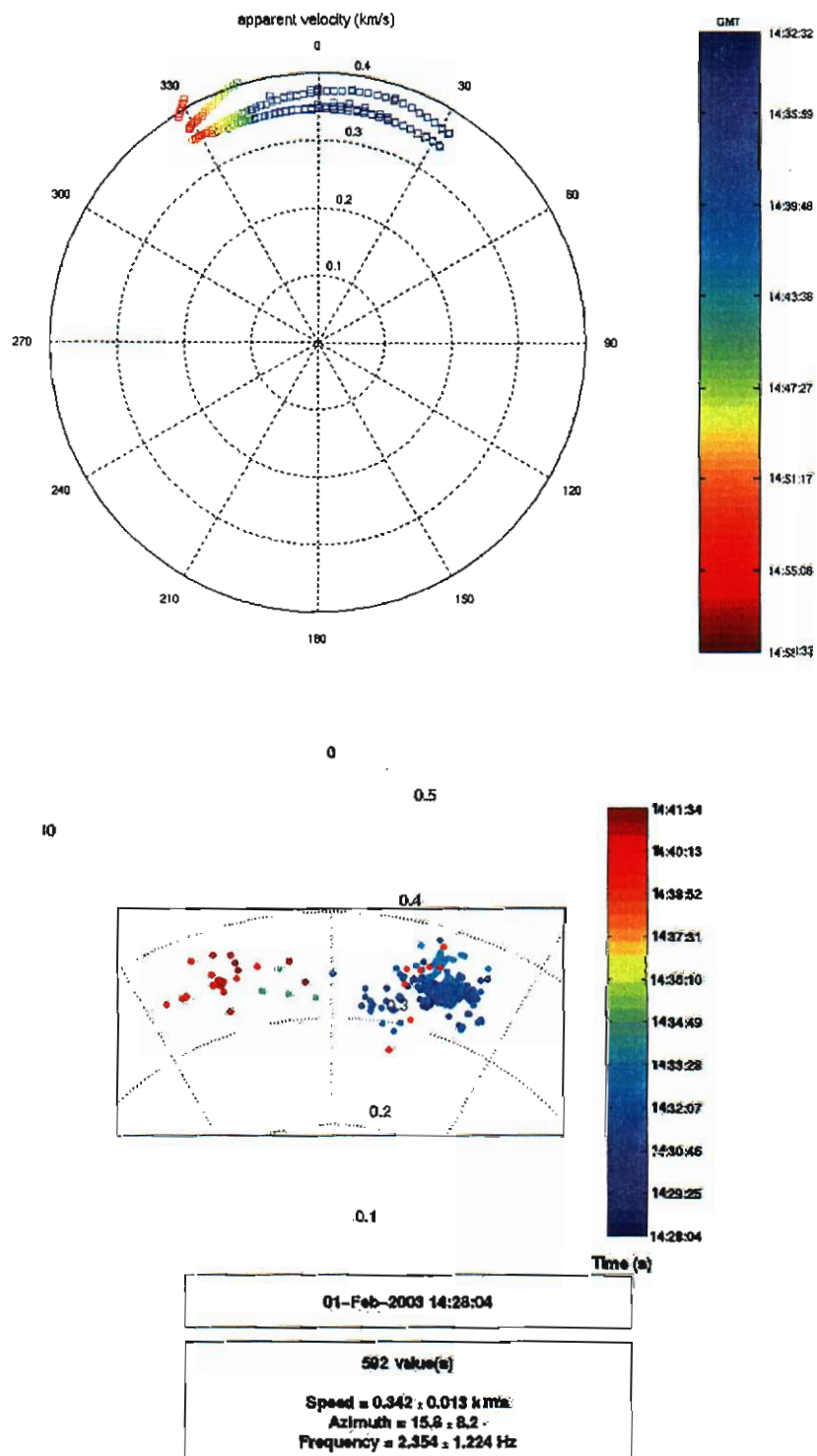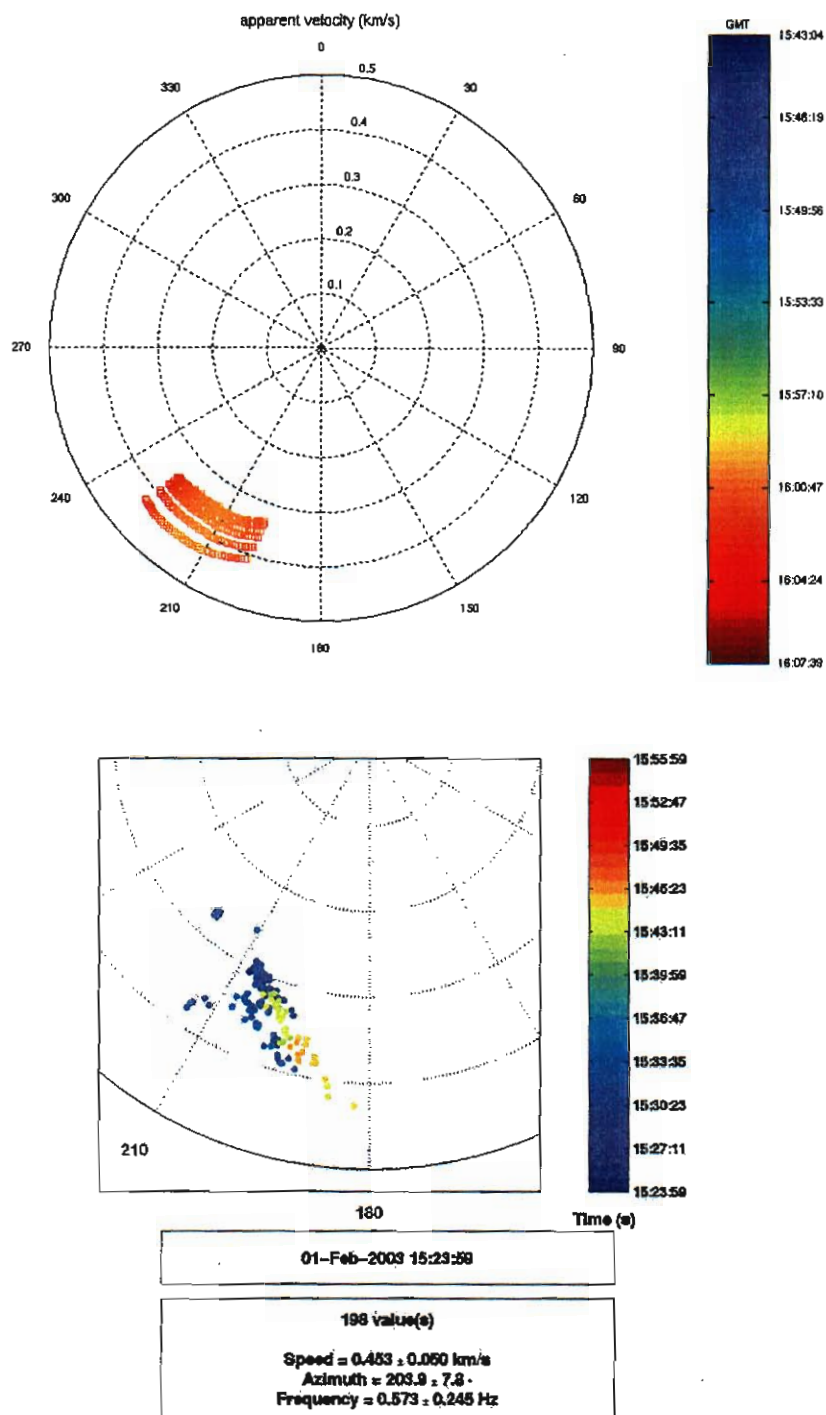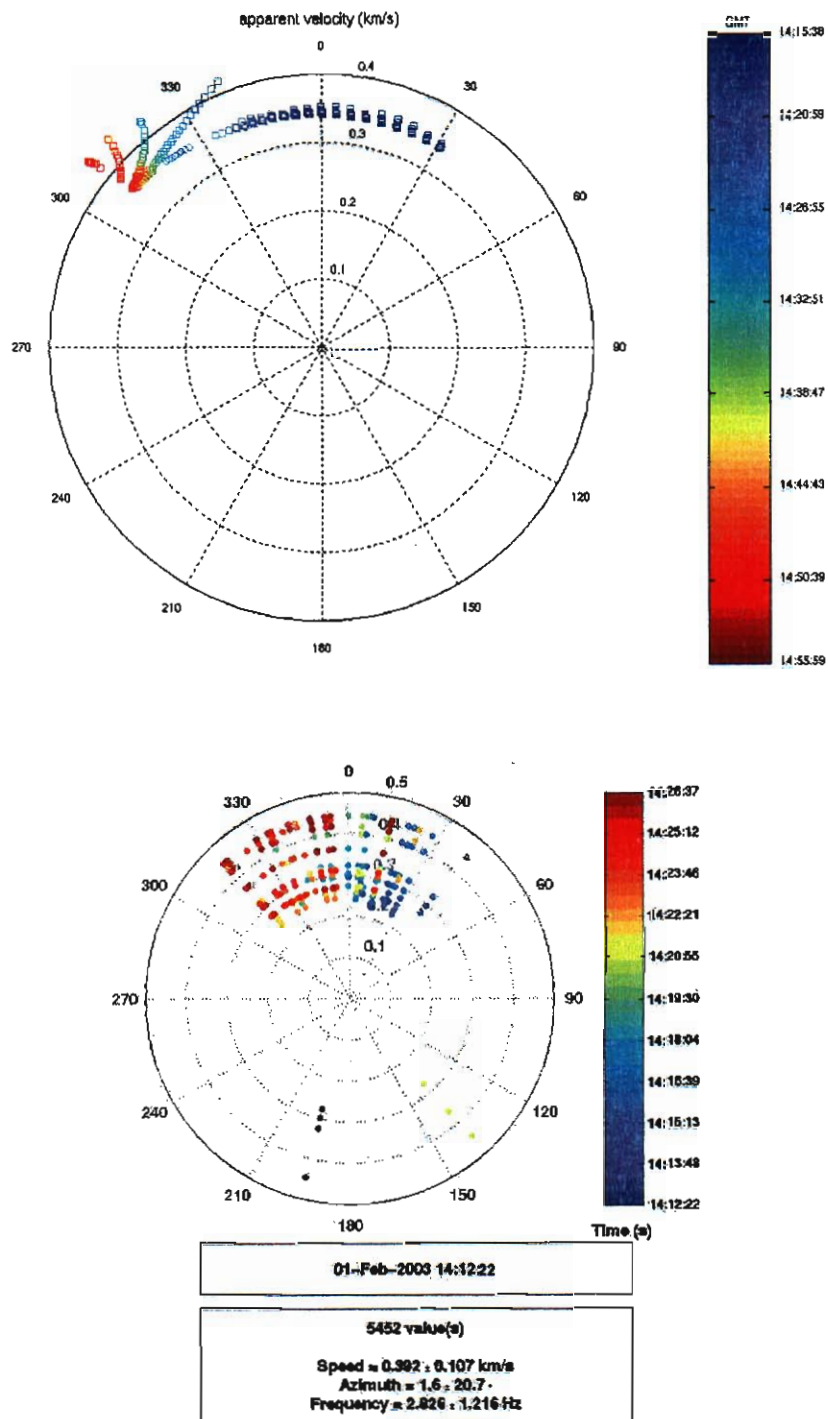
Figure 4. HARPA predictions (upper panel, Gibson and Norris, 2003b) and PMCC observations (lower panel) for PDIAR

Figure 5. HARPA predictions (upper panel, Gibson and Norris, 2003b) and PMCC observations (lower panel) for I56US.

Figure 6. HARPA predictions (upper panel, Gibson and Norris, 2003b) and PMCC observations (lower panel) for DLIAR

Figure 7. HARPA predictions (upper panel, Gibson and Norris, 2003b) and PMCC observations (lower panel) for TXIAR

Figure 8. HARPA predictions (upper panel, Gibson and Norris, 2003b) and PMCC observations (lower panel) for I10CA

Figure 9. HARPA predictions (upper panel, Gibson and Norris, 2003b) and PMCC observations (lower panel) for White Sands (WSMR).

159
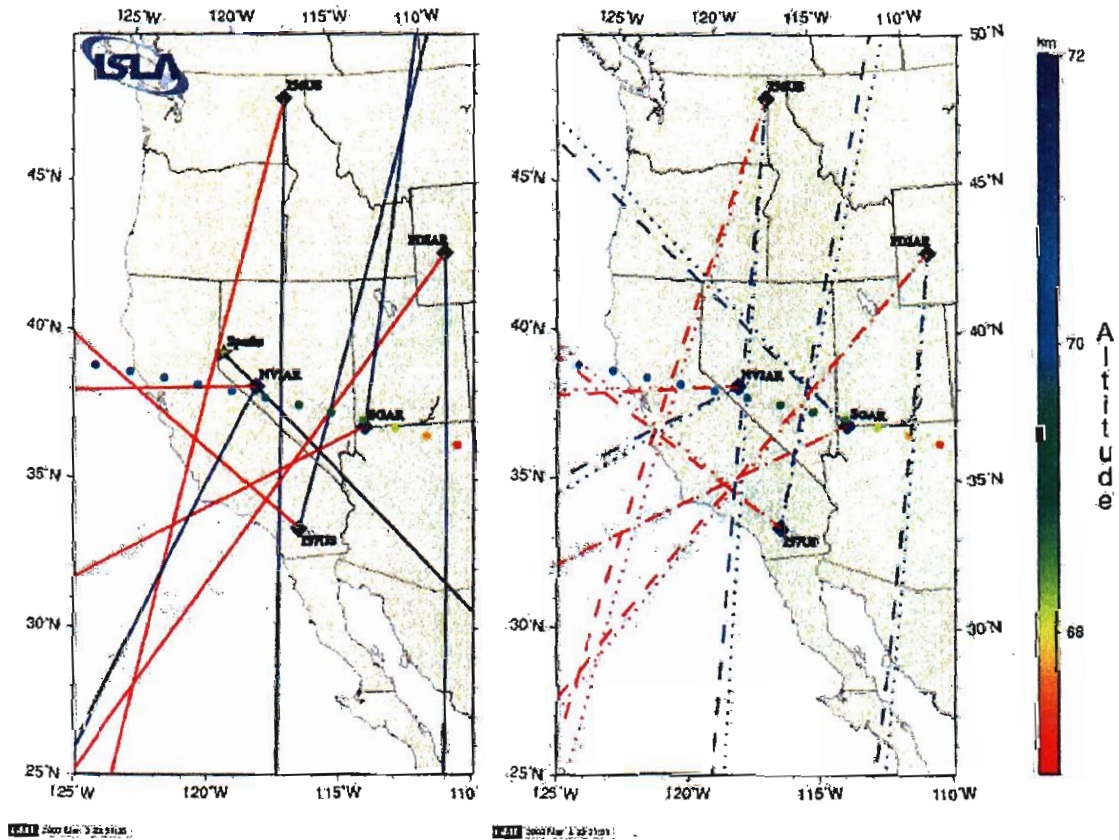
Figure 10. Backazimuth windows at each array for the Western sector of the Columbia approach. The left hand panel of each plot shows the backazimuth windows at each array including the sonic boom arrival and uncorrected for the wind. The panels on the right show the backazimuth windows at each array after exclusion of the N-wave and after azimuth corrections due to the wind component transverse to the propagation direction. The dashed line shows the maximum deflection and the dotted line shows the minimum deflection for all phases listed in Appendix A.

160
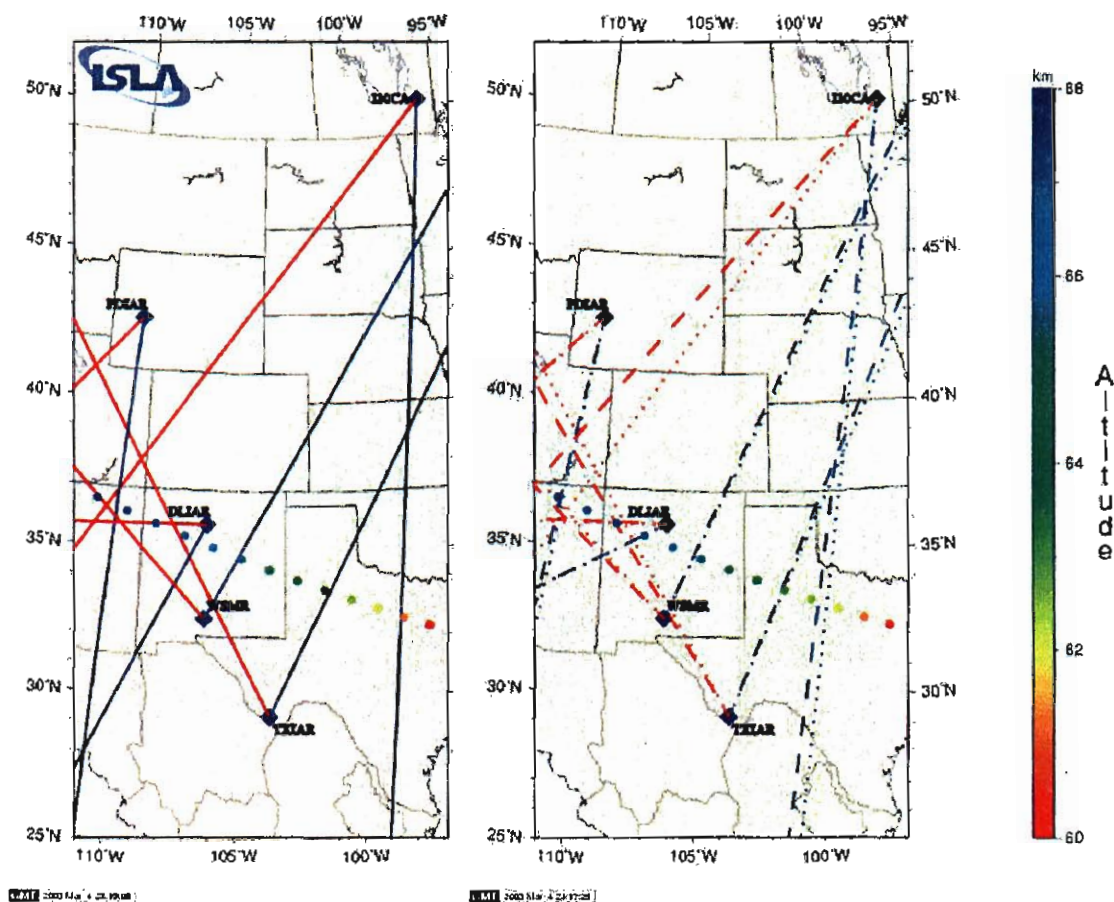
Figure 11. Backazimuth windows at each array for the Eastern sector of the Columbia approach. The left hand panel of each plot shows the backazimuth windows at each array including the sonic boom arrival and uncorrected for the wind. The panels on the right show the backazimuth windows at each array after exclusion of the N-wave and after azimuth corrections due to the wind component transverse to the propagation direction. The dashed line shows the maximum deflection and the dotted line shows the minimum deflection for all phases listed in Appendix A.
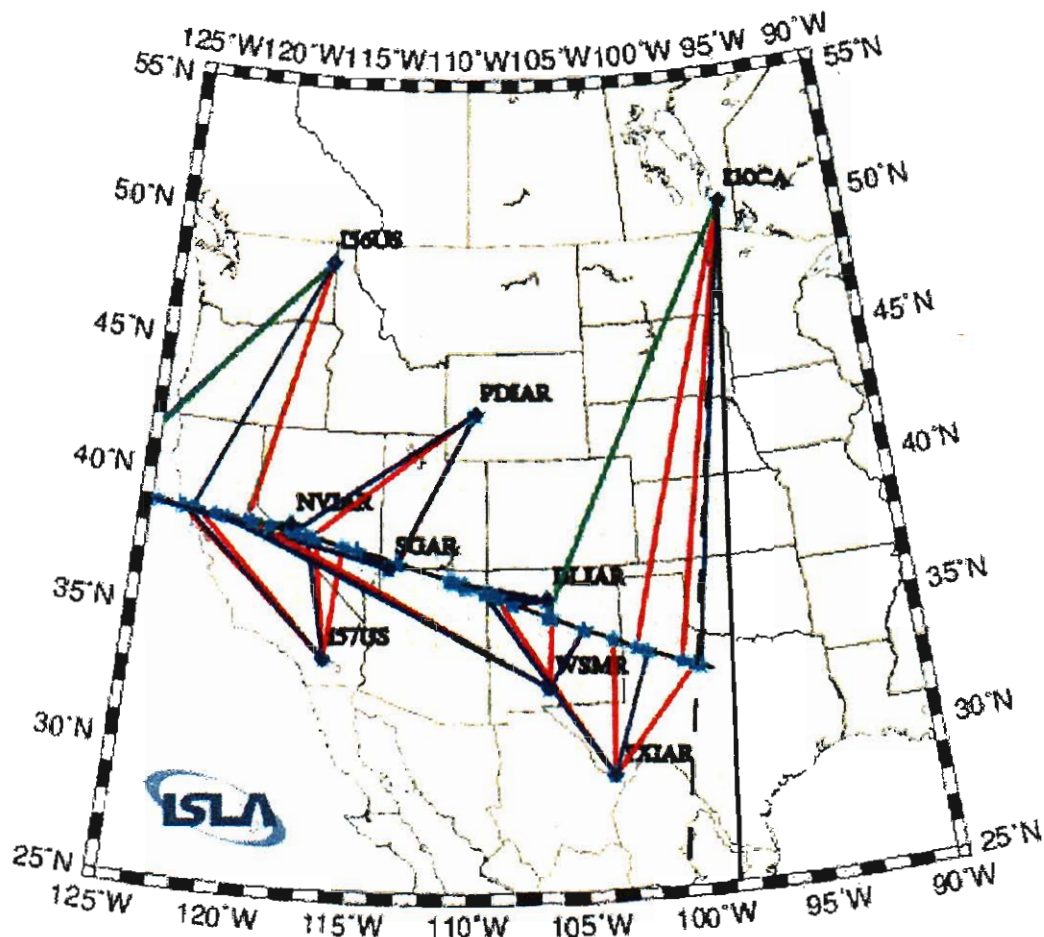
Figure 12. Predicted launch points of acoustic energy along the Columbia reentry based on the theoretical values provided in Appendix A. These results exclude the direct sonic boom arrival for NVIAR, SGAR, and DLIAR. Red lines correspond to arrivals refracted in the thermosphere, blue lines are used for stratospheric ducted phases, and green lines correspond to tropospheric arrivals. The solid black line denotes the Easternmost detected arrival backazimuth and the dashed black line is the wind-corrected backazimuth, as shown in Figure 11.
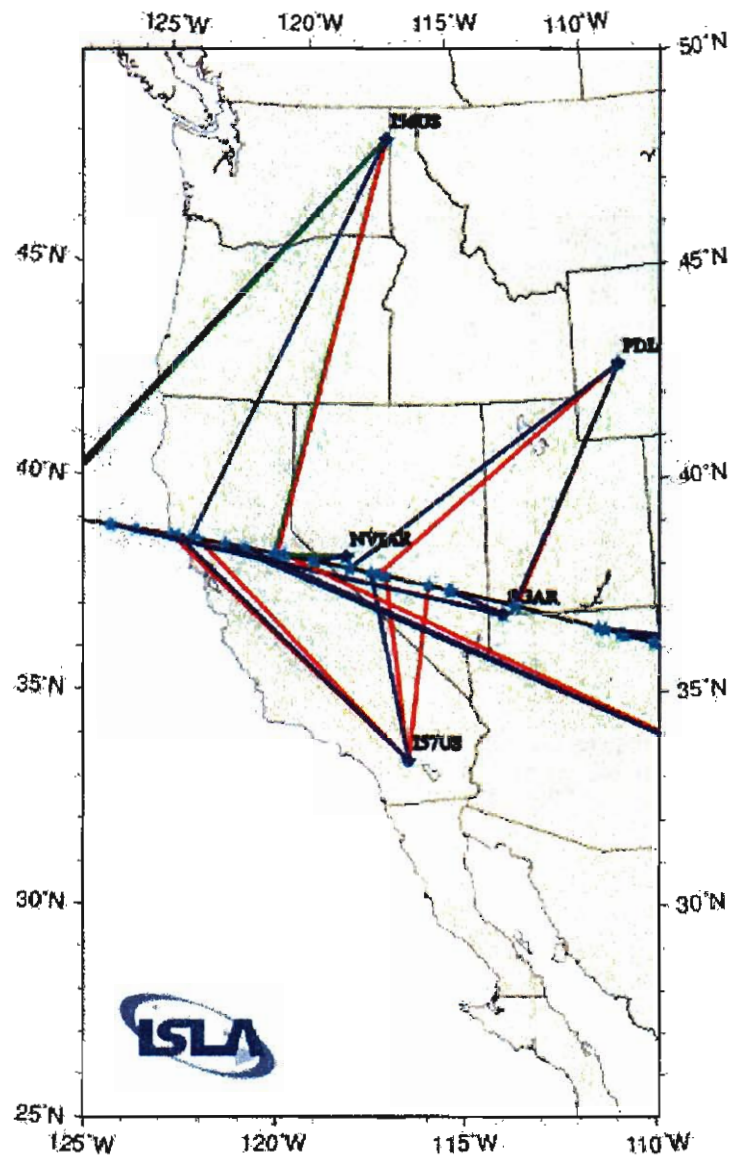
Figure 13. Closer view of the Westernmost stations, with color coding as in Figure A1. Gaps between azimuths are artificial, as lines denote only the theoretical maximum and minimum ranges for each station. Thermospheric arrivals for SGAR point to the same area as the stratospheric arrivals, and the former are not visible in the figure.
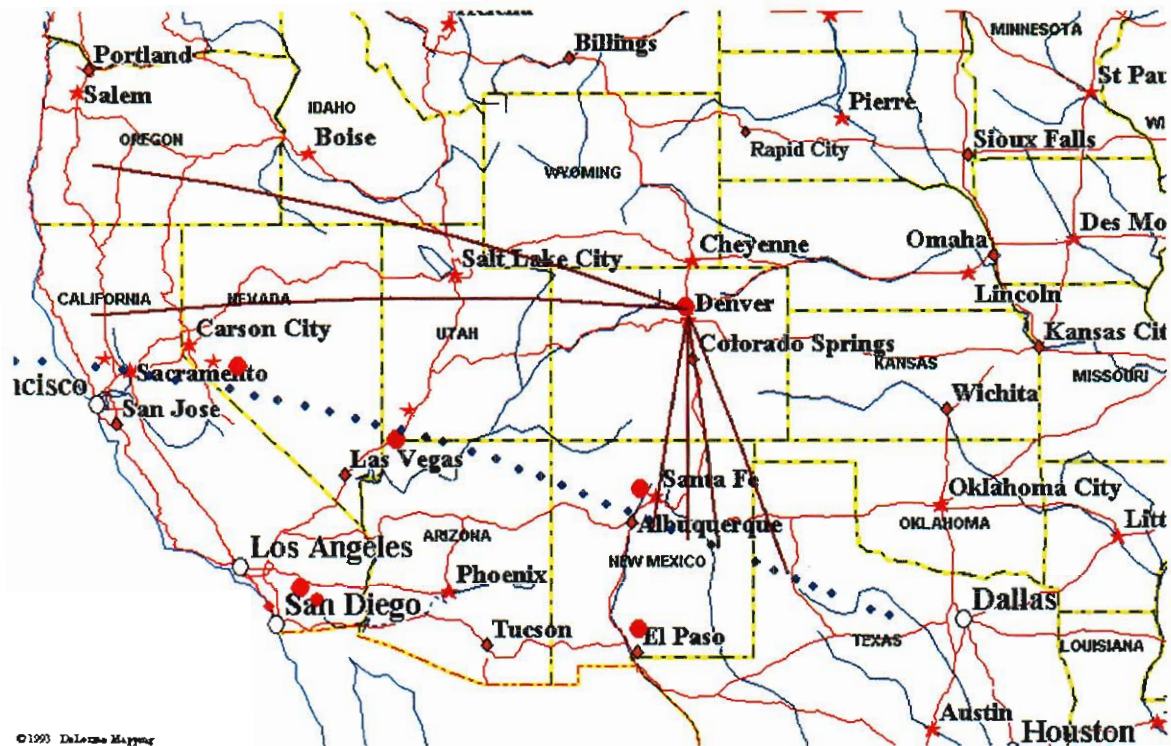
Figure 14. Map of key detections from infrasound station in Erie, Colorado, reproduced from Figure 7 of Bedard et al., 2003.
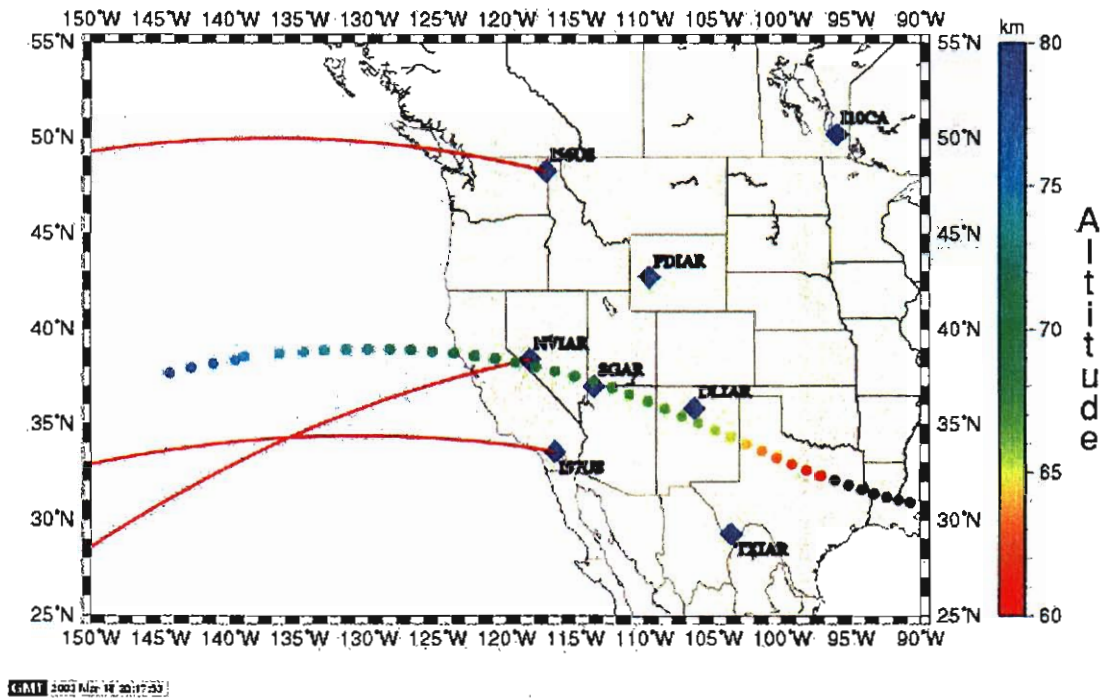
Infrasonic Arrivals from Columbia

Figure 15. Arrival azimuth of impulsive bursts at I57 and NVIAR mentioned in Bedard et al (2003), Appendix B, and a precursory event at I56US with an arrival time of ~14:33:30 UT.
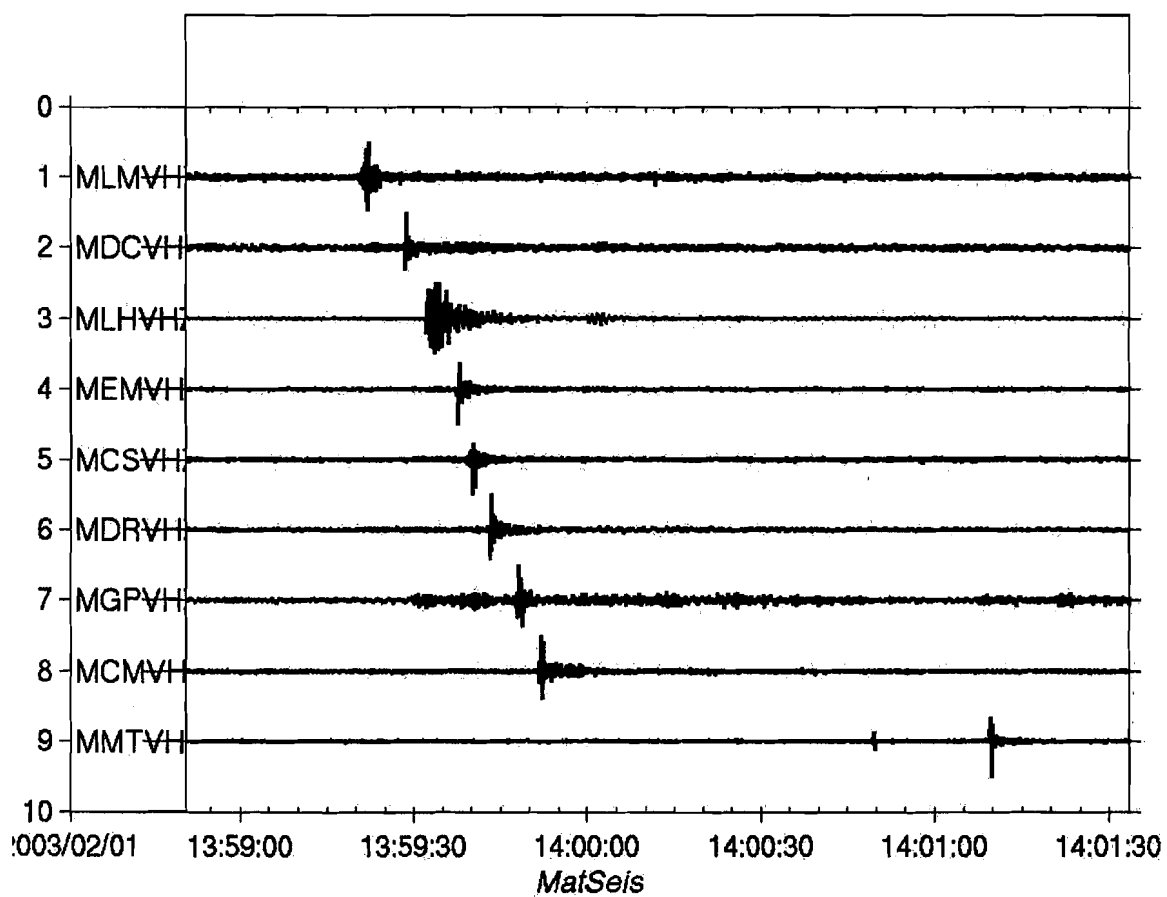
Figure 16. Seismic detections of the shuttle south of the CA-NV border. The larger arrivals appear to be from the sonic boom.

Appendix A. Predicted celerity and azimuth deviations for specified phases, excluding the bow wave.

Phase list for celerity and azimuth deviations
M. Garcés and C. Hetzer, ISLA
4-Mar-03

Station	Lat Degrees	Long Degrees	Azimuth Degrees	phase ID	max celerity m/s	mean az dev degrees	ETA
NVIAR	38.4296	-118.3036	240	it	298	2.5	13:58:37
				is	318	2	
				iw	346	-1	
				isd	313	2.2	
			268	it	299	0	13:59:29
				is	320	0	
				iw	343	-1.7	
				isd	310	0	
I57US	33.6065	-116.4532	15	it	283	-4.5	14:23:27
				itd	271	-4.2	
				isd	289	-3	
			310	it	291	-3.5	14:33:40
				is	306	-1.7	
				isd	302	-1.5	
I56US	48.264	-117.1257	180	it	275	4	14:51:08
				itd	288	4	
				iwd	322	3	
				isd	290	3	
			194	it	285	4	14:59:33
				is	327	3	
				iwd	326	2.5	
				isd	292	3	
SGAR	37.0153	-113.6153	245	it	298	2	14:01:58
				is	311	2	
				isd	307	1.8	
			321	it	289	-4.5	14:38:15
				is	306	-2.5	
				isd	307	-2.3	

PDIAR	42.7668	-109.5939	184	it	277	5.2	14:29:00	
				itd	288	5.5		
				isd	293	4.5		
			220	it	289	4.2	14:39:00	
				is	302	4		
				isd	302	3.4		
DLIAR	35.8676	-106.3342	240	it	300	2.5	14:02:45	14:10:17
				is	312	2.3		
				isd	299	2.4		
			270	it	306	0	14:04:09	14:12:03
				is	322	0.5		
				isd	306	1		
WSMR	32.639	-106.3416	28	it	310	-4	14:12:41	
				itd	268	-3.7		
				isd	287	-3.3		
			317	it	286	-3.8	14:57:50	
				is	304	-2		
				isd	313	-1.5		
TXIAR	29.3338	-103.667	25	it	311	-3.5	14:28:19	
				itd	269	-3.5		
				isd	287	-2.5		
			333	it	293	-4	14:42:00	
				is	303	-2		
				isd	303	-2.5		
I10CA	50.2015	-96.0269	186	it	283	4.2	15:48:09	
				iw	326	4		
				itd	291	5		
				isd	294	4		
			220	it	281	4.3	15:25:09	
				is	301	4		
				iw	324	-0.4		
				isd	291	3.5		

Appendix B. USGS Preliminary Information on Sonic Wave in N California
David Oppenheimer
Project Chief of the Northern California Seismic Network
February 04, 2003

Date: Mon, 3 Mar 2003 17:38:59 -0800
From: "David Oppenheimer" <oppen@usgs.gov>
To: "Milton Garcés" <milton@isla.hawaii.edu>

-----Original Message-----
From: David Oppenheimer [mailto:oppen@usgs.gov]
Sent: Tuesday, February 04, 2003 9:15 PM
To: Paul.s.hill@nasa.gov; sharon.c.conover@nasa.gov
Cc: Bill Ellsworth; Hiroo Kanamori; Bob Uhrhammer (UCB); Hiroo Kanamori;
Andy Michael
Subject: USGS Preliminary Information on Sonic Wave in N California

This email provides preliminary information regarding observations of the Shuttle Columbia sonic wave as recorded by seismic networks in northern California and northern Nevada. There are two images in the attached zip file. If you have trouble opening this document, please let me know and I will resend.

Data and Observations
Seismic networks recorded sonic waves beginning at 13:57:15 UTC. The earliest observation was at USGS station GDC north of San Francisco. The attached image (shuttle_sonic.pdf – *editor's note: the attached files are included as figures at the bottom of the document*) shows the pattern of arrival times across seismic networks operated by the USGS, University of California Berkeley, and the University of Nevada Reno. The reference time of the data is 13:57:15 UTC, and the contour interval is 10 sec. Contours outside the range of labeled data are considered unreliable. Arrival time observations at individual seismic stations are shown as solid dots.

The sonic waves were recorded by more than 140 seismic stations. Most of the observations were made on vertical, short-period seismometers that record frequencies in the range of 1-25Hz. The 2nd attachment (example_waveforms.bmp) shows a typical observation on 2 such stations (the tick interval is 1 sec). The duration of the signals vary from a few seconds to 10's of seconds. Observations were also observed on few broadband seismometers which have greater frequency bandwidth (i.e., 100s-20Hz), but with a typical duration of ~3 minutes. Finally, the signal was observed on a few microbarographs operated by the University of California Berkeley, where the signal is above unity in the 0.08-0.4 Hz band and peaks at ~20 dB at a frequency of 0.2 Hz.

Preliminary Interpretation
The azimuth of the wave is approximately N95E as measured between seismic stations GDC and MMC (indicated on pdf map). The apparent velocity of the wavefront is approximately 7.8 km/s

as measured between these two stations, which are separated by 361 km and by a relative travel time of 44 sec.

The following calculations are "back-of_the_envelope". If we assume that the observed sonic wave was generated when the shuttle was directly overhead and that the shuttle was at an altitude of 60 km (~200,000 ft), and that the average speed of sound is 300 m/s, it took 60/0.3 = 200 seconds for the shock wave to reach the ground. This means that the shuttle passed overhead of this station at roughly 13:54.

Assuming a propagation speed of the shock front across the region of 7.8 km/s, by the time that the shock reached the ground, the shuttle would have been on the order of 1560 km to the east. Sharon, you mentioned that at 13:57:15 the shuttle was over Albuquerque, which is 1532 km from GDC, so this result seems reasonable.

Next step
The above interpretation is obviously simplistic. We are willing to assemble a group of experts (which I am not) to conduct a more sophisticated interpretation. If you concur, we request information on the Shuttle flight path.

We are preparing the seismic data for submission to NASA after completion of quality control. We expect to complete this effort early next week, but we can send the data sooner if requested.

The media has been alerted to the existence of the sonic data. We request your advise on whether to discuss these observations with the media and whether to release to them the attached images.

We also request your permission to make the raw seismic information available at our datacenters (the standard practice in the seismic community). Please note that data at our datacenters are freely accessible via the Internet. If these data are to be embargoed, we would like some understanding of how the embargo can be lifted.

Sincerely,

David Oppenheimer
Project Chief of the Northern California Seismic Network

David Oppenheimer   office:650.329.4792
U.S. Geological Survey   fax: 650.329.4732
345 Middlefield Road.-MS 977   email: oppen@usgs.gov
Menlo Park, CA 94025
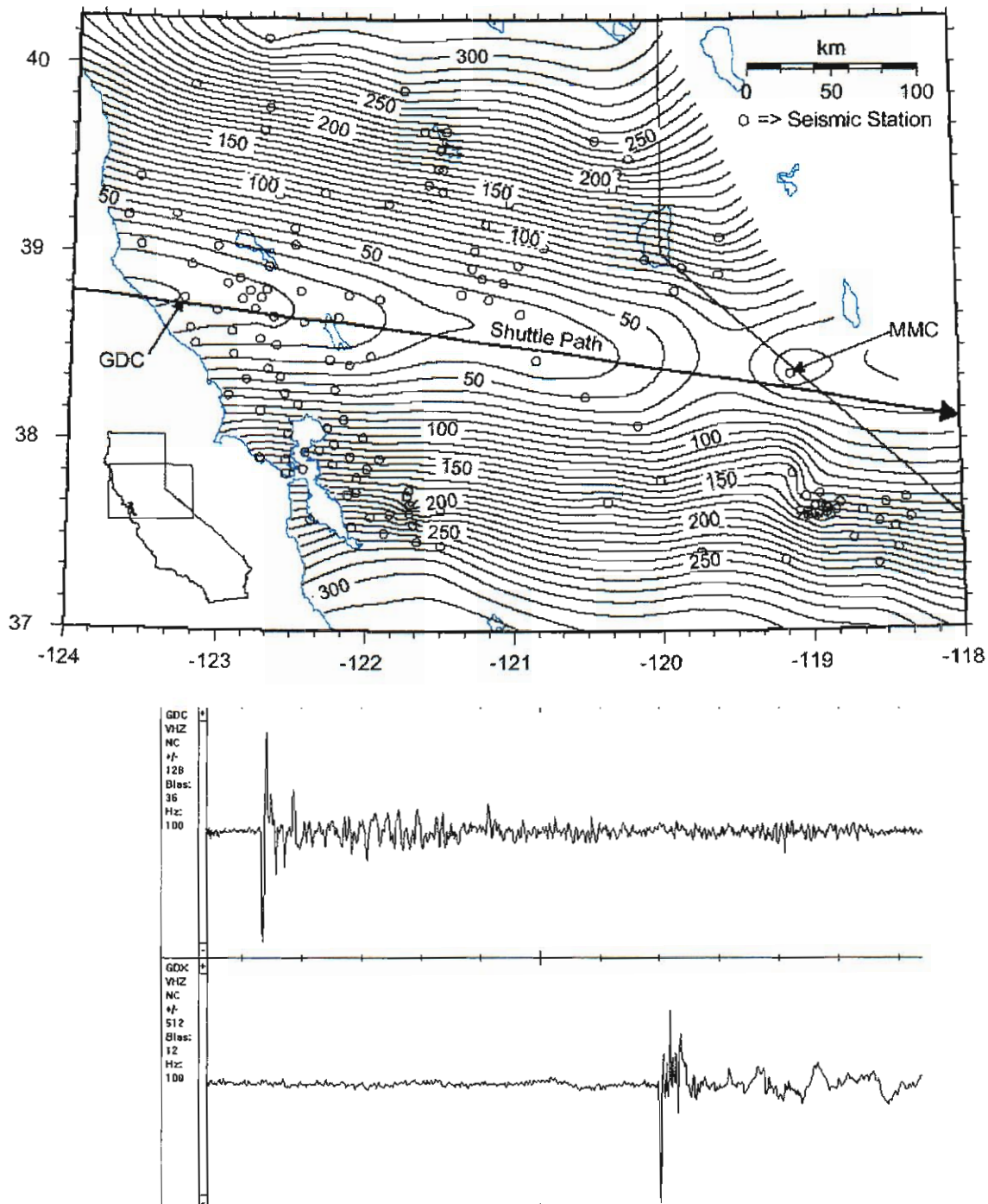
Figure B1. Image files attached with the original message.
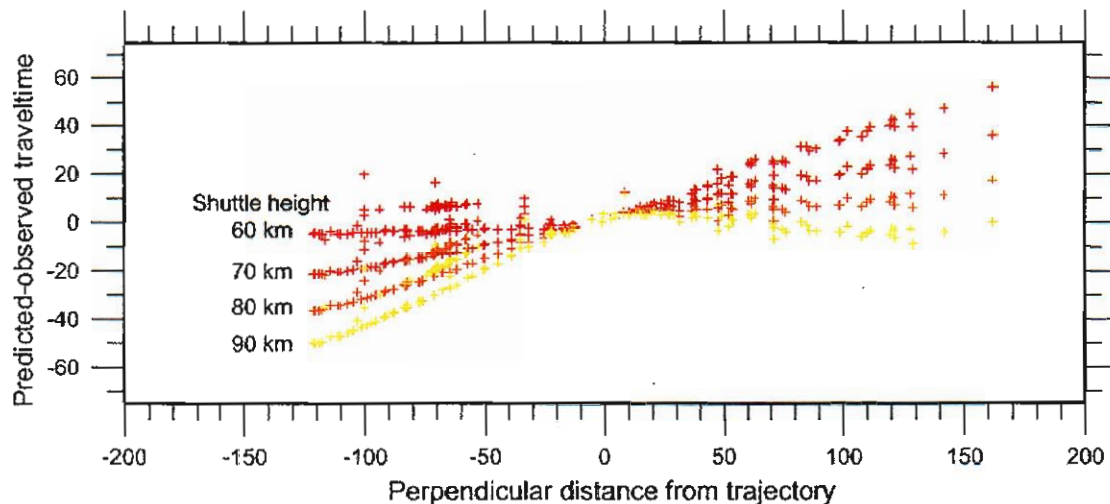
Figure B2. Predicted-observed traveltime vs the perpendicular distance from the shuttle trajectory as a function of different shuttle elevations. The predicted traveltimes were computed using eqn 2 of Qamar, 1995, SRL, p 5-12 with the values v_sound = 0.31 km/s (assumed), v_shuttle = 7.33 km/s (from Columbia data over CA), beta = -0.1819 (from Columbia data over CA). Positive distance values are north of the shuttle path. The sonic boom is propagating slower south of the path, and hence the predicted-observed values are relatively smaller south of the path (*editor's note: as discussed with Dr. Oppenheimer in a separate correspondence, this observation is consistent with the Northward winds in the stratosphere and thermosphere along the Columbia's trajectory, see Garcés et al., 2003, Part 2*).

James C. Pechmann
University of Utah
February 21, 2003

Date: Mon, 3 Mar 2003 17:39:14 -0800
From: "David Oppenheimer" <oppen@usgs.gov>
To: "Milton Garcés" <milton@isla.hawaii.edu>

-----Original Message-----
From: James C. Pechmann [mailto:pechmann@seis.utah.edu]
Sent: Friday, February 21, 2003 3:50 PM
To: james.k.lawson1@jsc.nasa.gov; john.m.curry@nasa.gov; oppen@usgs.gov
Cc: benz@usgs.gov; wallace@geo.arizona.edu; pechmann@seis.utah.edu;
terra@seis.utah.edu; pankow@seis.utah.edu; arabasz@seis.utah.edu
Subject: Utah Seismic Records of Columbia Overflight,, Feb. 1, 2003

Dear Drs. Lawson, Curry, and Oppenheimer:

In response to your requests, I have examined data from the University of Utah seismograph stations in southwestern Utah for the following time period of interest to the space shuttle Columbia investigation: 13:58 to 14:46 UTC on Feb. 1, 2003. I was assisted in this effort by Fabia Terra, Kris Pankow, and Walter Arabasz.

SUMMARY

We did not observe any seismic signals which we can unambiguously attribute to falling objects hitting the ground. However, we did observe some seismic signals on one of the stations which we cannot readily identify. These signals might be (a) reflected sonic booms from the shuttle, (b) seismic and/or sonic waves generated by impacts of shuttle debris, or (c) signals of some other origin. If these observations are of potential value to the Columbia investigation, we recommend that they be examined by someone with greater expertise in interpreting seismic records of sonic booms and impacts.

DATA

The University of Utah operates two different computer systems designed to detect seismic events (primarily earthquakes and blasts) which are large enough to be recorded on multiple stations of the University's regional seismic network. Neither system detected any seismic events during the time period of interest.

To search for seismic events below the detection thresholds of the automatic systems, and to search for sonic signals, we examined data from six different stations of the University of Utah network for the time period 13:58 to 14:46 UTC on Feb. 1, 2003: EKU, ICU, BHU, ARUT, BTU, and DWU (Figure 1). All of these stations are equipped with short-period, vertical-component velocity sensors and analog telemetry systems. BHU is also equipped with

horizontal-component sensors. The instrumentation at these stations is sensitive to ground motions primarily in the frequency range 1 to 10 Hz. We corrected the data from station DWU for a polarity reversal by multiplying it by -1.
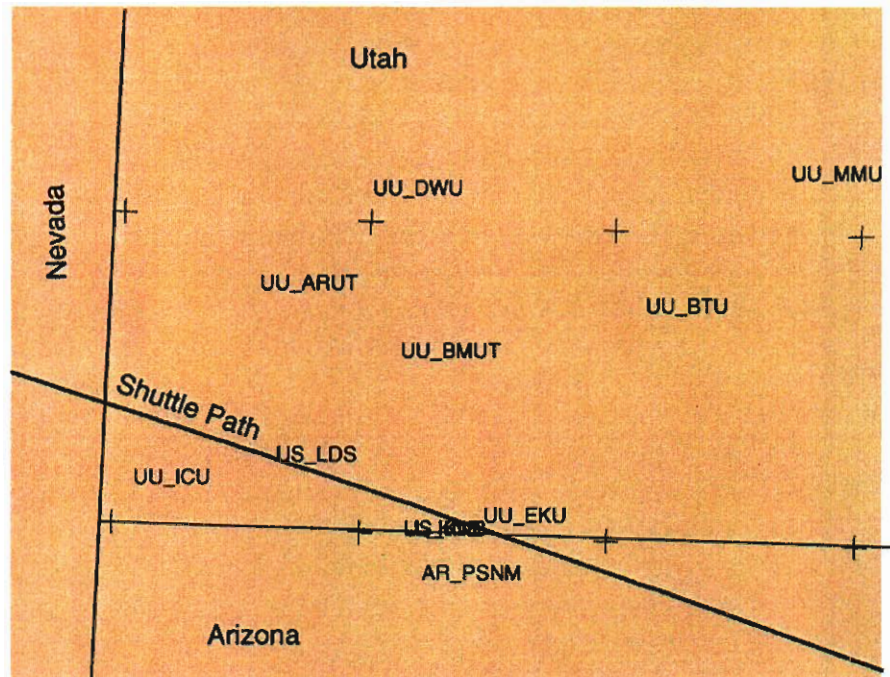
Figure 1 is a map of southwestern Utah and vicinity showing the locations of the seismic stations we used, other seismic stations, and the path of the shuttle. It is a modified enlargement of a figure provided to us by David Oppenheimer of the U.S. Geological Survey. The first two letters of the station labels are network codes: UU for the University of Utah Seismic Network, US for the U.S. National Seismic Network, and AR for the University of Arizona Seismic Network. Note that the station labeled UU_BMUT is actually UU_BHU. The station US_LDS no longer exists. Data from station US_KNB for the time period of interest are not available from either the IRIS data center or the U.S. National Seismic Network data center. We do not have access to the data from the University of Arizona station AR_PSNM.

I have put the vertical-component records from the six stations we used on our anonymous ftp site at ftp.seis.utah.edu in the file /pub/users/pechmann/shuttledata.tgz . This file is a gzipped UNIX tar file containing six data files in Seismic Analysis Code (SAC) format. All of the data from the University of Utah seismic network are available on-line from the IRIS data center at www.iris.washington.edu.

OBSERVATIONS

Figure 2 shows the 48-minute-long vertical-component records from the six stations. The records are plotted in order of increasing distance from the shuttle path.

We interpret the first large signal on all of the stations to be ground motions induced by the sonic boom from the shuttle. The arrival times of the largest energy pulse in these signals ranges from 13:59:24 at ICU to 14:01:58 at DWU. These arrival times are roughly consistent with the expected arrival times for the shuttle sonic boom, but we did not rigorously calculate the latter for comparison purposes. Figure 3 shows enlargements of the sonic boom signals for 20-sec-long time periods beginning seven seconds before the largest energy pulses. The first two numbers at the right of each record indicate the time period of the record in the same units as the time scale on Figure 2: seconds relative to 13:58:00. Note that with the possible exception of BTU, the first motion of the largest energy pulse at each station is downward. This first motion direction is consistent with the sudden increase in atmospheric pressure which occurs at the onset of a sonic boom.

The sonic boom signal at station EKU is much longer in duration than those at the other stations. We speculate that this longer duration is due to the close proximity of EKU to the shuttle path (Figure 1). We note that the EKU sonic boom signal has a sudden onset and gradual decay of amplitude with time which is more characteristic of earthquake signals than sonic booms. However, if the EKU signal was from an earthquake, then its total duration of about 200 seconds would indicate a magnitude of about 3. A magnitude 3 earthquake would be clearly visible on the records from the other stations.

The only station which shows any significant signals after the initial large sonic boom is ICU (37.1497 N 113.9235 W). Following the initial sonic boom at 13:59:24, ICU recorded an 8-sec-long series of waves beginning at 14:01:57, another 8-sec-long series of waves beginning at 14:02:5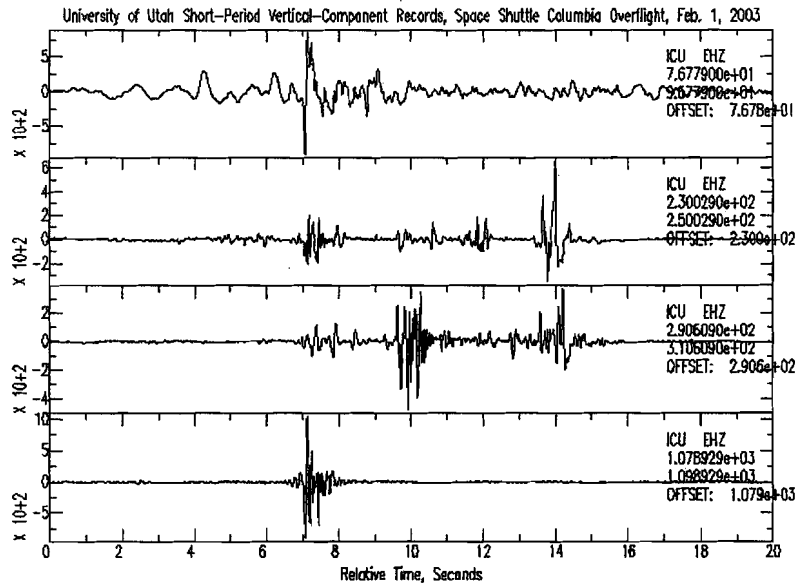7, and a 2-sec-long wavetrain beginning at 14:16:05. Figure 4 compares the waveforms of the initial sonic boom at ICU (top box) with the waveforms of the three groups of later arrivals (bottom three boxes). The waveforms of the second group of arrivals, and to a lesser extent the third group, are similar in character to the waveforms of the initial sonic boom--especially if one allows for polarity reversals. This observation suggests that at least some of the later arrivals might be reflected sonic booms. The last significant arrival at ICU is 1002 sec after the initial sonic boom, and has a rather different waveform. If it is a reflected sonic boom, then its travel path would have to be about (1002 sec)(0.3 km/sec) = 300 km longer than the travel path of the direct sonic boom. It is difficult to understand why a reflected sound wave with such a long travel path would not be seen on any other stations, as the station spacing is only 50 to 125 km.

Unfortunately, the waveform comparison in Figure 4 does not by itself provide a solid basis for identifying the three groups of later arrivals at ICU. Although these signals might be reflected sonic booms from the shuttle, we cannot rule out other possible origins. In particular, we cannot rule out the possibility that they are seismic and/or sonic waves generated by impacts of shuttle debris. As we do not have much experience with seismic signals from impacts and space shuttle sonic booms, we suggest that our data be further examined by someone else who does.

Sincerely,

James C. Pechmann

James C. Pechmann	Tel: (801) 581-3858
Research Associate Professor	FAX: (801) 585-5585
University of Utah	
Dept. of Geology & Geophysics	E-mail: pechmann@seis.utah.edu
135 S 1460 E Rm 705 WBB	
Salt Lake City, Utah 84112-0111	

Figure C1. Map of southwestern Utah and vicinity showing the locations of the seismic stations we used, other seismic stations, and the path of the shuttle.
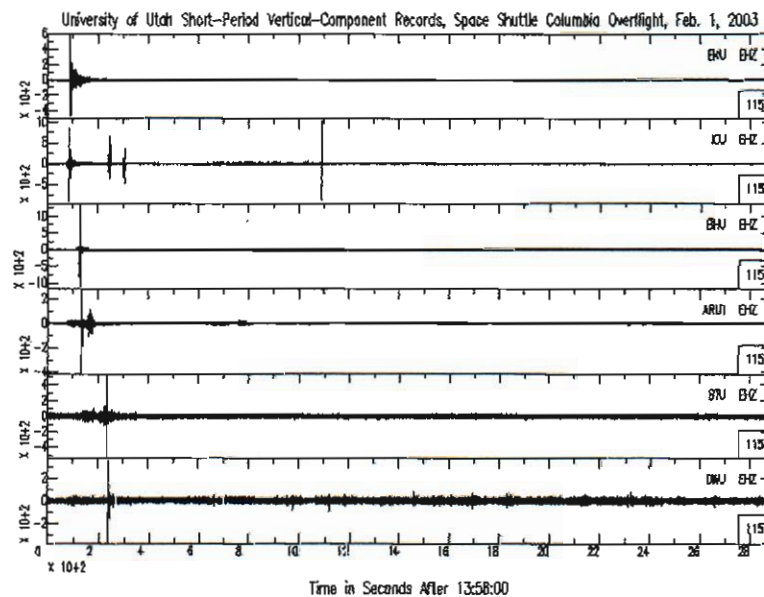
Figure C2. The 48-minute-long vertical-component records from the six stations. The records are plotted in order of increasing distance from the shuttle path.

176

University of Utah Short-Period Vertical-Component Records, Space Shuttle Columbia Overflight, Feb. 1, 2003
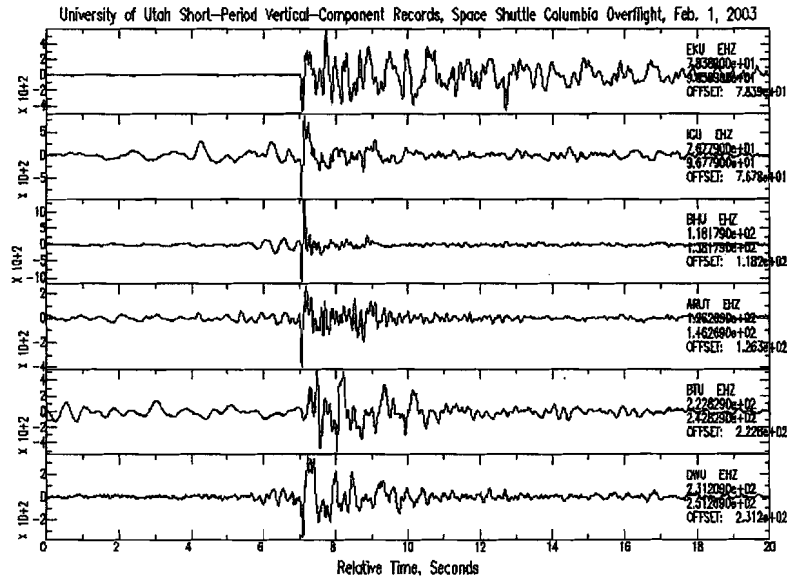
Figure C3. Enlargements of the sonic boom signals for 20-sec-long time periods beginning seven seconds before the largest energy pulses

University of Utah Short-Period Vertical-Component Records, Space Shuttle Columbia Overflight, Feb. 1, 2003

Figure C4. Comparison of the initial sonic boom at ICU (top box) with the waveforms of the three groups of later arrivals (bottom three boxes).

Appendix D. Further inspection of SGAR detections for STS-107

M. Garcés and C. Hetzer, ISLA
March 17, 2003

As noted in this and other documents, backazimuths are useful for first estimates but may be misleading in the determination of a precise source location. For the April 23, 2001 and August 25, 2000 bolides, the backazimuth for the DOE array in Fairbanks, Alaska, had a deviation of approximately 10 and 14 degrees, respectively, from the satellite locations. During the Columbia reentry, the SGAR station appeared to observe detections from the W and WSW which exceed our preconceptions of how far azimuth deviations are permitted to diverge from predicted values. Figure D1 shows a 2h segment for SGAR, and illustrates that there are abundant coherent ambient signals arriving from the Western quadrant (240-330 degrees) that may not be associated with the Columbia. However, there is a clear increase in signal energy associated with the passing of the Columbia, starting with the sonic boom and lasting over 40 minutes. A closer inspection of the most energetic arrivals after the sonic boom are shown in Figure D2, and show that there appears to be coherent acoustic energy arriving from the West. As we select later arriving energy, there appear to be some excursions towards the WSW (Figure 3, lower panel, from Garcés and Hetzer, Part 3). It is possible that the southward azimuth excursions are due to the superposition of the Columbia signals with the ambient infrasound field, but due to the continuous temporal extent of the later arrivals we may not be able to discriminate between coincident background signals and the Columbia arrival. However, we take the increase in acoustic energy from the ambient levels to be indicative of the Columbia arrivals, and thus retain the time of the latest arrival for SGAR given in Appendix A.

An integral part of the PMCC detection parameters is the family size, which specifies how many adjacent pixels must be within the specified thresholds before a coherent arrival is sustained enough to be worthy of a detection flag. To try eliminate small noise bursts, we experimented with increasing the family size from 5 to 15. Not only were the arrivals from the W and WSW still present, but the specification of a higher family size may yield a false sense of security on the accuracy of the detections. It appears the same problems with interfering signals are still present with the larger family size.

In conclusion, the backazimuth estimates at SGAR may be biased towards the south by the ambient infrasound field. However, it is not clear how to discriminate this effect from extreme southwards excursion of infrasonic waves induced by the wind or local site effects. For STS-107, sound waves coming from the West towards SGAR would be traveling along the dominant stratospheric wind direction, and may be more vulnerable to rapidly changing lower atmosphere perturbations not captured by the climatological models we have presently available. However, analysis of STS-78 and STS-90 also show similar southerly azimuthal excursions (see Garcés and Hetzer, Part 5). Since these reentries with the same 39 degree orbital inclination as STS-107 occurred in Summer, when the stratospheric winds are generally reversed, it may be hypothesized that local site effects may also influence the detected direction of arrivals at SGAR.
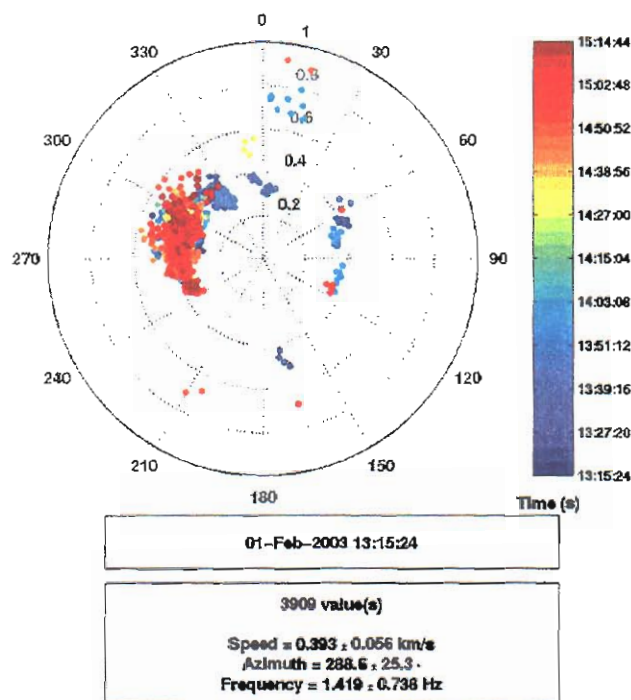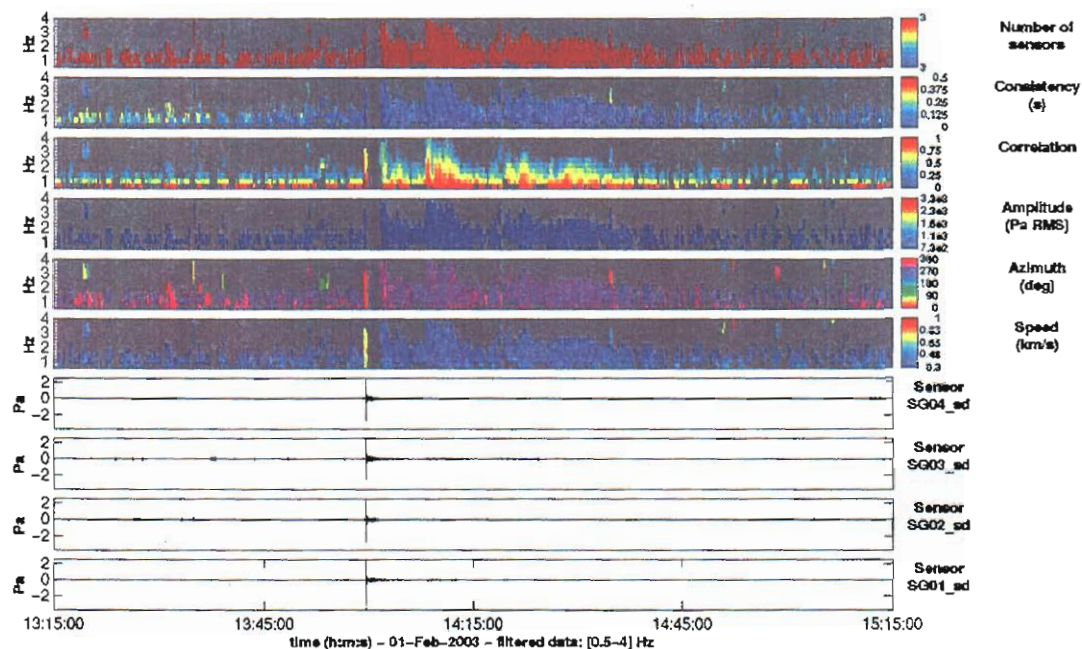
Figure D1. PMCC detections for a 2 hour data segment of SGAR. The detection parameters are: 30s window, 25s overlap, consistency of 0.5, 0.5-4 Hz, and apparent horizontal phase speed of 0.2 to 1 km/s.
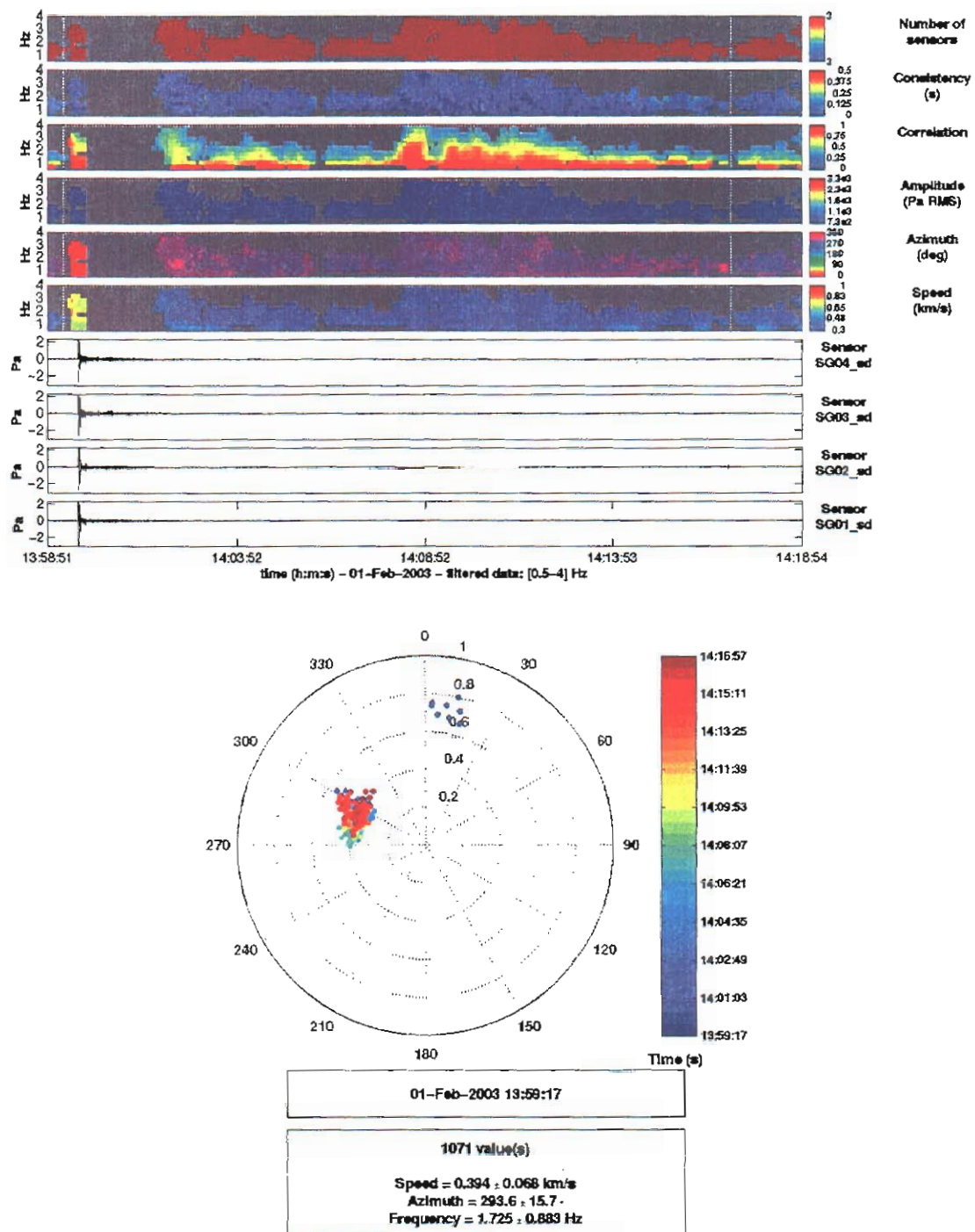
Figure D2. PMCC detections for a narrow data segment of SGAR, corresponding only to the energetic time segment between the dotted lines in the upper panel. The detection parameters are as in Figure D1.

Appendix F

Infrasonic Investigations of the Columbia Re-Entry
Part 5. Analysis of infrasonic signals for Shuttle reentries with 39 degree orbital
inclinations: STS-78, STS-90, and STS 77

Milton Garcés and Claus Hetzer
Infrasound Laboratory, University of Hawaii, Manoa
March 21, 2003, *Revision 2*

1. Introduction

At the request of various members of the US Infrasound Team, ISLA analyzed infrasound data provided by CMR and associated with Shuttle reentries with orbital inclination angles of 39 degrees (Table 1). Since this is the same orbital inclination as STS-107, we hoped to find some features in common that may help us unravel the details that led to the Columbia accident. The most obvious difference between STS-107 and the three missions listed in the table below is the time of year: Columbia STS-107 entered in Winter (February 1, 2003) and all other reentries were in Summer.

Table 1. Previous shuttle missions with orbital inclination of 39 degrees for which infrasound data is readily available.

Mission	Orbital Inclination (deg)	LandDate	Time(local)	Time(GMT)	Loc
STS-77	39	05/29/96	7:09:18	11:09:18	KSC
STS-78	39	07/07/96	8:36:45	12:36:45	KSC
STS-90	39	05/03/98	12:08:59	16:08:59	KSC

2. Available Data

We processed the available infrasound data from SGAR, LSAR, and TXIAR for STS-78, SGAR, LSAR, PDIAR, and TXIAR STS-90, and TXIAR for STS-77. Figure 1 shows the location of these stations relative to the trajectory of STS-78, STS-77, STS-90, and STS-107, as provided on March 21, 2003 by Natalie J. Dworak, NASA.

2.1. STS-78, SGAR

The lower panel of Figure 1 shows the SGAR detection for STS-78. Based on their azimuth, arrivals can be separated into five distinct packets: sonic boom, westerly arrival, and three large easterly arrivals. Figure 2 shows the sonic boom arrival at SGAR, its clear time progression westward towards the approach direction, and a decrease in phase speed with increasing time. Figure 3 shows a closeup of the second energy packet, corresponding to arrivals from the west. Note that, as in STS-107, there appears to be a southwards azimuth deflection below what we

would expect to see from the approach track (Appendix D of Part 4). Figures 4 and 5 concentrate on the detections arriving predominantly from the east, although there are some westerly arrivals also in the last three energy bundles. The polar plot in Figure 5 shows that in the first easterly arrival has a progression towards the south and towards lower phase speeds with increasing time. This is consistent with energy arriving later from more distant parts of the receding trajectory. These easterly arrivals may be explained by easterly stratospheric winds during Summer. No arrivals from the east were observed at SGAR from the STS-107 reentry, probably because the stratospheric winds were blowing from the west in February. However, the character of the late arriving coda for STS-78 is reminiscent of STS-107.

2.2. STS-78, TXIAR
The TXIAR data set for this event had an outage between what appears to be the first arrival and the main arrival, and these two data segments are shown in Figures 6 and 7. In contrast to STS-107, the main arrival does not appear to have clearly distinct bursts, although there are some common features between the two reentry signals, such as the (generally) westward progression with increasing time.

2.3. STS-78, LSAR
Unusable data. This is unfortunate, as the shuttle passed directly overhead.

2.4. STS-90, SGAR
The SGAR data set for this event had an outage in the trailing edge of the coda. The sonic boom and the arrivals corresponding to the approach are shown in Figures 8 and 9, with a clear westward progression. In contrast to STS-78, except for the N-wave there are no clear easterly arrivals. The arrival sequence is somewhat reminiscent of STS-107, in particular with regards to the southwards excursions in the backazimuth which would not be expected for the specified orbital inclination. The second part of the coda (after the outage), shown in Figure 10, is rather confused and has energy from multiple directions. From the trajectory shown in Figure 1, we would not expect any shuttle reentry sound to arrive from the south.

2.5. STS-90, TXIAR
Poor quality data set, with possible detections shown in Figure 11.

2.6. STS-90, LSAR
Clear N-wave, with some later arrivals (Figure 12). Some of the arrivals following the N-wave are suspect due to a rather high ambient sound field.

2.7. STS-90, PDIAR
Dubious results in PDIAR, data drops in midst of candidate waveform. Signal appears uncorrelated across array.

2.8. STS-77, TXIAR
Poor quality data set, with possible detections shown in Figure 13.

3. Concluding Remarks

The SGAR detections for STS-78 seemed the most similar in structure to those of STS-107, although the dominant stratospheric wind was probably reversed and led to different arrival azimuths from those of STS-107. However, the westward trend with increasing time for the SGAR detection of STS-90 was also reminiscent of the STS-107 detections. It is of interest to note that although both STS-78 and STS-90 occurred in Summer, the SGAR detections for the latter did not have as clear easterly arrivals as the former. In both STS-78 and STS-90 we observe a southwards trend in the backazimuth with increasing time which appears to exceed the expected trajectory projections. As noted in Appendix D of Part 4, Revision 3, this may be due to a site effect at SGAR. The TXIAR data for STS-78 showed some marked differences from that of STS-107, lacking the clear distinct pulses observed from the latter. However, the westward progressions with increasing time were similar for both STS-78 and STS-107 detections at TXIAR.

Only the stations close to the track recorded an N-wave associated with the sonic boom, and these waveforms are shown in Figure 14. The most anomalous waveform appears to be that at NVIAR, which has quite a bit more structure than at the other stations. The NVIAR array is close to the Nevada-California border, which has been identified in previous reports as an acoustically hot region for the STS-107 reentry. Some of the variability in the N-waves may be attributed to changes in bearing or elevation of the shuttle (Figure 15), although no significant changes are reported in the track history (Figure 16) except near NVIAR, where the start of the slow aileron trim change was initiated.
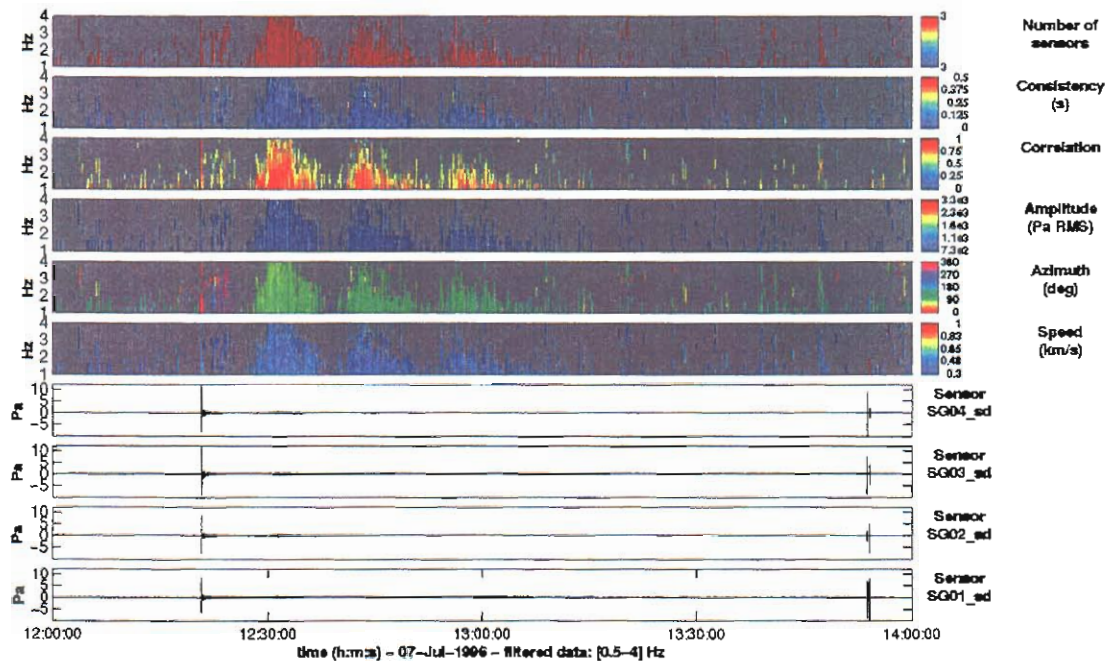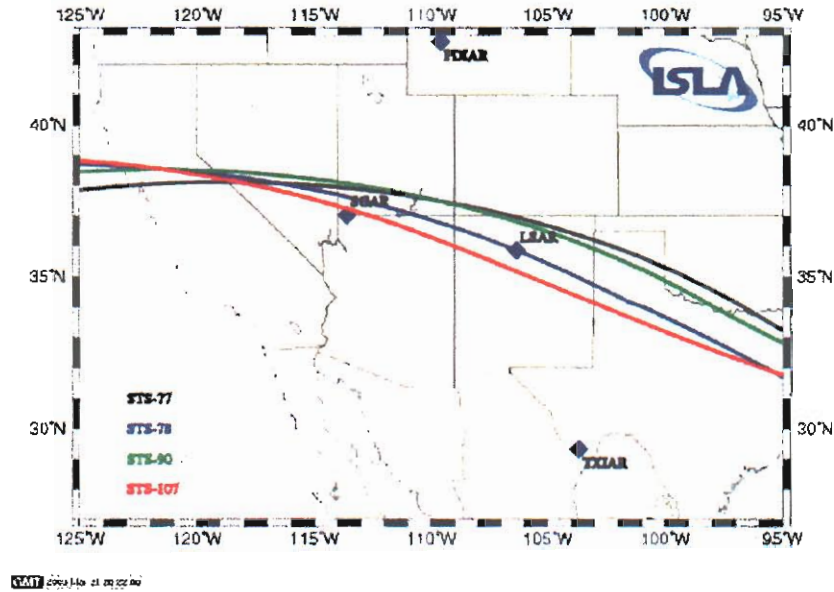
Figure 1. STS-78 track and SGAR detection. Ambient field is predominantly from the East. Arrivals can be separated into five distinct packets: sonic boom, westerly arrival, and three large easterly arrivals. The detection parameters are: frequency band of 1-4 Hz, 5s window, 4s overlap, 1s consistency, speed of 0.2 –1 km/s.
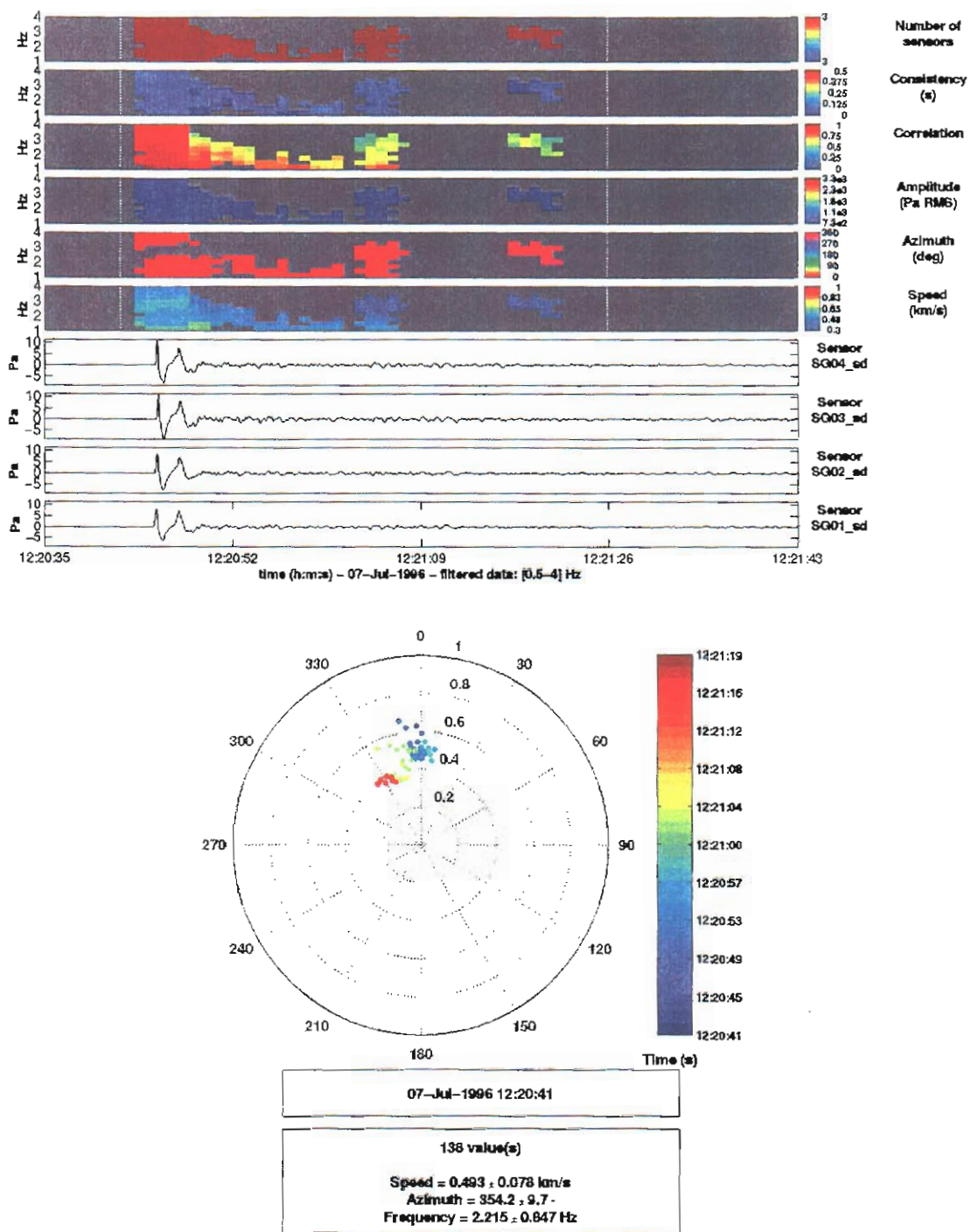
**Figure 2.** Sonic boom (N-wave) of STS-78 at SGAR, with the same detection parameters as in Figure 1. Note clear time progression Westward, towards approach direction, and decrease in phase speed with increasing time.
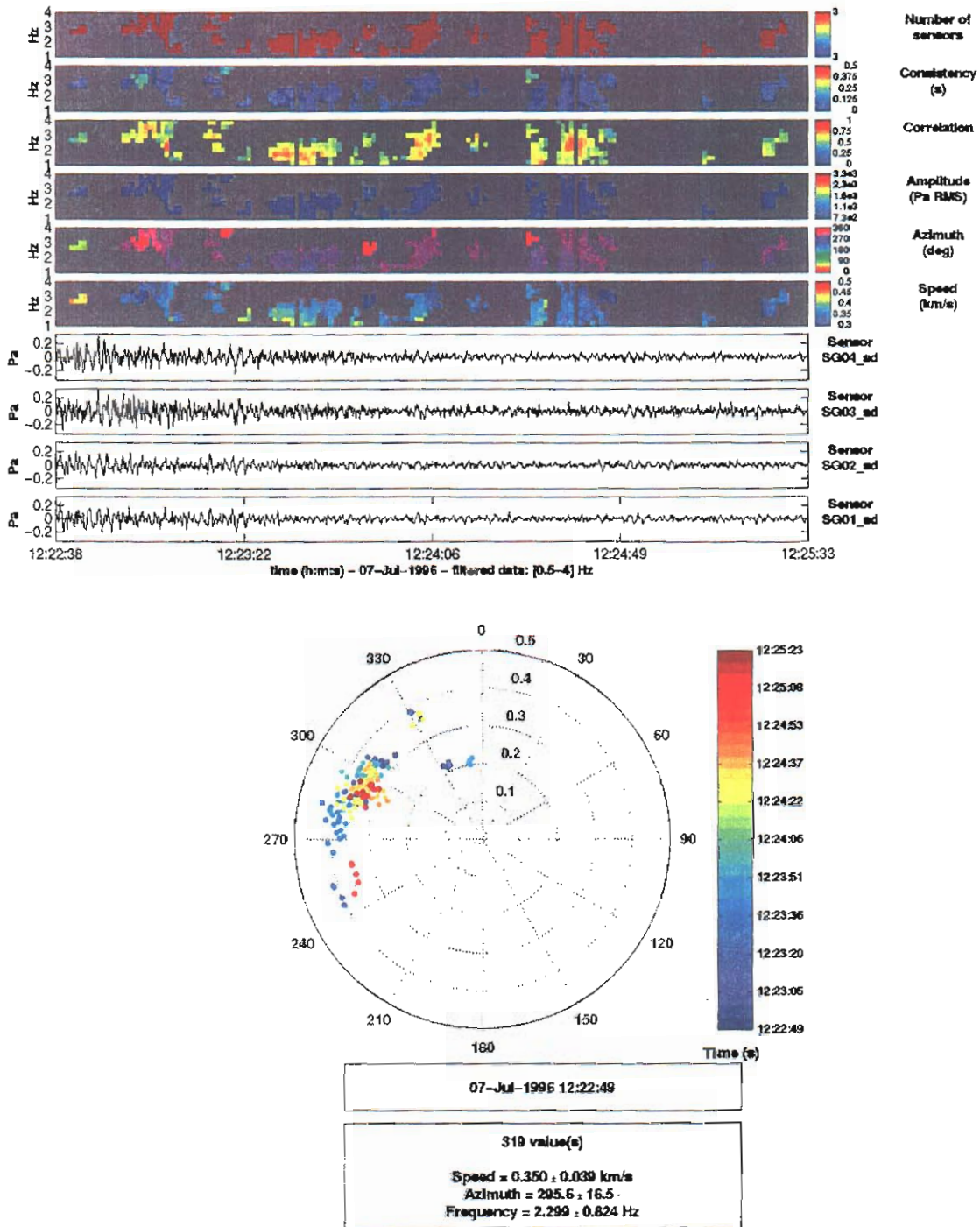
Figure 3. Westerly arrivals for the SGAR detection of STS-78, corresponding to the approach trajectory to SGAR (same detection parameters as in Figure 1).
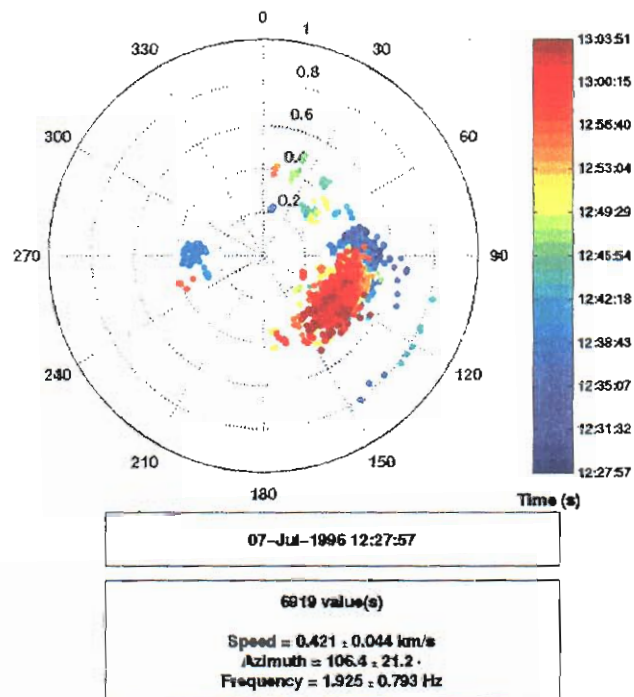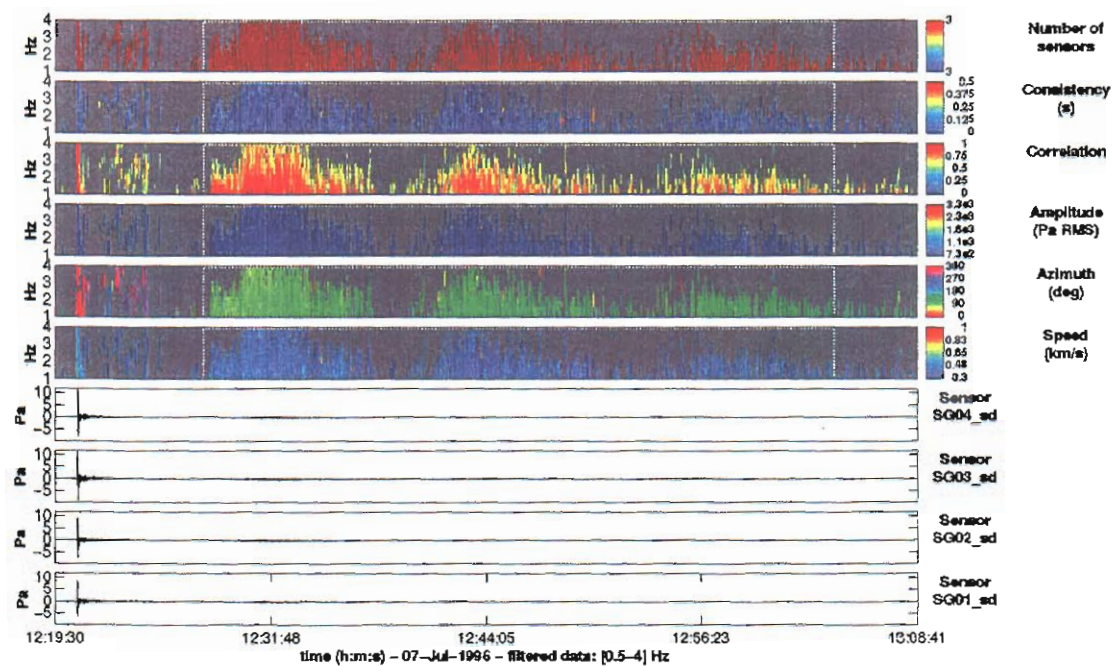
Figure 4. Easterly arrivals for the SGAR detection of STS-78, with the same detection parameters as in Figure 1. There also appear to be some late-arriving westerly signals.
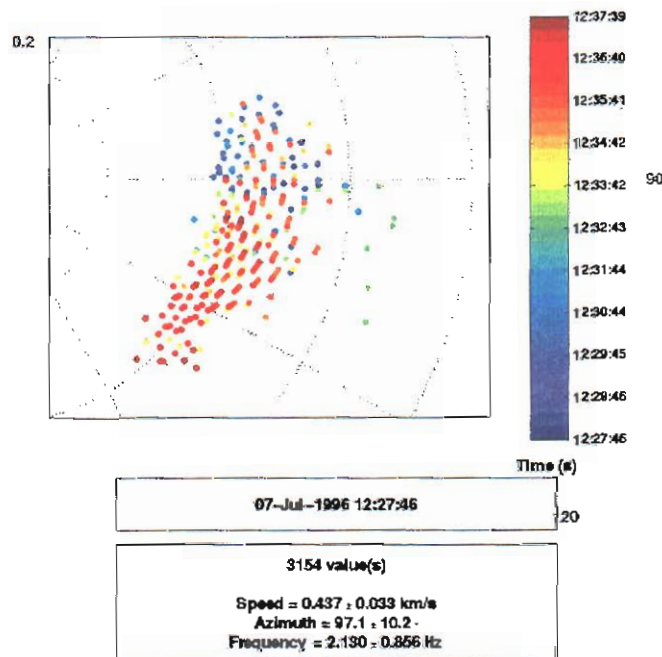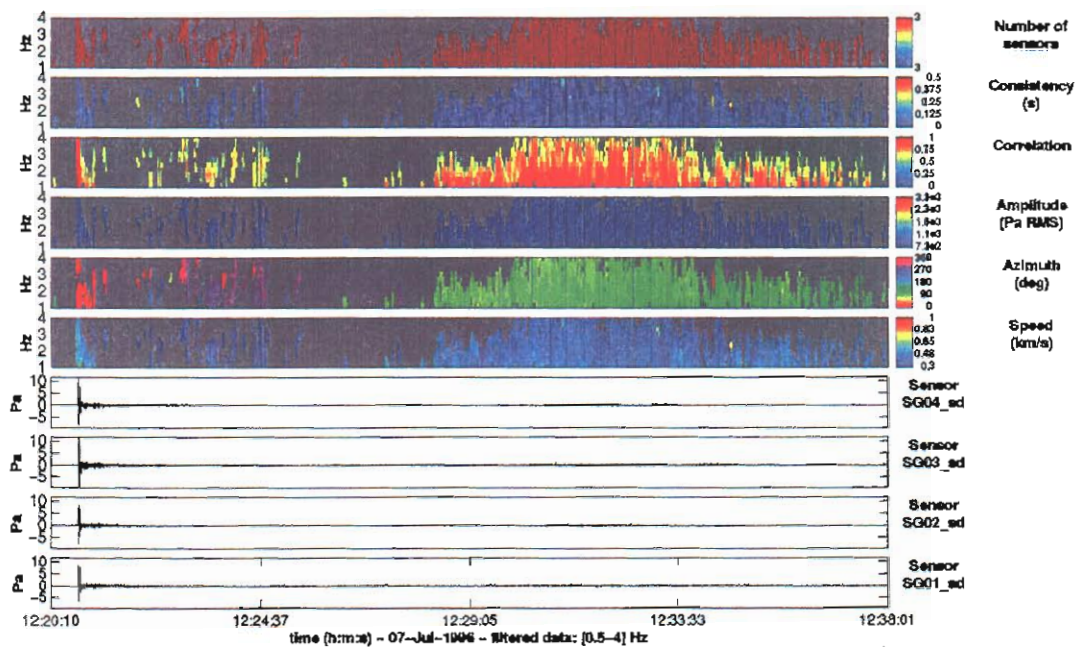
Figure 5. The upper panel shows the first three distinct arrival azimuths observed at SGAR associated with STS-78, corresponding to the N-wave, westerly arrivals, and easterly arrivals. The lower panel shows a polar plot with the azimuth and speed of the first bundle of easterly arrivals, illustrating a southwards progression and decreasing apparent horizontal phase speed with increasing time.
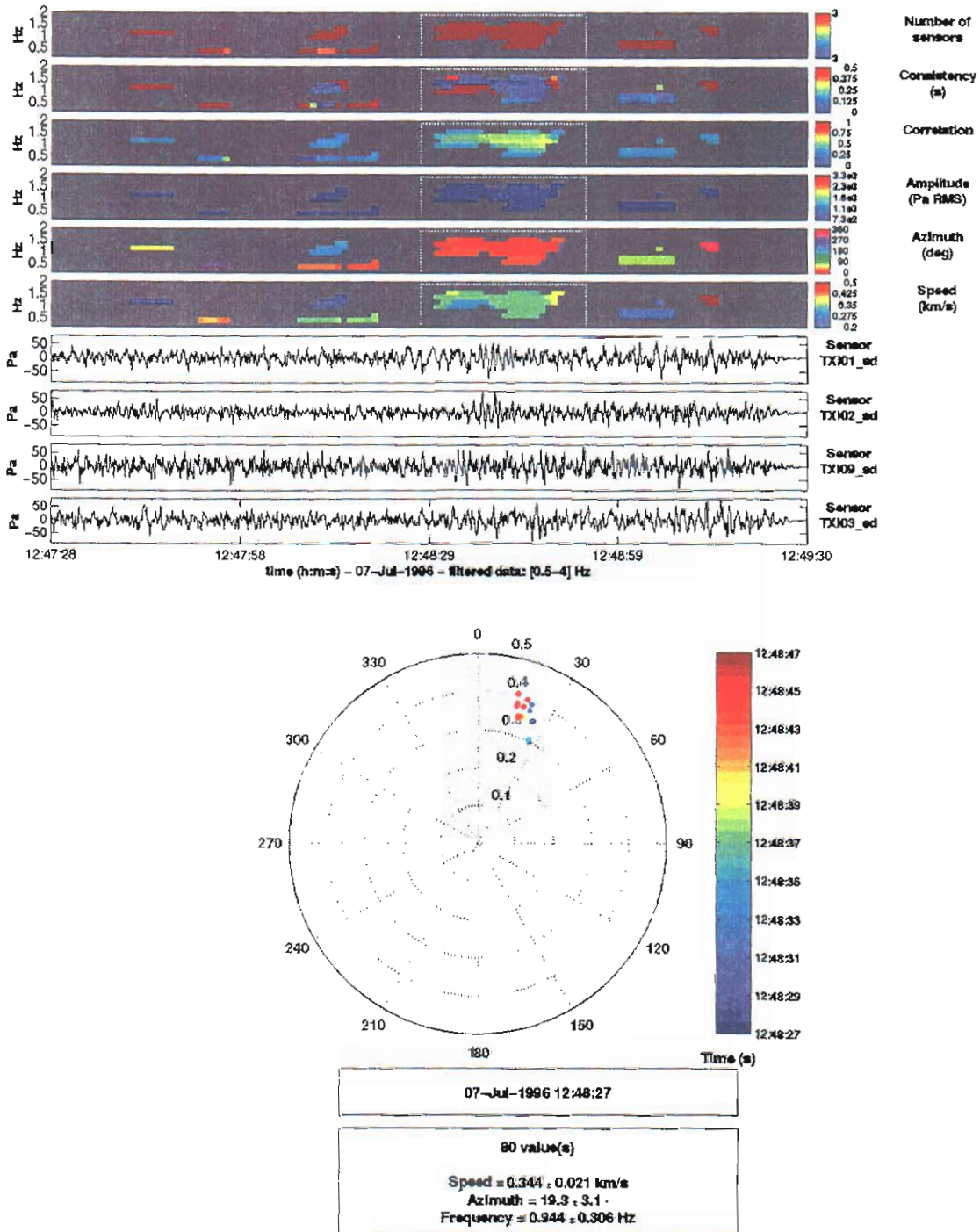
Figure 6. First arrival detected at TXIAR and associated with STS-78. The detection parameters are: frequency band of 0.1-2 Hz, 30 s window, 29 s overlap, 1 s consistency, speed of 0.2-0.7 km/s.
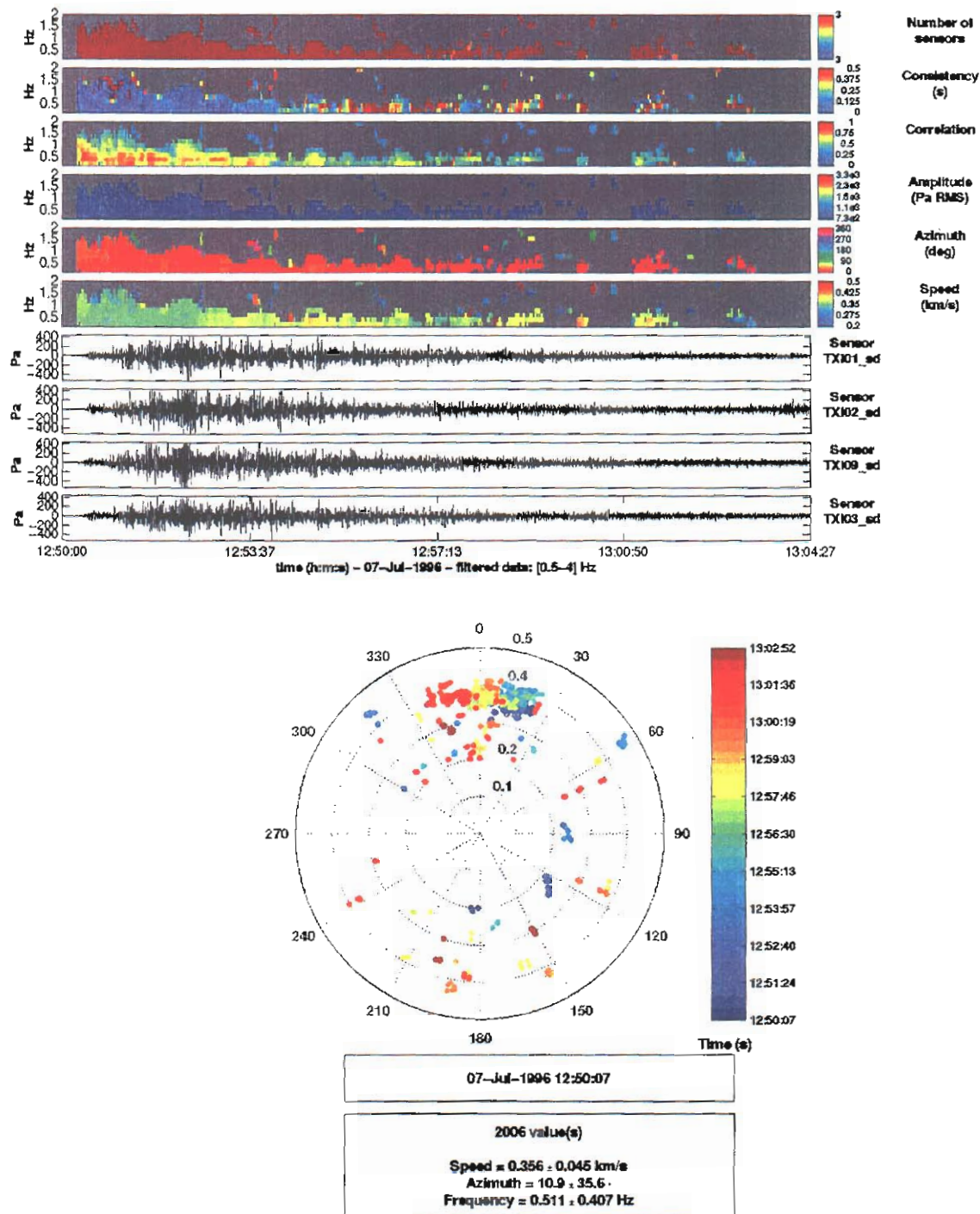
**Figure 7**. Main arrival detected at TXIAR and associated with STS-78. Same detection parameters as in Figure 6.
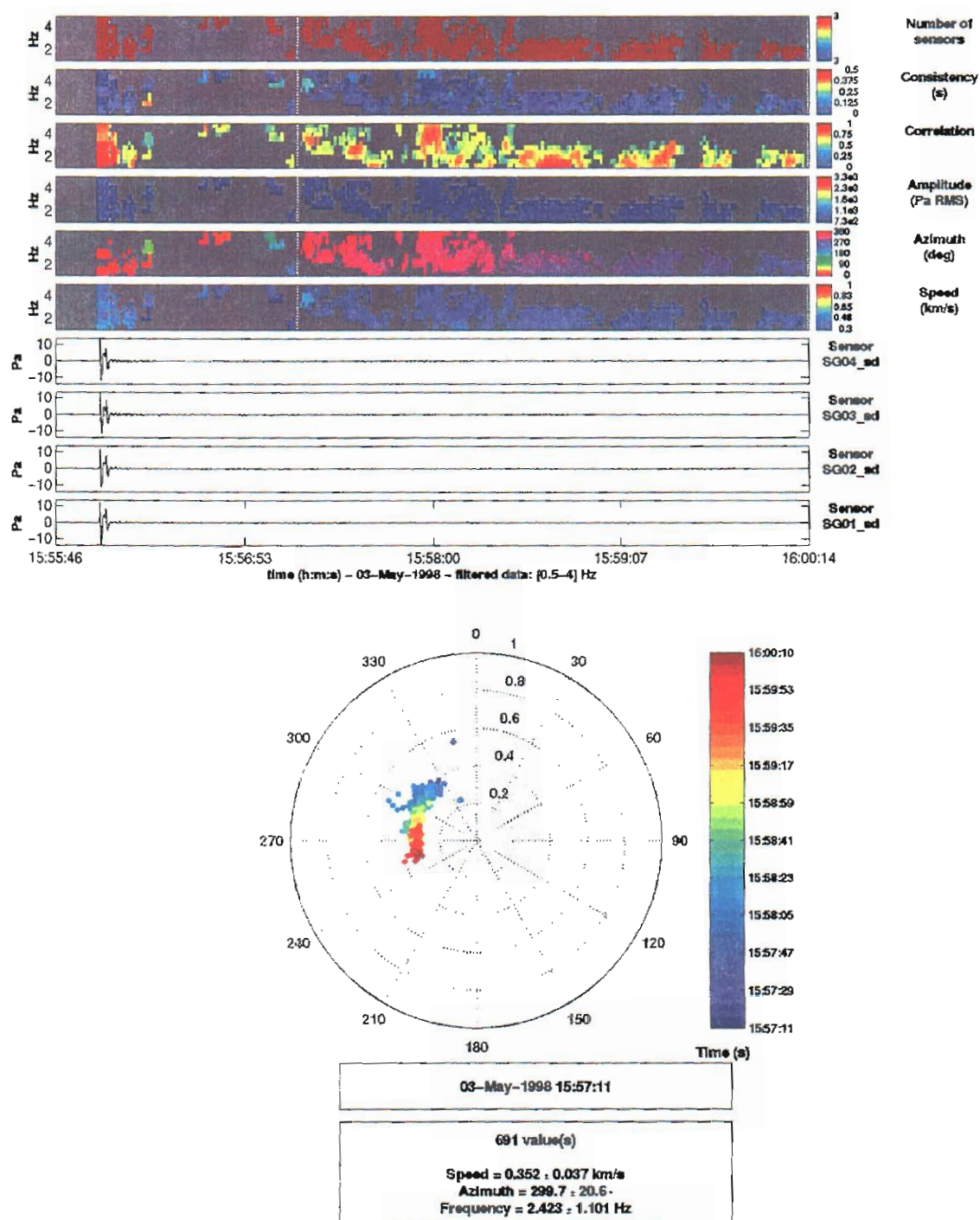
Figure 8. SGAR detection for STS-90. The polar plot shows only the arrivals after 15:57:11, past the N-wave. The detection parameters are: frequency band of 1-5 Hz, 5 s window, 4 s overlap, 1 s consistency, speed of 0.2 –1 km/s.
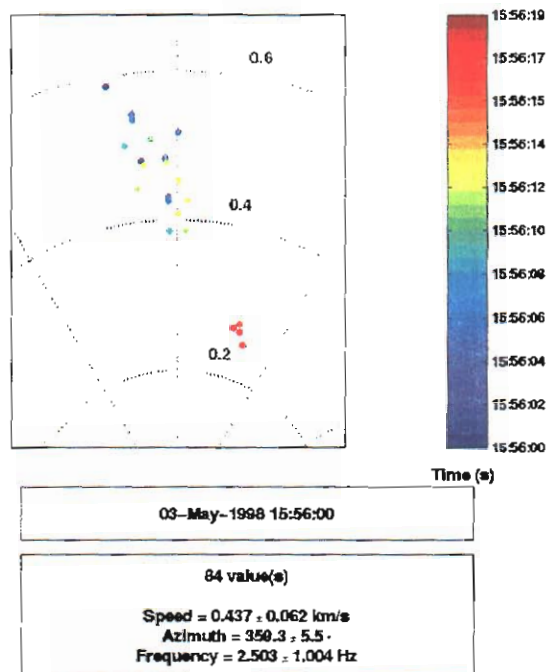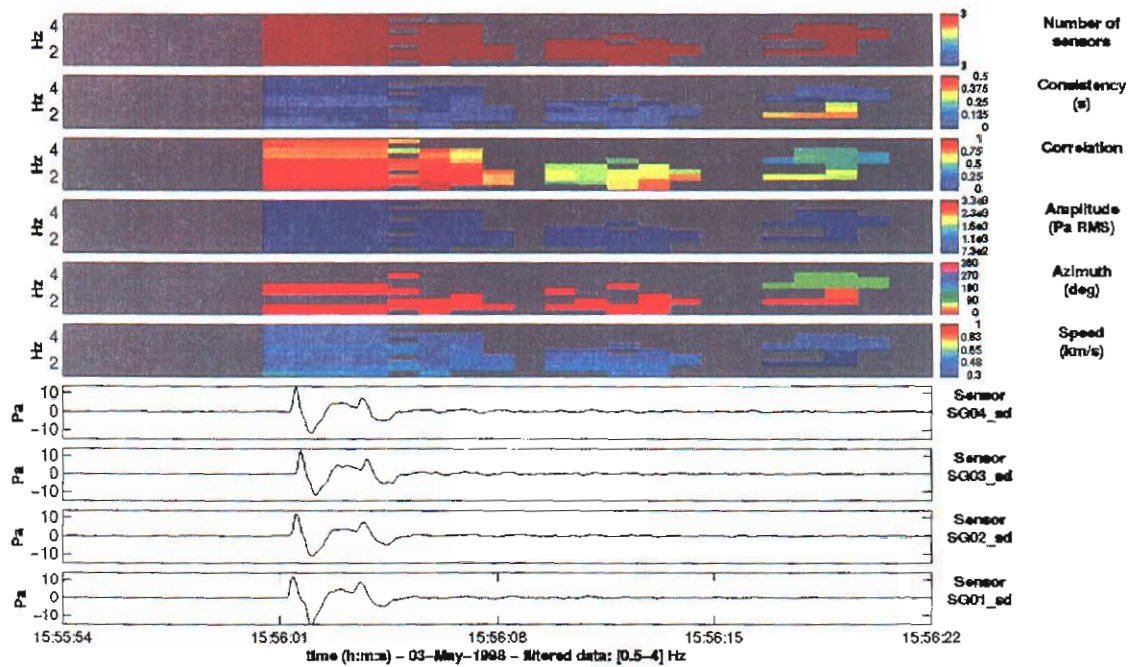
Figure 9. SGAR N-wave detection for STS-90. Same detection parameters as in Fig. 9.
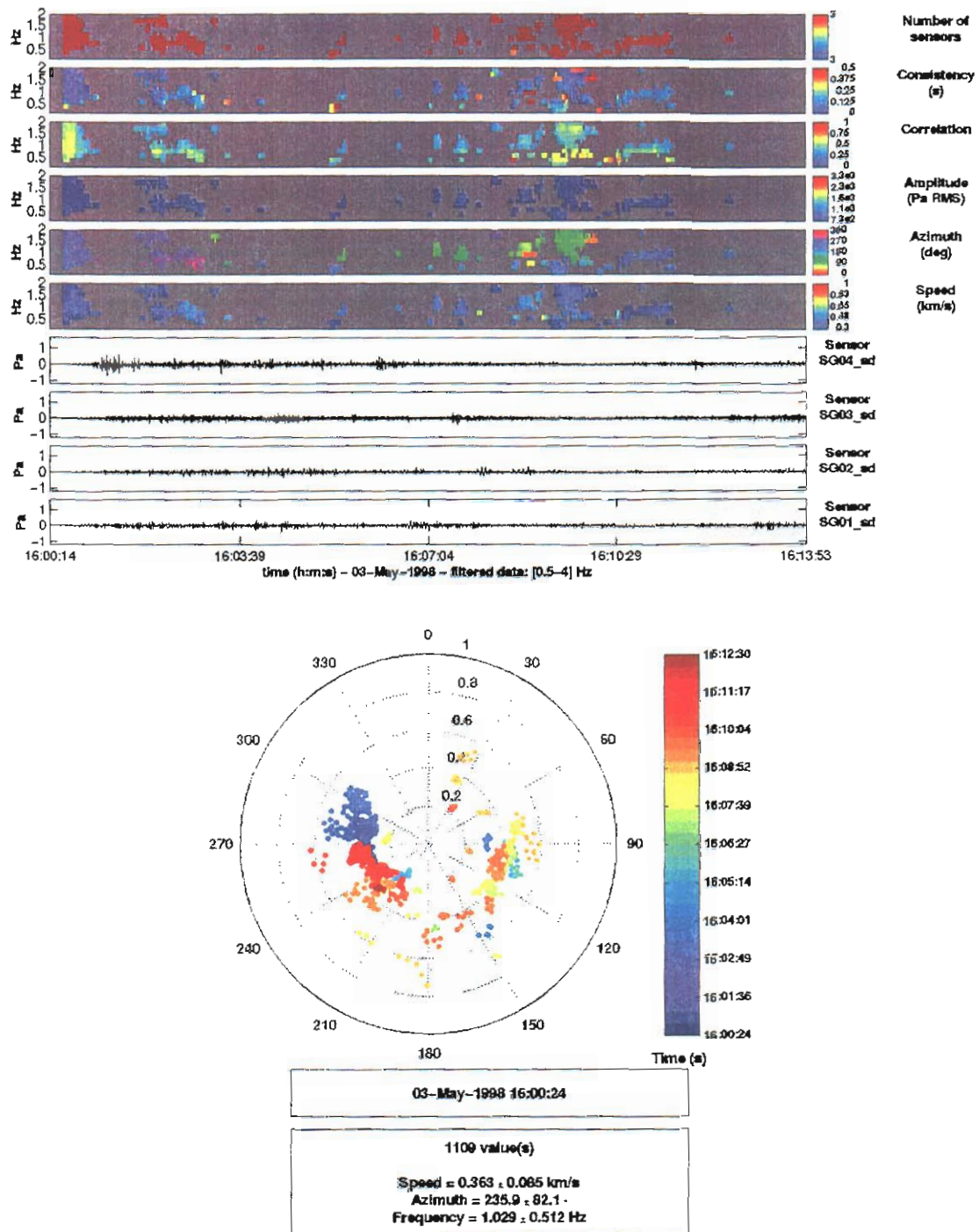
Figure 10. Coda for SGAR detection of STS-90. Data was separated by outage from previous segment. The detection parameters are: frequency band of 0.1-2 Hz, 30 s window, 29 s overlap, 1 s consistency, speed of 0.2 –1 km/s.
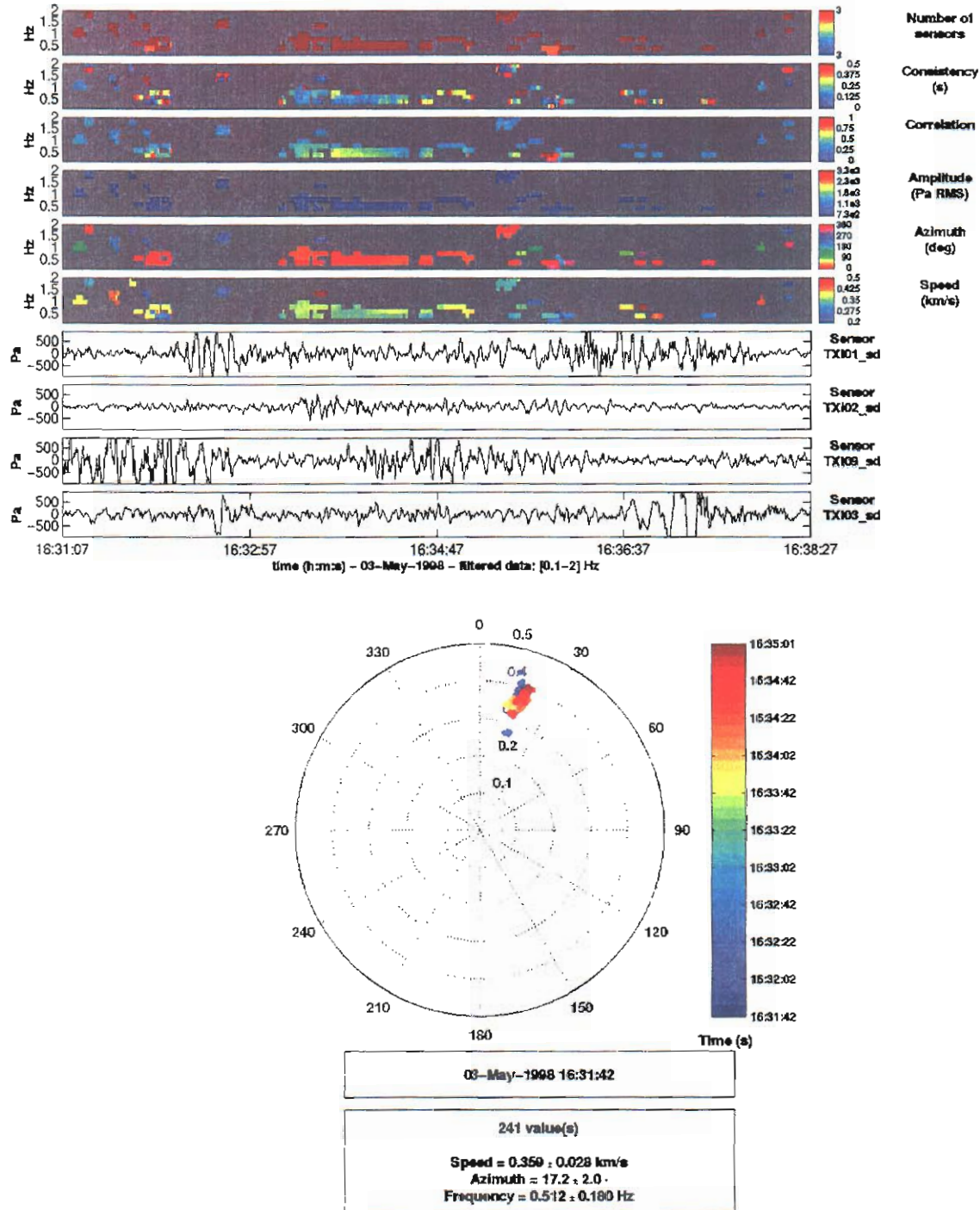
Figure 11. Possible TXIAR detection of STS-90. The detection parameters are: frequency band of 0.1-2 Hz, 30 s window, 29 s overlap, 1 s consistency, speed of 0.2 –0.7 km/s.
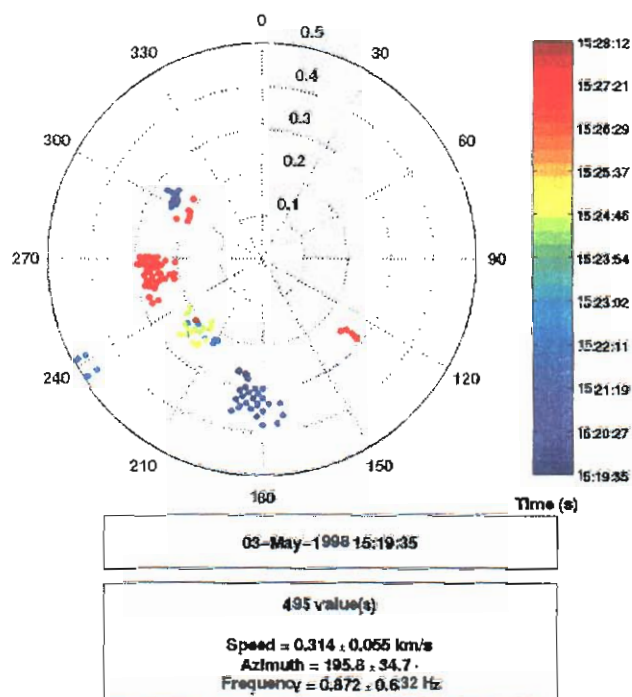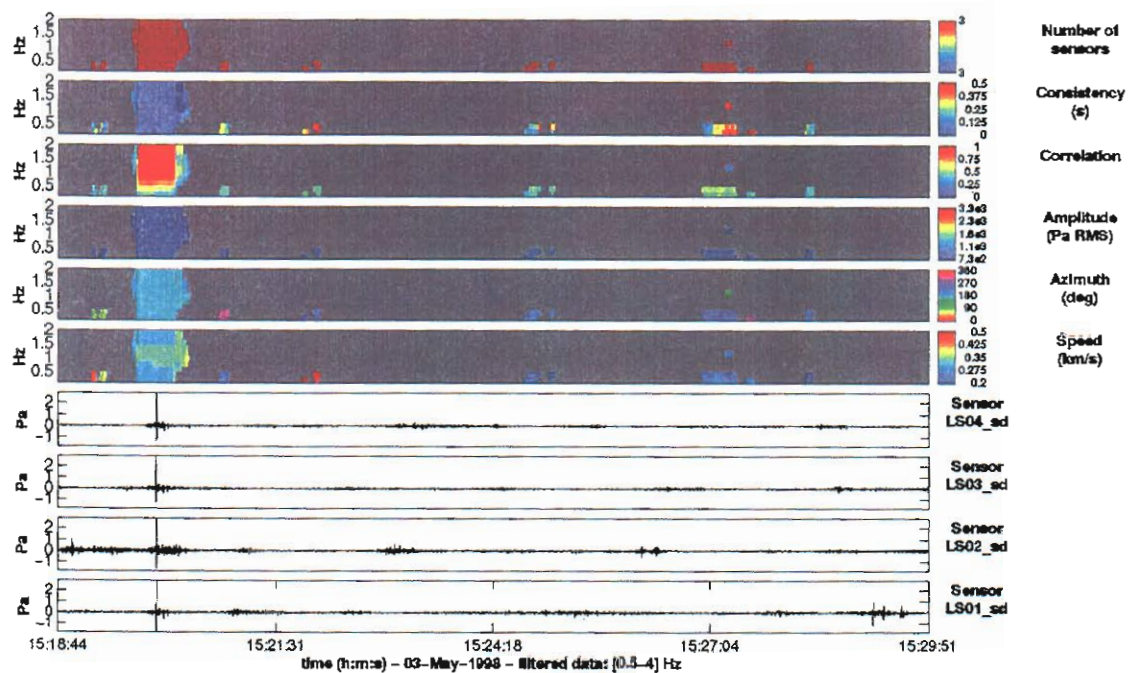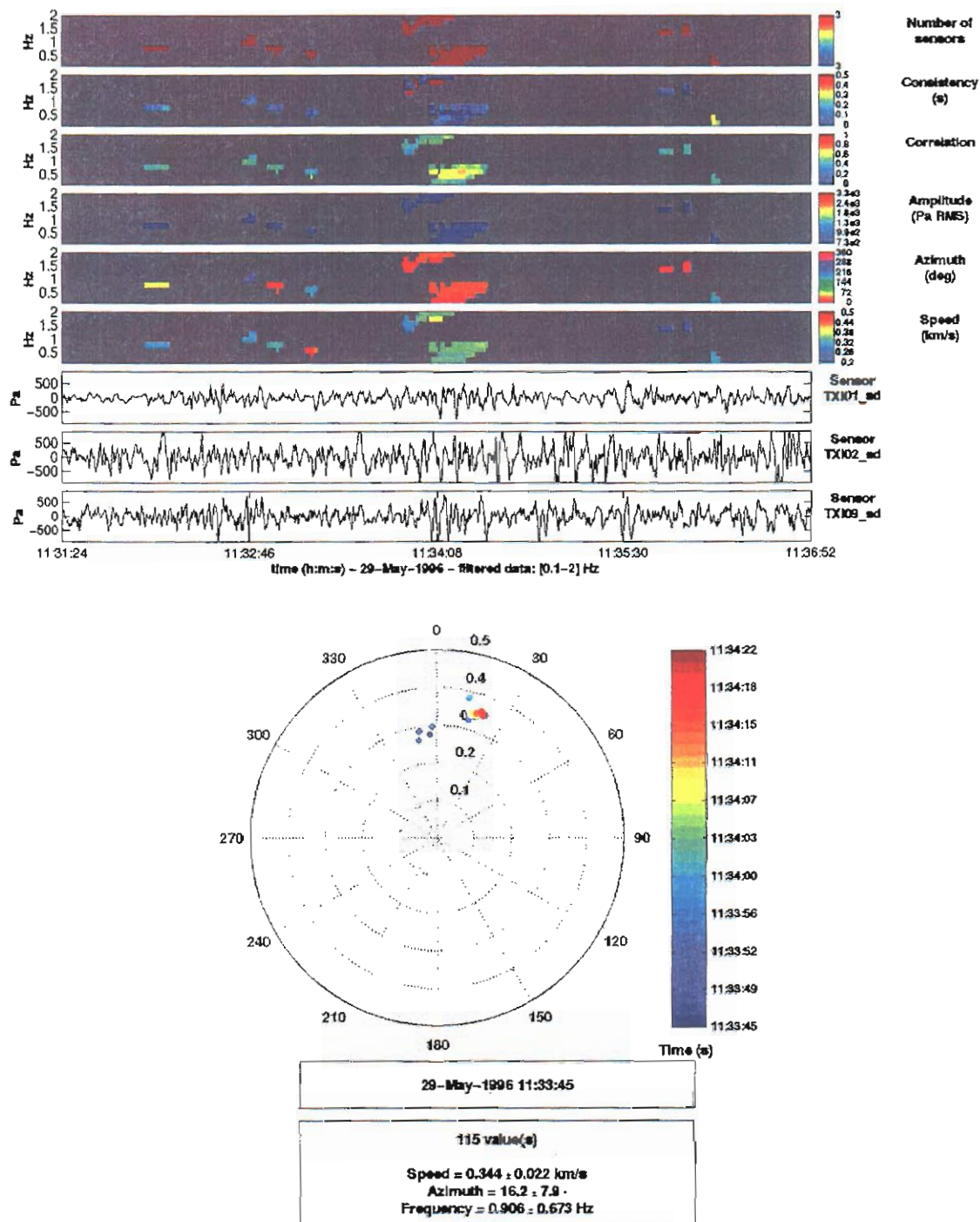
Figure 13. Possible TXIAR detection of STS-77. The detection parameters are: frequency band of 1-5 Hz, 10 s window, 8 s overlap, 1 s consistency, speed of 0.2 –0.7 km/s.
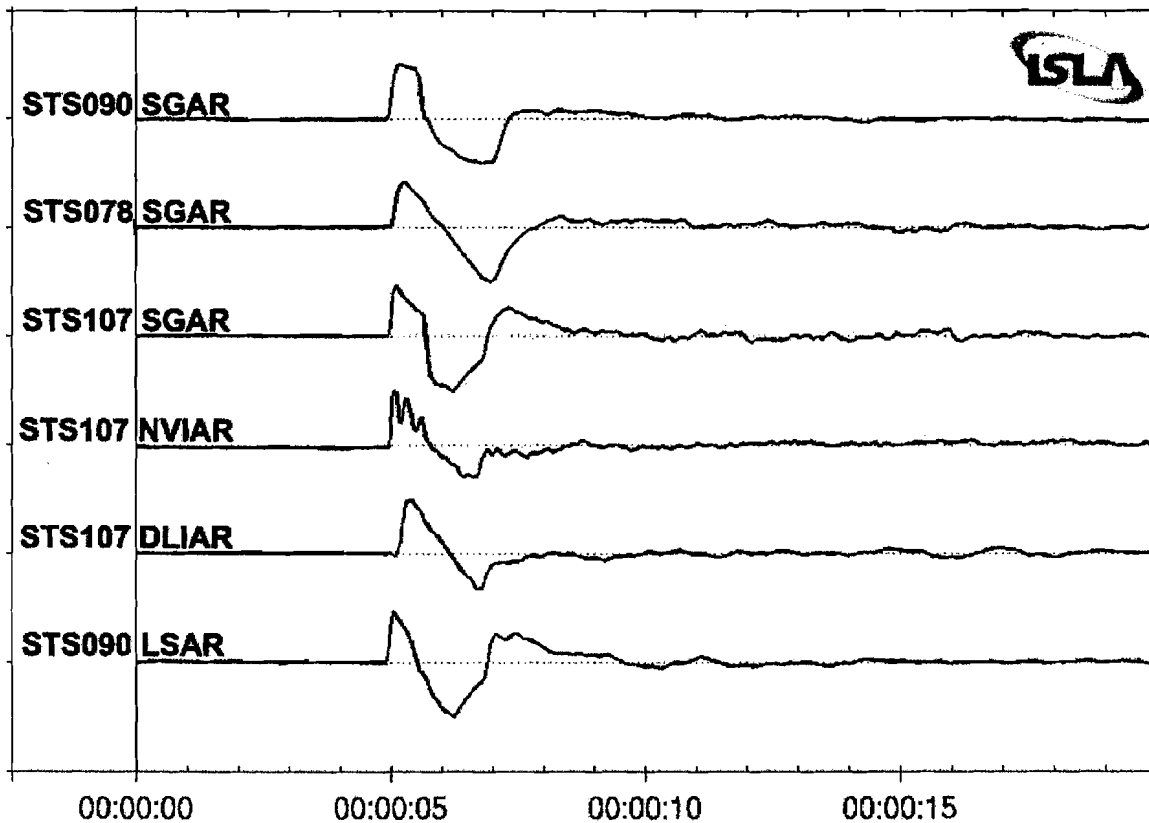
Figure 14. N waves for data sets discussed in this document. The following peak amplitudes may be estimated from the SGAR array:

STS78: Peak amplitudes 14.1112 and -16.9260 Pa (calib value of 0.0124 Pa/count)
STS90: Peak amplitudes 19.9888 and -16.1944 Pa (calib value of 0.0124 Pa/count)
STS107: Peak amplitudes 3.6936 and -3.9696 Pa (calib value of 0.0024 Pa/count)
Calibration values are under review.
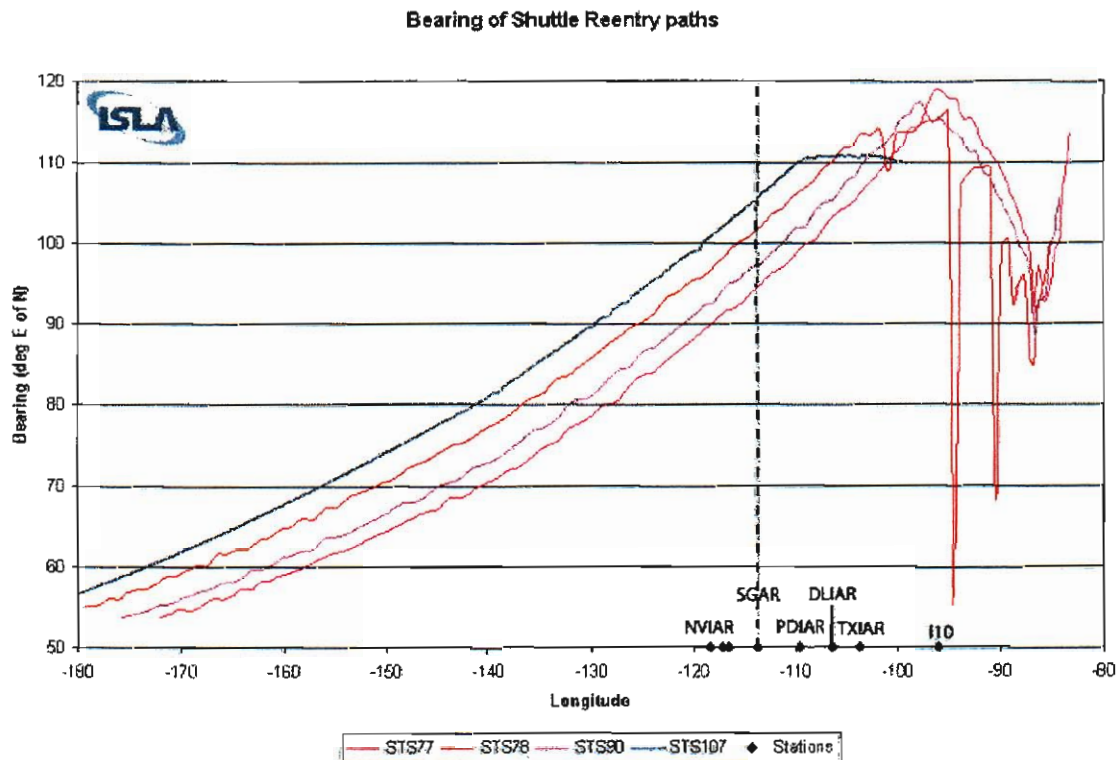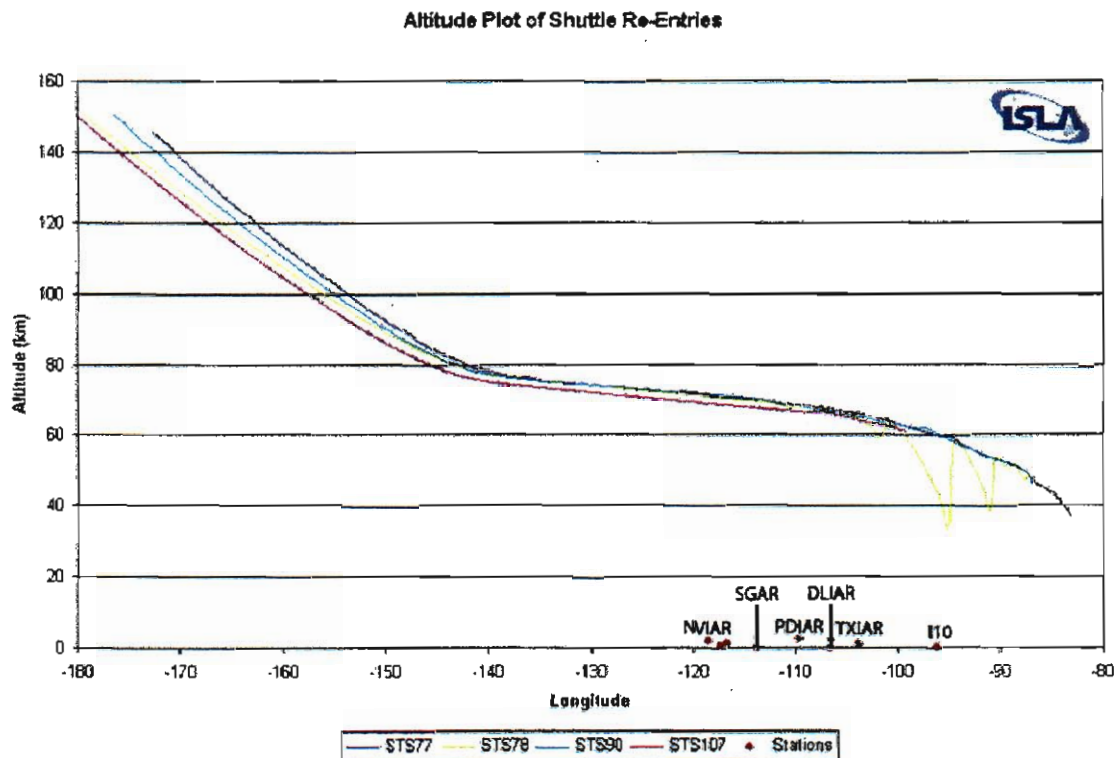
Figure 15. Altitude and bearing for STS-77, 78, 90, and 107. The bearing at each point in the trajectory is measured from the previous point. There appears to be a small change in bearing for STS-107 and STS-90 near SGAR.
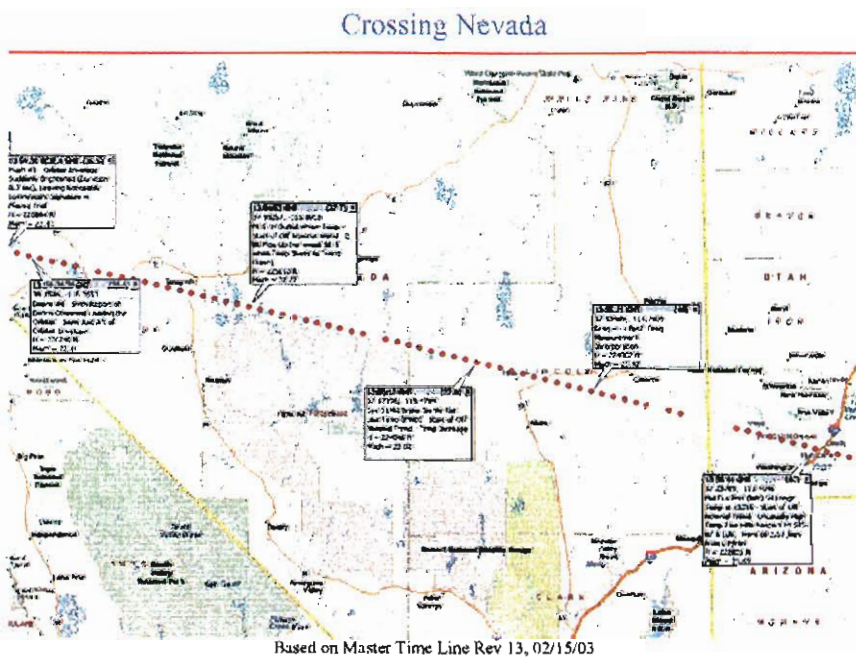
Figure 16. Detailed trajectory information for the California-Nevada-Utah sections. From NASA web site.

Appendix G: Evaluation of Wind Noise Reducing Filters at IS59

June 24, 2001

1. Introduction

The Chaparral 5 microphones deployed at IMS infrasound array IS59 in Kona, Hawaii, have been actively recording using a 15-meter porous-hose wind-noise-reducing filter since site activation in June 2000. Array IS59 is located in a pristine rain forest on the slopes of a dormant volcano, where the ground consists of lava rock. Due to the difficulty and environmental impact of trenching, the wind filters are deployed on the ground surface. Since the beginning of site activation, studies have been performed on the specifications and methods for the deployment of multi-port PVC wind-noise reducing filters. Initially, pressure seal tests were performed at 25 PSI. This specification was prescribed for underground wind filters, and its aim was to prevent water from leaking into the system. However, after the catastrophic failure of the glued seal in one of our PVC manifolds, we determined that a 5 PSI test pressure was sufficient for surface deployments.

Studies of the performance of PVC wind filters were initiated in May 2001. The aim of these studies is to optimize the wind filter design for the boundary layer conditions at IS59. The location of IS59 was selected for its low winds and relatively stable boundary layer. The wind filter studies consist of comparing the infrasonic noise levels recorded with different wind filter port arrangements to the noise levels observed at a reference station, and include investigations of alternative configurations.

2. Performance Studies

Throughout our performance studies, element H2 is used as a reference. The approximate deployment of the porous hose filter at station H2 is shown in Figure 1. Before our performance studies were initiated, all elements were connected to a porous hose filter as the one shown in Figure 1, with slight differences, and variations in the noise levels may be attributed to either site-specific conditions or differences in the porous hose deployment paths. Figure 2 shows the 120-port, 18m PVC wind noise reducing filter that was deployed at the central element, H1. The pressure sensor is connected to a central manifold encased in the center of the concrete vault, and each of the eight arms radiating outwards from the central manifold is connected to a valve. A 9-meter, ½" PVC connects from each of the 8 radial arms to a manifold. The manifolds in turn are connected to fifteen (15) 3-meter PVC pipes with a valve near the manifold to enable easy shutoff and wire-mesh ports on the other to reduce turbulence and prevent insect access. Thus each of the 120 port lines can be sealed by a valve. Pressure testing of the manifolds consisted of initially closing all the valves and from the central manifold sequentially pressurizing each manifold to 5-10 PSI. Manifold configurations alternated between "fan" arrangements, with the fifteen ports arranged in a continuous arc, and "wing" arrangements, with the ports distributed in two groups on opposite sides of the manifold. These configurations were designed to allow the ports to be deployed without overlap (Figure 2).

The initial implementation of the wind-noise-reducing filter system was installed at station H1 (the central element) on May 4, 2001. Due to uneven topography some of the pipes were installed with the ports suspended at different heights. In addition, the ideal geometry shown in Figure 2 could not be achieved, and some of the ports from different manifolds overlapped. At 2:30 UT the microbarograph was connected to the system with the four fan manifolds active (Figure 3). The filter arrangement was found to increase the signal amplitudes at high frequencies by approximately a factor of 8, but noise levels were also found to have been significantly increased. Specifically, power-spectral-density analysis showed a peak in the noise spectrum centered around 5 Hertz. This increase was believed to be due to resonance within the pipes.

On May 8, 2001, starting at 22:32 and ending at 22:34 UT, ports were closed so that the active system was as shown in Figure 4 in order to test the source of the spectral increase. No significant change was observed in the 5-Hz peak, but a second peak was observed at around 7-8 Hz. This suggested that the peak was not caused by wind coherence across the array due to the close proximity of the ports, and that the system was generating higher mode harmonics at irregular intervals due to the open pipe configuration and the slight asymmetry of the system.

On May 10, 2001, starting at 20:24 UT, the eight ports of the central manifold were open and all ports in the outer manifolds were closed to test whether lateral oscillation of the pipes between the manifolds was the cause of either of the peaks. As seen in Figure 5, the 5-Hz peak was eliminated by this action while the higher-mode 8-Hz harmonic remained, but the data from this time period may be suspect due to labor being carried out at the field site while this configuration was active and due to cracks in four of the valves. At 23:08 UT, all ports between the manifolds and the H1 vault were closed in order to see whether the problem could have been caused by the central summing manifold. The integrity of this manifold was demonstrated by the elimination of the high-frequency harmonics (Figure 6).

At 01:35 UT of May 12, the pressure sensor at H1 was disconnected from the central manifold to perform a pressure test. Four valves on the wing manifolds were found to be leaking. The cracked valves were replaced, the 6-meter pipes connecting the manifolds to the central vault were stabilized, and a successful pressure test at 5 PSI was conducted. The sensor was then connected to the full 120-port system at May 12 03:00 UT. As shown in Figure 7, the 5-Hz peak was greatly reduced, although the 8-Hz peak was still present, suggesting that the resonance phenomenon observed was more complex than originally thought. Also at this time the sensor at H4 was connected to its central summing manifold, which was then attached to a single port open approximately 1 meter from the manifold. The other seven radial pipes from the central manifold were capped. Small cracks in the central manifold caps at H4 significantly increased the noise levels at this station.

On May 16 at 22:00 UT, the configuration shown in Figure 8 was implemented at H1. This configuration was designed to further increase the physical distance between open ports, thereby reducing the possible coherence of wind eddies across the filter array. This configuration continued to significantly diminish the 5-Hz peak, but had little or no effect on the 8-Hz peak. A slight increase could also be seen at around 3 Hz. The lack of acoustic integrity in the central

manifold at H4 caused the high-frequency response to be augmented, eliminating the previously-observed rolloff at 4 Hz and extending noise levels out to the anti-aliasing filter at 9 Hz.

On May 18 at 20:20 UT the configuration shown in Figure 9 was implemented at H1 to further increase the physical distance between open ports and reduce the coherence of wind eddies across the filter array. This configuration showed the best noise response to about 3 Hz, but the 5-Hz peak had returned and was again of comparable amplitude to the 8-Hz peak. At 21:00 UT a new porous hose was installed at H3 with the same physical configuration as previous, to test whether regular replacement would improve noise levels. Changing the porous hose did not produce any marked changes, suggesting that the acoustic performance of the hose is unaffected after one year.

On May 23 at 22:18 UT the configuration was changed to that shown in Figure 10, to test whether the improvement seen in the previous configuration would continue. Unfortunately, the excellent low-frequency response seen in Figure 9 was not replicated by this configuration, although (interestingly) the 5-Hz peak became a spectral trough. While the 8-Hz peak remained stable with respect to the rest of the spectrum, it was reduced in absolute amplitude, and the previously-noted 3-Hz increase was augmented.

On May 25 at 23:08 UT, in an effort to iterate from the previous "best" configuration, the configuration shown in Figure 11 was implemented. The low-frequency response was preferable to that of Figure 10 but inferior to that of Figure 9. At higher frequencies the 5-Hz and 8-Hz modes appeared to have merged into one large, broad peak at about 6 Hz.

On June 2 at 00:13 UT the H1 configuration was again changed to that shown in Figure 12. This fan-manifold-weighted configuration was designed to further increase the physical distance between ports while at the same time keeping that distance as constant as possible and maintaining filter symmetry. While high-frequency response was encouraging, with some reduction of the broad noise peak seen in Figure 11, the low-frequency response was poorer above 1 Hz.

On June 14 a number of changes were made to the wind-noise-reducing filters at the other three sites. At 21:18 UT a new filter was installed at H3 consisting of eight 6-meter PVC pipes with open ports at the ends and valves installed at the midpoints of the pipes. This results in a similar arrangement to the "best" configuration seen at H1 in Figure 9, but with a smaller diameter so as to possibly increase the frequency of the fundamental mode of any in-pipe reverberations that might be increasing the noise levels. At 21:48 UT the porous hose filter at H2 was replaced in the same arrangement to test temporal variability of the hose, which had been deployed for approximately one year. At 22:48 a set of four 8-meter porous hoses was deployed at H4 in the shape of a cross. This arrangement was selected to allow comparison between the PVC filter at H3 and the porous hoses at H4. Also at this time the three cracked caps at H4 were replaced. As can be seen in Figure 13, the high-frequency response of H3 increases dramatically above 2 Hz, culminating in a noise peak at 7 Hz similar to that seen at H1. Similarly, H4's high-frequency response has drastically improved over the entire band, but can be seen to be peaking at almost the same point as H3. A slight peak can also be seen at about 4 Hz on H4. The presence of the 7-Hz peak at H3 is not due to transverse vibration because all elements of this filter are on the

ground, nor to lack of integrity of the system, as it passed a 5-PSI pressure test; port proximity also should be no issue. It follows that the noise peaks are most likely due to resonance within the pipes, and is present at H3 at a higher frequency than at H1 due to the difference in lengths between the filter components (6m arms at H3, 9m at H1).

On June 21 02:00 UT the configuration shown in Figure 9 was re-applied to H1 in order to facilitate comparison with the installations at H3 and H4. As can be seen in Figure 14, the spectral peak present at 5-6 Hz at H1 is present at 7-8 Hz at H3, suggesting again that the peaks result from resonance within the pipes and can be shifted in frequency by changing the diameter of the array.

On June 22 19:20 UT the porous hose configuration at H4 was changed to a circular loop approximately 9 meters in diameter. At 01:45 UT on June 22 the valves at the center of the arms of the H3 filter were partially closed in an attempt to attenuate the primary mode. The results can be seen in Figure 15. Partial closure of the H3 valves appears to have had little effect on the resonance peak seen at about 8 Hz, suggesting that the fundamental mode cannot be eliminated by this procedure. The slight peak seen at 4 Hz at H4 appears to have been augmented by the use of the circular hose arrangement. On June 23, one of the ends of the circular porous hose arrangement at H4 was sealed in an effort to reduce any resonance that may be induced by waves trapped in the circular loop. As can be seen in Figure 16, the 4-Hz peak appears to have actually been augmented by this procedure.

On June 26 at 21:15 UT the lengths of the pipe arms at H3 were reduced to ten feet in an attempt to increase the frequency of the resonance peak to a point beyond the antialiasing filter. The results are shown in Figure 17; the peak can be seen to have shifted to a slightly higher frequency, but not by as great an interval as is predicted by pipe resonance theory. This suggests that the presence of the noise peaks actually may not be due to resonance within the pipes.

On June 29 at 02:30 UT, after consultation with Douglas Christie of the CTBTO, a single port was again opened at H4, in order to test the effects of the fore-volume of the manifold. Results can be seen in Figure 18. Although the noise peak at 4 Hz has been eliminated, the high-frequency response has changed to resemble that of H1 and H3.

On July 13 at 17:08 UT all vaults were connected to 50-foot porous hose filter arrangements similar to that shown in Figure 1 in order to identify and quantify site-specific effects. On July 14 at 00:00 UT the hose at H1 was replaced with a new one due to suspicion of a possible clog or kink. As can be seen in Figure 19, all four vaults exhibit similar behavior to 2 Hz, after which differences due to site-specific parameters become dominant. In particular, it can be seen that the spectrum of H4 becomes highly variable in amplitude above 5 Hz, and that of H1 exhibits significant integral noise spikes whose cause is currently under investigation.

3. (Preliminary) Discussion of Results

The aim of this study is to identify the optimal wind-noise-reducing filter configuration for the low-wind conditions prevalent at IS59. A study was conducted comparing peak signal amplitudes observed at H1 and H2 in the band of 0.7-1.4 Hz. Since the H2 configuration was

changed very little over the course of the experiment, it should serve as an adequate control. As can be seen from Figure 16, relative signal strength has improved over the course of the experiment, with the most consistent improvement taking place around May 19, while the configuration shown in Figure 9 was in effect. This agrees with the previous statement that the simple 8-port configuration was performing the best at around 1 Hz. Under this configuration, no manifolds would be needed and the central manifold could be replaced with direct connections into the sensor. However, note that the H1/H2 amplitude ratio is still below unity: this may be an artifact of the site-specific response of H2, which consistently had the highest S/N ratios before our performance tests were initiated. An added complication is that the resonance peaks induced by the solid pipe filters introduce ringing into the signal, so that the system response is similar to that of an underdamped seismometer.

This study shows that the use of 18-m PVC pipe noise-reducing-filters at IS59 can improve signal-to-noise ratios in the 1 Hz band and appears to have little effect on the waveforms below 1 Hz. However, at higher frequencies the waveform can be severely distorted by the resonance of the pipes, which does not appear to occur as noticeably with hose filters. Thus far the best low-frequency signal-to-noise results appear with a simple 8-port configuration, with the frequency of the resonance partially depending on the diameter of the array. Consultation with Douglas Christie of the CTBTO raised the possibility that the noise peak may be due to transverse movement of the pipes due to inability to securely fasten the pipes in place on the lava rock. This explanation is improbable, as there is not sufficient wind in the area to warrant significant displacement of the pipes.

It also appears that the use of the solid pipe arrays improves the seismic sensitivity of the microbarograph. The peak signal strength of earthquakes recorded at H3 versus H2 is approximately six times greater than the signal strength enhancement of infrasonic signals. This may be due to the close proximity of the ports and pipes of H3 to the ground, which would permit better coupling of the ground vibration onto the pipes. This phenomenon would further lower the detection threshold of earthquakes at IS59, currently at local magnitude 2.7.

The most likely explanation for the spectral response of the pipe arrays may involve the acoustic interaction of the forevolume of the Chaparral 5 sensor and the pipe length, with the forevolume acting as a capacitive element which may lower the peak of the pipe resonance. Such low resonance peaks are not expected for 18m diameter wind filters, and are not observed with MB2000 sensors. Impedance matching at the sensor may be able to shift the resonance peak beyond the band of interest. Until these issues have been resolved, the Hawaii array will keep the porous hoses, which appear to perform well in this environment.
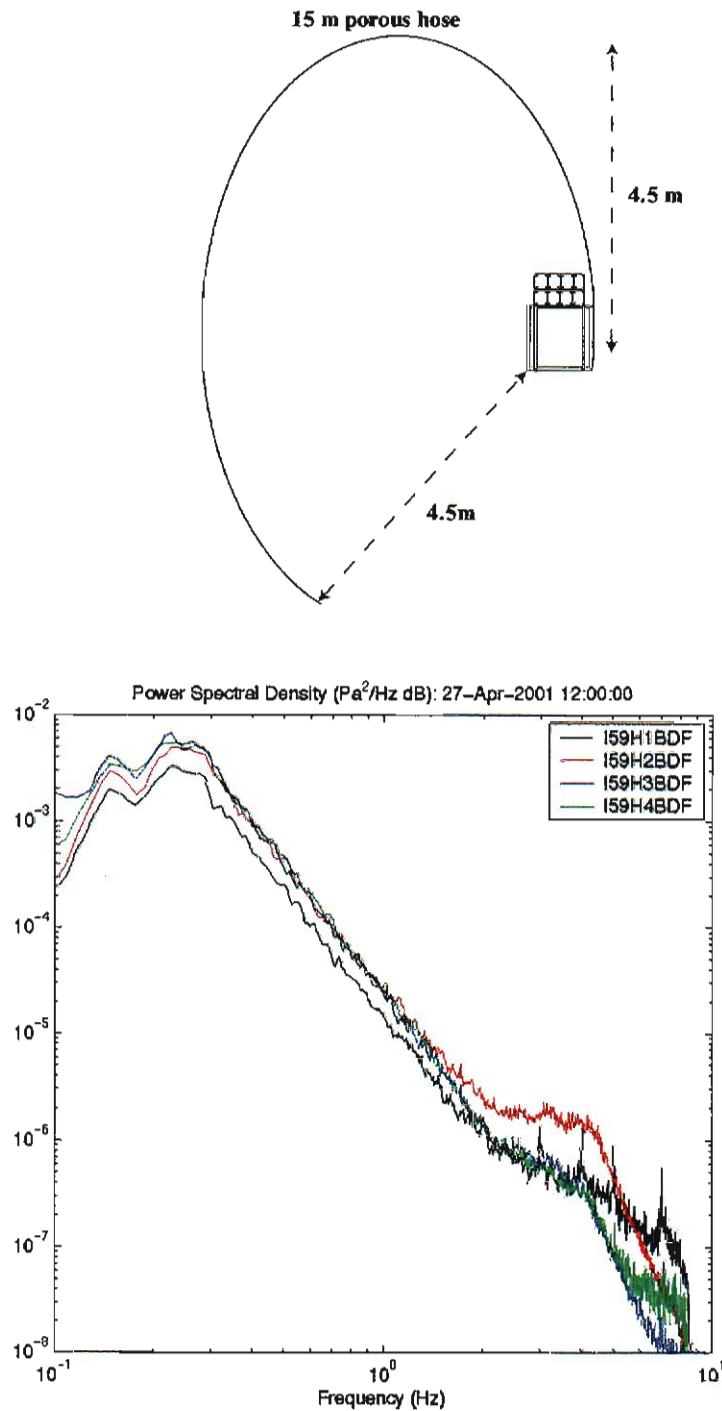
Figure 1. Reference wind noise reducing filter deployed at H2 (abolve). The filter consists of a 15m porous hose deployed in an arc around the vault and connected directly to H2. The lower panel shows the background noise levels recorded before the beginning of the performance tests in May 2001.
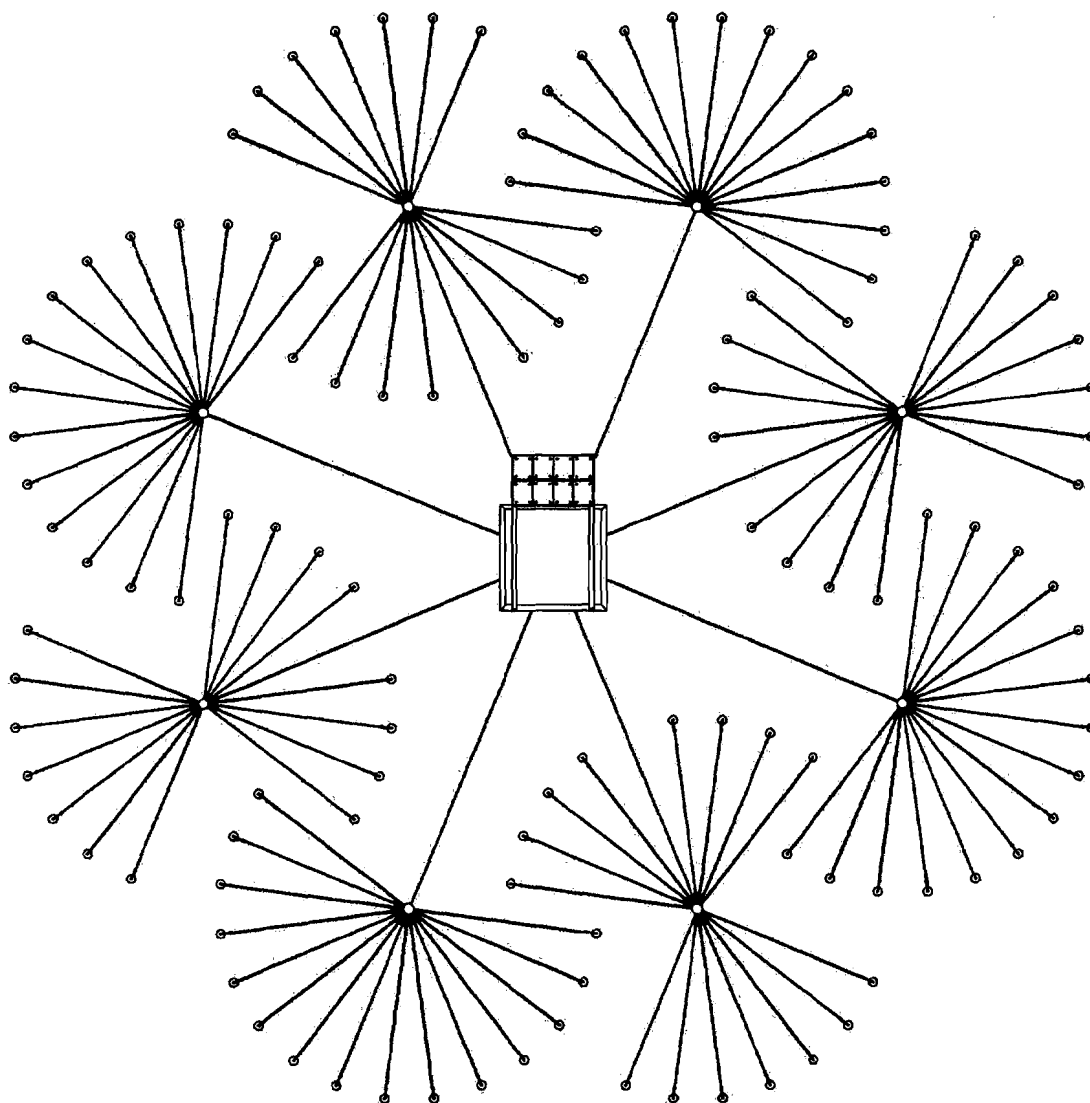
Figure 2: Wind-noise-reducing filter arrangement as implemented at H1, showing ideal location of the 120 ports. The ideal deployment was not possible in rough, forested terrain.
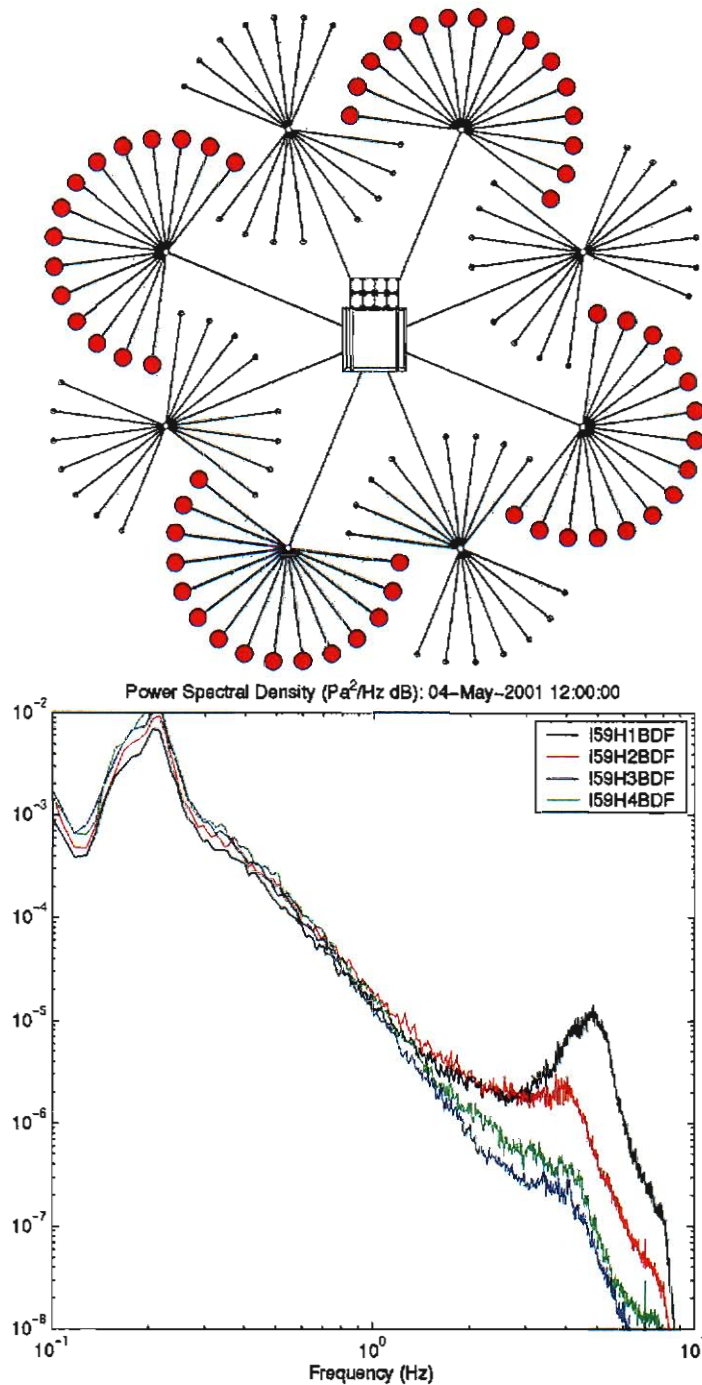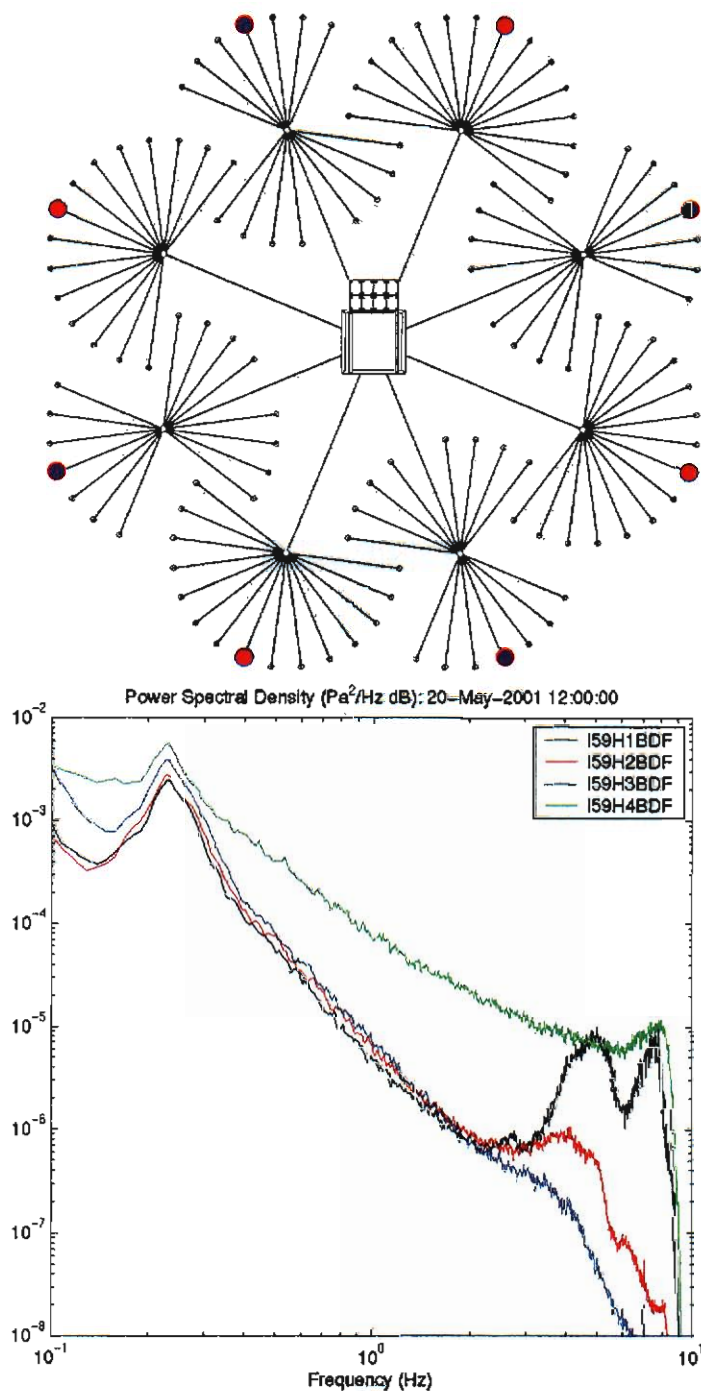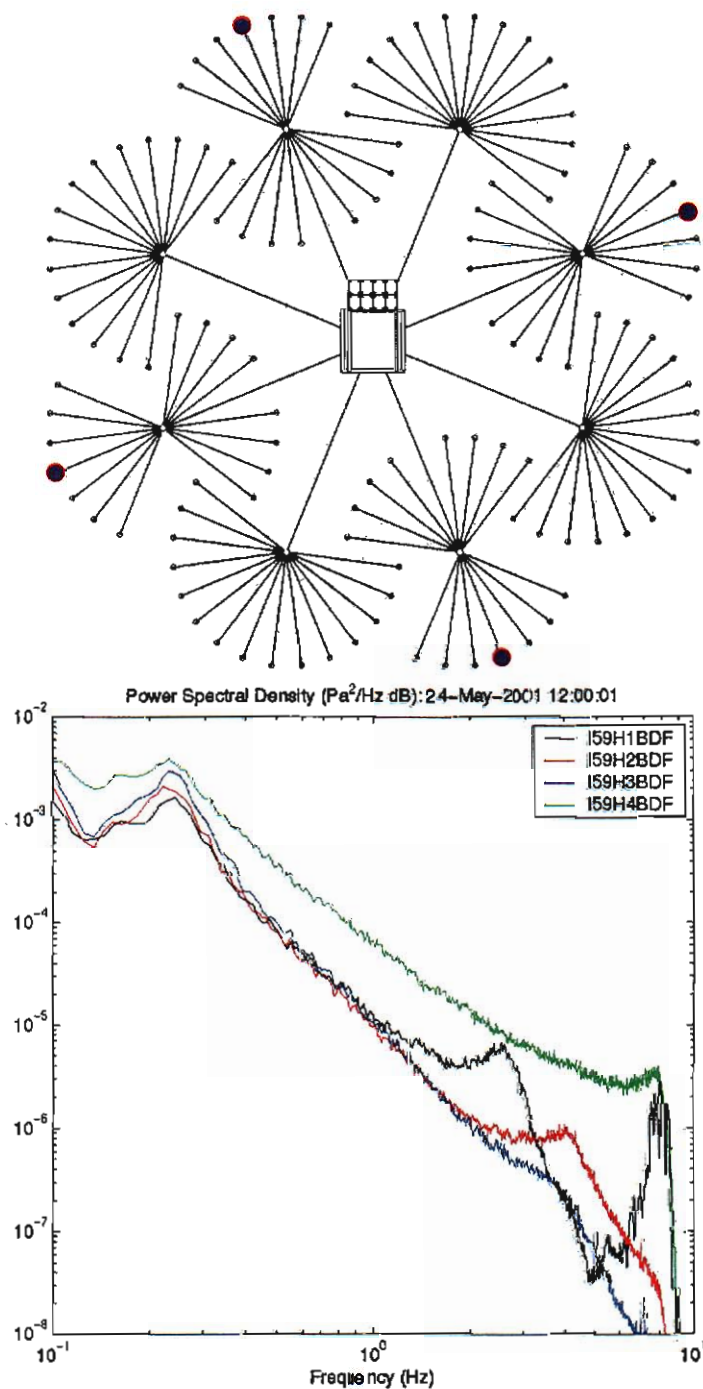
Figure 3: Wind-noise-reducing filter port arrangement (top) and resultant power-spectral density plot (below) from 5/4/01 02:30 to 5/8/01 22:34 UT. Mean wind speed was 0.769 m/s from 75.20°.
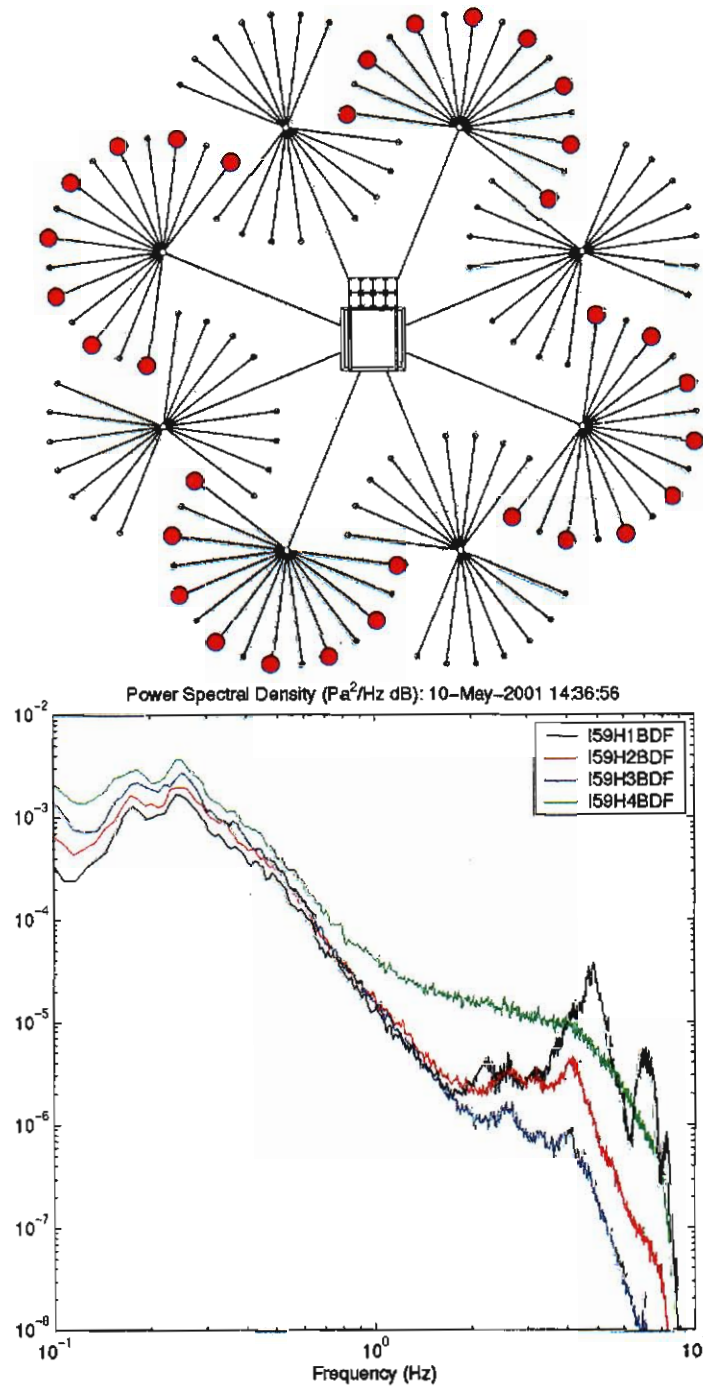
Figure 4: Wind-noise-reducing filter port arrangement (top) and resultant power-spectral density plot (below) from 5/8/01 22:34 to 5/10/01 20:24 UT. Mean wind speed was 0.857 m/s from 75.84°.
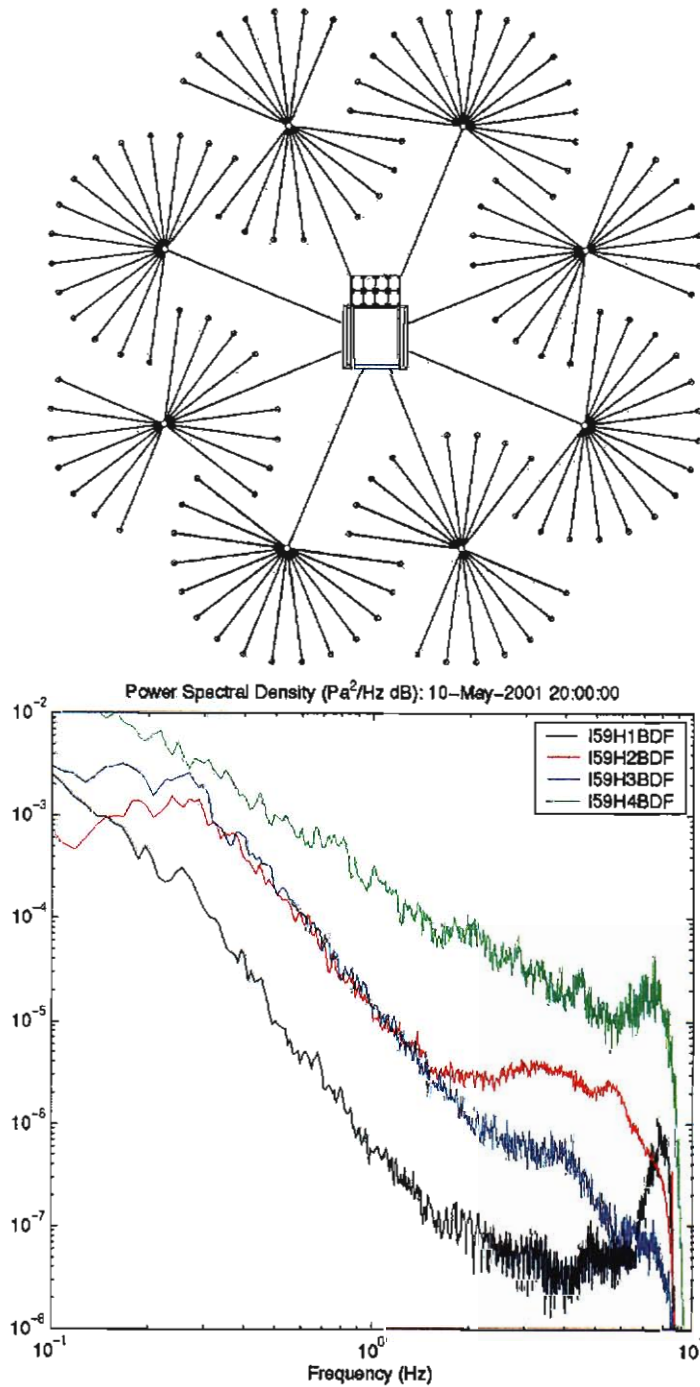
Figure 5: Wind-noise-reducing filter port arrangement (top) and resultant power-spectral density plot (below) from 5/10/01 20:24 to 5/10/01 23:08 UT. Mean wind speed was 0.406 m/s from 278.80°.
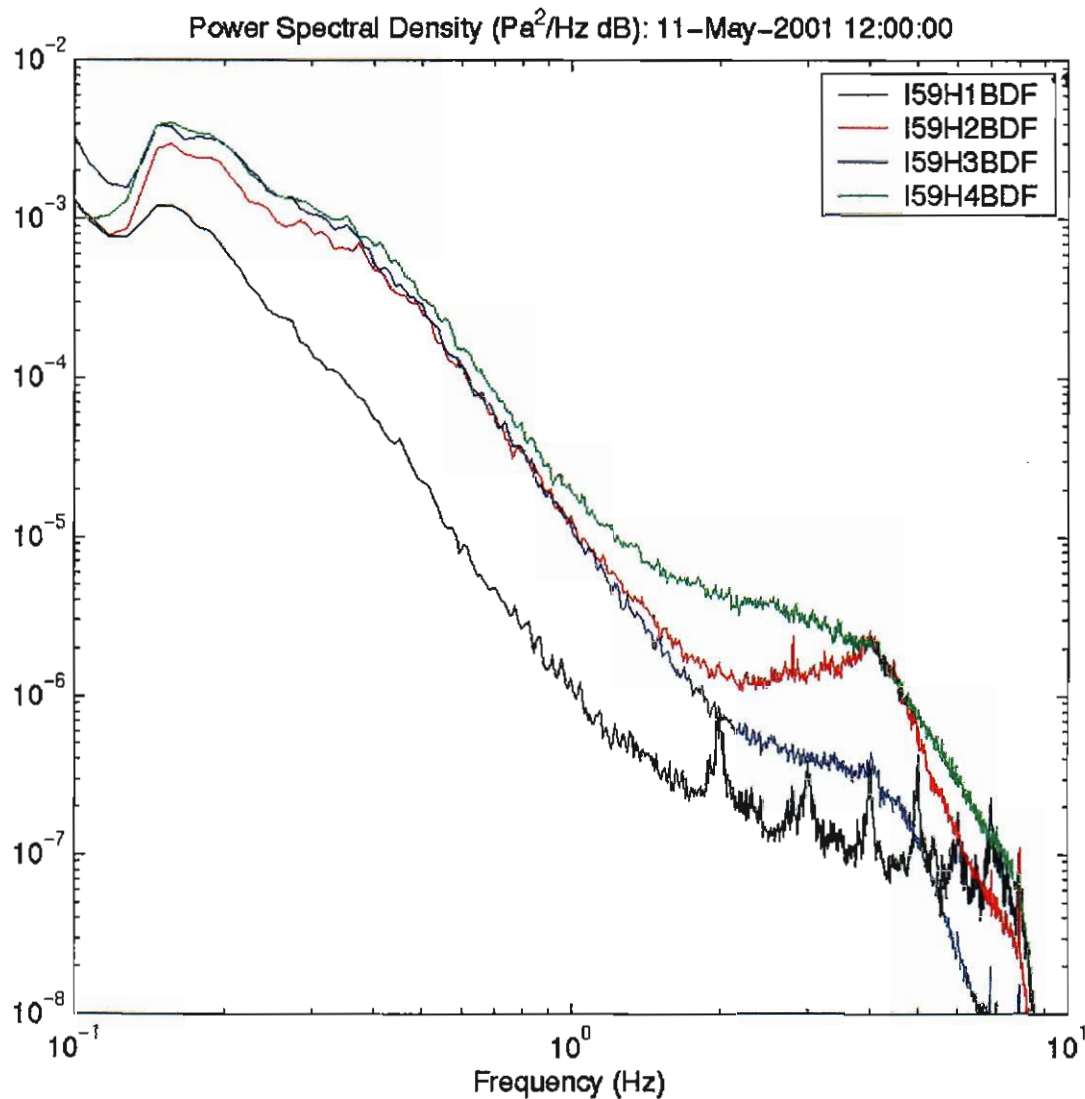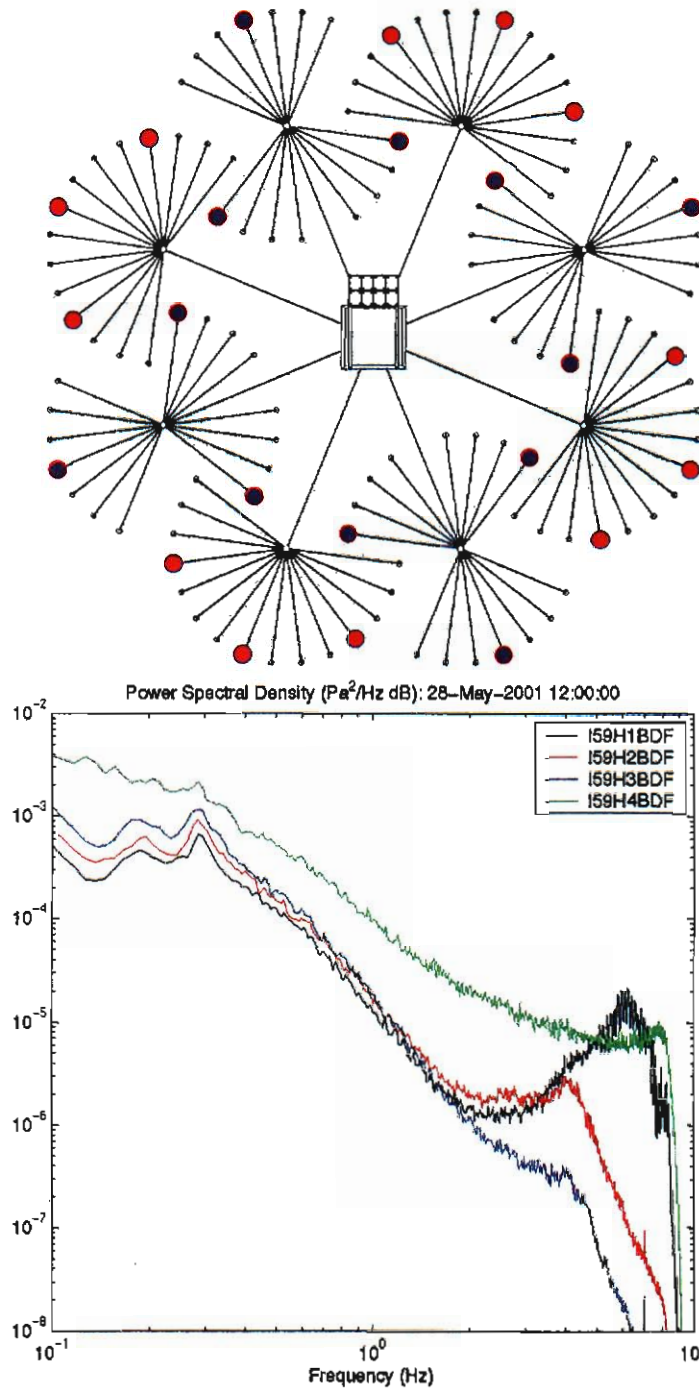
Figure 6: Power-spectral density plot from 5/10/01 23:08 to 5/12/01 01:35 UT after closure of all valves in wind-noise-reducing filter at H1. Mean wind speed was 0.988 m/s from 80.74°.
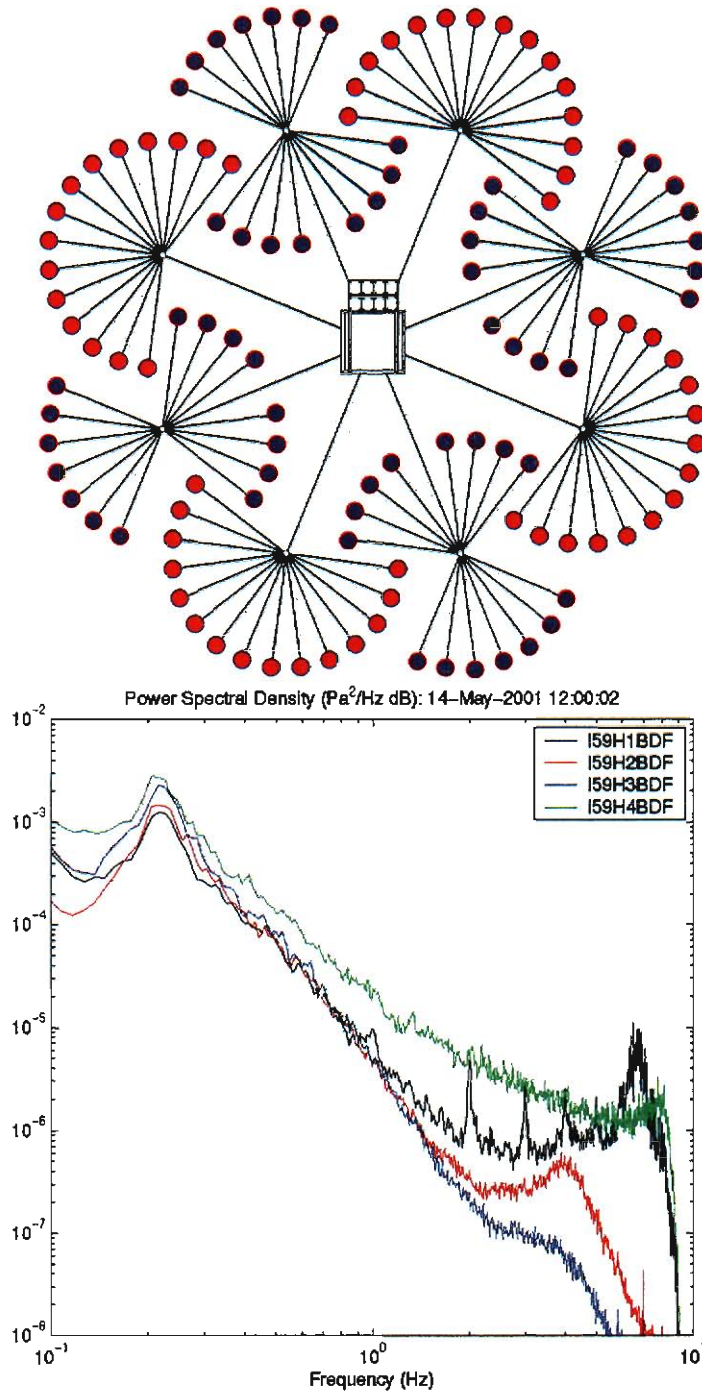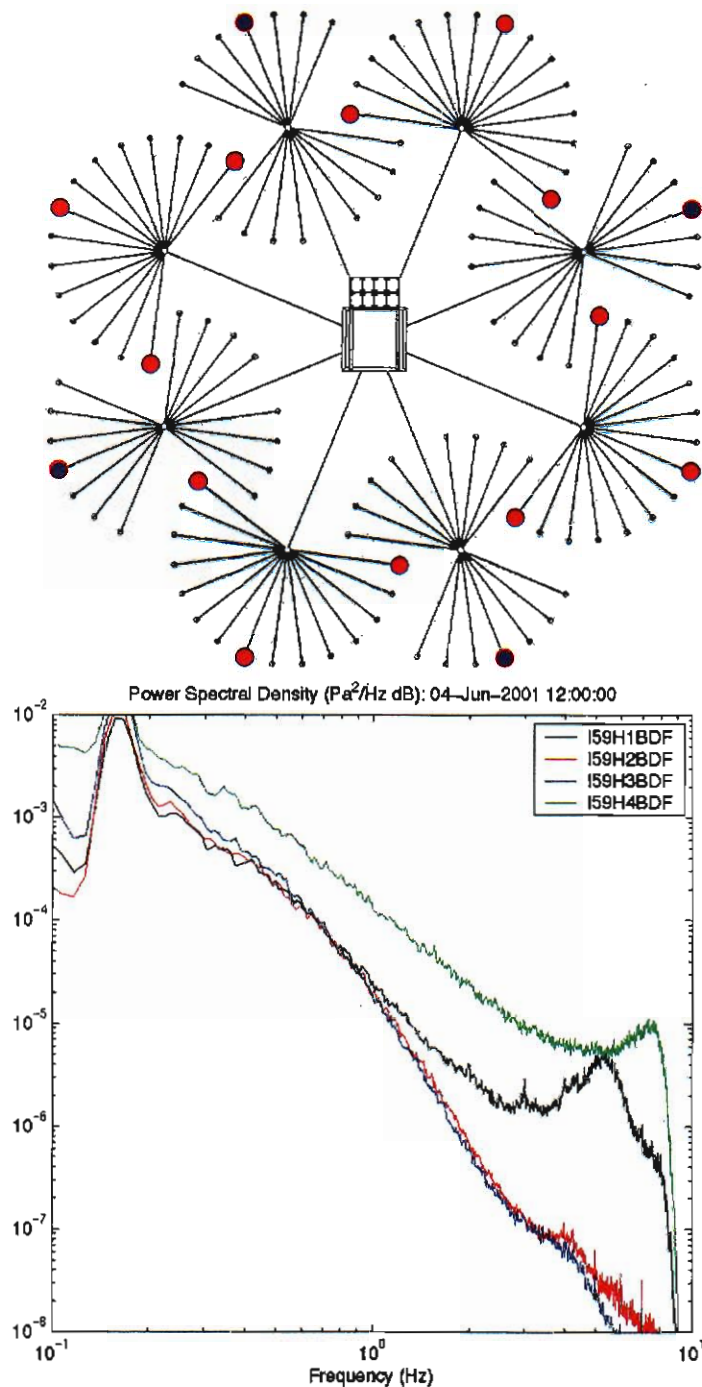
Figure 7: Wind-noise-reducing filter port arrangement (top) and resultant power-spectral density plot (below) from 5/12/01 03:00 to 5/16/01 22:00 UT. Mean wind speed was 0.678 m/s from 81.63°.
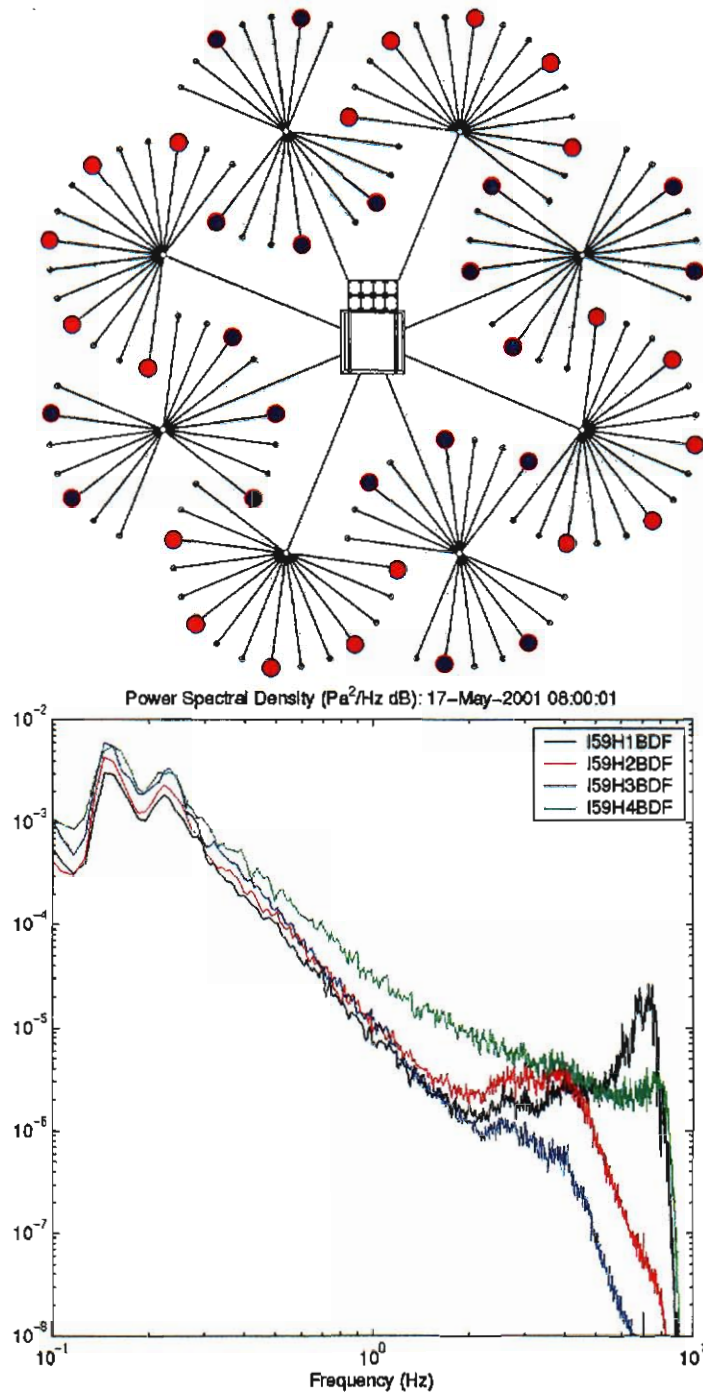
Figure 8: Wind-noise-reducing filter port arrangement (top) and resultant power-spectral density plot (below) from 5/16/01 22:00 to 5/18/01 20:20 UT. Mean wind speed was 0.911 m/s from 79.24°.
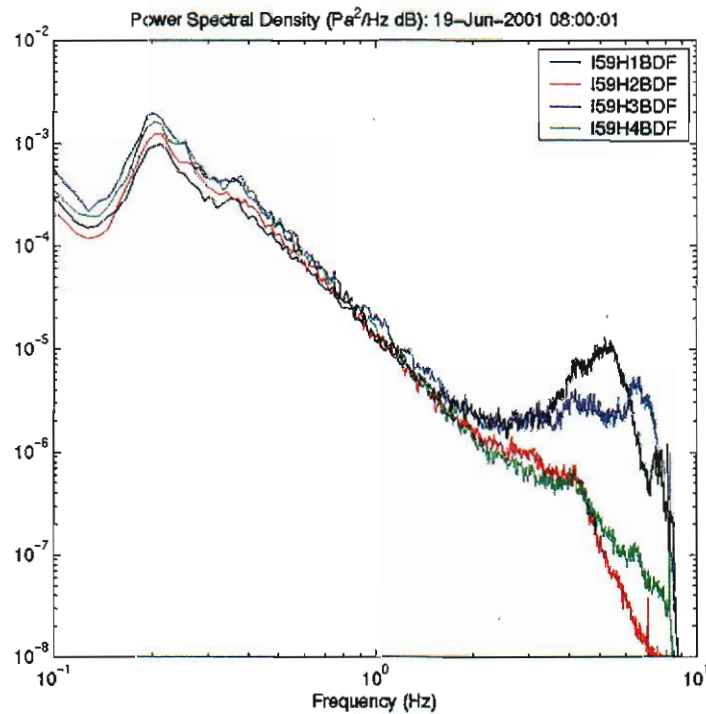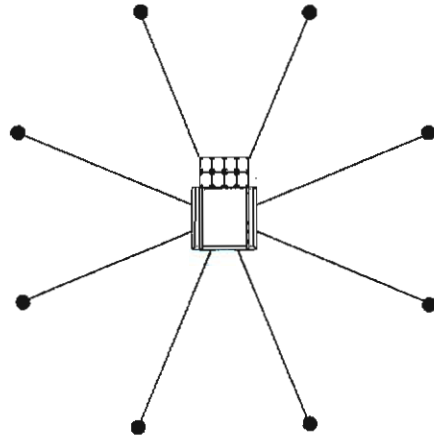
Figure 9: Wind-noise-reducing filter port arrangement (top) and resultant power-spectral density plot (below) from 5/18/01 21:00 to 5/23/01 22:18 UT. Mean wind speed was 0.963 m/s from 83.20°.

Figure 10: Wind-noise-reducing filter port arrangement (top) and resultant power-spectral density plot (below) from 5/23/01 22:18 to 5/25/01 23:08 UT. Mean wind speed was 0.846 m/s from 76.80°.
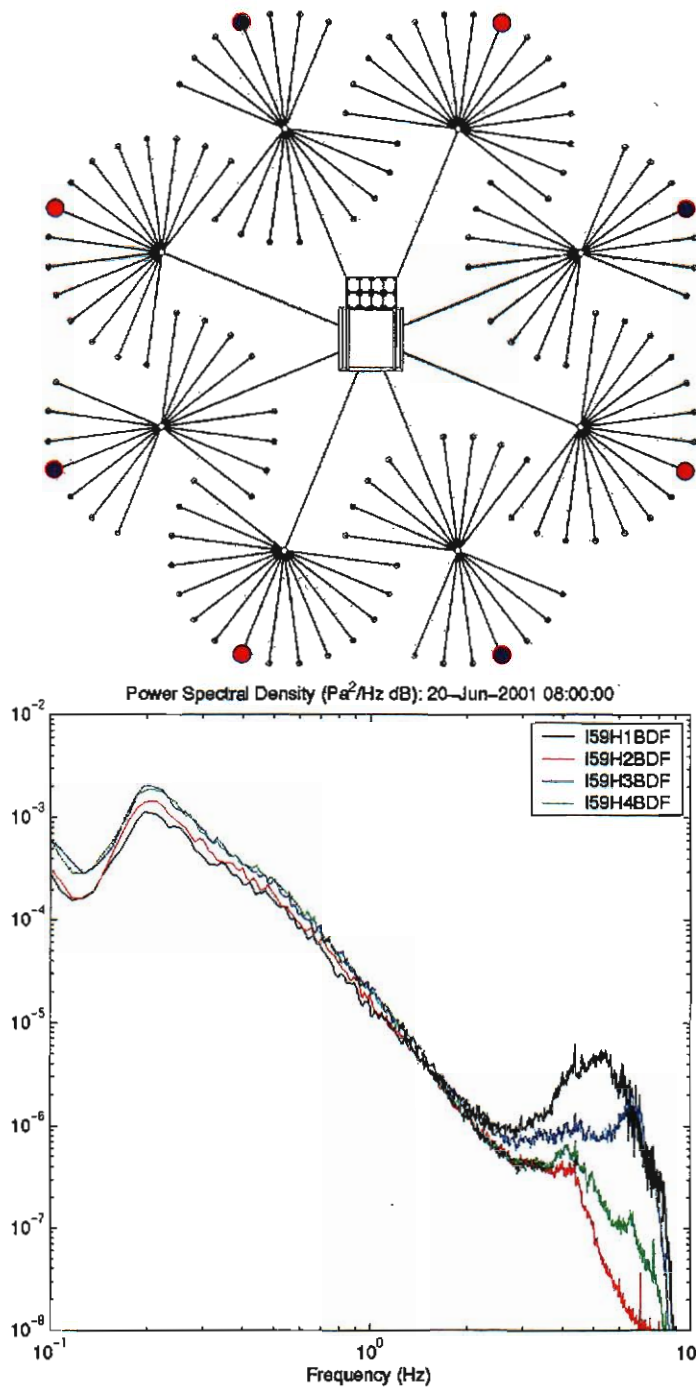
Figure 11: Wind-noise-reducing filter port arrangement (top) and resultant power-spectral density plot (below) from 5/25/01 23:08 to 6/2/01 00:13 UT. Mean wind speed was 0.959 m/s from 75.33°.

Figure 12: Wind-noise-reducing filter port arrangement (top) and resultant power-spectral density plot (below) from 6/2/01 00:13 to 6/14/01 19:10 UT. Mean wind speed was 0.959 m/s from 75.33°.

Figure 13: New wind filter at H3 (above) and power-spectral density plot (below) from 6/14/01 22:48 UT to 6/20/01 03:00 UT, showing results of new configurations at H3 and H4. Mean wind speed was 0.746 m/s from 82.23°. The porous hose configuration at H4 is similar in dimensions to H3, but with only four arms active.

Figure 14: Wind-noise-reducing filter port arrangement (top) and resultant power-spectral density plot (below) installed at 6/20/01 02:00 UT. Mean wind speed was 0.839 m/s from 80.79°.
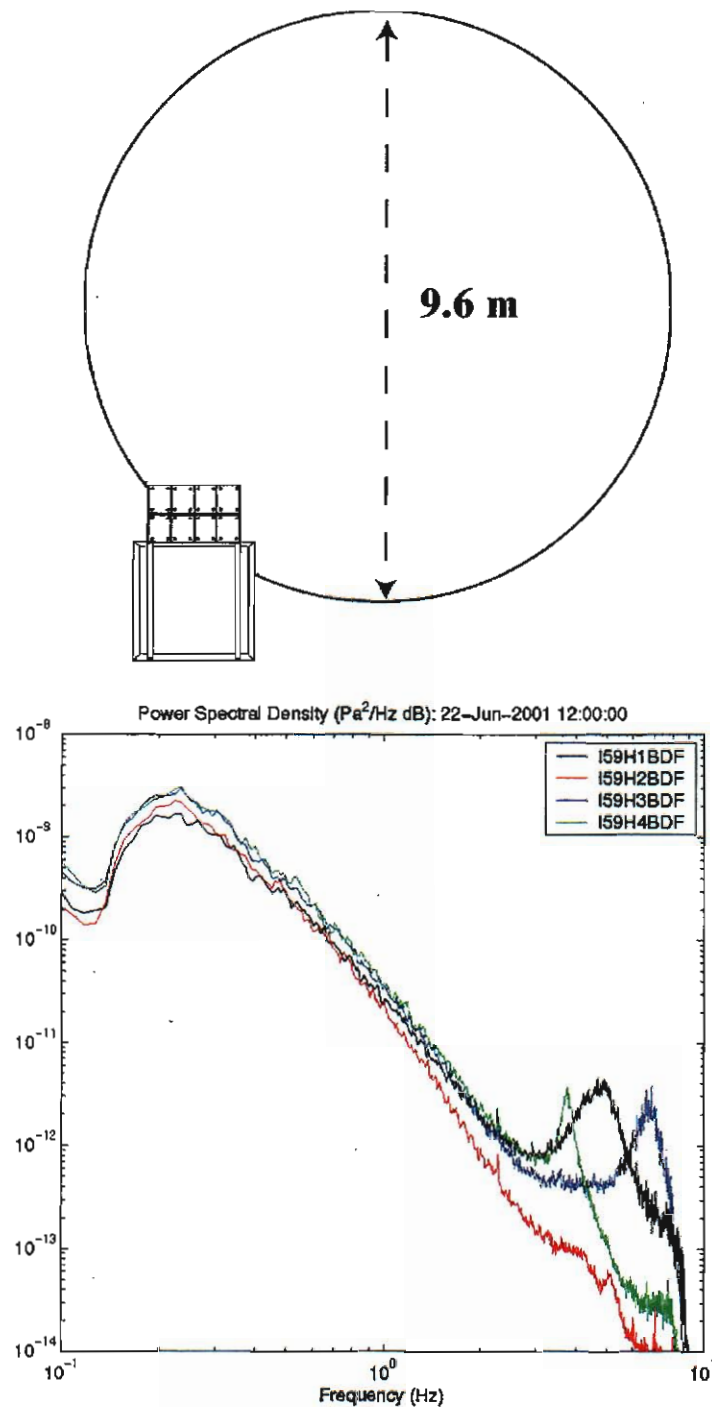
Figure 15: Diagram of circular double-open-ended hose filter applied 6/22/01 at H4 (above) and power-spectral-density plot (below) showing results of circular filter at H4 and partial closure of valves at H3. Mean wind speed was 0.905 m/s from 86.23°.
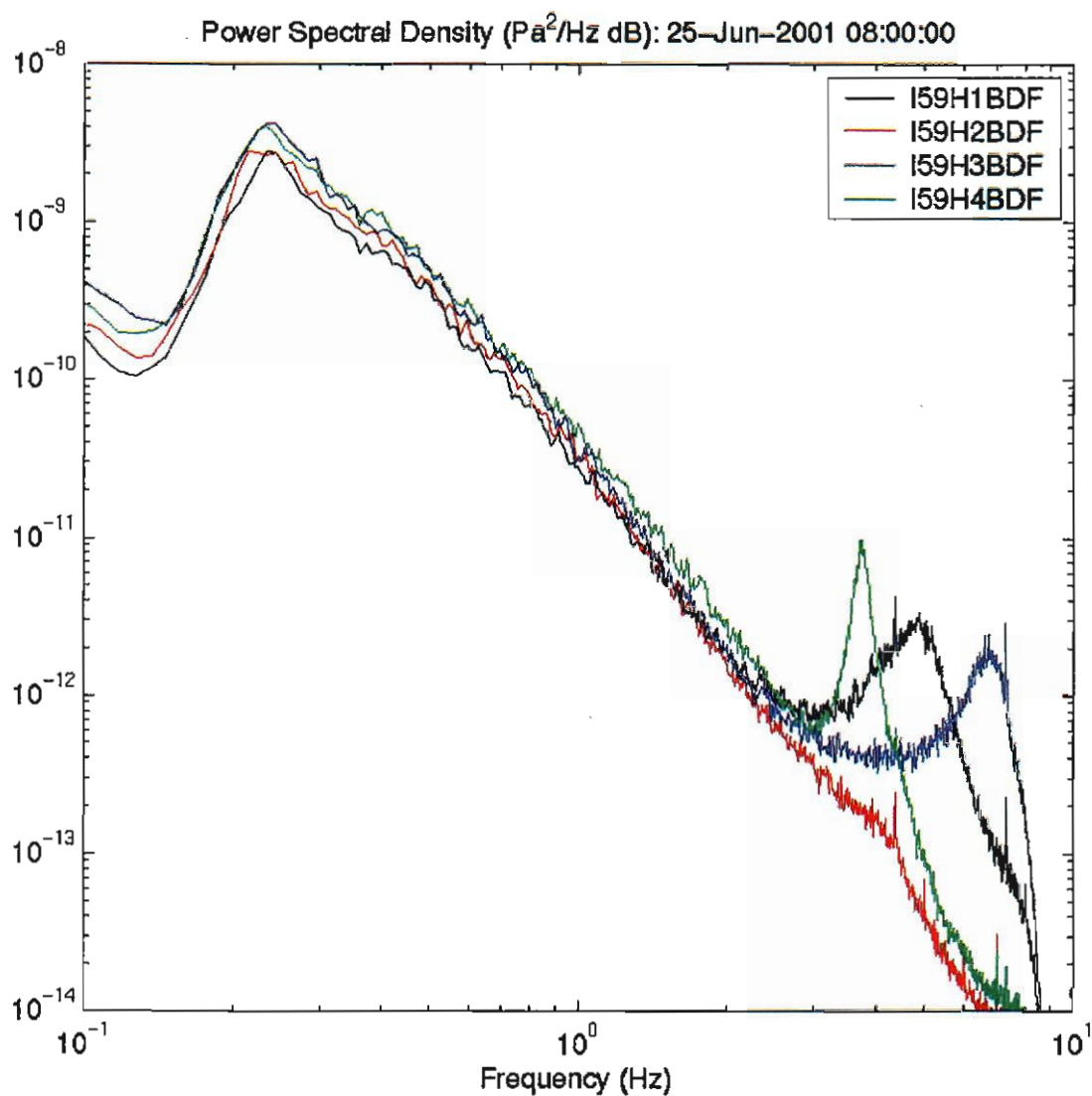
Figure 16: Power-spectral-density plot showing results of circular, single-open-ended porous hose filter applied 6/23/01 at H4. Mean wind speed was 0.868 m/s from 80.16°.
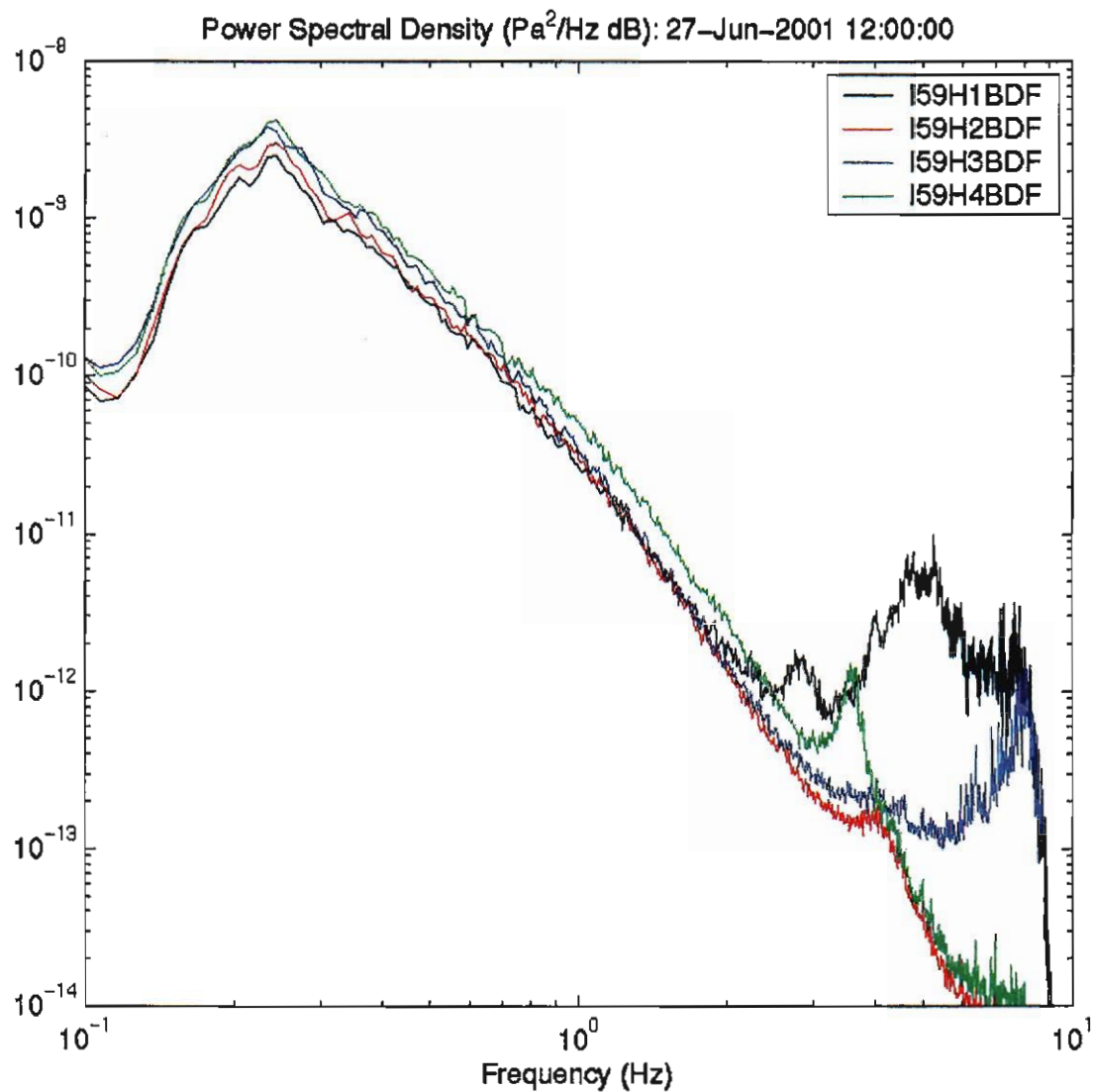
Figure 17: Power-spectral-density plot showing results of circular, single-open-ended porous hose filter applied 6/23/01 at H4. Mean wind speed was 0.415 m/s from 67.29°.
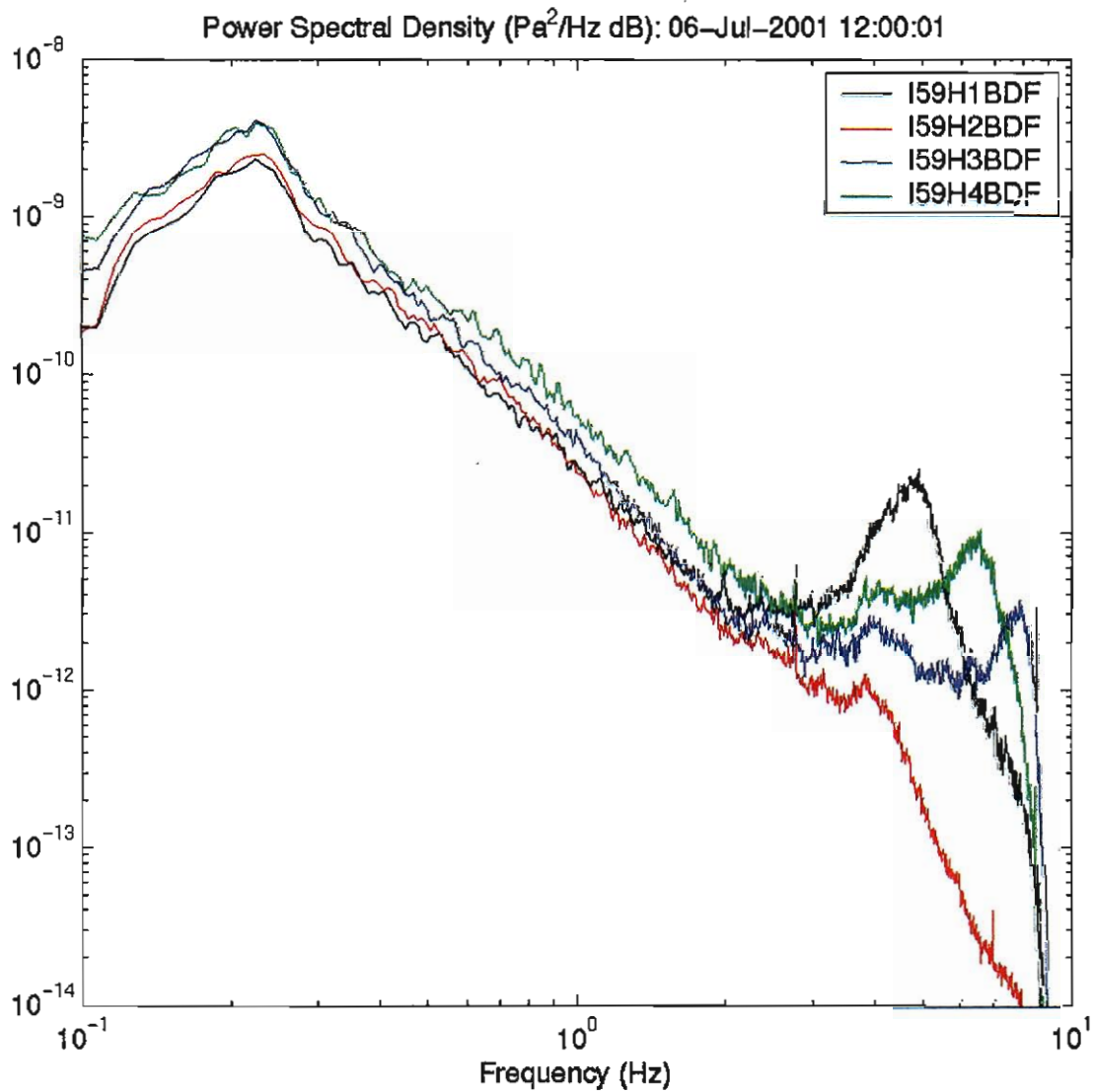
Figure 18: Power-spectral-density plot showing results o a single open port at H4. Mean wind speed was 0.742 m/s from 85.45°.
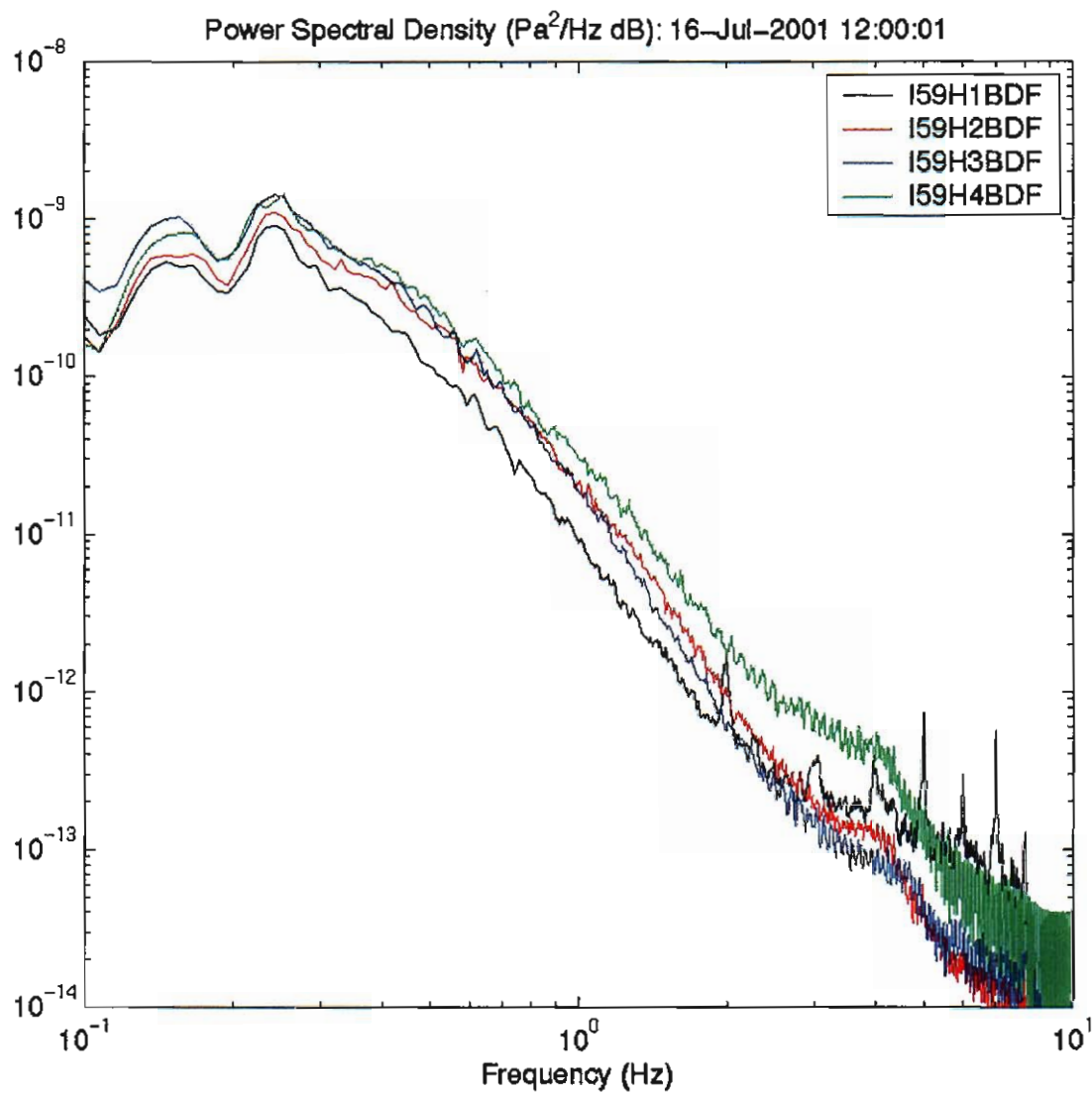
Figure 19: Power-spectral-density plot showing the results of installing identical porous-hose filters at all elements. Mean wind speed was 0.764 m/s from 80.35°.
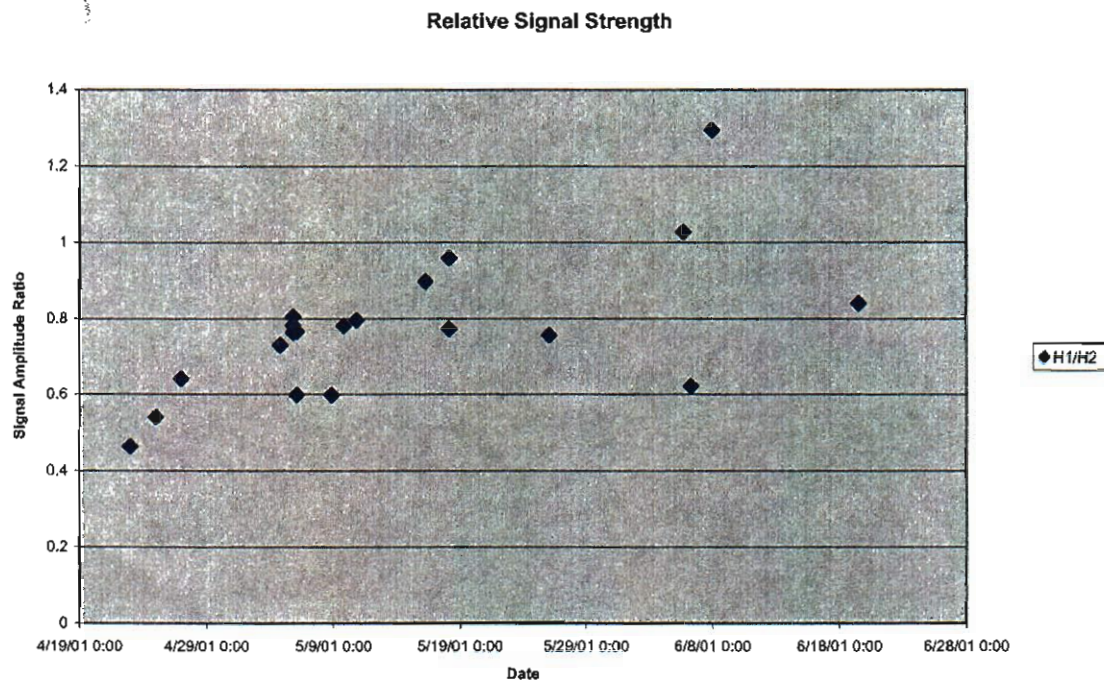
Relative Signal Strength

Figure 20: Plot showing relative signal strength of H1 as compared to H2 as a function of time. Optimal reliable signal strength occurs at around 5/19, during the life of the configuration shown in Figure 9.

DEPARTMENT OF DEFENSE

DEFENSE TECHNICAL
INFORMATION CENTER
8725 JOHN J. KINGMAN ROAD,
SUITE 0944
FT. BELVOIR, VA 22060-6201
2 CYS   ATTN: DTIC/OCA

DEFENSE THREAT REDUCTION
AGENCY
8725 JOHN J. KINGMAN ROAD,
STOP 6201
FT. BELVOIR, VA 22060-6201
2 CYS   ATTN: NTD/D. BARBER

DEPARTMENT OF DEFENSE
CONTRACTORS

ITT INDUSTRIES
ITT SYSTEMS CORPORATION
1680 TEXAS STREET, SE
KIRTLAND AFB, NM 87117-5669
2 CYS   ATTN: DTRIAC
        ATTN: DARE